A New Crystal Plasticity Formulation to Simulate Large-Strain Plasticity of Polycrystalline Metals at Elevated Temperatures

by

Edward D. Cyr

A thesis

presented to the University of Waterloo

in fulfillment of the

thesis requirement for the degree of

Doctor of Philosophy

in

Mechanical and Mechatronics Engineering

Waterloo, Ontario, Canada, 2017

Examining Committee Membership

The following served on the Examining Committee for this thesis. The decision of the Examining Committee is by majority vote.

External Examiner	Dr. Irene Beyerlein Professor, University of California Santa Barbara
Supervisor(s)	Dr. Kaan Inal Industrial Research Chair; Associate Professor
Internal Member	Dr. Hamid Jahed Associate Char, Graduate Studies; Professor
Internal Member	Dr. Adrian Gerlich Industrial Research Chair; Associate Professor
Internal-external Member	Dr. Hassan Baaj Associate Professor, Civil Engineering

Author's Declaration

This thesis consists of material all of which I authored or co-authored: see Statement of Contributions included in the thesis. This is a true copy of the thesis, including any required final revisions, as accepted by my examiners.

I understand that my thesis may be made electronically available to the public.

Statement of Contributions

The following co-authors have contributed to the current work as outlined below:

Professor Kaan Inal supervised this PhD thesis.

Dr. Raja K. Mishra provided EBSD measurements of the microstructure studied, provided various experimental data, such as coupon level experiments for calibrating and validation numerical frameworks.

Dr. Abhijit Brahme converted EBSD measurements to the synthetic microstructure for simulations, and he assisted the authors with editing parts of the work.

Professor Mohsen Mohammadi assisted in developing temperature dependent elasticity formulations and automating the M-K FLD framework. He also assisted the authors with editing parts of the work.

The balance of this work is my own.

Abstract

This dissertation explores the plasticity polycrystalline metals, with particular attention paid to aluminum and its alloys. Specifically aluminum Al-Mg sheet alloys, which are currently replacing steel parts for panel and some structural componentry in the automotive industry. At the forefront of this transition, is the problem of poor room-temperature formability of the aluminum sheet when compared to its steel counterparts. A promising solution to this has been the use of warm-forming to increase formability, preventing redesign of automotive parts from steel to aluminum (Li and Ghosh, 2003). In this thesis, a new constitutive framework and methodology is developed to accurately model elevated temperature behaviour of polycrystalline aluminum.

This study describes a picture of the physics behind slip dominated deformation in polycrystalline metals, and the mechanical characterization techniques used to determine modeling parameters for crystal plasticity. A review on modeling techniques and published work on the versatility of crystal plasticity theory and application is also presented. An initial model is then developed for a fully temperature dependent crystal plasticity framework. The model employs a generic hardening law to study the effect of temperature on material hardening, and conclusions are made on the lack of microstructural correlation between the model and physical behaviour of the material. The same framework is then implemented in the well known Marciniak-Kuzynski (1967) based limit strain formulation as an application study with Chang and Asaro (1981) type hardening. Temperature dependency is studied and formability is predicted for different aluminum alloys. The study reveals that, again, phenomenological-based hardening is only satisfactory for predicting elevated-temperature behaviour, and results are very sensitive to model input parameters.

In the second half of this dissertation, a physical model is carefully developed from fundamental dislocation theories. The model is formulated on the basis of accumulation of dislocations as the dominating strengthening mechanism in polycrystals, introduces recovery as a thermally activated process leading to temperature dependent softening. The model is used to study temperature dependency of slip deformation in pure aluminum, and the correlation between physical processes and model parameters. The model is able to capture and predict deformation response, as well as suggest explanation to the influence of temperature on microstructural behaviour. Finally, the model is applied to study the temperature dependency of microstructural parameters in 5xxx series Al-Mg sheet alloys. Experimental data is used to characterized material parameters at warm forming temperatures, and the model is used to predict stress-strain response. The model is then used to discuss the effect of temperature on two different alloys and suggests explanation on the microstructural causes leading to variation hardening behaviour between the two alloys over the temperature range studied. The work then concludes the improvement of model predictability, and the utility of such a model in microstructural design.

Acknowledgements

I would like to express my sincere gratitude to my supervisor Professor Kaan Inal for the years of support, leadership, assistance, and guidance he has provided me. My sincere thanks also goes to Dr. Abhijit Brahme and Dr. Mohsen Mohammadi for their amazing expertise, mentorship, and friendship for the past years during my PhD. Thank you also to Dr. Raj Mishra for his collaboration and knowledge of materials.

Next I would like to thank my friends and colleagues at the University of Waterloo, my coaches Jeff Slater, Jeff Beech, and Scott Allen for helping me achieve goals I never imagined possible, and my teammates on the Waterloo Varsity Curling and Swimming teams who have become one of the most important parts of my life.

Lastly, but definitely not least, I would like to express my love and thanks to my family. My mother Gisele Cyr, father and step-mother Ed and Anne-Marie Cyr, my sister Chantal Cyr, and all of my grand-parents, aunts, uncles, and cousins. I could not have done this without you.

This work was supported by the Natural Sciences and Engineering Research Council of Canada (NSERC) as well as the Automotive Partnership of Canada and General Motors of Canada.

Dedication

"I dedicate this thesis to my grandparents Donald White and Euclide Cléroux. No one has more love to give than you, and I thank you for everything that you have given me."

Table of Contents

List of Figures xi

List of Tables xvi

List of Symbols xvii

Chapter 1 – Introduction 1

1.1 Motivation 1

1.2 Objectives 3

1.3 Outline of Thesis 3

Chapter 2 – Background 5

2.1 Dislocations 5

2.2 Texture 9

Chapter 3 – Literature Review 12

3.1 Basic Phenomena and Terminology 12

3.2 Modeling Deformation 14

3.3 Crystal Plasticity Finite Element Modeling (CPFEM) 16

3.3.1 Phenomenological CPFEM 18

3.3.2 Physics Based CPFEM 20

3.3.3 Saimoto-Van Houtte Constitutive Model 20

3.3.4 Recrystallization 22

Chapter 4 – Part I: 25

A Three Dimensional (3D) Thermo-Elasto-Viscoplastic Constitutive Model for FCC Polycrystals 25

4.1 Background 26

4.2 Approach 28

4.3 Thermo-Elasto-Viscoplastic (TEV) Constitutive Model 29

4.3.1 Kinematics of Deformation 29

4.3.2 Constitutive Model 31

4.3.3 Temperature Dependency of Elastic Constants 31

4.3.3.1 Numerical Implementation 32

4.3.4 Shear Rates and Rate Sensitivity 33

4.3.5 Proposed Thermal Softening Model 34

4.3.6 Hardening Model 36

4.4 Finite Element Implementation 39

4.4.1 Forward Euler Algorithm 39

4.4.2 Construction of Finite Element Model 40

4.4.3 Construction of Microstructure 41

4.5 Results and Discussion 42

4.5.1 Uniaxial Tension 43

4.5.1.1 Material Calibration 43

        - 4.5.1.2 Temperature Dependence of Hardening Parameters 44
        - 4.5.1.3 Model Verification 46
    - 4.5.2 Simple Shear 47
        - 4.5.2.1 Model Validation 49
    - 4.5.3 Numerical Analysis 50
    - 4.5.4 Effect of Thermal Softening Sensitivity Index 54
    - 4.5.5 Elastic Stiffness Parameter Sensitivity 56
- 4.6 Conclusions 59

Chapter 5 – Part II: 61

Modelling Formability of Aluminum Alloys at Elevated Temperature Using a New Thermo-Elasto-Viscoplastic Crystal Plasticity Framework 61

- 5.1 Introduction 62
- 5.2 Thermo-Elasto-Viscoplastic (TEV) Crystal Plasticity Framework 64
- 5.3 Marciniak and Kuczynski (M-K) Formulation 68
- 5.4 Material Properties 69
    - 5.4.1 AA5754 69
    - 5.4.2 AA3003 70
- 5.5 Model Calibration 71
    - 5.5.1 AA5754 71
    - 5.5.2 AA3003 72
- 5.6 Results and Discussion 73
    - 5.6.1 FLDs 73
        - 5.6.1.1 AA5754 73
        - 5.6.1.2 AA3003 75
    - 5.6.2 Groove Orientations 77
        - 5.6.2.1 AA5754 77
        - 5.6.2.2 AA3003 78
    - 5.6.3 Effect of Thermal Softening 79
- 5.7 Proposed Model for Predicting FLD up to Warm Forming Regime 80
    - 5.7.1 Effect of Temperature on Hardening Parameters 80
    - 5.7.2 Effect of Temperature on Initial Imperfection 83
    - 5.7.3 FLD Predictions 84
- 5.8 Summary and Conclusions 85

Chapter 6 – Part III: 86

Temperature-Dependent Plasticity: A New Constitutive Formulation of Polycrystalline Metals 86

- 6.1 Introduction 87
- 6.2 Background 88
- 6.3 Work Hardening Model 91
    - 6.3.1 Dynamic Recovery 94
    - 6.3.2 Determination of Hardening Parameters 96

6.3.3 Elevated Temperature 99
6.4 Results 101
6.4.1 Stress-Strain Calibration 101
6.4.2 Work Hardening 102
6.4.3 Dynamic Recovery 103
6.4.4 Mean Slip Distance 105
6.4.5 Strain Rate Dependence 106
6.4.6 Model Validation 107
6.5 Discussion 110
6.6 Conclusion 114
Chapter 7 – Part IV: 115
Temperature-Dependent Plasticity: A New Constitutive Formulation using Crystal Plasticity for 5xxx Series Al-Mg Aluminum Alloys 115
7.1 Introduction 116
7.2 Constitutive Relations 117
7.2.1 Kinetics of Slip 118
7.2.2 Material Hardening 118
7.2.3 Critical Resolved Shear Stress (CRSS) 120
7.3 Problem Formulation 120
7.3.1 Stress-Strain Curves and Initial Texture 120
7.4 Results 122
7.4.1 Dynamic Strain Aging 123
7.4.1.1 Numerical Implementation 124
7.4.2 Temperature Dependency of Material Parameters 125
7.4.3 Mechanical Response of 5182-O 126
7.5 Discussion 127
7.5.1 Influence of Mg on Temperature Dependency 127
7.5.4 Strain Hardening 129
7.6 Conclusions 130
Chapter 8 – Conclusions 132
8.1 Elevated Temperature Behaviour 132
8.2 Developed Model 132
8.3 Recommendations for Future Work 133
References 135
Appendix 148

List of Figures

Figure 1-1 Continuous casting of aluminum sheet. After initial rolling, sheet is hot or cold rolled to final dimensions and coiled or cut for distribution. 2

Figure 2-1 Edge dislocation propagation (top) and screw dislocation propagation (bottom) through a crystal lattice. Edge dislocation motion acts parallel to shear stress while screw dislocation motion is normal to applied shear stress. 6

Figure 2-2 Burgers circuit around an edge dislocation and screw dislocation. 7

Figure 2-3 Geometry of slip in crystals. In general, $(\lambda + \phi) \neq 90°$. The Burgers vector of an edge dislocation is perpendicular to the line of dislocation. The Burgers vector of a screw dislocation is parallel to the line of dislocation (Hull and Bacon, 2001). 8

Figure 2-4 (001) (left) and (111) (right) Pole figures for typical FCC rolled texture (Brahme, 2005). 10

Figure 2-5 {111} Pole figures for computationally generated textures of: (a) Cube component; (b) Goss component; (c) Brass component; (d) Copper component; (e) S component (Rossiter et al., 2013). 10

Figure 2-6 Example of orientation distribution in Bunge Euler Space for computationally generated textures from Figure 2-5 with (a) all components having equal volume fraction, (b) with high Brass, and (c) without Brass (Rossiter et al., 2013). 11

Figure 3-1 Flow stress and strain hardening of anisotropic materials are tensor quantities (Roters et al., 2010). 17

Figure 4-1 Decomposition of total deformation tensor to plastic, thermal expansion, and elastic - rigid body rotation components. 29

Figure 4-2 Calculated adiabatic elastic stiffness constants of aluminum obtained from equation (4.22) 33

Figure 4-3 Comparison of thermal slip-softening models. 37

Figure 4-4 The effect of softening intensity index on the thermal softening factor obtained from equation (4.29) for proposed model for aluminum with θ_m = 873K. 37

Figure 4-5 Initial FE per grain microstructure and texture pole figure for uniaxial tension simulation. 41

Figure 4-6 3D finite element mesh with visible voxelized grains. 41

Figure 4-7 (a) Measured texture, and (b) statistically equivalent generated texture. 42

Figure 4-8 Experimentally measured and simulation uniaxial stress-strain results. 43

Figure 4-9 Single slip hardening exponent vs. temperature and equation (4.32). 45

Figure 4-10 Reference CRSS vs. temperature and equation (4.33). 45

Figure 4-11 Reference single slip shear hardening rates vs. temperature using equation (4.34). 46

Figure 4-12 Simulated vs. experimental uniaxial tension stress-strain curves using predicted hardening values. 48

Figure 4-13 Contours of Effective Strain (Von-Mises) at 25ºC and 232ºC. The overall effective strain localization appears to have no temperature dependency. 48

Figure 4-14 Initial experimental texture (a) and statistically equivalent initial texture (b). 49

Figure 4-15 Normalized shear stress vs. shear strain for experimental (Pandey et al. 2013) and simulated AA5754 polycrystal at 25ºC, 150ºC, and 232ºC. 50

Figure 4-16 Pole figures for experimentally measured texture of deformed specimens ($\gamma/\sqrt{3} = 0.2$) at 25ºC and 232ºC from experiment (Pandey et al. 2013). 51

Figure 4-17 Pole figures of deformed texture ($\gamma/\sqrt{3} = 0.2$) at 25ºC and 232ºC from CPFEM simulation. 51

Figure 4-18 Simulation of simple shear deformation to $\gamma = 0.3$ at 25ºC, 150ºC and 232ºC with contours of local accumulated shear (γ_a) and outlined "hot spots" with high local accumulated shear. 52

Figure 4-19: Macroscopic shear stress-shear strain curves for 25ºC, 150ºC and 232ºC simulations corresponding to the contour plots presented above. 53

Figure 4-20 Simple shear macroscopic hardening rates for 25ºC, 150ºC and 232ºC. 53

Figure 4-21 Simple Shear average single-slip shear rates at 25ºC, 150ºC and 232ºC. 54

Figure 4-22 Uniaxial tension average macroscopic stress for varying thermal softening sensitivity. 55

Figure 4-23 Uniaxial tension macroscopic hardening rates for varying thermal softening sensitivity. 55

Figure 4-24 Constant C_{ij} vs. temperature variable C_{ij} under uniaxial tension at 232ºC. 56

Figure 4-25 Uniaxial stress-strain response at 25ºC for elastic constants corresponding to Aluminum, Copper, and Lead. 58

Figure 4-26 Uniaxial stress-strain response at 148ºC for elastic constants corresponding to Aluminum, Copper, and Lead. 58

Figure 4-27 Uniaxial stress-strain response at 232ºC for elastic constants corresponding to Aluminum, Copper, and Lead. 59

Figure 5-1 Decomposition of total deformation tensor to plastic, thermal expansion, and elastic - rigid body rotation components. 64

Figure 5-2 Schematic of the sheet metal, the groove, and geometric parameters used for the M-K FLD analysis. 68

Figure 5-3 {111} stereographic pole figure calculated using Electron Backscatter Diffraction (EBSD) data taken from continuous cast AA5754. The peak intensity is 3.64 times random. 70

Figure 5-4 {111} stereographic pole figure of AA3003 sheet obtained from Electron Backscatter Diffraction (EBSD) data. The peak intensity is 3.16 times random. 70

Figure 5-5 Uniaxial stress-strain curves for AA5754 and corresponding fitted curves generated with TEV crystal plasticity simulation at different temperatures. 71

Figure 5-6 Uniaxial stress-strain curves for AA3003 at various temperatures and corresponding fitted curves generated with TEV crystal plasticity simulation at different temperatures. 72

Figure 5-7 Predicted FLDs at 25ºC, 150ºC, and 200ºC along with the corresponding experimental FLD data (Naka et al. 2001) for AA5754. The groove orientation is allowed to change in order to record the minimum limit strains. 74

Figure 5-8 Predicted FLDs at 25ºC, 150ºC, and 200ºC along with the corresponding experimental FLD data for AA5754 texture when the groove orientation is fixed at 0º in the biaxial region to predict the limit strains. 75

Figure 5-9 Comparison of FLDs with and without temperature dependent hardening at 200ºC along with the corresponding experimental FLD data for AA5754 texture. It is clear that correctly modeling hardening behaviour provides closer fit between simulation and experimental data. 76

Figure 5-10 Predicted FLDs at 25ºC, 200ºC, and 250ºC along with the corresponding experimental FLD data for AA3003. The groove orientation is allowed to change in order of record the minimum limit strains. 77

Figure 5-11 The critical groove orientation corresponding to lowest predicted limit strain versus loading path, ρ, for AA5754. 78

Figure 5-12 The critical groove orientation corresponding to lowest predicted limit strain versus loading path, ρ, for AA3003. 78

Figure 5-13 Effect of thermal softening resistance parameter “ p ” on forming limits for AA5754 at 200ºC. 79

Figure 5-14 Effect of thermal softening resistance parameter “ p ” on groove orientations resulting in lowest limit strains for AA5754 at 200ºC. 80

Figure 5-15 Initial hardening rates and saturated hardening rates for Asaro hardening law determined from AA3003 at 25ºC, 200ºC, and 250ºC, along with corresponding fits using equation (5.15) and (5.16). 82

Figure 5-16 Initial slip strength and saturated slip strength from Asaro hardening law determined from AA3003 at 25ºC, 200ºC, and 250ºC, along with corresponding fits using equation (5.17) and (5.18). 82

Figure 5-17 Initial imperfection for AA3003 (from section 6.5), curve fitted using equation (6.20). 83

Figure 5-18 Simulated limit strains for AA3003 at 100ºC plotted with experimentally determined limit strains. Parameters for the simulation were determined using temperature dependency equations (5.15)–(5.18) and (5.20). 84

Figure 5-19 Simulated limit strains for AA3003 at warm forming temperatures. Hardening parameters and initial imperfection are determined using equations (5.15)–(5.18) and (5.20) and fitting parameters in tables 5-7 and 5-8. 85

Figure 6-1 Geometry of randomly distributed obstacles. (Friedel, 1964). 90

Figure 6-2 A schematic representation of recovery mechanisms in two components, at low temperatures recovery is assisted by cross-slip and at high temperatures recovery is dominated by vacancy climb. 94

Figure 6-3 (left) polynomial fit to experimental stress-strain data of pure aluminum and (right) log(λ) and log(ℓ) jointly plotted vs. log(τ) with ϕ^{-1} adjusted to match log(λ) and log(ℓ) at low strains. The dotted tangent line depicts the minimum mean slip distance λ_{min}. The experimental stress-strain data is taken from Kocks (1976). 98

Figure 6-4 Fitted – curve (solid line) and its match with the experimental 99.99% pure aluminum data at 300K (Kocks 1976). The contribution of individual material hardening parameters and recovery is also presented as dashed lines. The geometric sum of the Λ_s and Λ_g curves produce the ‘Fit’ curve. 99

Figure 6-5 Experimental (points) and simulated (lines) $\tau - \gamma$ stress-strain curves at 200K to 600K for commercially pure aluminum ($\dot{\epsilon} = 1/min$). Hardening parameters were determined by the method presented in section 3 and values presented in Table 6-1. 102

Figure 6-6 Work hardening versus flow stress of equation (6.35) at the five fitted temperatures. The work hardening is normalized by the temperature dependent shear modulus. The dotted line denotes an estimate of the τ_{III} transition from stage II to stage III. The dashed line represents the end of the experimental data with hardening extrapolated to show the model–predicted stage IV type hardening behaviour where the hardening plateaus. 104

Figure 6-7 Presents (left) the dynamic recovery factor Ω vs. temperature for pure aluminum and equation (6.27) with parameters determined from fitting in (right), the dynamic recovery factor Ω plotted against exp $\left(-Q_m/3RT\right)$ with, A_0 and Ω_0 determined from the linear fit. 104

Figure 6-8 The linear dependencies of mean slip distance parameter and temperature at $\dot{\varepsilon} = 1/min$ are shown with blue (Λ_g) and orange (Λ_s) points representing the values determined from fitted data. The dotted lines highlight the linearity of the inverse square root of Λ_s and the inverse of Λ_g relationships with temperature. At 200K, the steep increase in $1/\Lambda_g$ alludes to a mechanism activation point, having significant effect on the geometric necessary dislocations. 106

Figure 6-9 The vertical translation of slip distance parameters from $\dot{\varepsilon} = 1/min$ in blue (from Figure 6-8) to $\dot{\varepsilon} = 100/min$ in orange represents the strain-rate dependence of the mean slip distance parameters. In both cases, increasing the strain-rate results in an increase in the inverse slip distance—corresponding to a decrease in the mean slip distance of both statistically-stored and geometrically-necessary dislocation types. 108

Figure 6-10 The measured low strain rate (blue) and predicted high strain rate (orange) dynamic recovery factors for pure aluminum between 300K and 600K. The open point represents the calibrated recovery factor used to determine the predicted values (dotted line) at higher temperatures. Although 200K is not shown, the recovery factor at both strain rates corresponds to the same $\Omega_0 = 2.5$. 109

Figure 6-11 Predicted shear stress-strain curves for the four high strain rate ($\dot{\varepsilon} = 100/min$) and high temperature conditions corresponding to the material parameters shown in Figures 6-9 and 6-10. The 300K curve was calibrated to determine the high strain rate properties for the higher three temperatures. Experimental curves for 500K and 600K were only available to approximately 10% engineering strain. 110

Figure 6-12 A plot of the inverse of geometric slip distance parameter versus the inverse root of statistical slip distance parameter. Both fitted ($\dot{\varepsilon} = 1/min$) and predicted $\dot{\varepsilon} = 100/min$ data points fall coincident with the dotted line, representing the constant ratio between these two parameters over the studied range of strain rates and temperatures. The utility of this diagram is the precise determination of the Λ_g parameter upon measuring Λ_s by the method outlined in section 6-3. 111

Figure 6-13 shows the individual contributions of the statistically-stored and geometrically-necessary dislocations according to the model. The plateau behaviour of the statistically-stored contribution represents an equilibrium between dislocation storage and recovery, and occurs at lower strains with increasing temperature. Solid black curves correspond to the fitted curves for 300K and 500K at $\dot{\varepsilon} = 1/min$ and hardening parameters shown in Figures 6-9 and 6-10. 112

Figure 6-14 The plots show the sensitivity of the material hardening parameters Λ_s (left) and Λ_g (right) with values denoted at the end of each curve and all other parameters held constant. Solid black curves correspond to the fitted curves for 300K and 500K at $\dot{\varepsilon} = 1/min$ and hardening parameters shown in Figures 6-9 and 6-10. 113

Figure 6-15 Presented is the recovery factor Ω sensitivity with values for recovery denoted at the end of each curve and all other parameters held constant. Solid black curves correspond to the fitted curves for 300K and 500K at $\dot{\varepsilon} = 1/min$ and hardening parameters shown in Figures 6-9 and 6-10. 113

Figure 7-1 True stress-true strain curve (reproduced from original data published in Abedrabbo et al., 2007). 121

Figure 7-2 {111} recalculated pole figure of rolled sheet AA5754-O used as input. 121

Figure 7-3 ODF of the input AA5754-O sheet. 122

Figure 7-4 Simulated stress-strain curves at 25ºC, 148ºC, 177ºC, 204ºC, 232ºC, and 260ºC and experimental data plotted as points. 123

Figure 7-5 Stress-strain curves with and without the solute drag effect for the simulated polycrystal and cube single crystal at room temperature. For simulating solute drag $f_c = 0.85$ and $\dot{\gamma}_1 = 10^3\ s^{-1}$ provided the best results. 125

Figure 7-6 Temperature dependency of mean slip distance parameters for simulated AA5754-O. 125

Figure 7-7 Temperature dependency of dynamic recovery factor for simulated AA5754-O with exponential according to equation (7.10). Fitting constants were determined to be $\Omega_0 = 3.0$ and $A = 2.9 \times 10^3$ and activation energy for diffusion Q_m taken from Cyr et al., (2016) for aluminum. R is the gas constant. 126

Figure 7-8 Simulated stress-strain curves for 5182-O at 25ºC, 148ºC, 177ºC, 204ºC, and 260ºC and experimental data plotted as points. 127

Figure 7-9 Temperature dependency of dynamic mean slip-distance parameters for simulated AA5182-O and AA5754-O for comparison. 128

Figure 7-10 Temperature dependency of dynamic recovery factor for simulated AA5182-O and AA5754-O for comparison with equation (7.10). Fitting constants for AA5182 were determined to be $\Omega_0 = 3.5$ and $A = 3.9 \times 10^3$ and activation energy for diffusion Q_m taken from Cyr et al., (2016) for aluminum. R is the gas constant. 129

Figure 7-11 Normalized Work hardening versus flow stress of simulated stress-strain curves for AA5182. The inset plot highlights the transition of the 25ºC across the intermediate temperature curves due to the solute drag effect. 130

List of Tables

Table 2-1 Common texture components in FCC metals. 10

Table 3-1 Applications of the CPFE method (Roters et al., 2010). 19

Table 4-1 Value of parameters in equation (4.22) (Varshni, 1970). 33

Table 4-2 Chemical composition of AA5754 aluminum alloy (wt%). 41

Table 4-3 Material hardening properties used to generate stress-strain curves in Figure 4-8. 44

Table 4-4 Single-slip hardening parameters. Values in white were used in calibration while shaded values were predicted from equations (4.32) to (4.34). 46

Table 4-5 Elastic stiffness parameters for Al, Cu, and Pb (from Varshni, 1970). 57

Table 5-1 Chemical composition of AA5754 aluminum alloy. 69

Table 5-2 Chemical composition of AA3003 aluminum alloy. 70

Table 5-3 Material parameters for Asaro-Lowe hardening law (Harren et al. 1989) at three temperatures using AA5754 texture. 72

Table 5-4 Material parameters for Asaro hardening law at three fitted simulation temperatures using AA3003 texture. 73

Table 5-5 The imperfection parameter f associated with the simulated temperatures to generate FLDs for AA5754. 73

Table 5-6 The imperfection parameter f associated with the simulated temperatures to generate FLDs for AA3003. 76

Table 5-7 Fitting values using equation (5.15)–(5.18) for Asaro hardening parameters and AA3003 texture. 83

Table 5-8 Fitting values using equation (6.20) for initial imperfection and AA3003 texture. 83

Table 6-1 Measured hardening parameters of 99.99% pure aluminum at 200K - 600K taken at strain rate of $\dot{\varepsilon}$ = 1/min. The value for τ_0 was scaled with shear modulus $\mu(T)$ such that τ_0/μ is constant, as determined from Varshni (1970). 102

Table 7-1 Chemical composition of aluminum alloys (wt%). 120

Table 7-2 Hardening parameters from 5754-O simulated uniaxial tension tests. Slip distance parameters are in units of microns and were calculated from their inverse. 122

Table 7-3 Hardening parameters from 5182-O simulated uniaxial tension tests. Slip distance parameters are in units of microns and were calculated from their inverse. 127

List of Symbols

A, A^{-1}	area, annihilation factor
$\tilde{A}$	slip patch area
A_0	recovery proportionality constant
a	hardening exponent (exponential)
α	obstacle strength parameter
α_T	thermal expansion coefficient
$^{\alpha}$, $_{\alpha}$	slip system (superscript/subscript alpha)
b	burgers vector
β	mean slip approximation exponent
C_1	mean slip approximation constant
C_{ij}	reduced elastic moduli
c_{ij}^0	elastic constants at absolute zero
D	symmetric (stretch) of velocity gradient
D, D_0	diffusion coefficients
D^*	elastic component of stretch
D^θ	thermal component of stretch
D^P	plastic component of stretch
δ	distance traveled by diffusing particle
η_f	bulk elastic constant
F	force
$\varepsilon, \dot{\varepsilon}$	true strain, strain rate
$\dot{\varepsilon}_0$	reference strain rate ($10^7 s^{-1}$)
F	deformation gradient
F^*	elastic-rigid rotation deformation gradient
F^θ	thermal deformation gradient
F^P	plastic deformation gradient
F_c	critical force
F_0	thermal activation energy
f	imperfection parameter
f_c	critical slip ratio for jerky flow
ΔG	activation energy
g_α	slip system strength
γ^a	accumulated slip (shear)
$\gamma^\alpha, \dot{\gamma}^\alpha$	slip shear, shear rate
$\dot{\gamma}_0$	reference slip rate
$\dot{\gamma}_1$	reference slip rate for jerky flow behaviour
H_m	activation enthalpy for grain boundary mobility
h	outside band thickness (M-K analysis)
h_b	inside band thickness (M-K analysis
h_β	single slip hardening rate
$h_{\alpha\beta}$	slip hardening matrix
h_0	initial hardening parameter
h_s	saturated hardening parameter
$\mathbf{I}$	identity tensor
J	Jacobian (det(F))
$\mathcal{K}$	proportionality constant (diffusion)
k	Boltzmann constant
κ	proportionality constant (dislocation array)
$\mathbf{L}$	elastic tensor
L	velocity gradient
L^*	elastic-rigid rotation velocity gradient
L^θ	thermal velocity gradient
L^P	plastic velocity gradient
l, ℓ	inter-obstacle spacing
λ	angle between traction vector and slip direction, dislocation mean slip-distance/ mean free path
λ_e	dislocation line energy
λ_s	mean slip-distance of statistically-stored dislocations
λ_g	mean slip-distance of geometrically-necessary dislocations
Λ_s	statistically-stored mean slip-distance parameter
Λ_g	geometrically-necessary mean slip-distance parameter
M	Taylor Factor
M_0	grain boundary mobility
m	slip rate exponent
m^α	slip plane normal vector
M_α^*	stretched and rotated slip plane normal vector
μ, μ_f	shear modulus
N	volume density of slip patches (Taylor analysis)
$\mathcal{N}$	number of vacancies reaching cell walls
n	exponential proportionality constant, hardening exponent
n_0	vacancy density
Ω	recovery factor
Ω_0	recovery factor (cross-slip)
$\Omega(\dot{\gamma}, T)$	recovery factor (vacancy-climb)
P	dislocation perimeter geometry factor
P_α	symmetric Schmidt tensor
p	slip softening exponent
$\mathcal{P}$	stored deformation energy
Q	orientation matrix
Q_m	energy of vacancy diffusion

R	dislocation bowing radius, gas constant
ϕ	angle between traction vector and slip plane normal, geometric factor (mean slip analysis)
ϕ_1, Φ, ϕ_2	Bunge Euler angles
ψ	dislocation breaking angle
ψ_1	groove angle (M-K analysis)
$q_{\alpha\beta}$	latent hardening matrix
ρ	planar dislocation density
ρ	proportional loading constant (M-K analysis)
ρ_g	density of geometrically-necessary dislocations
ρ_s	density of statistically-stored dislocations
ρ_T	total dislocation density
ρ_{Mg}	density of solute Mg
$\rho^{\alpha}_{GN(e)}$	edge-type geometrically-necessary dislocation density
$\rho^{\alpha}_{GN(s)}$	screw-type geometrically-necessary dislocation density
S	Read-Shockley grain boundary energy
s^{α}	slip direction vector
S^{*}_{α}	stretched and rotated slip direction vector
s_{ij}	temperature dependent coefficient of elastic moduli
σ	Cauchy stress tensor
σ_0	mechanical strength, yield stress
$\dot{\sigma}^0$	viscoplastic stress rate
$\overset{\nabla}{\sigma}$	Jaumann rate of Cauchy stress tensor
T	temperature
T_s	thermal softening factor
T_m, θ_m	melting temperature
$t, \bar{t}$	wait time for vacancy to reach cell wall
t_{ij}	temperature dependent coefficient of elastic moduli
τ, τ_0	Kirchoff stress tensor, shear stress, shear strength
$\hat{\tau}$	obstacle strength (mechanical threshold model)
$\overset{\nabla}{\tau}$	Jaumann rate of Kirchhoff stress tensor
τ_{th}	theoretical critical shear stress
τ^{α}	resolved shear stress
$\tau^{\alpha}_c, \tau^{\alpha}_s, \tau^{\alpha}_y$	slip shear strength
$\theta, \dot{\theta}$	temperature, temperature rate of change
θ	strain hardening rate
V	volume
v_{disl}	dislocation velocity
v	grain boundary velocity
W	anti-symmetric (spin) of velocity gradient
W^*	elastic-rigid rotation spin
W^P	plastic spin
W_{α}	anti-symmetric Schmidt tensor
χ	proportionality constant for temperature dependent hardening

Chapter 1

Introduction

1.1 Motivation

The need for vehicle light weighting to achieve CAFÉ regulations is one of the forefront issues faced by automotive manufacturers (NAO Sciences, 2002). Aluminum has been presented as a good solution due to its relatively high strength to weight, when compared to steel providing excellent corrosive properties. The forecast for aluminum content in vehicles based on historical trends is 550lbs per light vehicle by 2025, far above the current content of approximately 350lbs. This increasing trend is driven further by the development of new aluminum applications.

Advances in aluminum engineering over the last few decades has led to the invention of a wide number of alloys for many applications. Typically, these alloys are labeled as AAxxxx where AA represents “aluminum alloy” followed by a 4-digit number corresponding to the major alloying element(s). For example AA5754 is a common aluminum alloy in automotive applications such as door panels with major alloying element magnesium (for all AA5xxx series alloys). AA6xxx series alloys are another common automotive alloys with magnesium and silicon as the major additive elements (Ravichandran and Prasad, 1991).

Particular to automotive applications, sheet aluminum (as well as extrusions) has been widely used to replace steel for vehicle components, including door outers/inners, roof panels, deck lids, etc. Although sheet aluminum has significantly improved corrosion resistance and strength to weight properties, it is still outperformed in formability compared to steel. This is a significant drawback as vehicle designs are becoming more intricate and demands for increased formability are growing. Thus, several methods have been provided to improve the formability of aluminum sheet. Controlling the alloying content and alloying elements can improve the materials ductility, but at the cost of some desired properties such as strength. The material microstructure can also be controlled; however, this requires complex material processing and is difficult to control. The simplest way to increase formability is through warm and/or hot forming (Li and Ghosh, 2003, 2004).

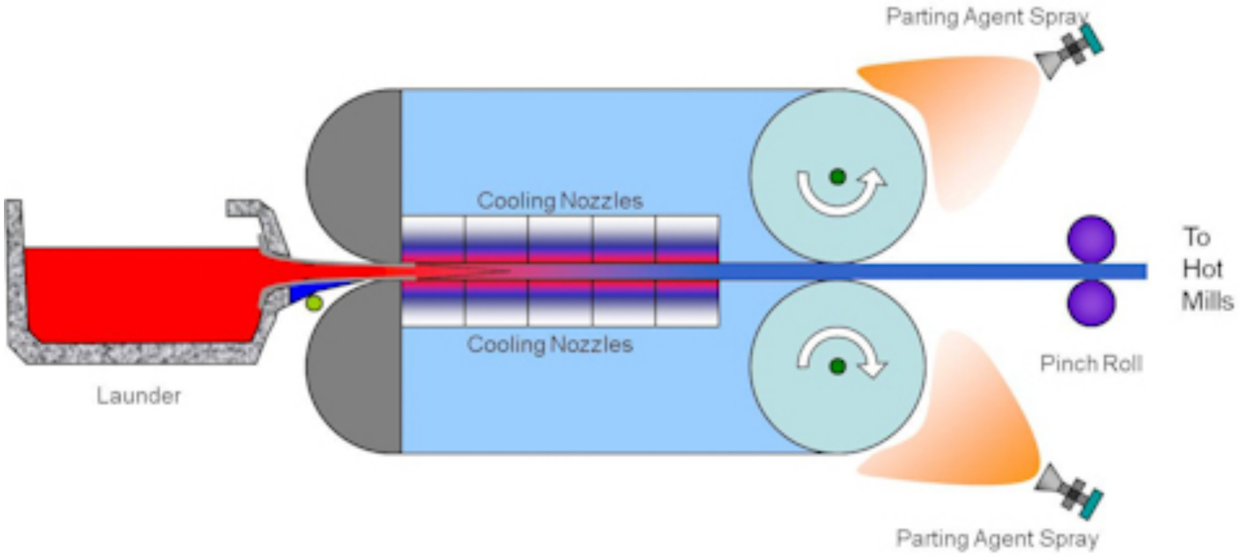

Figure 1-1 Continuous casting of aluminum sheet. After initial rolling, sheet is hot or cold rolled to final dimensions and coiled or cut for distribution[1].

The overall objective of this thesis is to develop a thorough 3-dimensional mechanism based material model for the thermo-mechanical processing of aluminum alloys. Typical automotive aluminum sheet alloys are AA5xxx and AA6xxx; however, this study is not limited to those two grades and other available alloys will also be studied. The goal of the model is to predict the material response, which depends greatly on the linkage between initial microstructure and microstructure evolution, thermo-mechanical history, and alloy chemistry.

A typical manufacturing process for a sheet or panel component on a vehicle starts with continuous casting and rolling as shown in Figure 1-1. This process usually includes: roll casting to produce the initial sheet, homogenization, cold rolling, heat treating, cold/warm forming, stamping. Additional heat treatments may be used, such as intermediate annealing to improve formability, making them expensive for high production parts. Another common problem is poor surface finish and fracture limiting formability when compared to steel counterparts. Understanding the cause and being able to predict this behaviour using a mechanistic model based on the material physics can open an opportunity to improve forming processes and even engineer new materials.

The structure of aluminum can be discussed in terms of crystal structure and microstructure. Crystal structure is the position of atoms within the unit cell, while microstructure is the arrangement of phases and defects within a material. All aluminum alloys have a face-centered cubic (FCC) crystal structure. Microstructure is completely determined by the manufacturing process. In cold rolled aluminum sheet, some microstructural aspects tend to be similar, such as texture, grain size, and grain shape; however, different alloying elements significantly affect the formation of precipitates and/or secondary phases. In this research, the cold rolled state, including any subsequent heat treatments, will be considered as the initial state.

---

[1] http://www.novelis.com/en-us/pages/Casting.aspx

In order to optimize properties of the final product, there must be a good understanding of the physics of microstructure evolution. Many different methods have been employed to study material behaviour and microstructure evolution during production. One such method is experimental trials where differences in material responses are measured as process variables are varied. This is time consuming and only allows for analysis before and after the process is completed for a limited number of process conditions. The most effective method is to develop mathematical models and validate them experimentally. Similarly, there is a wide range of mathematical models available; however, due to the complexity of this problem in its entirety, the available models are catered to a specific range of conditions and need extensive calibration.

1.2 Objectives

Up to the knowledge of the authors, there is no physically based constitutive model that can be used to accurately describe and predict metal forming behaviour at any temperature (up to hot forming at elevated temperatures) for polycrystals. In the contributions with coupled thermo-mechanical crystal plasticity models, temperature dependence has not been incorporated completely. For example Jain and Agnew (2007) employed Asaro and Needleman (1985) framework to model temperature dependence of twinning in HCP Magnesium alloys without incorporating components for temperature, such as thermal deformation gradient and thermal slip softening. Furthermore, some of the more comprehensive coupled thermo-mechanical crystal plasticity models (Clayton, 2005; Lee et al., 1997) consider constant single slip hardening parameters with respect to temperature. Thus, for modeling different strain paths, such as uniaxial tension, shear, or compression at elevated temperatures, separate experiments need to be completed to calibrate single slip hardening parameters to predict each corresponding stress-strain curve. Lastly, it is observed that the temperature dependence of elastic coefficients has a considerable effect on the deformation field in some warm forming processes, such as spring-back. This phenomenon has not been investigated in regards to polycrystal deformation at elevated temperatures.

The goal of this work is to develop a new 3D thermo-elasto-viscoplastic constitutive model based on the crystal plasticity framework of Asaro and Needleman (1985) and Rossiter et al., (2010). The model will be able to predict the behaviour of aluminum alloys at elevated temperatures up to, recrystallization temperatures. The original crystal plasticity formulation will be reformulated to include the effects of thermodynamics during deformation. The commercial finite element package LS-DYNA, an in-house Taylor-type crystal plasticity framework, will be used to implement the new thermo-elasto-viscoplastic constitutive model in order to investigate capabilities of the model.

1.3 Outline of Thesis

This thesis consists of nine chapters. The first chapter presents the introduction and describes the motivation for and objective of the thesis. Chapters two and three present general background knowledge of dislocation theory, slip deformation, and a literature review of crystal plasticity and its applications. Chapters four through seven are published and submitted publications illustrating studies that have been conducted. Chapter four develops a new thermo-elasto-viscoplastic crystal plasticity framework along with a general power-law phenomenological hardening implementation as a predictive tool for stress-strain response in new strain-paths and temperatures with minimal calibration. Chapter five applies this new model to the application of forming limit diagrams (FLDs) and investigates model parameters with a more complex hardening model to better capture the effects of temperature on warm forming of aluminum sheet. Chapter six presents the development of a new hardening model derived from the physics of dislocation movement, accumulation, and annihilation as a primary deformation mechanism. Model parameters can then be related directly to material microstructure and determined from experimental data, and accounts for such mechanisms as dislocation annihilation via vacancy climb to be able to predict behaviour during dynamic recovery. Finally, chapter seven implements the new mechanistic hardening model into the previously derived elasto-visco-plastic crystal plasticity framework to predict material behaviour and microstructure evolution of common aluminum sheet alloys at high temperatures. The model is then used to relate temperature and alloying to the effect on microstructural properties such as the mean-free path of dislocations, and deformation mechanisms such as dynamic recovery. Lastly, chapter eight summarizes the thesis with a conclusion of the contribution of this projects developed tool for microstructure engineering, and presents some opportunities for future work.

Chapter 2

Background

2.1 Dislocations

Dislocations are an important subset of defects in crystalline solids; therefore an elementary understanding of crystal structure is required. Metals and some non-metals exhibit crystalline atomic structure, where atomic arrangement is a periodic repeating pattern in three dimensions. The repeated 'block' is what is described as the crystal structure. For most pure metals, the structure is quite simple with the most common being body-centered cubic (BCC) such as ferritic steels, face-centered cubic (FCC) such as aluminum and copper, and hexagonal close-packed (HCP) such as magnesium and titanium (Hirth and Lothe, 1982)

The arrangement of the atoms in the crystal can be described in terms of lattice parameters identifying the spacing between atoms. The smallest repeating 'block' of atoms is called the unit cell and an entire crystal is comprised of perfectly aligned stacks of the unit cell in three dimensions. Positions of planes, directions, and point sites in a lattice are expressed by reference to the unit cell and principal axes. For cubic materials, the principal axes are the Cartesian axes and the unit cell is a cube. For FCC structures, atoms are located at the four outer corners of the unit cell and at all of the centers of the cube faces.

Although there are many techniques available to directly observe dislocations, the existence of dislocation (line defects) was assumed during early studies when unexplained discrepancies arose between the theoretical and experimental values of applied shear stress to deform a single crystal. This deformation occurs by the sliding of atomic planes, and in a perfect crystal, the rigid movement of all atoms simultaneously. First calculations of the required shear stress to impose this deformation were by Frenkel in 1926. The theoretical maximum or critical value of shear stress (τ_{th}) was found to be many orders of magnitude greater than the experimentally obtained values. Orowan (1934), Polanyi (1934), and Taylor (1934) independently were able to account for this by the presence of dislocations.

The most useful definition of a dislocation is given in terms of the Burgers circuit. A Burgers circuit is a planar closed loop atom-to-atom path. If the circuit encloses a dislocation, it does not close due to an atomic mismatch and the vector required to close the circuit is known as the Burgers vector. Two important rules regarding edge and screw dislocations are as follows: (i) the Burgers vector of an edge dislocation is perpendicular to the line of dislocation and (ii) the Burgers vector of a screw dislocation is parallel to the line of dislocation. The two basic dislocation variants are edge and screw dislocations. This simply refers to the relative direction of dislocation line and its Burgers vector. Figure 2-1 depicts these two distinct types of dislocation and their direction of propagation. In an edge dislocation, the dislocation propagates along the line of the applied shear stress. In a screw dislocation, the atoms 'twist' propagating the dislocation line perpendicularly to the applied stress. In the example below both types of dislocation yield the same final deformation after the dislocation has completely passed through the crystal.

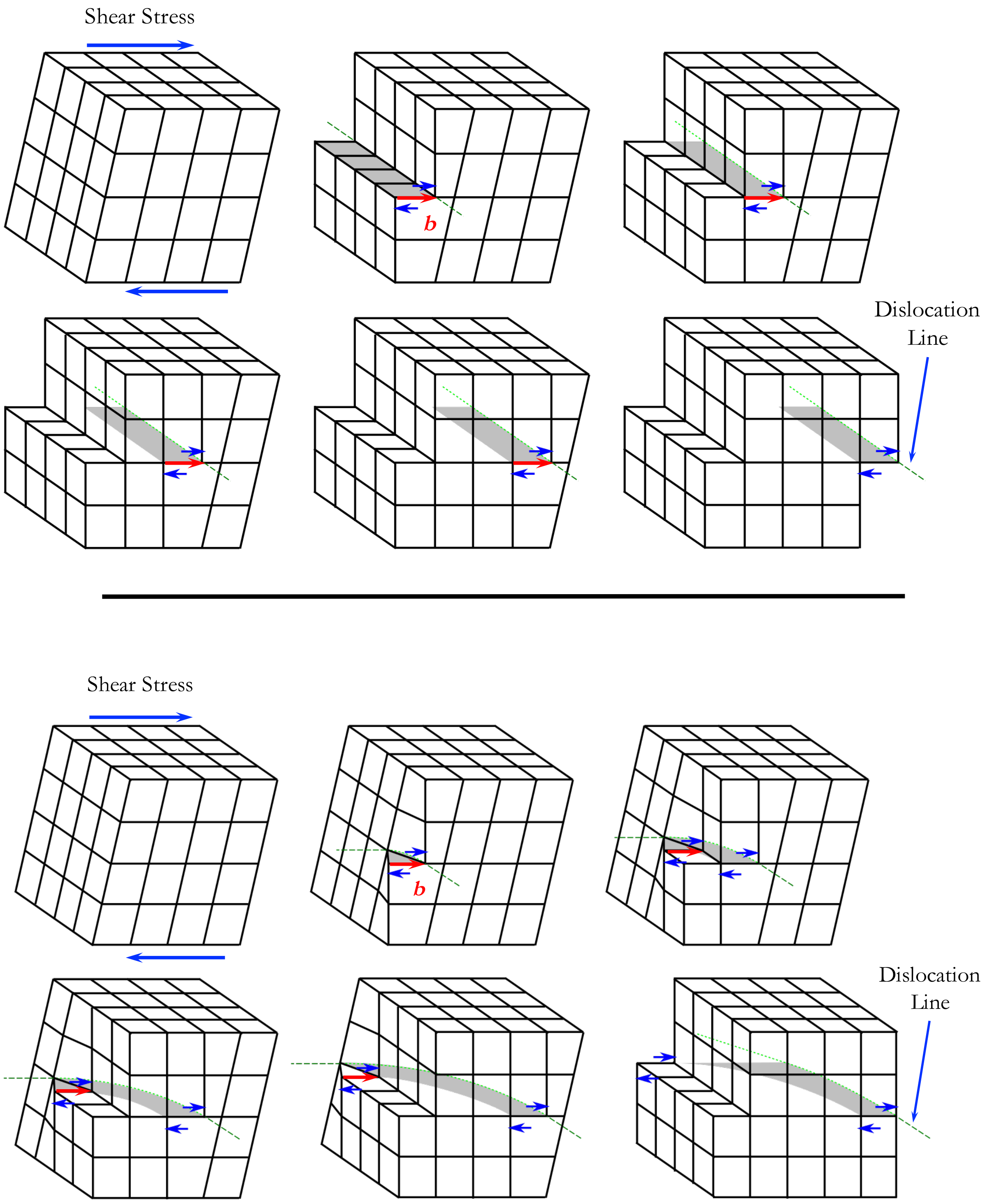

Figure 2-1 Edge dislocation propagation (top) and screw dislocation propagation (bottom) through a crystal lattice with Burgers vector *b*. Edge dislocation motion acts parallel to shear stress while screw dislocation motion is normal to applied shear stress[2].

---

[2] https://commons.wikimedia.org/wiki/File:Dislocation_coin_et_deformation_3d.svg

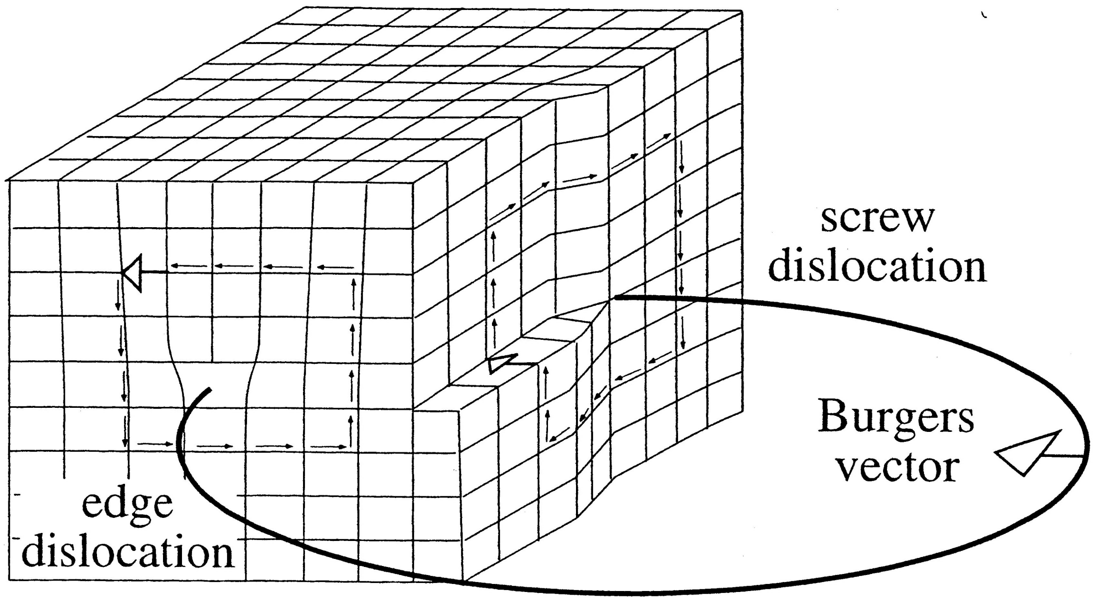

Figure 2-2 Burgers circuit around an edge dislocation and screw dislocation[3].

In general cases, the burgers vector can have mixed edge and screw components; however, for a single dislocation the Burgers vector has a fixed length and direction. Figure 2-2 shows the Burgers circuit for an edge and screw dislocation (Hull and Bacon, 2001).

There are two basic modes of dislocation movement: glide and climb. Dislocation glide is when the dislocation motion, line, and Burgers vector all shares the same plane. This is also known as conservative motion and when many dislocations glide, the results is slip, which is the most dominant manifestation of plastic deformation in crystalline solids such as aluminum. Climb, or non-conservative motion, occurs when the dislocation motion is out of plane and normal to the Burgers vector.

Slip planes and slip directions in crystals have discrete forms and usually coincide with the lattice planes and lattice lines containing the highest density of atoms. 12 slip directions on 4 slip planes exist in FCC crystals. Vector representations of slip directions and slip plane normal are the <110> directions on the {111} planes. Thus, FCC crystals have 4 slip planes with 3 slip directions on each, totaling 12 slip systems.

A characteristic shear stress is required for slip to occur. For example in Figure 2-3 a crystal is deformed under tension by an applied force F along the axis of the cylinder. Assuming the cross sectional area to be A, the stress developed parallel to the applied force is $\sigma = F/A$. This force has a component in the slip direction $F\cos\lambda$ with λ being the angle between F and the slip direction. This force component acts over the slip surface with an area $A/\cos\phi$, where angle ϕ is the rotation from F to the slip plane normal. Therefore, the resolved shear stress on a given slip plane and given slip direction can be represented as

$$\tau = \frac{F}{A} cos\lambda cos\phi \tag{2.1}$$

---

[3] http://www.geology.um.maine.edu/geodynamics/AnalogWebsite/UndergradProjects2010/PatrickRyan/Pages/Background.html

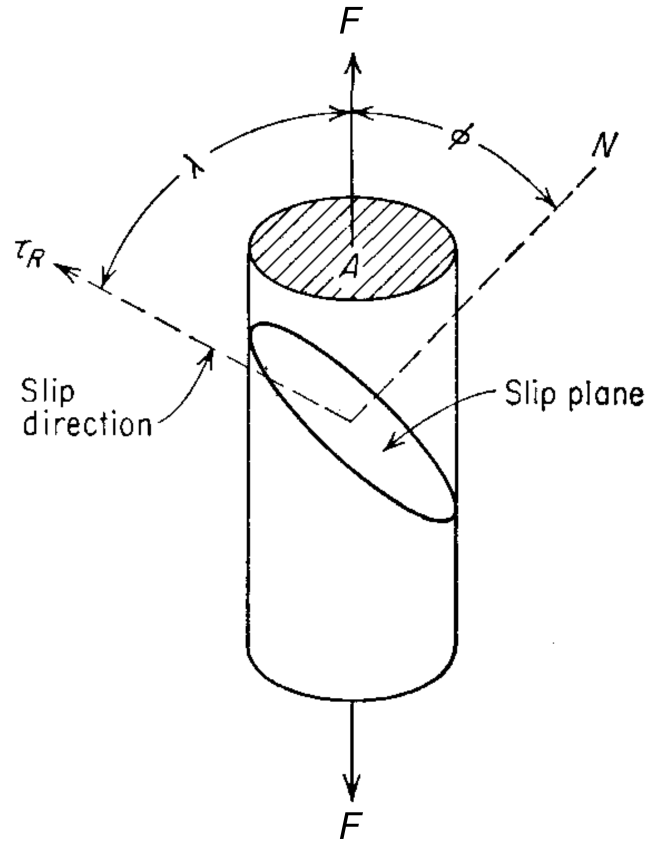

Figure 2-3 Geometry of slip in crystals. In general, ($\lambda + \phi$) ≠ 90°. The Burgers vector of an edge dislocation is perpendicular to the line of dislocation. The Burgers vector of a screw dislocation is parallel to the line of dislocation (Hull and Bacon, 2001).

Throughout this work, τ is used to represent the shear stress resolved on to a slip system in this way. Furthermore, if a critical force F_c is required to initiate slip, the corresponding shear stress is denoted τ_c or critical resolved shear stress (CRSS). The translation $\cos\lambda\cos\phi$ from σ to τ is known as the Schmid factor.

Dislocations move by glide at a velocity dependent on the magnitude of the applied shear stress, the purity of the crystal, temperature, and the type of dislocation. A method of measuring dislocation velocities developed by Johnson and Gilman found that in the range of 10^{-9} to 10^{-3} ms^{-1}, the logarithm of the dislocation velocity was linearly proportional to the logarithm of applied stress, such that

$$v_{disl} \propto \left(\frac{\tau}{\tau_0}\right)^n \tag{2.2}$$

where τ is the applied shear stress and τ_0 is the shear stress such that $v_{disl} = 1$ms^{-1}, and n is a proportionality constant. It should be noted that, the above relation is purely empirical, with no implied physical interpretation of dislocation motion mechanisms.

At low temperatures diffusion is extremely difficult and the movement of dislocations is nearly entirely restricted to dislocation glide. However, at elevated temperatures where thermally motivated diffusion is active, an edge dislocation can move out of its slip plane through a mechanism called dislocation climb. Physically, climb is the diffusion individual, or clusters, of vacancies toward or away from the dislocation.

The result of dislocation climb is what is known as a *jog* and only occurs on edge dislocations (Hirth and Lothe, 1982).

All of these factors play an important role in work hardening, especially in dislocation dominant materials such as aluminum. When dislocations move, interact, and change their distribution or density in the material, the glide resistance increases. For almost all metals, this has been used as an improvement to the material by increasing the strength through plastic deformation. The first work in realizing the connection between dislocation interactions and work hardening was completed by Taylor (1934). Taylor proposed the shear stress that is required to move two parallel plane edge dislocations separated by l past each other to be

$$\tau = \alpha \mu b / l \tag{2.3}$$

where α is a constant of order 0.1 related to the strength of obstacles in the matrix, μ is the shear modulus, and b is the Burgers vector. The average dislocation spacing l is proportional to the inverse root of the dislocation density, i.e. $l \approx \rho^{-1/2}$. Taylor extended this to a parabolic relation for stress-strain, which decently fits the behavior of many polycrystalline materials; however, single crystals may not behave in the same manner (Taylor, 1934). This will be discussed further in section 3.2.

2.2 Texture

Almost all crystalline materials exhibit some degree of preferred crystallographic orientations or textures. The distribution of these orientations within a polycrystalline material is an important property governing the anisotropy of the material. Of the various methods used to represent texture, this work will employ pole figures and 3x3 orthogonal rotation matrices (Kocks et al., 2001).

To represent a crystallographic orientation, we use three independent parameters to identify the microtexture with respect to a fixed reference frame. These three parameters are known as Euler angles (ϕ_1, Φ, ϕ_2), which describe rotations from the sample frame coordinate axis to the crystal coordinate axis.

Most cold worked materials develop strong textures during deformation, and specific processes tend to produce typical and recognizable textures. Figure 2-4 shows typical cold rolled texture for an FCC metal. Texture can further be broken down into frequently occurring texture components. Some of the common texture components in cold rolled FCC metals are summarized in Table 2-1 and Figure 2-5.

Copper, Brass, and S orientations form most of the rolled texture with some small amounts of others present. Cube orientation is typical during annealing and appears during recrystallization in aluminum, even though the deformed microstructure may exhibit only trace amounts of cube (Brahme, 2005).

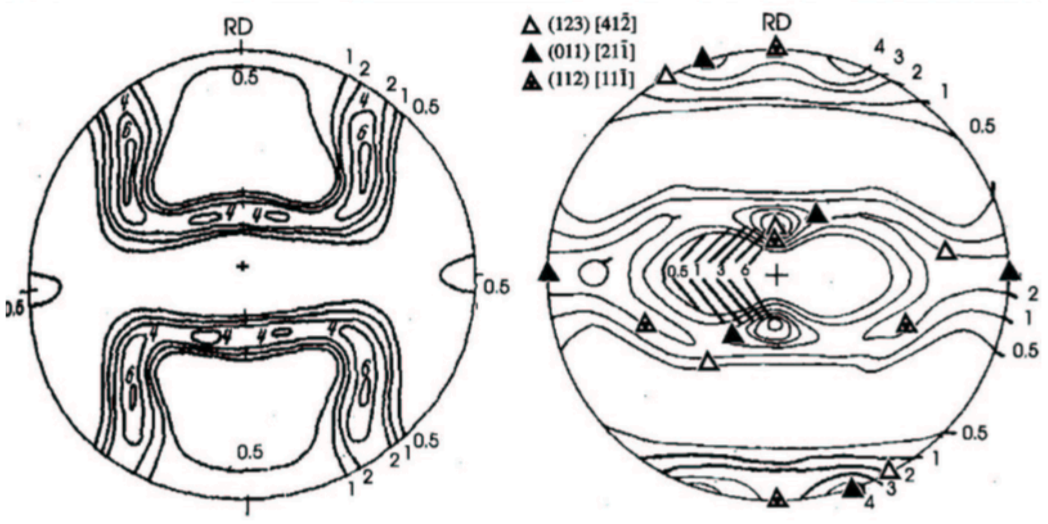

Figure 2-4 {001} (left) and {111} (right) Pole figures for typical FCC rolled texture (Brahme, 2005).

Table 2-1 Common texture components in FCC metals.

Component	Euler angles (ϕ_1, Φ, ϕ_2)
Cube	(0,0,0)
Copper	(0,35,45)
S	(64.93,74.50,33.69)
Goss	(0,45,0)
Brass	(35,45,0)
Dillamore	(0,27,45)

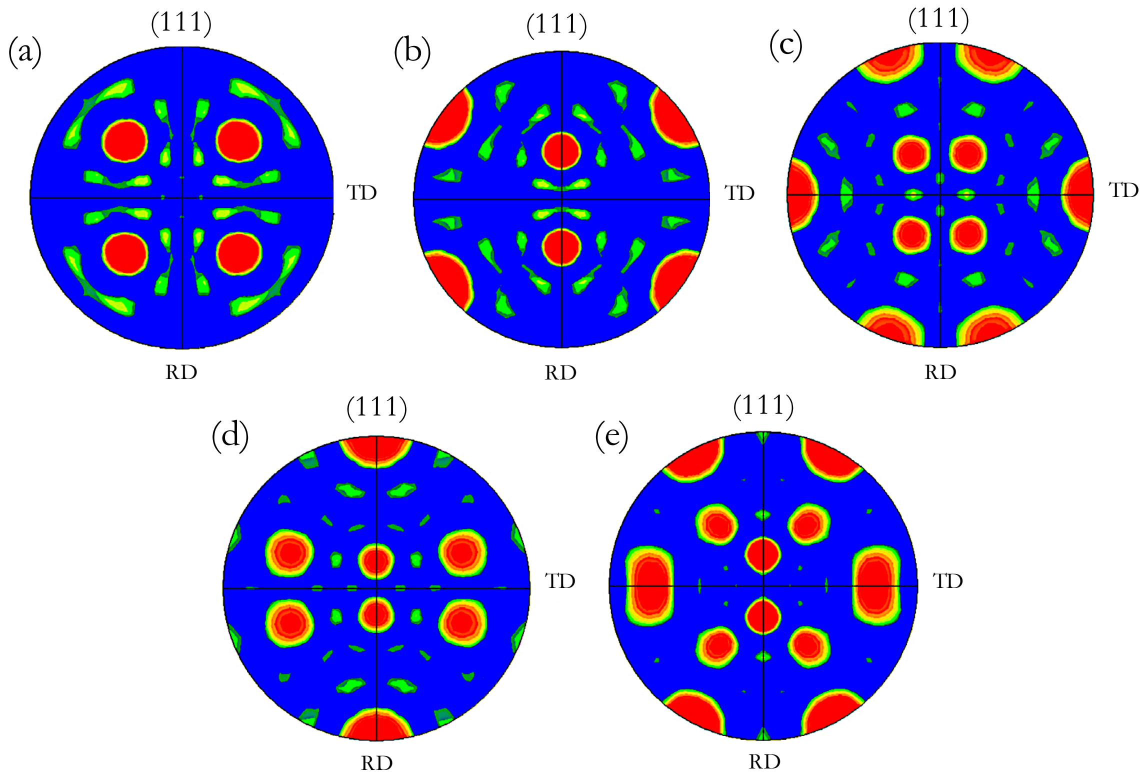

Figure 2-5 {111} Pole figures for computationally generated textures of: (a) Cube component; (b) Goss component; (c) Brass component; (d) Copper component; (e) S component (Rossiter et al., 2013).

Another method of representing the material texture is to use Bunge Euler space. This is shown in Figure 2-6 as a series of *sections* (one square box per section) showing the variation in orientation distribution (OD) intensity for fixed values of angle ϕ_2. The contours are generated by interpolating between discrete points (as with pole figures), and higher intensities correspond to common orientations. The example below shows a generic OD in Bunge Euler space where each section represents a slice of the ϕ_2 plane and the horizontal and vertical axes of each section represent the ϕ_1 and Φ angles from 0º to 90º, respectively.

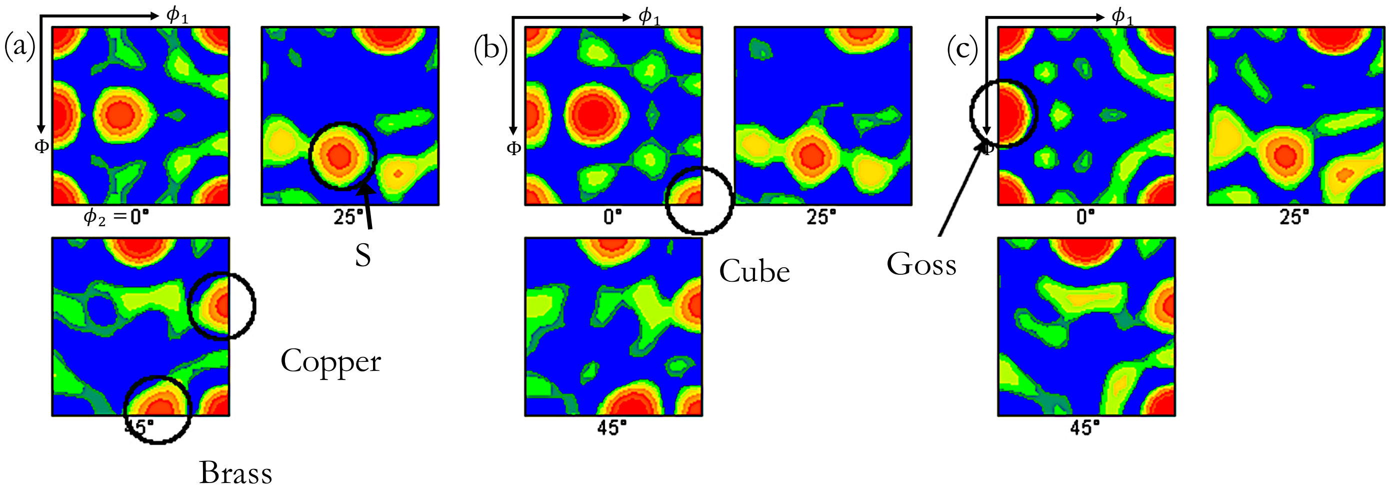

Figure 2-6 Example of orientation distribution in Bunge Euler Space for computationally generated textures from Figure 2-5 with (a) all components having equal volume fraction, (b) with high Brass, and (c) without Brass (Rossiter et al., 2013).

Chapter 3

Literature Review

This section will provide comprehensive background on the physics of deformation for aluminum. This includes dynamics and kinetics of deformation and how it is affected by temperature as well as previous work that has been completed to understand this physics. Subsequently, an in-depth study on the mathematical models available to predict the behaviour of aluminum deformation will be presented.

3.1 Basic Phenomena & Terminology

In terms of engineering processing, severe plastic cold working is typically carried out in order to change the shape of a metallic work piece. In terms of physical metallurgy, cold deformation is an increase of internal stored energy specifically associated with the accumulation of lattice defects. Even more specifically, the majority of stored energy in a cold worked metal (in our case aluminum) is in the form of dislocations (Orowan, 1934; Taylor, 1934; Polanyi, 1934). Other defects, such as point defects (i.e. vacancies and interstitials) or interfaces developed during athermal processes, only contribute a minor portion of the stored energy in the metal (Wever, 1924; Swan et al., 1963; Keh and Weissman, 1963). When observing the total deformation energy imposed on a metal during plastic straining, as small a fraction as 5-10% of this energy is actually stored in the material and most is dissipated as heat. In some cases at high strain rates, this can lead to significant temperature increases in the material up to several hundred degrees Celsius. However, the resulting build-up of defects in heavily cold worked materials is still great enough to be the driving force for non-equilibrium transformation phenomena summarized here as recovery, recrystallization, and grain coarsening (Kalisher, 1881; Sorby, 1886, 1887; Stead, 1898; Rosenhain, 1914; Ewing and Rosenhain, 1899, 1900a, 1900b; Alterthum, 1922; Carpenter and Elam, 1920; Czochralski, 1927; Burgers and Louwerse, 1931).

The order of dislocation density in most metal alloys ranges from 10^{10}–10^{11} /m^2 in the annealed state to 10^{12}–10^{13} /m^2 after modest deformation. At low temperatures, dislocation density can be upwards of 10^{16} /m^2 after heavy deformation. By taking the inverse of these we can estimate the average spacing between dislocations to be 1m for weakly deformed materials and 10 nm for heavily deformed materials. These high dislocation densities have a number of effects on the material properties; however, in this work we will focus only on the effect of mechanical behavior, such as hardness and strength.

If one then observes the metal deformation in the meso-scale, the grain shape evolves and becomes distorted with cold working. Severe deformation can lead to the formation of new grains through grain refinement, restricting the mobility of dislocations. Often, especially in aluminum alloys, shear bands of high local deformation will appear at higher stages of plastic straining.

For continued cold working of heavily deformed materials, high strength and hardness associated with a decrease in ductility and toughness usually requires some method of restoration to the original soft material state. In this context, recovery, recrystallization, and grain growth are the most important and effective thermodynamic processing methods to return heavily cold-worked materials back to a soft and easily formable state (Burke and Turnbull, 1952; Smith, 1948; Beck and Hu, 1966; Haessner, 1978; Humphreys and Hatherly, 1995, 2004; Doherty et al., 1997; Doherty, 2005). Thus, the microstructure and mechanical properties of crystalline materials, after severe deformation, can be restored to their pre-deformed states before any further manufacturing steps. More recently, manufacturing techniques have been improved such that the material experiences these thermodynamic softening during plastic deformation, known as warm and hot forming.

Recovery involves the thermally activated motion, condensation, and annihilation of point defects. In terms of forming, and for the purposes of this work, recovery is specifically the annihilation and rearrangement of dislocations within the material (Burgers and Louwerse, 1931; Doherty et al., 1997). During deformation, the formation of subgrains with low-angle tilt and twist grain boundaries is pronounced. With continued recovery, dislocation annihilation and competitive subgrian growth take place (Humphreys, 1997). Recovery does not, however, affect the grain topology of the deformed polycrystal as it does not involve the motion of high-angle grain boundaries. Instead, dislocation rearrangement described above occurs within the deformed grain, yielding relatively small and continuous changes in hardness essentially due to the gradual decrease in elastic distortion (Clareborough et al., 1955).

The mechanism of recovery overlaps with the onset of recrystallization, which can be characterized by discontinuous nucleation phenomena. In most materials (including aluminum) recrystallization nucleation is a result of sub-grain growth and a sufficiently high misorientation between the sub-grain and the surrounding deformed microstructure (Burgers, 1941; Doherty et al., 1997; Humphreys, 1997; Himmel, 1962). In other words, recrystallization describes the mechanism by which the formation and subsequent motion of new high-angle grain boundaries is concerned. The newly formed boundaries sweep through the inherited deformation substructure discontinuously yielding a softer polycrystal microstructure (i.e. with lower dislocation density).

Recrystallization can occur only when there is significant thermal activation (usually at temperatures about half of the absolute melting temperature) and sufficient stored energy, and leads to the nucleation and growth of new strain-free grains in the deformed matrix (Kolmogorov, 1937). Since this process is discontinuous, recrystallized microstructures inherit local strain-free zones. These new strain-free zones are surrounded mostly by the sweeping front of new mobile high-angle grain boundaries (Beck and Hu, 1966; Humphreys and Hatherly, 1995; Humphreys, 1997; Himmel, 1962; Cahn, 1965, 1966; Kolmogorov, 1937; Johnson and Mehl, 1939; Avrami, 1939, 1940; Doherty and Cahn, 1972; Humphreys and Ferry, 1997; Faivre and Doherty 1979; Bhatia and Cahn, 1978; Srolovitz et al., 1986; Sebald and Gottstein, 2002; Engler et al., 1996; Engler, 1997; Humphreys, 1992a). During recrystallization, the strength and hardness of the material decreases considerably faster than during recovery, and original ductility prior to forming can be restored. The recrystallization temperature, where the first stress-free grains appear, is dependent on the grain size, degree of plastic deformation, strain path, and presence of alloying solutes or secondary phase materials.

Recrystallization is finished when either all of the originally deformed grains are swept by the mobile high-angle boundaries, or the temperature is lowered below the recrystallization temperature. In the case of the former, competitive grain coarsening begins, changing the material strength and further increasing the average grain size contributing to decreasing the Hall-Petch effect. Grain growth is also thermodynamically motivated and aims towards the reduction of total grain boundary area in the material. The grain growth and recovery processes are relatively slow when compared to recrystallization. Recrystallization can occur very rapidly after the initial nucleation period, and in most cases can be modeled using sigmoidal-type kinetics (Raabe et al., 2014).

Experimental research and phenomenological modeling of metals at elevated temperatures has been widely studied, see e.g. (Abedrabbo et al,. 2006). Experimental studies in the low temperature regime (Park and Niewczas, 2008) and warm forming temperature regime show strong thermal influence on the dynamic viscoplastic response of metals (Klopp et al., 1985) and strain-rate sensitivity (Li et al., 2007). Constitutive models to investigate the thermal elastic-plastic behaviour of metals have been developed; see e.g. (Kim et al., 2013; Kabirian et al., 2013; Khan and Baig, 2011; Perzyna, 1988).

3.2 Modeling Deformation

The primary goal of a work hardening theory is a prediction and/or explanation of the stress-strain curve. This is linked with the development of dislocations and substructures, and even a simple description of substructure requires many model parameters. Thus, any model beginning with the material's known substructure must involve substantial collation of information as just the basic part of the model. On the other hand, any theory that starts with the stress-strain curve can at best hope to be in agreement with a very rudimentary approximation of substructural features.

Mahabunphachai and Koc (2010) have reported the effect of temperature on the stress response of aluminum and aluminum alloy. Van Den Boogard and Huétink (2006) have used uniaxial tension experiments at elevated temperatures to fit a Vegter yield function and Bergstrom hardening model. Experiments revealed that local necking occurred far beyond the uniform strain at elevated temperatures and they postulated that this was caused by the strain rate sensitivity of AA5754. It was also observed that room temperature necking occurs at a slight diagonal across the test specimen, different from observations at elevated temperatures where necking orientation is perpendicular to the tensile direction. Li and Ghosh (2003) have studied temperature and strain rate effects on 5XXX and 6XXX series aluminum alloys during uniaxial tension. Investigations in the warm forming temperature regime showed a decrease in hardening and increase in strain rate sensitivity with increasing temperature. They concluded that the warm formability of strain-hardenable 5xxx series alloys is superior to that of the 6xxx series precipitation hardened alloys.

Macroscopic hardening behaviour at elevated temperatures for aluminum has been studied and numerical models have been developed to predict temperature and strain rate dpendent material hardening (Abedrabbo et al., 2006; Toros et al., 2008). Experimental studies with AA5754 show that the temperature dependence of the viscoplastic behaviour and the strain-rate sensitivity during uniaxial tension is minimal at temperatures below 100ºC (Abedrabbo et al., 2007; Toros et al., 2010). Phenomenological models for warm forming processes (Kurukuri et al., 2009) and high temperature closed die forging of aluminum (Ganapathysubramanian and Zabaras, 2002) have been developed to account for such behaviour.

Warm forming leads to decreased flow stress and increased ductility in all sheet alloys, allowing for deeper drawing and more stretching without design modifications or material microstructure refinement. Early studies on warm forming of aluminum alloys were performed by Dawson (1984) and Beaudoin et al. (1993, 1994). Palumbo and Tricarico (2007) conducted experimental work on optimizing the warm deep drawing process of circular AA5754 sheets. It has been demonstrated that higher uniform temperatures improve formability, but the biggest gains can be obtained by applying temperature gradients. In addition, warm forming allows one to overcome serrated flow due to dynamic strain aging, the Portevin-Le Chatelier effect and Luder's band formation resulting from interacting solutes and mobile dislocations (Abedrabbo et al. 2007). Van Den Boogaard et al. (2001) have shown improved formability of AA5754 sheets during deep drawing where the cylindrical cup limiting draw ratio could be improved from 2.1 to 2.6 by increasing the flange temperature to 250^0C. Van Den Boogard and Huétink (2006) used a Bergstrom hardening model to predict this behaviour but were unable to accurately capture the flow behaviour at high temperatures (above 200^0C). Kurukuri et al. (2009) applied the Nes (1998) dislocation based model to improve on the work of Van Den Boogaard and Huétink (2006) and concluded that, even with the correct description of a yield locus and the microstructure based work hardening model, deep-drawing simulations still differed from experimental results. This was especially the case for predicting thickness distributions.

Recent leaps in computational power have allowed the usage of advanced "mechanism" based models such as crystal plasticity for the numerical simulation of metal forming. Roters et al. (2010) has presented an excellent overview on mechanical constitutive laws, kinematics and mutli-scale methods in crystal plasticity finite-element modeling, and show that only works based on dislocation theory are capable of including thermal effects. Thermodynamical crystal plasticity, where temperature is introduced as a product of plastic work, has been used to study texture evolution and strain rate sensitivity of body-centred cubic (BCC) materials (Lee et al., 1997; Clayton, 2005). Kok et al. (2002) has developed a rate-dependent crystal plasticity framework based on isotropic mechanical threshold stress continuum model. Their model employed the Newton–Raphson algorithm to perform a minimization process to find the material properties. Thermodynamical crystal plasticity coupled with damage for aluminum alloys (Srikanth and Zabaras, 1999) and dislocation-based crystal plasticity multi-scale modeling has also been developed for metallic single crystals (Groh et al., 2009; Hansen et al., 2013). Thermal loading in thin film crystals using various thermodynamics based micro-mechanical models (Yu et al., 1997; Faghihi et al. 2013) and on the latent hardening of face-centred cubic (FCC) polycrystals under complex loading paths (Gerard et al., 2013) have also been reported.

A better understanding of the temperature effects on the crystal lattice can be achieved by investigating fundamental physical behaviour of the material. It has been shown that thermodynamics is an integral part of molecular dynamics and dislocation dynamics (Amodeo and Ghoniem, 1990). Studies also show a strong temperature dependence of the elastic behaviour of metallic single crystals (Varshni, 1970). Kocks (1976) also discussed a non-linear material strain-rate dependence on both temperature and crystal elastic moduli. Crystal Plasticity Finite Element Method (CPFEM) has been a valuable tool for studying elasto-viscoplastic behaviour of materials. The mechanical response of materials using 2D CPFEM has been widely studied (i.e., Kuroda and Tvergaard, 2004, 2007; Hu et al. 2010). However, it has also been shown that the 2D CPFEM is inadequate for modeling accurately the state of strain and stress as well as many other phenomena in sheet metal forming such as bending and surface roughness (Rossiter et al., 2013).

3.3 Crystal Plasticity Finite Element Modeling (CPFEM)

The elastic-plastic deformation response of crystalline materials depends on the loading direction. This anisotropic behavior is due to the directional dependence of deformation mechanisms (such as dislocations in aluminum polycrystals), and the orientation of the anisotropic elastic tensor. The result of this is that all associated mechanical phenomena, including but not limited to, shape change, crystallographic texture, strength, strain hardening, deformation-induced surface roughening, and damage are also dependent on crystallographic orientation.

The most important mechanical measure in structural design is the uniaxial stress-strain curve (Roters et al., 2010). This is a convenient description of plastic deformation as it reduces a six-dimensional yield surface and its evolution during loading to a one-dimensional yield curve. An example of this is presented in Figure 3-1, where the anisotropy of an arbitrary material is shown by analyzing the varying flow stress behaviour in the three principle directions. Texture (orientation distribution) and texture evolution during deformation is also needed in plasticity theory. Texture can be used to describe the anisotropy of polycrystals by the individual tensor behavior of each grain and the interaction of grains at their boundaries. Texture evolution and its connection to shear can be explained by the decomposition of the deformation gradient into its skew-symmetric portion, which describes pure rotation and leads to texture change, and its symmetric portion that relates to pure stretching. Plastic shearing thus creates both shape and orientation changes during deformation. Given the above, a theory of mechanical properties must include, firstly, crystallographic and anisotropic definitions of those physical mechanisms that create shear, and secondly, the orientations of crystals relative to applied loadings and reference frame.

Early approaches to describe plastic anisotropy with simple boundary conditions such as Sachs (1928), Taylor (1938), Bishop-Hill (1951a,b), or Kröner (1961) formulations were developed by simplifying assumptions of strain or stress homogeneity. They were not designed to consider explicitly the mechanical interactions among crystals in a polycrystal or for responding to complex internal and external loading boundary conditions.

To overcome these issues, variational methods in the form of finite-element (FE) approximations have gained tremendous momentum in the field of plasticity; see e.g Arsinelis et al. (2004). These crystal plasticity finite-element (CPFE) models are based on the variational solution of equilibrium between forces and compatibility of displacements using a weak form of the principal of virtual work within a finite-volume element. The FE model is built by the discretization of the specimen into these elements. The CPFE method employs the extensive knowledge gained from experimental and theoretical studies on single crystal deformation and dislocation dynamics (Curtin and Miller, 2003; Arsinelis et al., 2004; Vitek et al., 2004) to inform the further development of continuum field theories (Zienkiewicz and Taylor, 2005).

The constitutive framework offered through variational crystal plasticity formulations provides a desirable tool for developing comprehensive theories of plasticity that applies the current knowledge of the physics of deformation processes to continuum mechanics computational tools with the goal of developing advanced and physically based engineering design methods (Roters et al., 2010). The success of CPFE methods can also be attributed to the ability to include various constitutive formulations for plastic flow and hardening at an elementary shear system level. The constitutive flow rules that have been suggested over the past few decades have developed from empirical viscoplastic formulations (Rice, 1971; Asaro and Rice, 1977) to physics-based models (Arsenlis et al., 2004; Arsenlis and Parks, 1999, 2002; Evers et al., 2002, 2004a,b; Cheong and Busso, 2004; Ma and Roters, 2004; Ma et al., 2006a,b). It should be reiterated at this point that the FE method itself is not the actual model but the variational solver for the applied constitutive equations that maps the material anisotropy of elastic-plastic shear associated with various lattice defects (specifically dislocations in aluminum). The first introduction of this method by Pierce et al. (1982) has matured into a wide collection of constitutive and numerical formulations to be applied to a very wide variety of crystal-mechanical problems. A summary of major contributions using different applications for the CPFEM is presented in Table 3-1.

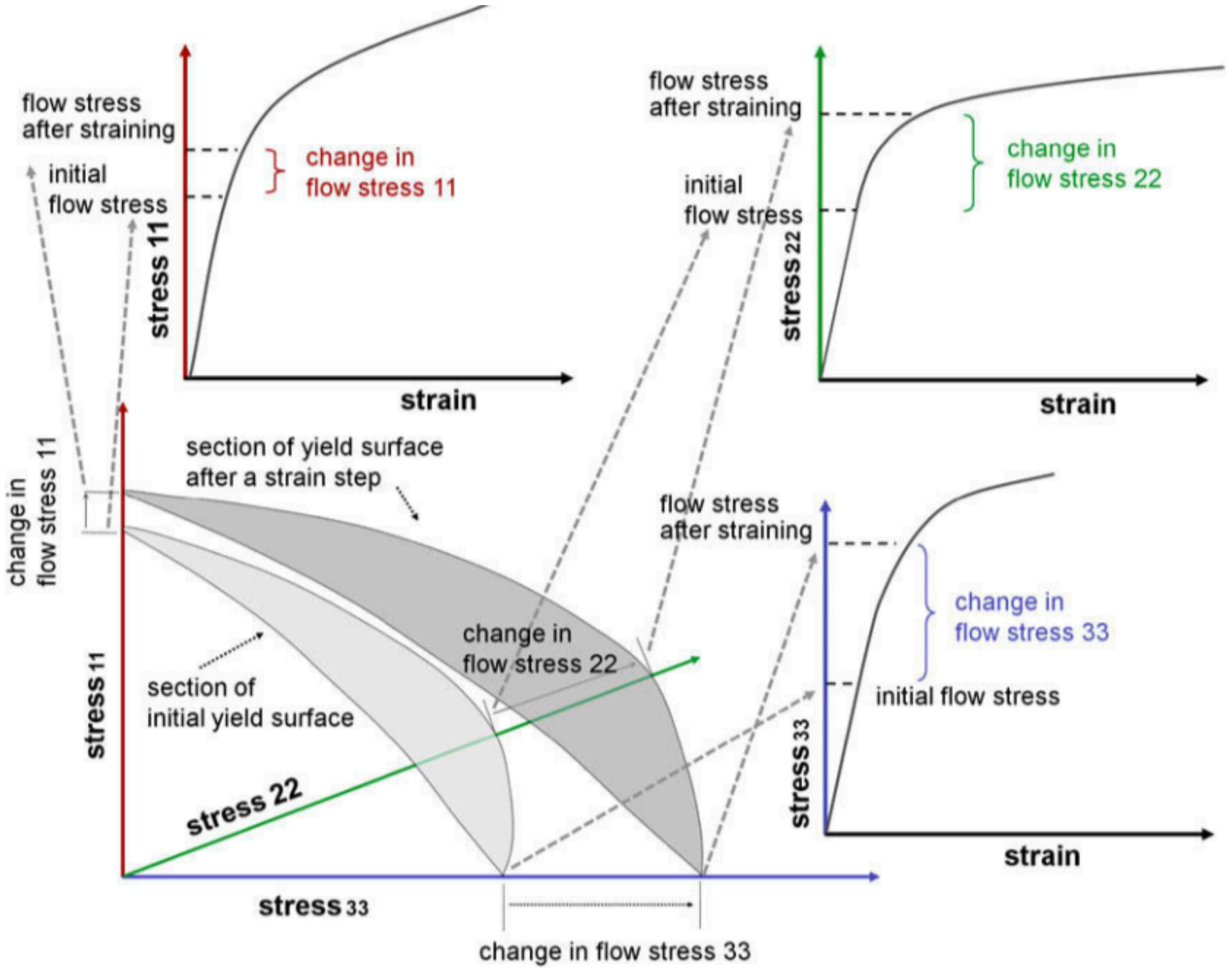

Figure 3-1 Flow stress and strain hardening of anisotropic materials are tensor quantities (Roters et al., 2010).

3.3.1 Phenomenological CPFEM

Phenomenological constitutive models use the critical resolved shear stress (CRSS), τ_c^α , as the state variable for each slip system, α. The slip system shear rate, $\dot{\gamma}^\alpha$, is then formulated as a function of the CRSS and the resolved shear stress, τ^α, such that:

$$\dot{\gamma}^\alpha = f(\tau^\alpha, \tau_c^\alpha) \tag{3.1}$$

The evolution of the CRSS is expressed as a function of the total accumulated shear, γ^a, and the shear rate, $\dot{\gamma}^\alpha$, as follows:

$$\tau_c^\alpha = g(\gamma^a, \dot{\gamma}^\alpha) \tag{3.2}$$

Early formulations in this framework were developed by Rice et al. (1971), Hutchinson (1976), and Peirce et al. (1982, 1983) for face-centered cubic metallic single crystals. In these works, the kinetic law for single slip is written as:

$$\dot{\gamma}^\alpha = \dot{\gamma}_0 sgn(\tau^\alpha)\left|\frac{\tau^\alpha}{\tau_c^\alpha}\right|^{\frac{1}{m}} \tag{3.3}$$

where $\dot{\gamma}_0$, and m are material dependent parameters that represent the reference shear rate and slip rate sensitivity, respectively. The influence of any slip system, β, on the hardening behaviour of the slip system of interest, α, can be represented by the hardening matrix, $h_{\alpha\beta}$, where:

$$\dot{\tau}_c^\alpha = \sum_\beta h_{\alpha\beta}|\dot{\gamma}^\beta| \tag{3.4}$$

Many empirical hardening models have been proposed to capture the micromechanical interactions between slip systems (Chang and Asaro, 1981; Asaro, 1983; Brown et al., 1989; Bassani and Wu, 1991). For instance, the following equation presents an exponential hardening law:

$$h_{\alpha\beta} = q_{\alpha\beta}\left[h_0\left(1 - \frac{\tau_c^\beta}{\tau_s^\beta}\right)^a\right] \tag{3.5}$$

where h_0, τ_s, and exponent a are hardening parameters. The latent hardening matrix $q_{\alpha\beta}$ has a value of 1.0 for coplanar systems of α and β, and 1.0-1.4 otherwise. A value other than 1.0 for non-coplanar systems leads to an anisotropic-type hardening model.

Table 3-1 Applications of the CPFE method (Roters et al., 2010).

Surface roughening, ridging, roping, thin film mechanics	Becker (1998), Raabe *et al*. (2003), Zhao *et al*. (2004, 2008), Yue (2005), Siska *et al*. (2007)
Grain boundary mechanics, Hall–Petch behavior, grain interaction, grain size effects, strain gradient effects, non-local formulations, interface mechanics, superplasticity	Becker and Panchanadeeswaran (1995), Mika and Dawson (1998), Acharya and Beaudoin (2000), Meissonnier *et al*. (2001), Barbe *et al*. (2001), Raabe *et al*. (2001), Evers *et al*. (2002, 2004a,b), Park *et al*. (2002), Clarke *et al*. (2003), Wei and Anand (2004), Fu *et al*. (2004), Diard *et al*. (2005), Bate and Hutchinson (2005), Wei *et al*. (2006), Murphy *et al*. (2006), Deka *et al*. (2006), Ma *et al*. (2006a,b), Counts *et al*. (2008), Gurtin *et al*. (2007), Venkatramani *et al*. (2007), Okumura *et al*. (2007), Gerken and Dawson (2008a,b), Kuroda and Tvergaard (2008), Bitzek *et al*. (2008), Borg *et al*. (2008), Li *et al*. (2009)
Creep, high temperature deformation, diffusion mechanisms Dislocation-based constitutive modeling	McHugh and Mohrmann (1997), Balasubramanian and Anand (2002), Hasija *et al*. (2003), Bower and Wininger (2004), Venkatramani *et al*. (2007, 2008), Agarwal *et al*. (2007), Xu *et al*. (2009) Arsenlis and Parks (1999, 2009), Arsenlis and Tang (2003), Arsenlis *et al*. (2004), Evers *et al*. (2002, 2004a,b), Cheong and Busso (2004), Ma and Roters (2004), Ma *et al*. (2006a,b), McDowell (2008), Li *et al*. (2009)
In-grain texture, grain-scale mechanics, mesoscale, non-uniform deformation	Peirce *et al*. (1982, 1983), Beaudoin *et al*. (1995), Mika and Dawson (1998), Sarma and Dawson (1996a,b), Sarma *et al*. (1998), Forest (1998), Bhattacharyya *et al*. (2001), Raabe *et al*. (2001, 2002), Miller and Turner (2001), Sachtleber *et al*. (2002), Kim and Oh (2003), Clarke *et al*. (2003), Choi (2003), Zaefferer *et al*. (2003), Erieau and Rey (2004), Sarma and Radhakrishnan (2004), Roters *et al*. (2004), Kim *et al*. (2006), Murphy *et al*. (2006), daFonseca *et al*. (2006), You *et al*. (2006), Musienko *et al*. (2007), Han and Dawson (2007), Zhao *et al*. (2008), Zhang *et al*. (2009)
Texture evolution, texture stability, in-grain texture formation, anisotropy	Asaro and Needleman (1985), Becker (1991), Becker *et al*. (1991), Bronkhorst *et al*. (1992), Kalidindi *et al*. (1992), Beaudoin *et al*. (1996), Bertram *et al*. (1997), Becker and Panchanadeeswaran (1995), Mika and Dawson (1999), Miehe *et al*. (1999), Kalidindi (2001), Balasubramanian and Anand (2002), Van Houtte *et al*. (2002, 2005, 2006), Delannay *et al*. (2002, 2006, 2009), Raabe *et al*. (2002, 2004), Bate and An (2004), Li *et al*. (2004, 2005), Sarma and Radhakrishnan (2004), Anand (2004), Roters *et al*. (2005), Tang *et al*. (2006), Tikhovskiy *et al*. (2006, 2007), Lee *et al*. (2007), Mayeur *et al*. (2008)
Forming, deep drawing, process modeling, cup drawing, spring-back, earing, wire drawing, extrusion, anisotropy, design, fretting	Beaudoin *et al*. (1993, 1994), Neale (1993), Kalidindi and Schoenfeld (2000), Nakamachi *et al*. (2001, 2007), Zhao *et al*. (2001, 2004), Xie and Nakamachi (2002), Raabe *et al*. (2002, 2005), Goh *et al*. (2003), McGarry *et al*. (2004), Raabe and Roters (2004), Tugcu *et al*. (2004), Delannay *et al*. (2005, 2006, 2009), Li *et al*. (2005, 2008), Dick and Cailletaud (2006), Tikhovskiy *et al*. (2006, 2007), Chen *et al*. (2007), Raabe (2007), Ocenasek *et al*. (2007), Mayeur *et al*. (2008), Li *et al*. (2008), Zhuang *et al*. (2008), Zamiri *et al*. (2009)
Crystal plasticity and recrystallization	Bate (1999), Raabe and Becker (2000), Raabe (2000, 2002, 2007), Radhakrishnan *et al*. (2002), Takaki *et al*. (2007), Semiatin *et al*. (2007), Zambaldi *et al*. (2007), Loge *et al*. (2008)
Deformation twinning	Kalidindi (1998), Staroselsky and Anand (1998, 2003), Marketz *et al*. (2002, 2003), Salem *et al*. (2005)
Numerical aspects, FE shape effects, mesh dependence, accuracy, robust integration methods, texture discretization	Miehe (1996), Bachu and Kalidindi (1998), Harewood and McHugh (2006), Amirkhizi and Nemat-Nasser (2007), Harewood and McHugh (2007), Kuchnicki *et al*. (2006), Melchior and Delannay (2006), Zhao *et al*. (2007), Li *et al*. (2008), Ritz and Dawson (2009), Barton *et al*. (2001), Gerken and Dawson (2008b)
Damage, fatigue, cyclic loading, void growth	Bruzzi *et al*. (2001), Turkmen *et al*. (2002, 2003), Kysar *et al*. (2005), Sinha and Ghosh (2006), Potirniche *et al*. (2006), Zhang *et al*. (2007), Cheong *et al*. (2007), Dunne *et al*. (2007), Liu *et al*. (2007), Bieler *et al*. (2009), Kumar *et al*. (2008), Patil *et al*. (2008), Watanabe *et al*. (2008), McDowell (2008), Mayama *et al*. (2008), Borg *et al*. (2008)
Multiphase mechanics	Hartig and Mecking (2005), Tjahjanto *et al*. (2007), Mayeur *et al*. (2008), Inal *et al*. (2008), Vogler and Clayton (2008)

These kinetic formulations are the most widely used in current CPFE models, however they have a severe drawback in the sense that the material state is described using only a phenomenological description of the critical resolved shear stress τ_c. This is beneficial in simplifying a complex framework to a single state variable, however the model cannot capture directly the effects of lattice defect populations, such as alloying particles or dislocation densities.

3.3.2 Physics Based CPFEM

Recently, physically based models for CPFEM have become more prevalent. The physics based models, different from the phenomenological constitutive models in crystal plasticity, rely on internal state variables, most notably dislocation density. Models dependent on the evolution of dislocation densities to calculate flow stress have been proposed by many authors (Arsenlis et al., 2004; Arsenlis and Parks, 2002; Cheong and Busso, 2004; Ma et al. 2006a,b; Gao and Huang, 2003). Although dislocations are the most important internal variable for plastic deformation, more parameters are required for a full characterization of the material microstructure, such as; grain size, grain shape, precipitate morphology, etc. Up to now, only a few of these additional parameters have been implemented into dislocation-based CPFEM.

The dependence of flow stress on grain size was first hypothesized by Hall and Petch and their famous empirical equation (Hall, 1951; Petch, 1953). Many following studies have since shown the strengthening of a material by smaller grain sizes is due to a higher density of heterogeneous plastic deformation that develops near grain boundaries. Several explanations are available in literature based on dislocation mechanisms, such as mobile dislocation pile-ups at grain boundaries leading to strain gradients at the boundary interfaces, increasing the slip resistance (Evers et al., 2002). Furthermore, micro-scale experiments have also shown the length-scale dependence of flow stress beyond simple grain size effects. In these experiments non-uniform deformation leads to orientation and strain gradients that can be associated with geometrically necessary dislocations (GNDs) (Ashby, 1970). It is difficult to be able to incorporate GNDs into phenomenological CPFE models, while in dislocation density-based models; this concept can easily be integrated (Nye, 1953).

However, this introduces a new problem where calculation of strain gradients renders the constitutive model non-local, as it is now strongly coupled with it’s neighbouring points during the evolution of GNDs. This means that strain gradient calculations must converge for neighbouring points at each time increment. In order to achieve this, GNDs and statistically-stored dislocations (SSDs) are modelled to increase degrees of freedom for every material point, however this solution required additional boundary conditions for dislocation density flux (Roters et al., 2010). This increases the difficulty for complex loading cases.

3.3.3 Saimoto-Van Houtte Constitutive Model

An alternative and more concise approach to the problem of including dislocation physics into a local framework was developed by Saimoto and Van Houtte (2011). In this constitutive relation based on crystal plasticity, the energy required to generate dislocations required to produce the imposed increment strain is equated to the population of dislocations stored as determined from the flow stress. The amount of new dislocations generated can be calculated as follows

$$\Delta\rho^{create} = \frac{P\Delta\gamma}{\lambda b} \tag{3.6}$$

where, λ (mean slip distance of dislocations) can be approximated as $\lambda = C_1\tau^{\beta}$. Parameter P is related to perimeter geometry of moving dislocations, $\Delta\gamma$ is the shear strain increment and b is the burgers vector. Statistical annihilation of dislocations is accounted for by multiplying P with annihilation factor $\frac{1}{A}$. The amount of stored energy due to dislocations is calculated using Taylor's equation

$$\tau = \alpha\mu b\sqrt{\rho} \tag{3.7}$$

where α is a parameter related to the strength of obstacles (not to be confused with the superscript x^{α} denoting a particular slip system), μ is the shear modulus of elasticity, and ρ is the dislocations density. Using these equations they were able to obtain a constitutive relation between flow stress and strain in terms of the parameters related to the evolving microstructure and can be approximated experimentally. The relationship is as follows:

$$\tau = \left(\frac{(2+\beta)(\alpha\mu b)^2}{4b}\right)^{\frac{1}{2+\beta}} \gamma^{\frac{1}{2+\beta}} \cdot C_{P/A} \cdot \dot{\gamma}^{m} \tag{3.8}$$

which can be rearranged to the form of equation (3.3) where the CRSS becomes

$$\tau_c = C_{P/A}\left(\frac{(2+\beta)(\alpha\mu b)^2}{4b}\right)^{\frac{1}{2+\beta}} \gamma^{\frac{1}{2+\beta}} \tag{3.9}$$

The term $C_{P/A}$ is called the annihilation correction factor and represents the ratio P/A. The procedure for determining the material parameters used two curve-fits for aluminum—one for low-strain and another for high-strain—where the intersection of the two fits was suggested to be analogous to the stage II (athermal hardening) to III (dynamic recovery) transition denoted as τ_{III} (Kocks and Mecking, 2003). Analysis of the model and results provided insight into the effect of dynamic recovery in stage III hardening. This model has been previously implemented into crystal plasticity (Brahme et al. 2011) and shows good predictability of flow stress and forming limit strains (using an M-K type formulation) at room temperature (see Chapter 5 for M-K forming limit analysis method). This model in particular could provide a solid foundation for a physics based implementation of thermodynamics into a crystal plasticity framework.

3.3.4 Recrystallization

New technology improving experimental abilities and numerical techniques have led to a significant increase in the theoretical and experimental knowledge of the dynamic recrystallization (DRX) phenomenon in recent years; however, modelling of DRX is still a challenging problem. This difficulty is primarily due to the multi-scale nature of DRX phenomenon. It involves the effects of impurities, precipitation, dislocation motion, movement of the grain boundaries, etc. In addition, DRX is widely accepted as a relatively non-deterministic due to the concurrence of the grain boundary motion and the complexity of the solutions from dislocation based mechanics. One such example is that interactions between grain boundaries during recrystallization can have more than one stable state solution (Pond and Casey, 1992).

Numerous works on recrystallization modelling exists. DRX has been modelled in the past using cellular automata (CA) (Hesselbarth and Göbel, 1991; Raabe, 2002, 1999), Monte-Carlo Potts model (Anderson et al., 1984; Rollett and Raabe, 2001) and other techniques. In the CA models, the state of the entire aggregate is updated simultaneously, whereas in Monte Carlo models update of each site occurs randomly. Coupling these two approaches is a widely accepted method and is able to provide a better match with experimental data (Hesselbarth and Göbel, 1991; Goetz and Seetharaman, 1998; Raabe and Becker, 2000; Rollett and Raabe, 2001; Ding and Guo, 2001; Hallberg et al., 2010).

CPFEM coupled with various techniques has been used to model static and dynamic recrystallization (Radhakrishnan et al., 1998; Raabe and Becker, 2000; Takaki et al., 2007, 2009; Radhakrishnan and Sarma, 2008; Takaki and Tomita, 2010; Li et al., 2013). One of the most recent works couples the CA method with CPFEM presenting a numerical framework to predict flow stress as well as texture evolution driven by DRX during hot deformation of HCP metals (Popova et al. 2015). The model used CPFEM to account for microstructural characteristics such as grain size, shape, texture, as well as experimental measurements of flow stress and critical resolved shear stress. The CPFEM also calculates state variables for the CA process, such as dislocation density, crystal orientation update, and velocity). The cells for CA are represented by the finite elements, eliminating the need for mapping from one method to the other. The CA formulation is responsible for using the CPFEM state variables to determine the location of nuclei and their growth.

The crystal plasticity formulation used in this model is modified from the Asaro and Needleman (1985) formulation for HCP polycrystals. The kinematics of recrystallization can be separated into three parts: the critical condition for DRX initiation, nucleation, and growth.

The onset of DRX starts once the dislocation density reaches a critical threshold ρ_{crit} (Roberts and Ahlblom, 1978). According to the literature, DRX occurs with subgrain formation at boundaries reaching a critical size. Therefore the model incorporates the Takaki et al. (2009) condition for the onset of recrystallization as:

$$\rho_{crit} = \left(\frac{20S\dot{\varepsilon}}{3bLM\lambda_e^2} \right)^{\frac{1}{3}} \tag{3.10}$$

where S is the Read and Shockley (1950) grain boundary energy per unit area, L is the dislocation mean free path, M is the grain boundary mobility, and $\lambda_e = \alpha \mu b^2$ is the dislocation line energy.

Cahn (1950) first introduced the idea of recrystallization nuclei as initiators of growth based on dislocation density. Brahme et al. (2012) presented a nucleation criterion based on experimental observations, where regions containing lower dislocation content surrounded by high dislocation content neighbours were chosen as potential nuclei. In this work, the disparity in dislocation density tensor (DDT) between adjacent elements is calculated with the Nye's tensor (Nye, 1953) defined from the spatial gradient of the plastic component of the deformation gradient. The model proposed by Popova et al. (2015) instead uses the method of Arsenelis and Parks (1999) where the Nye's tensor is represented by the edge and screw parts of the geometrically necessary dislocation densities (GNDs) and calculated using the shear strain for each slip system as follows:

$$\rho^{\alpha}_{GN(e)} b = -\nabla \gamma^{\alpha} \cdot \mathbf{m}^{\alpha} \tag{3.11}$$

$$\rho^{\alpha}_{GN(s)} b = \nabla \gamma^{\alpha} \cdot \mathbf{n}^{\alpha} \tag{3.12}$$

where (e) and (s) correspond to edge and screw types of dislocations, respectively. The vector quantity $\mathbf{m}^{\alpha}$ represents the slip plane normal, and $\mathbf{n}^{\alpha} = \mathbf{s}^{\alpha} \times \mathbf{m}^{\alpha}$ where $\mathbf{s}^{\alpha}$ is the slip direction. This formulation provides more direct information about the individual contribution of a particular slip plane to the total GND density due to the local strain gradients. The total GND density can then be calculated by the vector sum of the edge and screw components and finally the adjacent grain mismatch can be calculated as the difference in total dislocation density.

The kinematics and growth of the recrystallized grains has been found to be a function of the grain boundary mobility M and the stored deformation energy $\mathscr{P}$ (Gottstein and Shvindlerman, 1999) such that

$$v = M\mathscr{P} \tag{3.13}$$

where v is the grain boundary velocity. The stored deformation energy and mobility can be calculated by:

$$\mathscr{P} = \frac{1}{2} \rho \mu b^2 \tag{3.14}$$

$$M = M_0 \cdot exp\left(\frac{H_m}{kT}\right) \tag{3.15}$$

where H_m is the activation enthalpy, k is the Boltzman constant, T is temperature and M_0 is an athermal term that depends on the grain boundary misorientation.

Lastly, during recrystallization, the sweeping grain boundaries leave behind strain-free grains. For the recrystallized elements, the flow stress needs to be updated from previous values by

$$\sigma = \alpha \mu b \sqrt{\rho} \tag{3.16}$$

This formulation is used as part of the CPFEM simulation along with the hybrid probabilistic CA method described in Popova et al. (2015). Although results from this work are impressive, the authors mention several areas for improvement, such as the inclusion of statistically stored dislocations in the formation. The model also ignores the thermodynamic effects of strain hardening before recrystallization, instead the CPFEM hardening parameters are calibrated from room temperature experimental data. Coupling this work with a thermo-elasto-viscoplastic formulation would provide a tool to predict a wealth of material behaviour from flow stress to microstructure evolution for any desired temperature.

Chapter 4

Part I: A Three Dimensional (3D) Thermo-Elasto-Viscoplastic Constitutive Model for FCC Polycrystals

Edward D. Cyr[1], Mohsen Mohammadi[1], Raja K. Mishra[2], Kaan Inal[1]

[1] *Department of Mechanical and Mechatronics Engineering, University of Waterloo, Waterloo, Canada, N2L 3G1*

[2] *General Motors Research & Development Center, Warren, MI 48090, USA*

Abstract

Temperature has significant effect on the mechanical response of metals and alloys. Industrial processes often use high temperature forming to fabricate components of complex shape from alloys such as aluminum or magnesium that have low room temperature formability. Accurate forming models to integrate warm forming in computer aided engineering (CAE) in production environment has been hampered by a lack of constitutive relations at elevated temperatures, forcing one to rely on experimental data for such integration. In this chapter, a new thermo elasto-viscoplastic (TEV) constitutive relation is developed to model the behaviour of face-centred cubic (FCC) polycrystals, especially aluminum alloys, at elevated temperatures. The model takes into account the temperature dependence of the single crystal elastic coefficients, single slip hardening parameters, thermal softening, rate sensitivity, and the total deformation. The TEV framework has been implemented into the commercial finite element code LS-DYNA to study the effects of temperature on metal forming. Uniaxial tension simulations at six different temperatures ranging from 25°C to 260°C have been performed and calibrated with published experimental results. Equations for the variation of single-slip hardening parameters with temperature have been developed for the AA5754 aluminum alloy. Shear test simulations at different temperatures have been used to validate the model. The proposed framework for the single slip parameters for uniaxial tension accurately predicts the shear stress-shear strain data without the need for any further fitting parameter. Temperature dependence of texture evolution, single slip hardening and hardening rates, thermal softening, and slip activity in AA5754 sheet alloy during temperatures corresponding to warm forming temperatures are investigated.

Keywords: *Cutting and forming; Constitutive behaviour; Crystal plasticity; Elastic-viscoplastic material; Finite elements.*

4.1 Background

With the need to form new and complex metallic components for industrial and commercial applications, warm forming has become an attractive technology to increase the formability of metals (Li and Ghosh, 2003). Automotive industries often use high temperature forming to manufacture vehicle parts from aluminum and magnesium that have low formability at room temperature. In engineering design and the production environment there is a need for constitutive relations at elevated temperatures to accurately model warm forming processes using computer-aided engineering (CAE). This lack of technology has forced industry to rely on costly experimental data for such integration. Better understanding of warm forming significantly improves the usage of metals such as aluminum and magnesium in light-weighting of vehicles. Aluminum provides many benefits over steel in automotive applications due to its corrosion resistance and high strength to weight ratio. Vehicle weight can be significantly reduced by replacing steel components with aluminum, such as door panels, deck lids, roof panels, and bumper beams (Toros et al., 2008). In an effort to reduce carbon emissions and improve fuel economy, vehicle weight reduction is one of the simplest solutions. In modern vehicles, aluminum AA5754 sheet has been most widely used to replace steel exterior panel components (Toros et al., 2008).

Experimental research and phenomenological modeling of metals at elevated temperatures has been widely studied, see e.g. (Abedrabbo et al., 2006). Experimental studies in the low temperature regime (Niewczas and Park, 2008) and warm forming temperature regime show strong thermal influence on the dynamic viscoplastic response of metals (Klopp et al., 1985) and strain-rate sensitivity (Li et al., 2007). Constitutive models to investigate the thermal elastic-plastic behaviour of metals have been developed; see e.g. (Kim et al., 2013; Kabirian et al., 2013; Khan and Baig, 2011; Perzyna, 1988).

Mahabunphachai and Koc (2010) have reported the effect of temperature on the stress response of aluminum and aluminum alloys. Van Den Boogaard and Huétink (2006) have used uniaxial tension experiments at elevated temperatures to fit a Vegter yield function and Bergstrom hardening model. Experiments revealed that local necking occurred far beyond the uniform strain at elevated temperatures and they postulated that this was caused by the strain rate sensitivity of AA5754. It was also observed that room temperature necking occurs at a slight diagonal across the test specimen, different from observations at elevated temperatures where necking orientation is perpendicular to the tensile direction. Li and Ghosh (2003) have studied temperature and strain rate effects on 5XXX and 6XXX series aluminum alloys during uniaxial tension. Investigations in the warm forming temperature regime showed a decrease in hardening and increase in strain rate sensitivity with increasing temperature. They concluded that the warm formability of strain-hardenable 5xxx series alloys is superior to that of the 6xxx series precipitation hardened alloys.

Macroscopic hardening behaviour at elevated temperatures for aluminum has been studied and numerical models have been developed to predict temperature and strain rate dependent material hardening (Abedrabbo et al., 2006; Toros et al., 2010). Experimental studies with AA5754 show that the temperature dependence of the viscoplastic behaviour and the strain-rate sensitivity during uniaxial tension is minimal at temperatures below 100ºC (Abedrabbo et al., 2007; Toros et al., 2010). Phenomenological model for warm forming processes (Kurukuri et al., 2009) and high temperature closed die forging of aluminum (Ganapathysubramanian and Zabaras, 2002) have been developed that account for such behaviour.

Warm forming leads to decreased flow stress and increased ductility in Al-Mg sheet alloys, allowing for deeper drawing and more stretching without design modifications or material microstructure refinement. Early studies on warm forming of aluminum alloys were performed by Dawson (1984) and Beaudoin et al. (1993, 1994). Palumbo and Tricarico (2007) conducted experimental work on optimizing the warm deep drawing process of circular AA5754 sheets. It has been demonstrated that uniform temperature increase improves formability, but the biggest gains can be obtained by applying temperature gradients. In addition, warm forming allows one to overcome serrated flow due to dynamic strain aging, the Portevin-Le Chatelier effect and Luder's band formation resulting from interacting solutes and mobile dislocations (Abedrabbo et al. 2007). Van Den Boogaard et al. (2001) have shown improved formability of AA5754 sheets during deep drawing where the cylindrical cup limiting draw ratio could be improved from 2.1 to 2.6 by increasing the flange temperature to 2500C. Van Den Boogard and Huétink (2006) used a Bergstrom hardening model to predict this behaviour but were unable to accurately capture the flow behaviour at high temperatures (above 2000C). Kurukuri et al. (2009) applied the NES dislocation based model to improve on the work of Van Den Boogaard and Huétink (2006) and concluded that, even with the correct description of a yield locus and the microstructure based work hardening model, deep-drawing simulations still differed from experimental results. This was especially the case for predicting thickness distributions.

Recent leaps in computational power have allowed the usage of advanced "mechanism" based models such as crystal plasticity for the numerical simulation of metal forming. Roters et al. (2010) has presented an excellent overview on mechanical constitutive laws, kinematics and mutli-scale methods in crystal plasticity finite-element modeling, and show that only works based on dislocation theory are capable of including thermal effects. Thermodynamical crystal plasticity, where temperature is introduced as a product of plastic work, has been used to study texture evolution and strain rate sensitivity of body-centred cubic (BCC) materials (Lee et al., 1997; Clayton, 2005). Kok et al. (2002) has developed a rate-dependent crystal plasticity framework based on isotropic mechanical threshold stress continuum model. Their model employed the Newton-Raphson algorithm to perform a minimization process to find the material properties. Thermodynamical crystal plasticity coupled with damage for aluminum alloys (Srikanth and Zabaras, 1999) and dislocation-based crystal plasticity multi-scale modeling has also been developed for metallic single crystals (Groh et al., 2009; Hansen et al., 2013). Thermal loading in thin film crystals using various thermodynamics based micromechanical models (Yu et al., 1997; Faghihi et al. 2013) and on the latent hardening of face-centred cubic (FCC) polycrystals under complex loading paths (Gerard et al., 2013) have also been reported.

Single crystal elastic coefficients are important material properties and the temperature dependences of the elastic coefficients for alloys and compounds at different temperatures and pressures have received significant amount of interest (i.e., Wang et al., 2005; Bouhemadou et al., 2012). Different experimental methods have been used to measure single crystal elastic constants (Hearmon et al., 1946; Yoo et al., 1997). Simmons and Wang (1971) summarized the single crystal constants of different metals and aggregates for various temperatures including aluminum-magnesium alloys. However, measuring these constants at different temperatures and pressures for alloys of different compositions is both time and money consuming. Thus, different computational techniques such as first-principle calculations based on density functional theory have been recently employed to calculate the elastic constants of materials (Shang et al., 2007; Kim et al., 2009; Yu et al., 2009).

4.2 Approach

Better understanding of the effect of temperature on the crystal lattice can be achieved by investigating the fundamental physical behaviour of the material. It has been shown that thermodynamics is an integral part of molecular dynamics and dislocation dynamics (Amodeo and Ghoniem, 1990). Studies also show a strong temperature dependence of the elastic behaviour of metallic single crystals (Varshni, 1970). Kocks (1976) also discussed a non-linear material strain-rate dependence on both temperature and crystal elastic moduli. Crystal Plasticity Finite Element Method (CPFEM) has been a valuable tool for studying elasto-viscoplastic behaviour of materials. The mechanical response of materials using 2D CPFEM has been widely studied (i.e., Kuroda and Tvergaard, 2004, 2007; Hu et al. 2010). However, it has also been shown that the 2D CPFEM is inadequate for modeling accurately the state of strain and stress as well as many other phenomena in sheet metal forming such as bending and surface roughness (Rossiter et al., 2013).

Up to the knowledge of the authors, there is no physically based constitutive model that can be used to accurately describe and predict metal forming behaviour at elevated temperatures for polycrystals. In the contributions with coupled thermo-mechanical crystal plasticity models, temperature dependence has not been incorporated completely. For example Jain and Agnew (2007) employed Asaro and Needleman (1985) framework to model temperature dependence of twinning in HCP Magnesium alloys without incorporating components for temperature, such as thermal deformation gradient and thermal slip softening. Furthermore, some of the more comprehensive coupled thermo-mechanical crystal plasticity models (Clayton, 2005; Lee et al., 1997) consider constant single slip hardening parameters with respect to temperature. Thus, for modeling different strain paths, such as uniaxial tension, shear, or compression at elevated temperatures, separate experiments need to be completed to calibrate single slip hardening parameters to predict each corresponding stress-strain curve. Lastly it is observed that the temperature dependence of elastic coefficients has a considerable effect on the deformation field in some warm forming processes, such as spring-back. This phenomenon has not been investigated in regards to polycrystal deformation at elevated temperatures.

In this chapter, a new 3D thermo elasto-viscoplastic (TEV) constitutive model based on the work of Asaro and Needleman (1985) and Rossiter et al., (2010) is developed to accurately model the behaviour of aluminum alloys at elevated temperatures up to the recrystallization temperature. The original crystal plasticity formulation has been improved to comprehensively include the effects of temperature. The thermal deformation gradient and temperature dependence of elastic coefficients is considered. A new thermal slip-softening model is developed and employed to control the thermal effect on slip rates. Lastly, three new equations are developed to describe the temperature dependence of single-slip hardening parameters. The commercial finite element package LS-DYNA is used to implement the new 3D thermo elasto-viscoplastic constitutive model in order to investigate the three-dimensional capabilities of the model. Uniaxial tension simulations for different temperatures between 25ºC and 260ºC are performed and the constitutive model is calibrated with existing experimental data for AA5754. The three hardening parameter equations are developed from the uniaxial data to predict the variation of slip hardening. Furthermore, simple shear simulations are carried out to validate the uniqueness of the identified equations for the single-slip hardening determined from uniaxial simulations.

4.3 Thermo-Elasto-Viscoplastic (TEV) Constitutive Model

The rate-dependent polycrystal plasticity framework developed by Asaro and Needleman (1985) and further by Inal et al. (2002) and Rossiter et al. (2010) is used as the basis of this analysis. The constitutive law is developed for a FCC single crystal and then is implemented in 3D finite element commercial software.

4.3.1 Kinematics of Deformation

In order to completely capture the kinematics of deformation for a single crystal under both thermal and mechanical loads, the material and the total lattice deformation are decomposed into elastic and rigid body rotation, permanent plastic deformation, and thermal deformation. These deformations are shown in Figure 4-1.

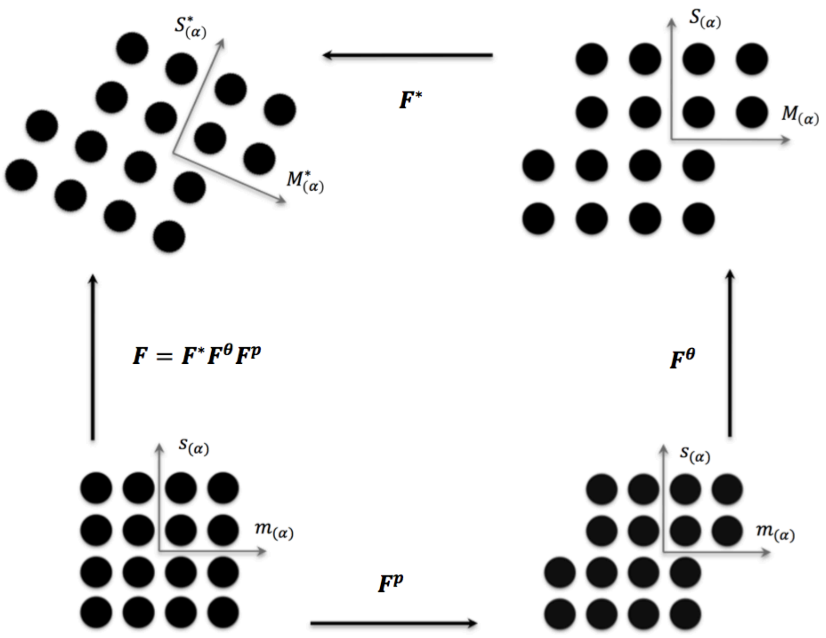

Figure 4-1 Decomposition of total deformation tensor to plastic, thermal expansion, and elastic - rigid body rotation components.

Thus, the total deformation gradient can then be written as

$$F = F^* F^\theta F^P \tag{4.1}$$

where, F^P considers only crystallographic slip and F^* embodies elastic deformation and rigid body rotation. Thermal deformation, F^θ, consists of the thermal expansion of the material and lattice during transient analysis.

The spatial velocity gradient in the current configuration then becomes

$$L = \dot{F}F^{-1} = L^{*} + L^{\theta} + L^{P} \tag{4.2}$$

where,

$$L^{*} = \dot{F}^{*}F^{*-1} \tag{4.3}$$

$$L^{\theta} = \dot{F}^{*}\left(\dot{F}^{\theta}F^{\theta^{-1}}\right)F^{*-1} \tag{4.4}$$

$$L^{P} = \dot{F}^{*}\dot{F}^{\theta}\left(\dot{F}^{P}F^{P^{-1}}\right)F^{\theta^{-1}}F^{*-1} \tag{4.5}$$

The thermal deformation is assumed to be isotropic (Lee et al., 1997), i.e.

$$\dot{F}^{\theta}F^{\theta^{-1}} = \alpha_{T}\dot{\theta}\mathbf{I} \tag{4.6}$$

where θ is the temperature change measured from the reference state, α_T is the coefficient of thermal expansion representing change in length per unit current length per unit increment θ, and $\mathbf{I}$ is the unit identity tensor.

Taking the symmetric and antisymmetric parts of the velocity gradient leads to the elastic, thermal, and plastic strain-rates D^{*}, D^{θ}, and D^{P}, and the rigid lattice rotation and plastic spin W^{*} and W^{P}.

$$D = D^{*} + D^{\theta} + D^{P} \tag{4.7}$$

$$W = W^{*} + W^{P} \tag{4.8}$$

It is assumed that the thermal expansion acts hydrostatically and therefore does not contribute to lattice spin, i.e. $W^{\theta} = 0$.

Lattice vectors $s_{(\alpha)}$ and $m_{(\alpha)}$ corresponding to slip direction and slip-plane normal are assumed to stretch and rotate by

$$S^{*}_{(\alpha)} = F^{*}F^{\theta}s_{(\alpha)} \tag{4.9}$$

$$M^{*}_{(\alpha)} = m_{(\alpha)}F^{\theta^{-1}}F^{*-1} \tag{4.10}$$

where α represents the 12 slip systems in an FCC crystal. The following symmetric and skew-symmetric tensors are calculated for each slip system α

$$P_{(\alpha)} = \frac{1}{2}\left(S^{*}_{(\alpha)} \otimes M^{*}_{(\alpha)} + M^{*}_{(\alpha)} \otimes S^{*}_{(\alpha)}\right) \tag{4.11}$$

$$W_{(\alpha)} = \frac{1}{2}\left(S^*_{(\alpha)} \otimes M^*_{(\alpha)} - M^*_{(\alpha)} \otimes S^*_{(\alpha)}\right) \tag{4.12}$$

The crystal plastic strain-rate and spin can then be written as

$$D^P = \sum_{\alpha} P_{(\alpha)}\dot{\gamma}_{(\alpha)} \tag{4.13}$$

$$W^P = \sum_{\alpha} W_{(\alpha)}\dot{\gamma}_{(\alpha)} \tag{4.14}$$

where $\dot{\gamma}_{(\alpha)}$ is the shear-rate on slip system α.

4.3.2 Constitutive Model

Introducing $\overset{\nabla}{\tau}$ as the Jaumann rate of the Kirchoff stress tensor τ (where $\tau = J\sigma$), the elastic constitutive equation for a single crystal can be written as

$$\overset{\nabla}{\tau}{}^* = \dot{\tau} - W^*\tau + \tau W^* = \mathbf{L}D^* \tag{4.15}$$

where the symmetric tensor **L** is the tensor of elastic constants. To configure the constitutive equation in terms of the Jaumann rate of Cauchy stress ($\sigma = det(F)^{-1}\tau$), the second order tensor $R_{(\alpha)}$ is introduced as follows

$$R_{(\alpha)} = \mathbf{L}P_{(\alpha)} + W_{(\alpha)}\sigma - \sigma W_{(\alpha)} \tag{4.16}$$

Using (4.7), (4.8), (4.13), (4.14) and (4.16) the constitutive equation can be rewritten as follows

$$\overset{\nabla}{\sigma} = \mathbf{L}D - \dot{\sigma}_0 - \sigma trD \tag{4.17}$$

where $\dot{\sigma}_0$ is a slip-rate dependent viscoplastic-type stress rate defined as

$$\dot{\sigma}_0 = \sum_{\alpha} R_{(\alpha)}\dot{\gamma}_{(\alpha)} \tag{4.18}$$

4.3.3 Temperature Dependency of Elastic Constants

The symmetric anisotropic elastic constants tensor **L** is well known and it is written as

$$\begin{bmatrix} C_{11} & C_{12} & C_{13} & 0 & 0 & 0 \\ C_{21} & C_{22} & C_{23} & 0 & 0 & 0 \\ C_{31} & C_{32} & C_{33} & 0 & 0 & 0 \\ 0 & 0 & 0 & C_{44} & 0 & 0 \\ 0 & 0 & 0 & 0 & C_{55} & 0 \\ 0 & 0 & 0 & 0 & 0 & C_{66} \end{bmatrix}.$$

For the FCC single crystal, $C_{11} = C_{22} = C_{33}$, $C_{12} = C_{13} = C_{23}$, and $C_{44} = C_{55} = C_{66}$. Therefore, the tensor can be simplified to 3 elastic constants C_{11}, C_{12} and C_{44}.

Numerous investigations were made during 1950s and 1960s to formulate the temperature dependence of elastic constants (i.e., Bornand and Huang (1954), Alers and Waldorf (1961)). Slagle and McKinstry (1967) proposed a polynomial equation for the temperature dependence of elastic constants. Subsequently, Watchman et al. (1961) proposed an exponential temperature variation for Young's modulus. Based on the work of Slagle and McKinstry (1967) and Watchman et al. (1961), Varshni (1970) postulated two equations to formulate temperature dependence of stiffness coefficients C_{ij}.

The following general theoretical model was first proposed by Watchman et al. (1961) and Varshni (1970) in order to formulate the temperature dependence of elastic coefficient

$$C = C_0 - \frac{s}{\left(e^{t/T} - 1\right)} \tag{4.19}$$

where C, C_0, s and t are elastic coefficients and T is temperature in Kelvin. A brief discussion on the origins of Equation (33) was first presented by Varshni (1970). It has been derived from work done by Leibfried and Ludwig (1961) and Einstein's model for a harmonic crystal (Girifalco, 2000). The coefficient C_0 represents the elastic constants at 0 Kelvin, t is related to Einstein characteristic temperature (A. Einstein, 1907; L. Girifalco, 2000), and s is another known material constant, which is related to zero-temperature harmonic elastic stiffness coefficient (Suzuki et al. 2011). In equation (4.19), the coefficients s and t are defined as (Slagle and Mckinstry, 1967)

$$s = C_0 B h v \tag{4.20}$$

$$t = hv/k \tag{4.21}$$

Where B is a coefficient related to the type of crystal and h, v and k are material constants. The coefficients s and t are found from measured (or calculated) data rather than equations (4.20) and (4.21).

4.3.3.1 Numerical Implementation

Equation (4.22) represents the tensor form of equation (4.19), and was used by Varshni (1970) to accurately predict elastic constants for aluminum to within 0.04% average error over 16 sample temperatures between 0 and 300K. However, it is acceptable to use this equation to formulate the temperature dependence of alloys for most of the temperature range (Varshni, 1970).

$$C_{ij} = c_{ij}^0 - \frac{s_{ij}}{\left(e^{t_{ij}}/\theta - 1\right)} \tag{4.22}$$

where c_{ij}^0, s_{ij} and t_{ij} are material constants. Table 4-1 contains these material constants for aluminum (Varshni, 1970) and Figure 4-2 demonstrates the temperature dependence of aluminum using equation (4.22) for temperature between 0 and 800 K.

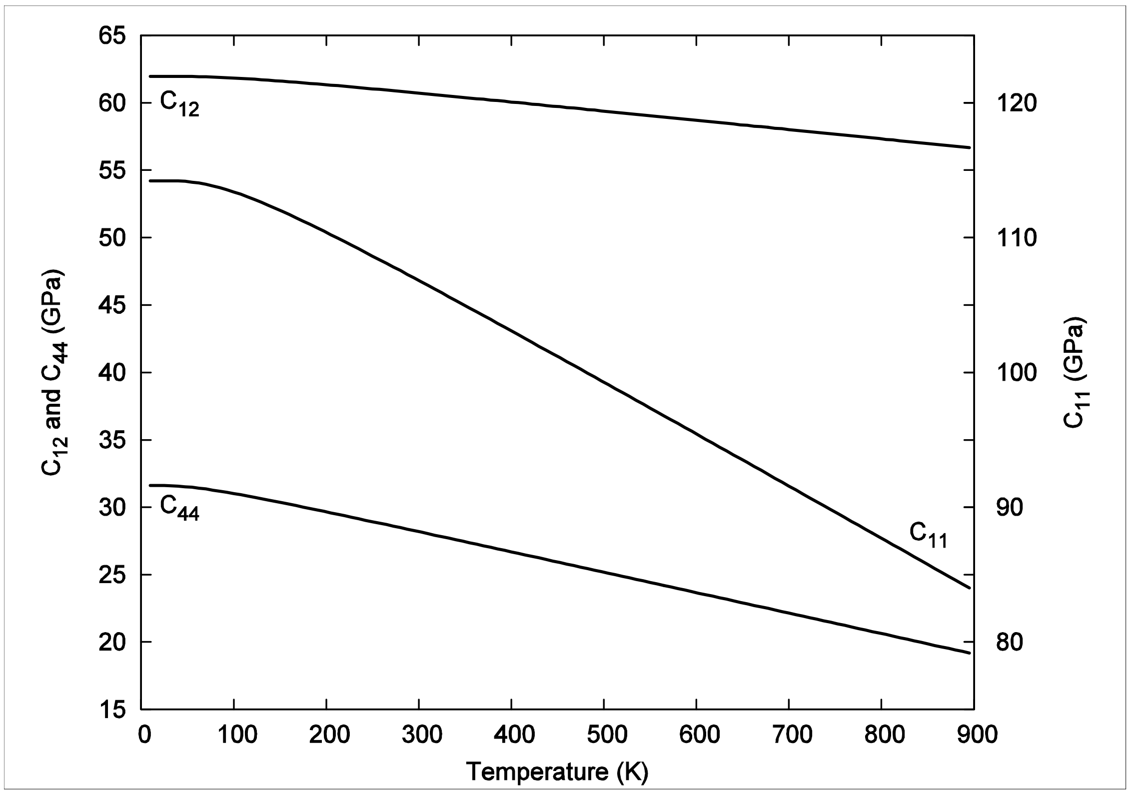

Figure 4-2 Calculated adiabatic elastic stiffness constants of aluminum obtained from equation (4.22).

Table 4-1 Value of parameters in equation (4.22) (Varshni, 1970).

	c_{ij}^0 *(GPa)*	s_{ij} *(GPa)*	t_{ij} *(°K)*
C_{11}	114.2	10.1	258.4
C_{12}	61.95	2.05	293.6
C_{44}	31.60	2.56	168.0

4.3.4 Shear Rates and Rate Sensitivity

The well-known power-law rule is employed in this model to govern shear slip rates as follows

$$\dot{\gamma}_{(\alpha)} = \dot{\gamma}_0 \mathbf{sgn} \tau_{(\alpha)} \left| \frac{\tau_{(\alpha)}}{g_{(\alpha)}} \right|^{1/m} \tag{4.23}$$

where $\dot{\gamma}_0$ is a reference shear rate assumed to be constant across all slip systems, $\tau_{(\alpha)}$ is the resolved shear stress on slip system, $g_{(\alpha)}$ is its current hardness, and m is the strain-rate sensitivity. In this framework, the slip-rate effect of temperature is embedded in $g_{(\alpha)}$. This is described in further detail in Section 4.3.4.

The new model employs a power law model for crystallographic slip with a temperature dependent strain rate exponent. The temperature dependence of strain-rate sensitivity is accounted for using the formulation suggested by Kocks (1976);

$$m = \frac{9k\theta}{b^3\sqrt{\mu_f(\mu_f - \eta_f)}} \tag{4.24}$$

where, k is the Boltzmann constant, b is the Burgers vector and θ is temperature in Kelvin. The elastic parameters can be related to the classical elastic stiffness parameters from the previous section as $\mu_f = C_{44}$ and $\eta_f = C_{44} + 1/2(C_{12} - C_{11})$.

4.3.5 Proposed thermal softening model

In the current crystal plasticity formulation, slip hardening is due to the accumulation of slip or shear on active slip systems. The proposed model employs a thermal softening function to update $g_{(\alpha)}$ by

$$g_{(\alpha)} = g_{0(\alpha)}T_s(\theta) \tag{4.25}$$

where $T_s(\theta)$ represents a thermal softening function (factor) of current temperature θ, and $g_{(\alpha)}$ is the slip hardening at reference temperature θ_0. Rossiter et al. (2010) proposed a linear model for thermal slip softening where at room temperature $T_s(\theta_r) = 1$, and at melting temperature $T_s(\theta_m) = 0$,

$$T_s(\theta) = \frac{\theta_m - \theta}{\theta_m - \theta_r} \tag{4.26}$$

Clayton (2005) used a power law type model suggested by Klopp et al. (1985) of the form

$$T_s(\theta) = \left(\frac{\theta}{\theta_0}\right)^p \tag{4.27}$$

where p is the thermal softening exponent ($p < 0$) and θ_0 a reference temperature. Klopp et al. (1985) used equation (4.27) to predict softening behaviour for pure aluminum and Clayton (2005) for tungsten.

Lee et al. (1997) suggested an exponential form to represent thermal softening that applies directly to the single-slip shear-rate equation, becoming

$$\dot{\gamma}_{(\alpha)} = \dot{\gamma}_0 \mathbf{sgn}\tau_{(\alpha)} \left|\frac{\tau_{(\alpha)}}{g_{(\alpha)}}\right|^{1/m} exp(-\lambda\Delta\theta) \tag{4.28}$$

where λ is the thermal softening parameter and $\Delta\theta$ is the total temperature increase.

The above equations of thermally induced slip-softening are reasonable representations at temperatures close to room temperature; however, they are not applicable at temperatures approaching melting and/or absolute zero. Clayton and Klopp's equations, i.e. equation (4.27), increase to infinity at 0K and do not decay to zero at melting temperature. Physically, this implies that the slip system has infinite strength at absolute zero and retains some strength as a liquid at melting temperature. The linear model also suggests an increasing slip strength to several times that of room temperature at 0K.

Remark 1: Due to the aforementioned issues, a new thermal softening equation is proposed to represent thermal softening on the range of absolute zero to melting temperature that can be written as

$$T_s(\theta) = 1 - \left(\frac{\theta}{\theta_m}\right)^p \tag{4.29}$$

where, p is the softening sensitivity index of the temperature effect on slip softening and θ_m is the material's melting temperature.

Predictions with the discussed thermal-softening models are presented in Figure 4-3, where thermal softening equations are plotted against temperature. The data suggests that behaviour of alloyed aluminum, specifically AA5754, is different from that of the pure metal where variations in temperature near ambient show significant stress-strain variations. For alloyed AA5754, stress response is not noticeably affected until temperatures of approximately 350–400 Kelvin (Abedrabbo et al., 2007). If thermal softening is correctly represented by these functions, the corresponding plot should approach unity at cryogenic temperatures and decay to zero from ambient to melting temperature. The findings in literature also suggest that the effect of thermal softening increases non-linearly with increasing temperature.

The form of Eq. (4.25) along with Eq. (4.29) is intuitively chosen based on the macroscopic uniaxial stress-strain data presented by (Abedrabbo et al., 2007) for different temperatures. This is of similar form to the work presented by Kocks et al. (1975) in lower scales for the activation energy to overcome glide resistance and the mechanical threshold stress theorem (Follansbee and Kocks, 1988). In their work, the resistance to dislocation glide was presented using a thermodynamical framework; however, in the present work, this effect is described in the hardening equation, where higher temperature leads to easier glide. Finally, it is noted that, equation (4.29) is valid in the temperature range that the present analysis is based on for AA5754, i.e. $0.3\theta_m < \theta < 0.5\theta_m$. It was shown by Kocks et al. (1975) that the material behaviour is different in different temperature regimes and the physics has to capture these effects via different equations in other regions.

Figure 4-4 presents a summary of the effect of the thermal softening sensitivity index, p, on the proposed thermal softening equation. When the sensitivity index is unity, the thermal softening equation linearly decreases from the absolute zero to melting temperature. An increase in the sensitivity index increases the curvature of the softening equation. Physically, this means that a greater sensitivity corresponds to an increased resistance to thermal softening with respect to increasing temperature. For higher values, such as six, the thermal softening factor, T_s, stays near unity up to 0.5 of homologous temperature, at which point it starts to rapidly decay to zero. In this study, a thermal softening sensitivity index of $p = 4.0$ provided the best results.

The proposed equation (4.29) agrees well with the experimental stress-strain data found in literature. At low temperatures (below ambient temperature) the effect of thermal softening is minimal and increases with increasing temperature. A thermal softening intensity of $p = 4.0$ was chosen for this model and can reproduce reported experiments, where the effect of temperature on stress response is not significant until temperatures near 350–400K for aluminum (Abedrabbo et al., 2006; Toros et al., 2010).

4.3.6 Hardening model

The evolution of the slip system hardening function $g_{0(\alpha)}$ is defined in rate form $\dot{g}_{0(\alpha)}$ so that;

$$\dot{g}_{0(\alpha)} = \sum_{\beta} h_{(\alpha\beta)} \left|\dot{\gamma}_{(\beta)}\right| \tag{4.30}$$

where $h_{(\alpha\beta)}$ are the components of the hardening moduli defined as

$$h_{(\alpha\beta)} = q_{(\alpha\beta)} h_{(\beta)} \quad (no\ sum\ on\ \beta) \tag{4.31}$$

Here $h_{(\beta)} = h_{(\beta)}(\theta)$ is a temperature dependent single slip hardening rate, and $q_{(\alpha\beta)}$ is the matrix describing the latent hardening behaviour.

The components of $h_{(\alpha\beta)}$ depend on deformation history and accumulated slip. This formulation considers the simple power-law form for single slip hardening (Peirce et al. 1983) modified to include temperature dependence;

$$h_{(\beta)} = h_0 \left(\frac{h_0 \gamma_a}{\tau_0 n} + 1 \right)^{n-1} \tag{4.32}$$

where $h_0 = h_0(\theta)$ is the reference hardening rate, $n = n(\theta)$ is the hardening exponent, and $\tau_0 = \tau_0(\theta)$ is the reference shear strength. This was considered in phenomenological modeling previously by Abedrabbo et al. (2007), where they studied the temperature effects on the flow rule proposed by Wagoner et al. (1988). They experimentally showed that the material hardening coefficients varied with temperature and from their flow rule developed equations to describe the temperature dependence of hardening parameters for 5xxx series aluminum alloys.

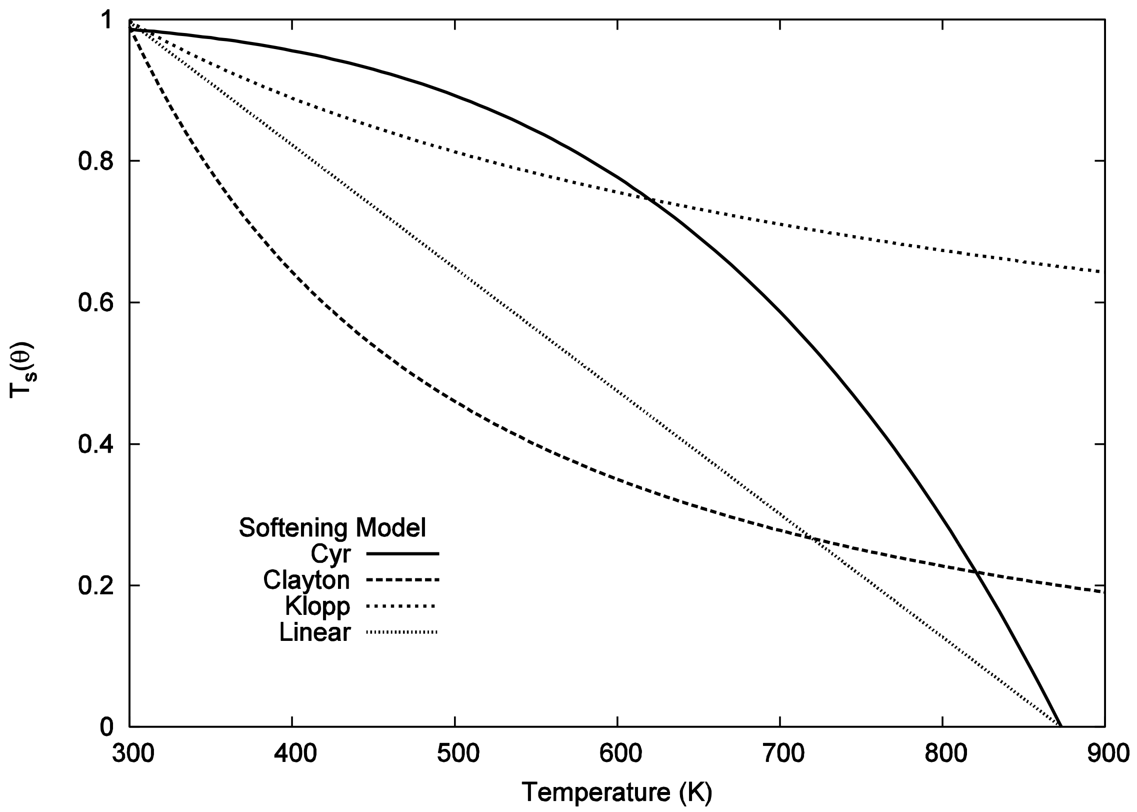

Figure 4-3 Comparison of thermal slip-softening models.

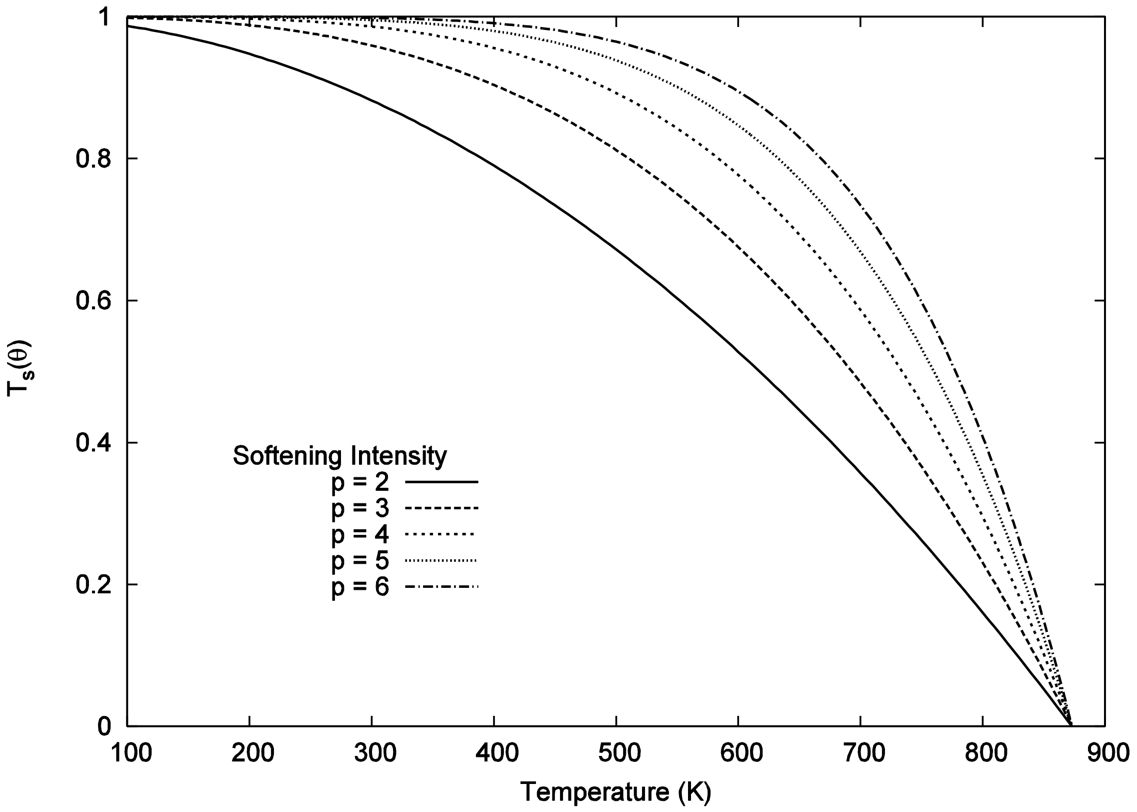

Figure 4-4 The effect of softening intensity index on the thermal softening factor obtained from equation (4.29) for proposed model for aluminum with $\theta_m = 873K$.

Remark 2: The difficulty in determining temperature dependence is capturing the correct hardening. In an attempt to do this, experimental data was examined for AA5754 over a wide range of temperatures and strain rates. The temperature dependence of the material strain-rate sensitivity has been studied extensively and the proposed relationship is described previously (see section 4.3.4). For this work, the above relationship for strain rate sensitivity will be employed.

In regards to the hardening parameters n, τ_0, and h_0, temperature dependency was estimated using knowledge of related physical phenomenon during elevated temperature forming in conjunction with the available experimental data. The hardening exponent, n, can be considered as a rate of dislocation pile-up during deformation. The rate of dislocations stored in the material is a result of the plastic deformation and strain-rate leading to dislocation production, and the thermally dependent rate of dislocation annihilation. Dislocation annihilation, leading to material softening, is a thermally motivated process. Thus, at increasing temperatures, this mechanism competes with dislocation recovery and the rate of dislocation pile-up, n, decreases. The experimental data suggests that for AA5754 this is a linear dependence, in the temperature range (25ºC – 260ºC) studied.

The second hardening parameter τ_0 is related to the initial slip strength, or physically speaking, the mechanical stress required on a given slip direction to cause slip or dislocation. In terms of energy, the mechanical and thermal inputs contribute to overcoming this “slip activation energy” barrier. If we assume the resistance to slip is material dependent and constant for a single material, then if we increase the input from thermal energy, the mechanical input may be lessened while still causing slip. Thus, the slip strength in terms of energy remains constant, however the contribution required through mechanical stress can be adjusted by changing the thermal contribution, i.e. temperature. Experimental data in the warm forming regime suggested a linear dependence between the slip strength and temperature.

The last parameter h_0 is related to the mechanism at the transition from elastic to plastic deformation. The onset of plastic deformation occurs when the applied mechanical stress overcomes the slip strength. It is assumed that the material is initially without dislocations, or at least the dislocation content is insignificant. Therefore the initial hardening rate h_0 can be considered purely as the rate of dislocation production. The initial rate of dislocation annihilation is assumed to be negligible due to the lack of dislocations present in the materials. Furthermore, at high temperatures where dislocation annihilation and dynamic recovery are certain to be dominant, there is still material hardening that occurs during the initial plastic deformation. This was also confirmed by the experimental stress-strain data. The difficulty, however is determining the temperature dependence, which is not linear. After examination of the experimental stress-strain data, it was assumed that this dependence was exponential with respect to temperature.

In this formulation the hardening exponent, reference slip strength, and hardening rate are assumed to be temperature dependent as follows

$$n = \bar{n}_0 + \psi \left(\frac{T}{T_m} \right) \tag{4.32}$$

$$\tau_0 = \bar{\tau}_0 + \phi \left(\frac{T}{T_m} \right) \tag{4.33}$$

$$h_0 = \bar{h}_0 \ exp\left(\chi \frac{T}{T_m} \right) \tag{4.34}$$

where $\bar{n}_0$, $\bar{\tau}_0$, and $\bar{h}_0$, are material constants representing the hardening exponent, mechanical threshold stress for slip, and transition hardening rate at zero Kelvin, respectively. Parameters ψ and ϕ describe the linear temperature dependence of the hardening exponent and CRSS, respectively, while χ describes an exponential temperature dependence for the transition hardening rate. The material temperature θ is normalized using the melting temperature θ_m in Kelvin. These parameters were calibrated using uniaxial tension experiments at four different temperatures. The process is described in Section 4.4 for AA5754.

4.4 Finite Element Implementation

In this section, the forward Euler subroutine for implementing the TEV crystal plasticity model in commercial explicit finite element software LS-DYNA is summarized. The details of the basic formulation can be found in Rossiter et al., (2010).

4.4.1 Forward Euler Algorithm

This approach employs slip rates and temperature at time to compute quantities for time. Known values for each subroutine entry are as follows

$$F_{(n+1)}, F_{(n)}, \theta_{(n+1)}, \theta_{(n)}, P^{\alpha}_{(n)}, W^{\alpha}_{(n)}, \sigma_{(n)}, \text{ and } \Delta t. \tag{4.35}$$

The time rate of temperature change for the current time-step is updated by

$$\dot{\theta} = \frac{\theta_{(n+1)} - \theta_{(n)}}{\Delta t} \tag{4.36}$$

and the thermal deformation for $t_{(n+1)}$ is

$$F^{\theta}_{(n+1)} = e^{\alpha_T \dot{\theta} \mathbf{I} \Delta t} F^{\theta}_{(n)}. \tag{4.37}$$

Lattice slip plane normal and slip direction can then be updated and rotated into the current configuration by the following equations

$$S^{*}_{\alpha(n+1)} = F^{*}_{(n+1)}F^{\theta}_{(n+1)}Q_{(n+1)}s_{(\alpha)} \tag{4.38}$$

$$M^{*}_{\alpha(n+1)} = m_{(\alpha)}Q_{(n+1)}(F^{\theta}_{(n+1)})^{-1}(F^{*}_{(n+1)})^{-1}. \tag{4.39}$$

Unlike in equations (4.9) and (4.10), which is for a single crystal formulation, here the crystal axis must be rotated into the lab system using the orientation matrix Q. The orientation matrix is updated using the method of Raphanel et al., (2004) and the Euler angles (ϕ_1, Φ, and ϕ_2) are computed and used to track the evolution of the texture of the material in polycrystal calculations (Kocks et al., 2001; Rossiter et al., 2010).

Lastly, the total slip γ_a, slip hardening $h_{(\beta)}$, and slip strengths $g_{(\alpha)}$ are updated as follows

$$\gamma_{a(n+1)} = \gamma_{a(n)} + \sum_{\alpha} \left| \dot{\gamma}_{(\alpha)_{(n)}} \right| \Delta t \tag{4.40}$$

$$h_{(\beta)}(\theta) = h_0 \left(\frac{h_0 \gamma_a}{\tau_0 n} + 1 \right)^{(n-1)} \tag{4.41}$$

$$g_{(\alpha)_{(n+1)}} = g_{(\alpha)_{(n)}} + \left(\sum_{\beta} h_{(\alpha\beta)_{(n+1)}} \left| \dot{\gamma}_{(\beta)_{(n)}} \right| \Delta t \right) \left(1 - \left(\frac{\theta_{(n+1)}}{\theta_m} \right)^{p} \right). \tag{4.42}$$

It is noted that total accumulated slip γ_a is not equal to $\gamma_{(\alpha)}$, and the coefficients h_0, τ_0, and n are all functions of temperature in this study.

4.4.2 Construction of Finite Element Model

In this chapter, numerical simulations of uniaxial tension and simple shear are performed for the AA5754 aluminum alloy sheet. The chemical composition of this alloy is listed in Table 4-2. The thermal expansion coefficient for this alloy is 24.1×10^{-6} $[1/K]$ (Hidnert & Krider, 1952). The three-dimensional (3D) grain structure and orientation data are obtained in a voxelized form from serial sectioning as in Schaffer et al. (2007). A statistically equivalent data set of the polycrystal structure is created for each simulation as explained in the following section, and the microstructure is converted into a 3D mesh for each simulation as explained in Sections 4.4.1 and 4.4.2.

Table 4-2 Chemical composition of AA5754 aluminum alloy (wt%).

Alloy	Mg	Mn	Cr	Fe	Si	Cu	Al
AA5754	3.1	0.25	<0.01	0.24	<0.1	0.02	Balance

4.4.3 Construction of Microstructure

Synthetic microstructures (both grain morphology and crystallographic orientation) are generated using experimental two-dimensional (2D) electron backscatter diffraction (EBSD) maps. Using the 2D maps, a 3D statistically equivalent microstructure is built via the so-called microstructure builder. The details of this method can be found in (Brahme et al., 2006).

The generated 3D microstructure for uniaxial tension simulations is shown in Figure 4-4. The FE mesh is built using a single finite element per grain in an 1800 x 1800 x 1800 cube. The polycrystal aggregate is comprised of 5832 grains. It is noted that, the grains are assigned at random and the grain colours have no reflection on grain orientations.

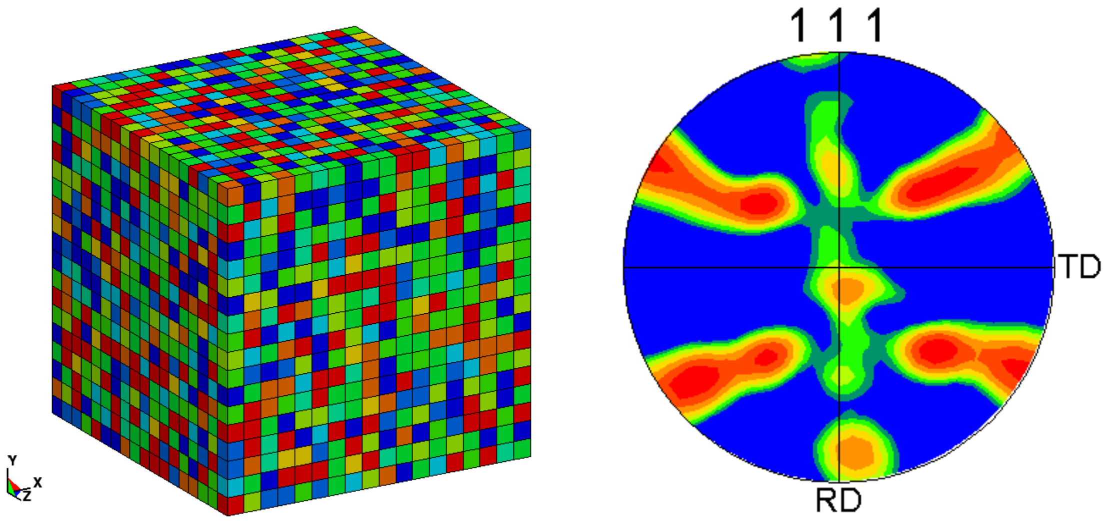

Figure 4-5 Initial FE per grain microstructure and texture pole figure for uniaxial tension simulation.

The microstructure generated for the simple shear simulations is presented in Figure 4-6. The microstructure is comprised of 175 grains and is sampled on a 180x30x30 element grid in x, y, and z directions respectively. As in the previous case, the grain colours do not reflect their crystallographic orientation.

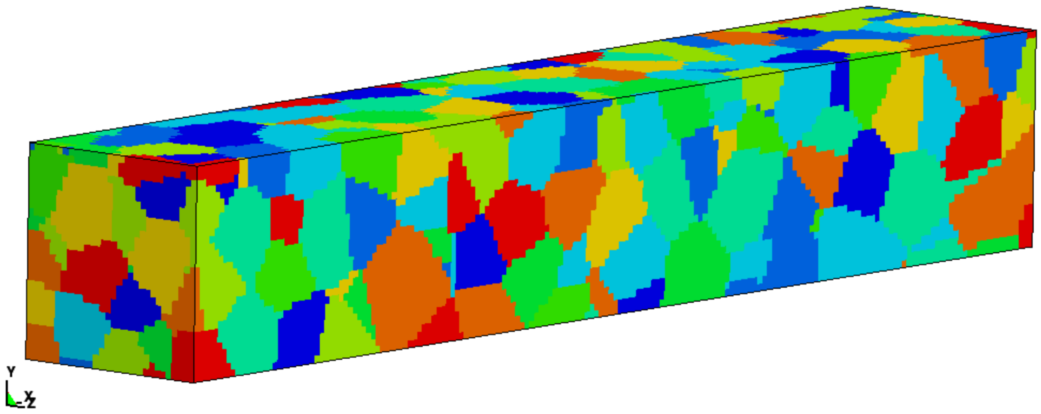

Figure 4-6 3D finite element mesh with visible voxelized grains.

Using the experimentally measured texture, shown in Figure 4-7(a), a statistically equivalent texture is generated, i.e. Figure 4-7(b). This generated texture is applied to a 3D finite element mesh constructed for the numerical simulations. Once the mesh is built, the boundary conditions are applied as described in Sections 4.5.1 and 4.54..2 and the numerical model presented in Section 4.4.1 is employed to study the effects of temperature on large plastic deformation.

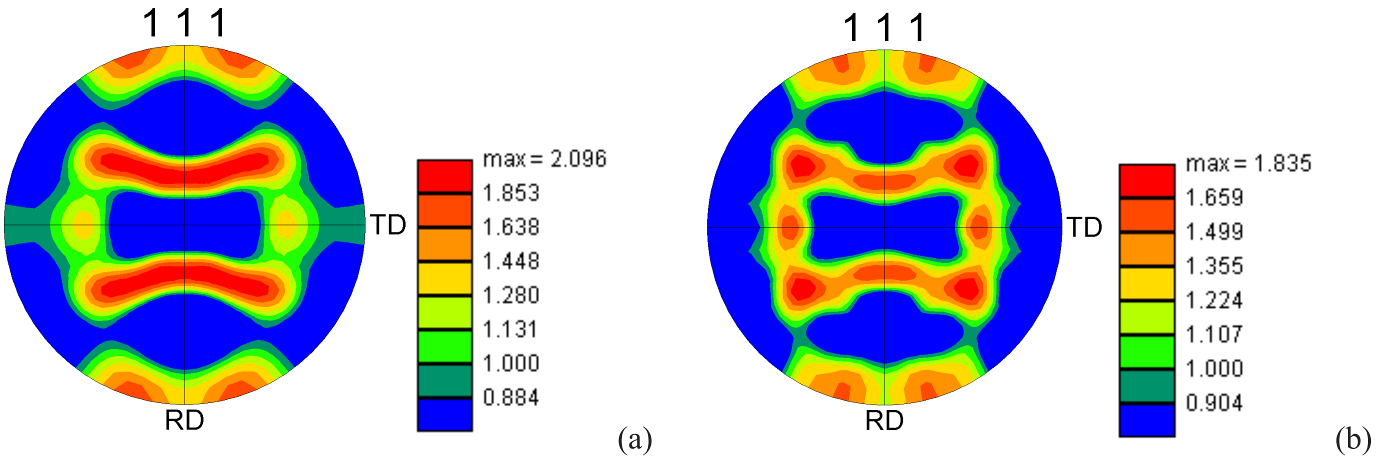

Figure 4-7 (a) Measured texture, and (b) statistically equivalent generated texture.

4.5 Results and Discussion

In this section, numerical simulations for uniaxial tension and simple shear are performed with the proposed thermo-plasticity constitutive model. As a first step the behaviour of the hardening parameters $h_0(\theta)$, $\tau_0(\theta)$, and $n(\theta)$ as a function of temperature are determined (as presented in equations (4.32)-(4.34). Experimental data for low strain rate is used from Abedrabbo et al. (2010) to eliminate the temperature effect on strain rate sensitivity in the model. For initial simulations, the new model assumes a constant strain rate sensitivity index of 0.02. Simulations of simple shear (at different temperatures) are then performed and the predictions are compared with available experimental data (Pandey et al. 2013). Parametric studies are presented on thermal softening intensity index, p, and its effect on the polycrystal response at various temperatures. Finally, analysis on the temperature dependence of elastic constants is also presented.

It is noted that, deformation mechanisms in “hot” temperatures such as dynamic recrystallization, grain boundary sliding, and dynamic recovery are not considered in this constitutive model. These mechanisms for most aluminum alloys are active above 250ºC (Doherty et al. 1997 and McQueen et al. 2011). The hot deformation of some of these alloys have been studied experimentally and numerically; i.e., Ravichandran and Prasad, (1991) and Yan et al. (2012). Van Den Boogaard et al. (2006) modeled warm cup drawing behaviour of aluminum sheet 5754 and was able to reasonably fit the flow stress below 200ºC. However, they were not able to predict the flow stress behaviour at 200ºC, suggesting a new physics involved with the material deformation mechanisms above this temperature.

4.5.1 Uniaxial Tension

The finite element (FE) mesh employed in the crystal plasticity numerical analyses is a representative volume element (RVE) of AA5754-O sheet, and has dimensions of 1.8mm x 1.8mm x 1.8mm. This corresponds to a polycrystal aggregate with 5832 grains and initial grain size of 100 microns. Finally, the model applies quarter symmetry boundary conditions and assumes no initial geometric imperfections.

4.5.1.1 Material Calibration

Four uniaxial tension simulations are completed at 25^{0}C, 148^{0}C, 204^{0}C, and 232^{0}C and associated hardening parameters are adjusted to fit the macroscopic stress-strain curves to experimental data from Abedrabbo, et al. (2007). Subsequently, material constants from the three equations for hardening parameters $h_0(\theta)$, $\tau_0(\theta)$, and $n(\theta)$ (presented in Section 4.3.6) are determined. Next, using these equations, new hardening parameters are estimated for two new temperatures: one within (177ºC) and one above (260ºC) the calibration data set.

Figure 4-8 shows the numerical simulation stress-strain curves for uniaxial tension at the calibration temperatures plotted with the corresponding experimental data (Abedrabbo, et al., 2007). The material properties employed to generate these curves are found in Table 4-3. The numerical simulations provide accurate predictions of experimental measurements. With increasing temperature, ductility increases and hardening decreases. This is well captured by the model up to the macroscopic failure strain.

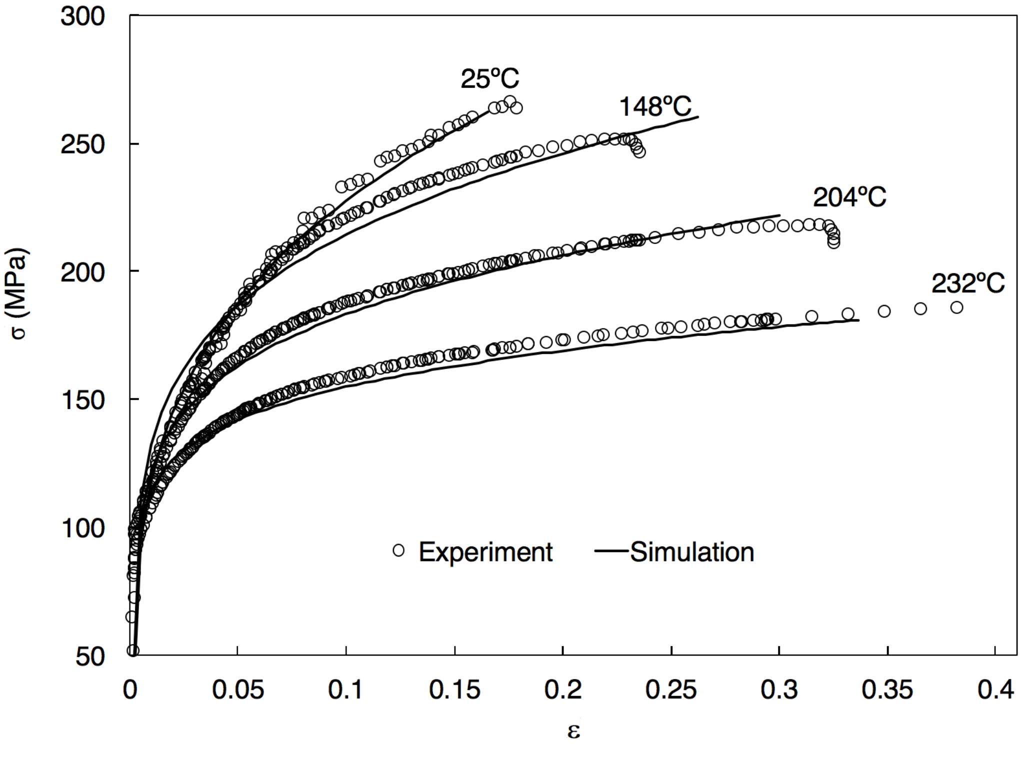

Figure 4-8 Experimentally measured and simulation uniaxial stress-strain results.

Table 4-3 shows that the hardening parameters have a strong dependence on temperature. The hardening exponent, n, is controlled by the first derivative of macroscopic stress with respect to strain ($\partial\sigma/\partial\gamma$) and as expected decreases with increasing temperature. The reference critical resolved shear strength (CRSS) τ_0, increases linearly with increasing temperature. Furthermore, due to the nature of the power-law hardening model, it was also expected that the reference hardening rate, h_0, would increase exponentially with increasing temperature.

Table 4-3 Material hardening properties used to generate stress-strain curves in Figure 4-8.

Temperature (^{0}C)	$\boldsymbol{n}$	$\boldsymbol{\tau_0\ (MPa)}$	$\boldsymbol{h_0\ (MPa)}$
25	0.255	20.5	3600
148	0.18	22.0	12000
204	0.15	22.5	25000
232	0.11	23.0	36000

4.5.1.2 Temperature dependence of hardening parameters

From the results summarized in Table 4-3, the constants from equations (4.32)–(4.34) are determined to describe the temperature dependence of the power-law hardening parameters and are plotted as solid black dots in Figures 4-9 to 4-11. From these equations, the material hardening properties for two new temperatures (177ºC and 260ºC) are determined and are represented in Figures 4-9 to 4-11 as open black dots. Equations (4.32)–(4.34) are shown as solid lines.

The linear relationship for the hardening exponent, n, presented in equation (4.32) as a function of absolute temperature is found to have constants $\bar{n}_0 = 0.4547$ and $\psi = -0.5767$. Figure 4-9 shows the fitted values for hardening exponent, n, vs. temperature from Table 4-4 as equation (4.32) with the values determined for $\bar{n}_0$ and ψ above. Predicted values for at 177ºC and 260ºC using equation (4.32) are truncated after two significant digits and provide sufficient accuracy.

The linear relationship for CRSS τ_0 presented in equation (4.33) as a function of absolute temperature is found to have constants $\bar{\tau}_0 = 17.01\ MPa$ and $\phi = 10.25$. Figure 4-10 shows the fitted values for CRSS, τ_0, vs. temperature from Table 4-4 as well as equation (4.33) with the values determined for $\bar{\tau}_0$ and ϕ above. For simulations, predicted values for τ_0 at 177ºC and 260ºC using equation (4.33) are sufficient with three significant digits.

Finally, the constants in the exponential relationship for reference hardening rate h_0 in equation (4.34), are found to be $\bar{h}_0 = 128.3\ MPa$ and $\chi = 9.640$. Figure 4-11 shows the fitted values for h_0 vs. temperature from Table 4-4 as equation (4.34) with above values for $\bar{h}_0$ and χ. Sufficient values predicted for h_0 at 177ºC and 260ºC from equation (4.34) require only two significant digits.

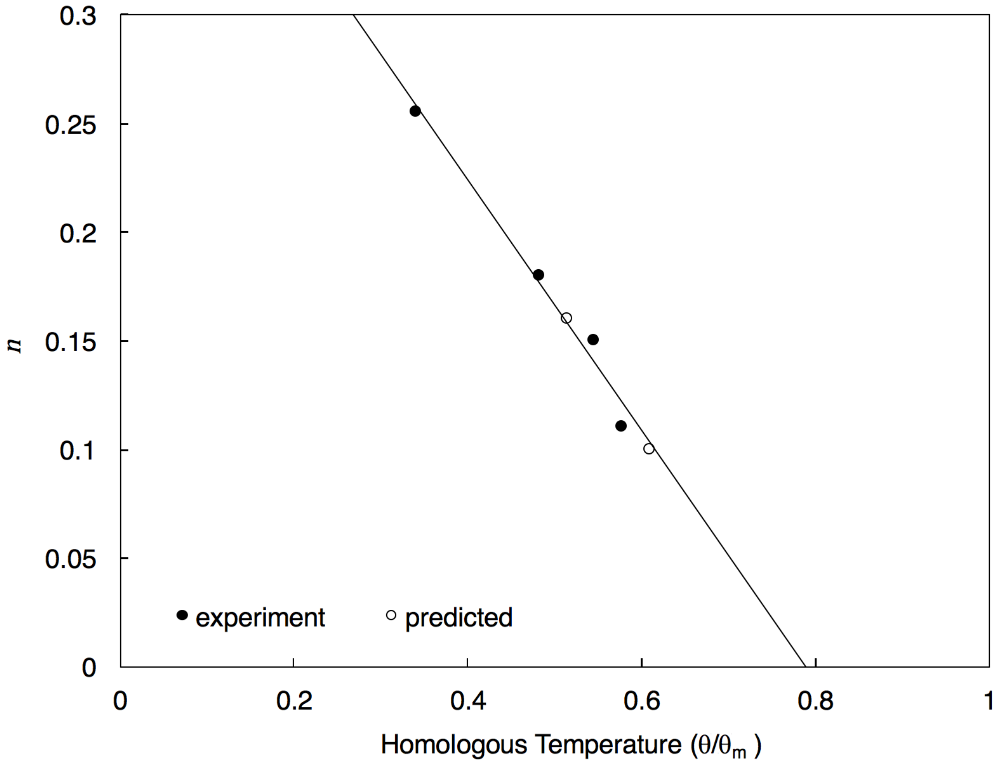

Figure 4-9 Single slip hardening exponent vs. temperature and equation (4.32).

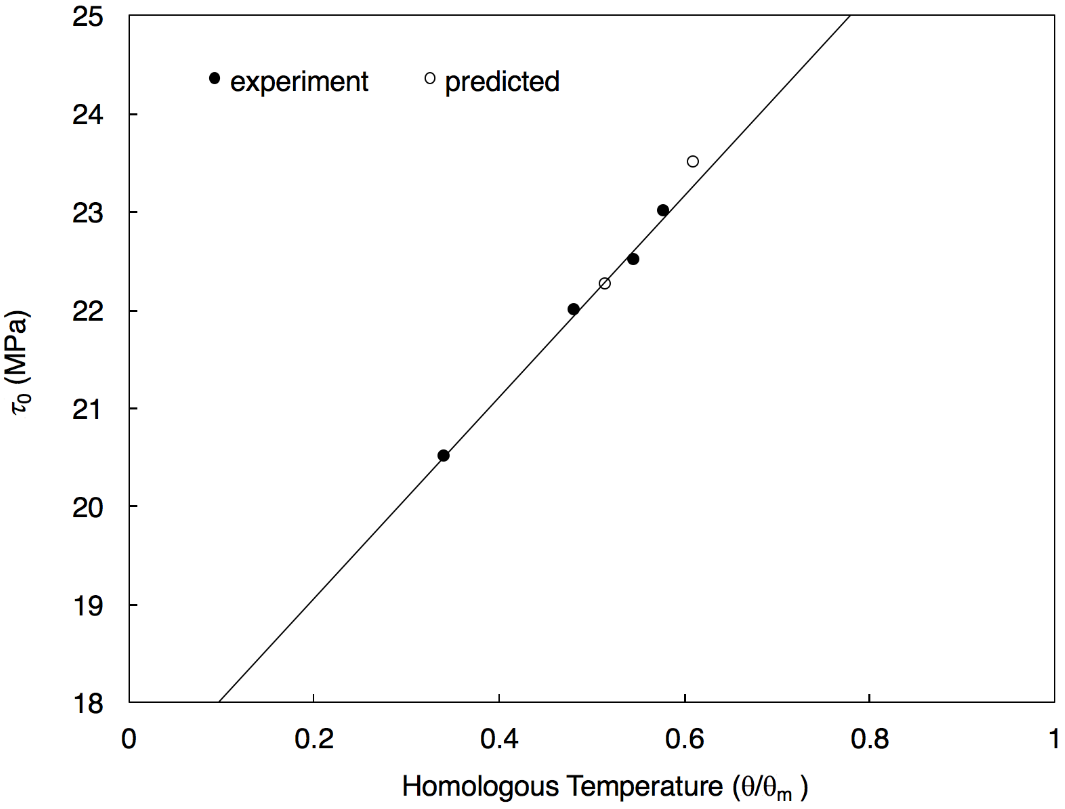

Figure 4-10 Reference CRSS vs. temperature and equation (4.33).

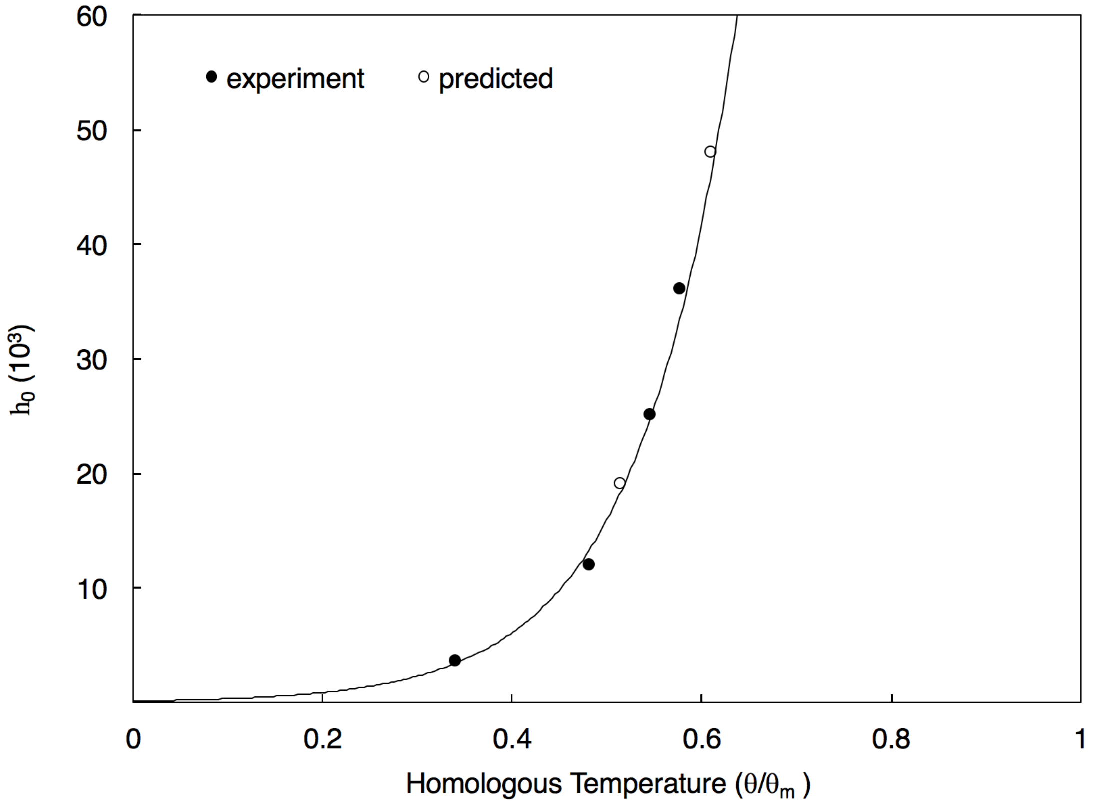

Figure 4-11 Reference single slip shear hardening rates vs. temperature using equation (4.34).

4.5.1.3 Model Verification

Due to the form of the employed hardening model, the results showed a strong temperature sensitivity of hardening exponent n, reference hardening rate h_0, and mild sensitivity of CRSS τ_0. Four temperatures are required for calibration due to the exponential behaviour of h_0. Using the above equations, parameters at two new temperatures are determined to predict the behaviour of one internal temperature of 177ºC (with respect to the calibration data) and one external temperature of 260ºC, as presented above. These temperatures are chosen to test the predictability of the new model within the calibrated temperature range, as well as above the calibrated temperature range. Table 4-4 presents the material hardening parameters obtained by curve fitting as well as the parameters predicted by the developed temperature dependent hardening equations (shaded).

Table 4-4 Single-slip hardening parameters. Values in white were used in calibration while shaded values were predicted from equations (4.32) to (4.34).

Temperature (ºC)	n	$\tau_0\ (MPa)$	$h_0\ (MPa)$
25	0.255	20.5	3600
148	0.18	22.0	12000
177	0.16	22.3	19000
204	0.15	22.5	25000
232	0.11	23.0	36000
260	0.10	23.5	48000

Using the predicted hardening values for 177ºC and 260ºC presented above, simulations of uniaxial tension are carried out and compared to the measured experimental data from Abedrabbo et al. (2007). Results are presented in Figure 4-12. It is noted that, the prediction for 177ºC is in very good agreement with the experimental results, while the prediction for 260ºC simulation slightly deviates from the experimental results after approximately 20% of true strain. This suggests that the deformation mechanisms at 260ºC are different than the deformation mechanisms active at 232ºC and below (Doherty et al. 1997). In addition, this can also be the effect of non-uniform flow at elevated temperatures and high strains.

Figure 4-13 shows the deformed 3D microstructure after uniaxial tension in two extreme temperatures of 25ºC and 232ºC. The mesh contour plots show the effective strain level at 20% macroscopic strain. It is clear in Figure 4-13 that the deformed shapes are similar for both cases, thus the plots at intermediate temperatures need not be presented here. Local hot spots can be seen close to the mesh edges and have slightly higher intensities at warmer simulated temperatures. It should be noted that, these local high strain regions could be the results of edge effects. The effective strains at failure are clearly different for different temperatures, which is not included here.

Prasad and Sasidhara (1997) have shown that for Al 2-5% Mg alloys, dynamic recrystalization is active at hot working temperatures above approximately 300–350ºC. They also present a general temperature range of 40-60% of the homologous temperature where dynamic recovery begins to become an active mechanism during deformation. This corresponds to approximately 250ºC–350ºC for AA5754. It should be mentioned that, in the power-law hardening model, only thermal softening due to crystallographic slip-strength is considered. The presence of other deformation mechanisms (thermally activated) above 250ºC is a possible explanation for the difference between the predictions at 260ºC and the experimental data. However, it is noted that, the initial yielding and hardening up to 20% true strain is still well captured by the simulation results. This suggests that up to this point, thermally induced slip-softening is still the governing thermal softening mechanism as the accumulated deformation energy has not yet exceeded a critical value for these high temperature mechanisms to initiate (Doherty et al. 1997, McQueen et al. 2011, and Popova et al. 2015).

4.5.2 Simple Shear

The predominant deformation mode during material failure is shear (Rossiter et al. 2010). Kang et al. (2006) experimentally investigated shear localization behaviour in the form of PLC bands in continuous cast (CC) and direct chill (DC) cast AA5754 sheets at room temperature. They use a novel set up and samples to capture the interaction of PLC bands with shear bands triggering localized necking in uniaxial tension tests. Yoon et al. (2005) have used crystal plasticity and a phenomenological yield surface model to predict anisotropic behaviour of aluminum due to texture evolution in simple shear, noticing a strong dependence of texture evolution on the anisotropic hardening behaviour. In this section, simple shear simulations employing a synthetic microstructure are presented using predicted hardening parameters from equations (4.32)–(4.34) and compared with normalized shear stress-shear strain data from literature.

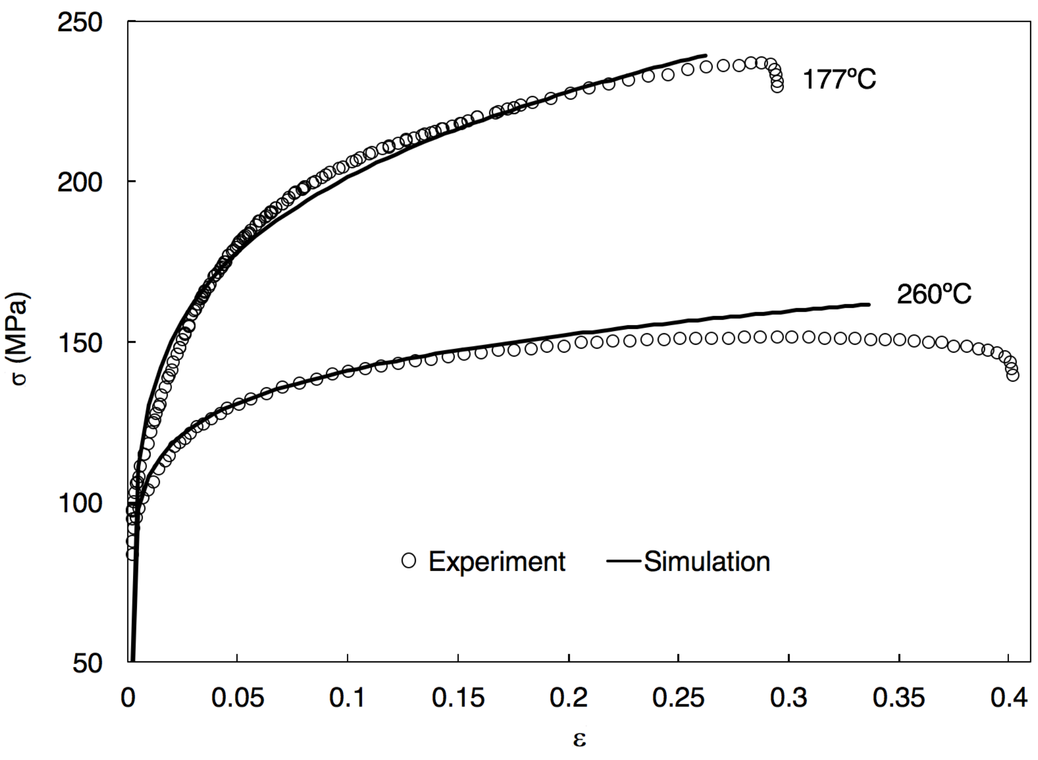

Figure 4-12 Simulated vs. experimental uniaxial tension stress-strain curves using predicted hardening values.

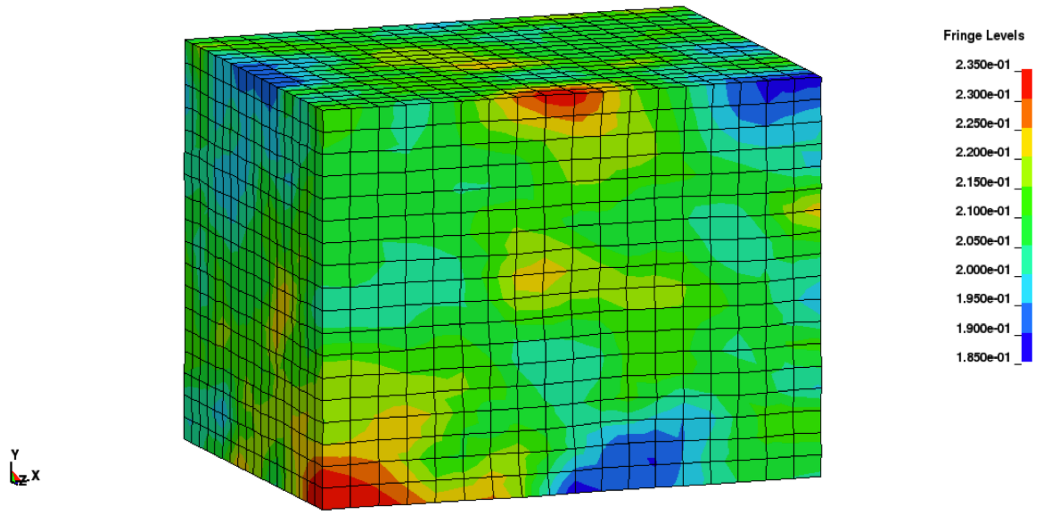

25ºC

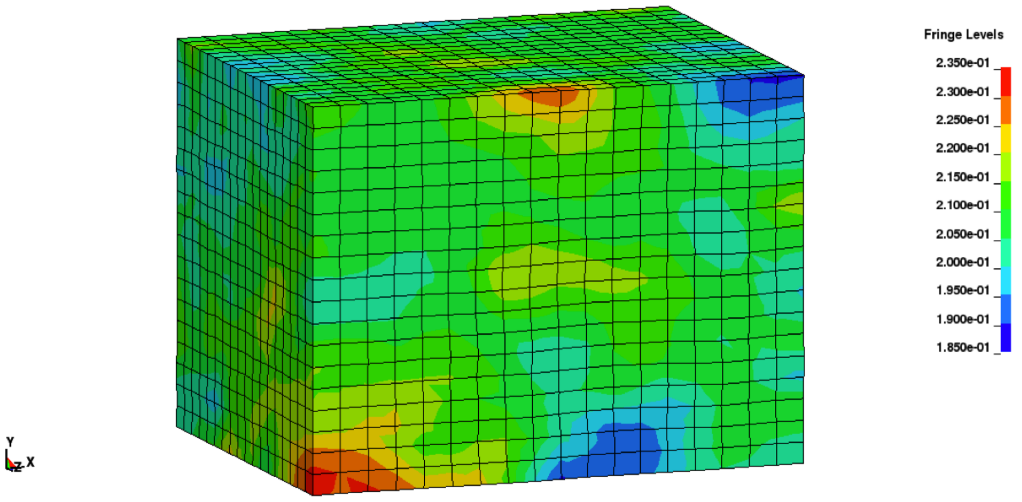

232ºC

Figure 4-13 Contours of Effective Strain (Von-Mises) at 25ºC and 232ºC. The overall effective strain localization appears to have no temperature dependency.

4.5.2.1 Model Validation

Numerical simulations of simple shear were performed and the predicted microscopic (texture evolution) and macroscopic (τ–γ) responses were compared to experimental data presented by Pandey et al. (2013). Boundary conditions employed for simple shear in the rolling direction are as follows. The y = 0 plane is constrained in the x and y-directions to prevent translation of the model. All nodes in the y = 300μm plane are constrained in the y-direction and are prescribed a constant velocity in the x-direction. The z = 0 plane is constrained in the z-direction only. All nodes in the z = 300μm plane are constrained to move uniformly in the z-direction to satisfy the plane stress assumption. Nodes in the x = 0 and x = 1800μm planes are not constrained.

A 3D finite element mesh was generated for the RVE for AA5754. The EBSD map was used to generate a 1800μm x 300μm x 300μm statistically equivalent 3D microstructure of 175 grains with average grain size of 60 microns. The FE model (for shear) shown in Figure 4-6 has 180 elements along the x-axis (RD) and 30 elements along the y-axis (TD) and z-axis (ND). Figure 4-14 shows the experimental initial texture measured by Pandey et al. (2013) and the statistically equivalent texture employed in the numerical analysis.

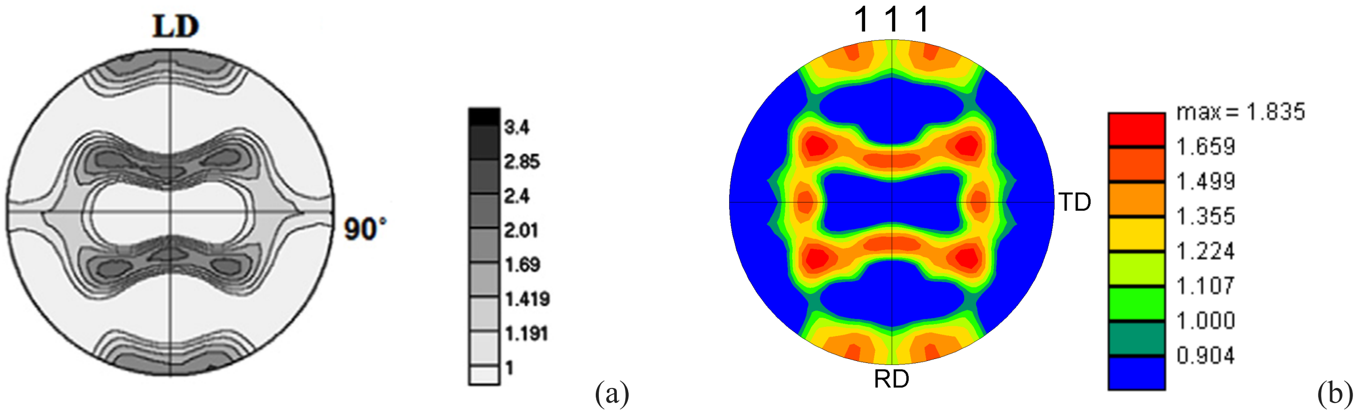

Figure 4-14 Initial experimental texture (a) and statistically equivalent initial texture (b).

Using the same material properties determined by uniaxial tension using equations (4.32)–(4.34), the shear stress-strain curves are calculated for 25ºC, 148ºC, and 232ºC. The predicted shear stress-shear strain (normalized) curves as well as the experimental curves at three different temperatures are presented in Figure 4-15. It can be seen that, without any modification of the material properties, the proposed model provides excellent matches with experimental results for all temperatures considered.

A texture analysis is completed to discuss the effects of texture evolution using TEV model. Final experimentally measured pole figures for 25ºC and 232ºC after the shear tests by (Pandey et al., 2013) are shown in Figure 4-16. Figure 4-17 shows the predicted pole figures for the deformed specimen at 25ºC and 232ºC using TEV model. Pandey et al. (2013) experimentally showed that there is no apparent effect of temperature or strain rate on the texture evolution of FCC aluminum under simple shear or uniaxial tension. It can be seen that, the numerical model also predicts this behaviour and well captures the deformed textures. The predicted textures for the intermediate temperatures are also in good agreement with the experimental data.

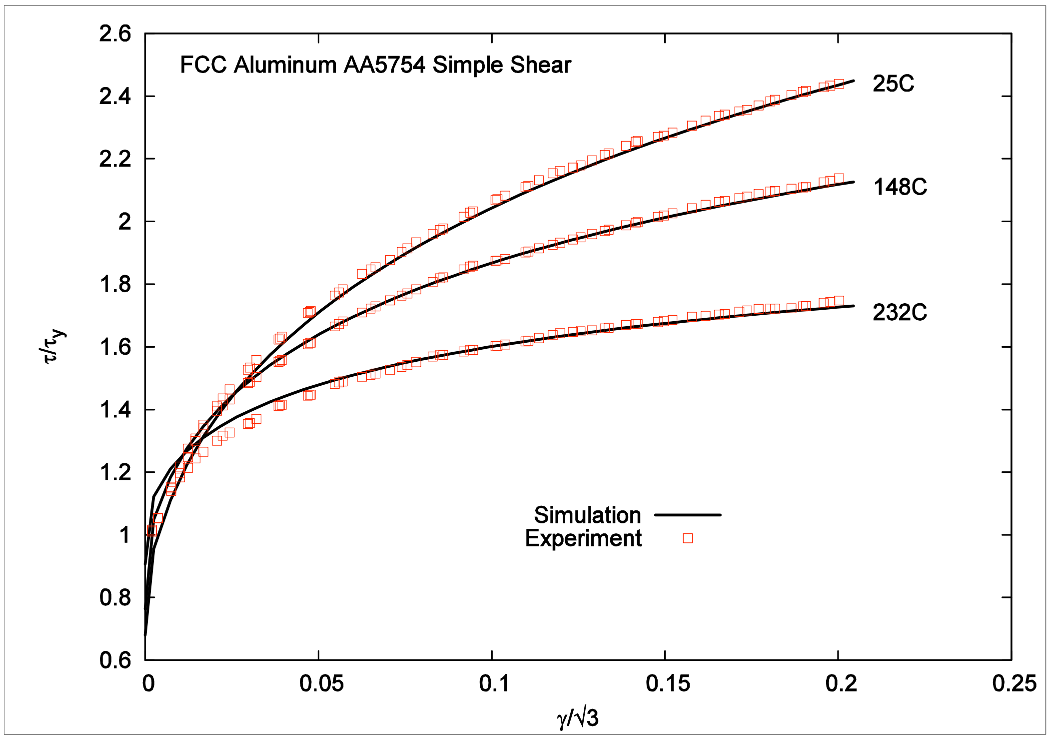

Figure 4-15 Normalized shear stress vs. shear strain for experimental (Pandey et al. 2013) and simulated AA5754 polycrystal at 25ºC, 150ºC, and 232ºC.

4.5.3 Numerical Analysis

Fringe plots of accumulated shear at 30% shear strain in simple shear tests are presented in Figure 4-18. The strain localization during deformation is similar at the three simulated temperatures. At all three temperatures, there are visible shear bands that have developed both in the plane of shear (x-y) as well as out of plane of shear (x-z). The high temperature simulation shows slightly greater peaks in accumulated shear at localization areas; however, the general strain development and strain pattern are not strongly affected by temperature. This agrees well with findings from Pandey et al. (2013). All numerical simulations have identical initial microstructures and crystal orientations, which are the only facets by which anisotropy is introduced to the material. This anisotropy, as well as the texture evolution, controls the local strain development during deformation. The experimental and numerical results show that texture evolution is not strongly influenced by temperature; therefore the strain localization in the deformed materials should be similar between 25ºC and 232ºC.

Presented in Figure 4-19 is a plot of shear stress vs. shear strain under simple shear at 25ºC, 150ºC and 232ºC. It is noted that, almost a 50% difference in final developed stress is observed in the simulation results between room temperature and 232ºC. Variation in initial yielding shows the reverse behaviour; where at higher temperatures the initial stress before yielding is greater. This can be explained by the definition of the CRSS (τ_0) behaviour with respect to temperature. The numerical analysis presented in Section 4.5.1.3 found a positively increasing relationship between CRSS and temperature to accurately capture the yielding in uniaxial tension. The result is observed as a minor variation in yield stresses in the simple shear simulations.

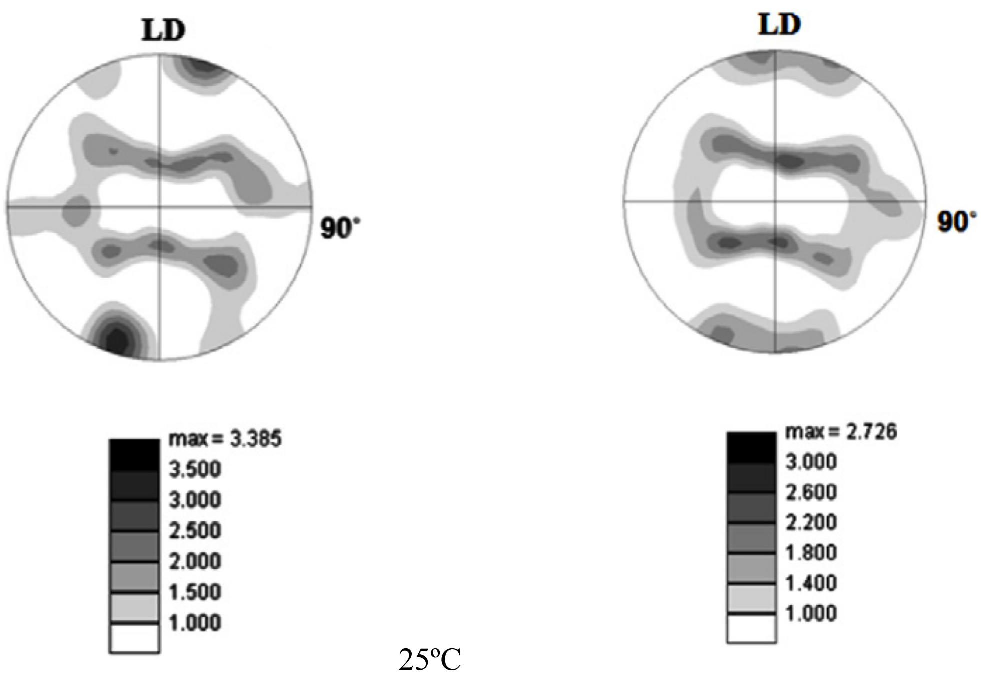

25ºC 232ºC

Figure 4-16 Pole figures for experimentally measured texture of deformed specimens ($\gamma/\sqrt{3} = 0.2$) at 25ºC and 232ºC from experiment (Pandey et al. 2013).

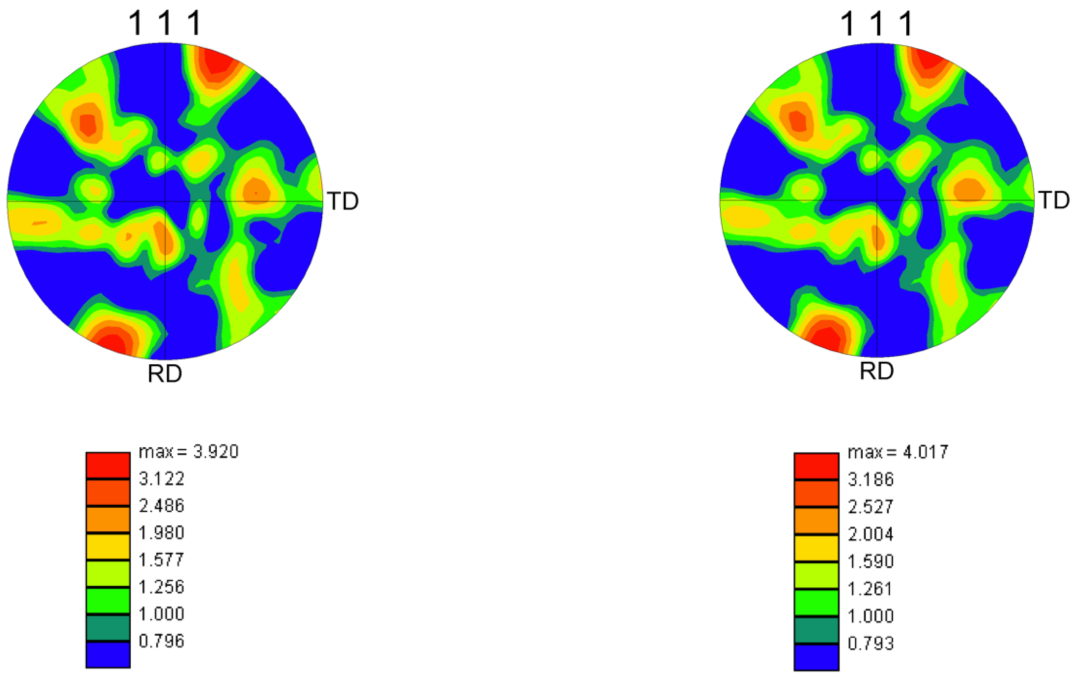

25ºC 232ºC

Figure 4-17 Pole figures of deformed texture ($\gamma/\sqrt{3} = 0.2$) at 25ºC and 232ºC from CPFEM simulation.

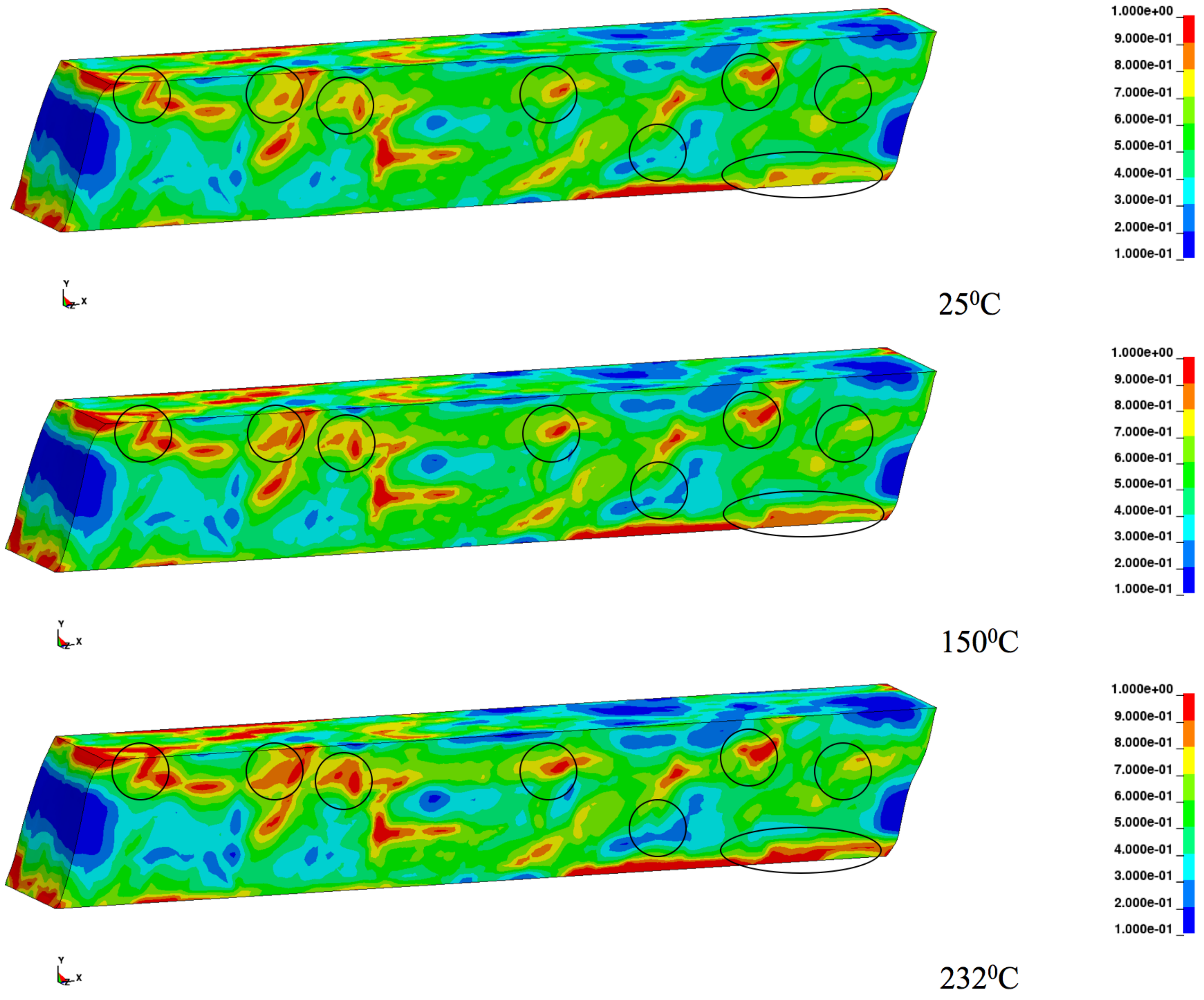

Figure 4-18 Simulation of simple shear deformation to $\gamma = 0.3$ at 25ºC, 150ºC and 232ºC with contours of local accumulated shear (γ_a) and outlined “hot spots” with high local accumulated shear.

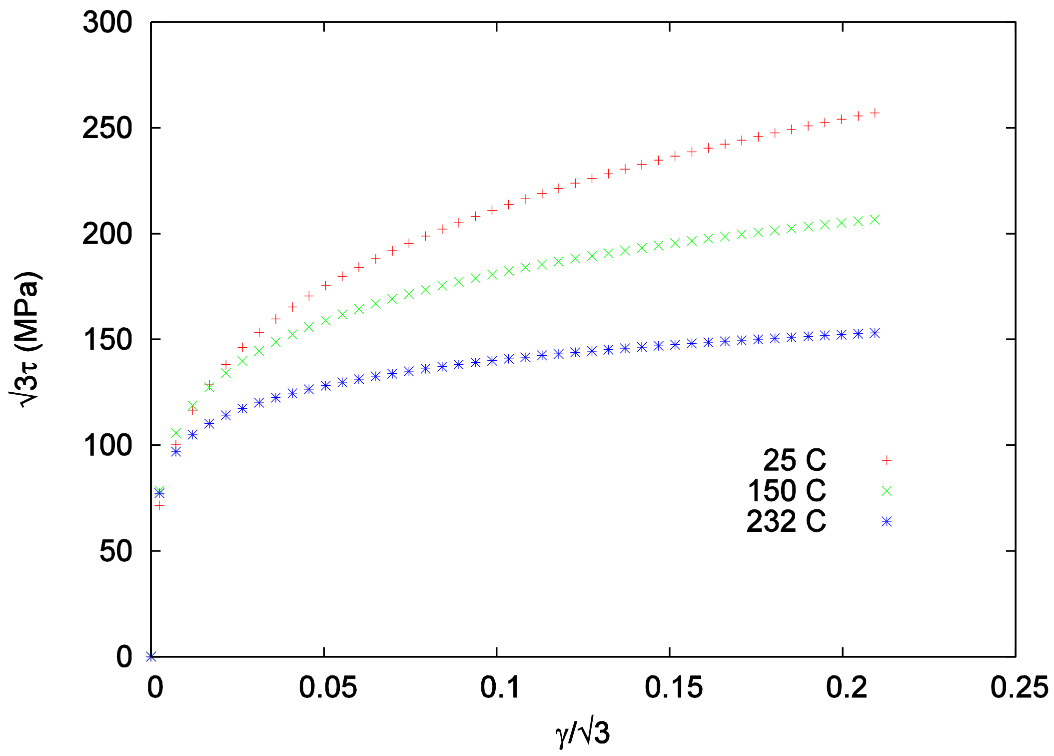

Figure 4-19: Macroscopic shear stress-shear strain curves for 25ºC, 150ºC and 232ºC simulations corresponding to the contour plots presented above.

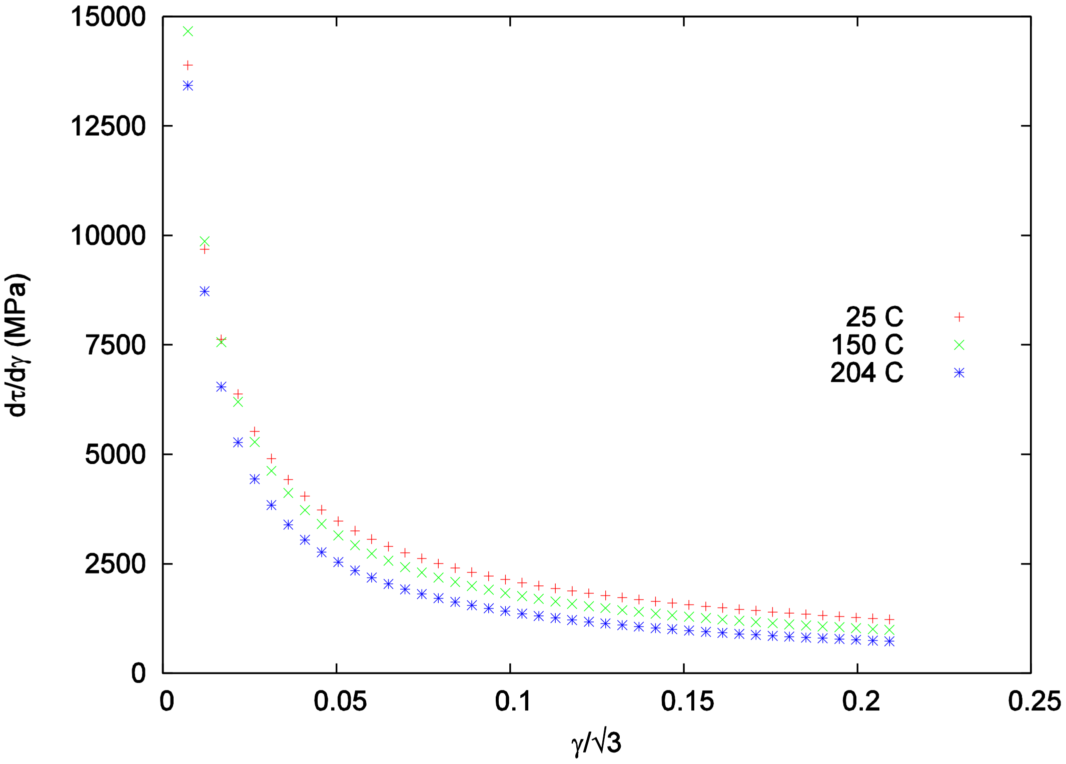

Figure 4-20 Simple shear macroscopic hardening rates for 25ºC, 150ºC and 232ºC.

Figure 4-20 shows the macroscopic hardening rates calculated from the shear stress-shear strain curves presented in Figure 4-19. The hardening rates curves are as expected where lower hardening rates correspond to higher temperature deformation. It is interesting to note that the hardening rates do not converge, but rather remain near parallel at high strain levels.

Lastly, Figure 4-21 presents the averaged single slip (absolute) shear rates for the polycrystal at the three simulation temperatures. Highest shear rates and slip activity are developed at 232ºC. Room temperature provides the lowest shear rates, and therefore the lowest slip activity. However, the difference between average slip activity is extremely small (on the order of 1% variation). This result agrees with the strain localization results presented previously, where temperature appears to have little effect on the strain localization and accumulation of the material.

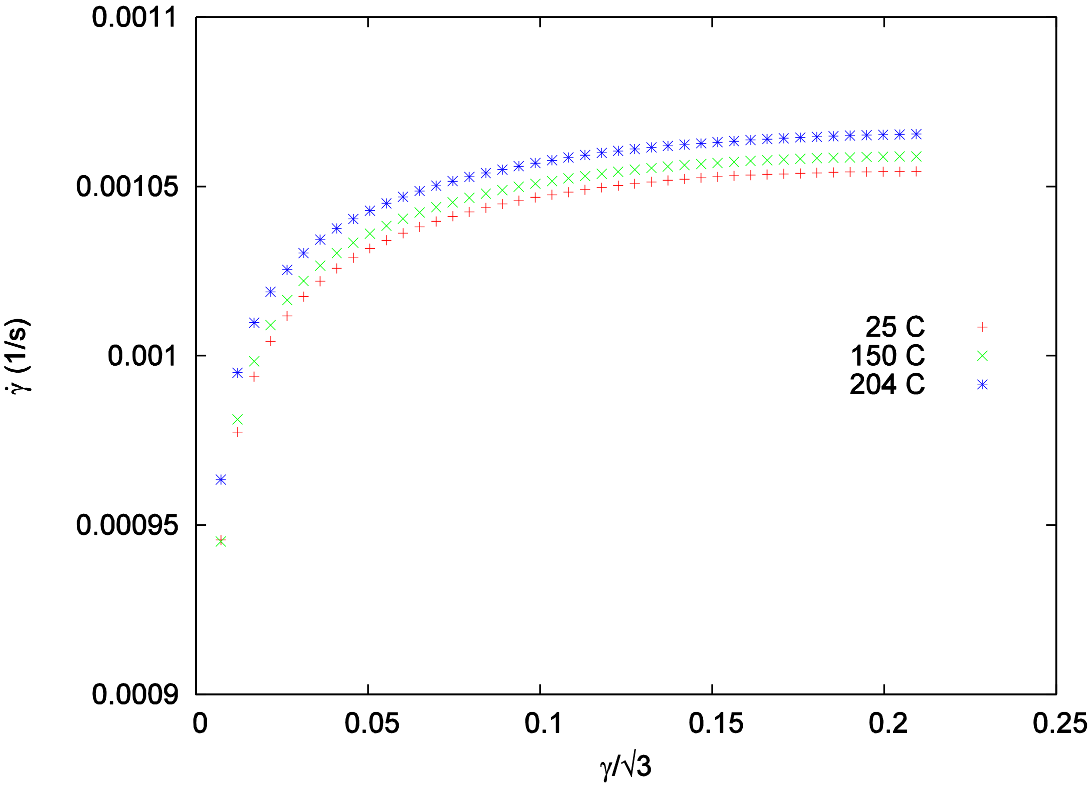

Figure 4-21 Simple Shear average single-slip shear rates at 25ºC, 150ºC and 232ºC.

4.5.4 Effect of thermal softening sensitivity index

Thermal softening sensitivity index *p*, i.e. equation (4.29), determines the sensitivity of the single crystal slip strength to an increase in temperature above absolute zero. A low sensitivity index, such as one, yields a linear relation between thermal softening and temperature. As the sensitivity index increases, the material becomes more resistant to thermal softening with increasing temperature. A large sensitivity index yields a highly non-linear relation between thermal softening and temperature, where noticeable effects of thermal softening are not present until above 50% of the homologous temperature (for example a sensitivity index of six). In this study, the thermal softening sensitivity index for AA5754 that provided the best results when compared to experimental data was when p was equal to four.

Uniaxial tension simulation stress-strain data at 25ºC, 148ºC, and 232ºC for various softening intensities are presented in Figure 4-22. For consistency with experimental results, the simulation data was truncated at the experimental failure strains. It can be seen from Figure 4-22 that softening sensitivity indices 4 and 6 yield similar results at room temperature, while a sensitivity of 2 lowers the stress response by approximately 50 MPa at 20% true strain. As temperature increases, a noticeable difference appears between sensitivity indices 4 and 6. The interesting behaviour to note is that, for all temperatures, a variation in the sensitivity index does not affect the hardening behaviour or shape; rather it acts similar to a linear translation of stress. This is made clearer by plotting the corresponding hardening rates.

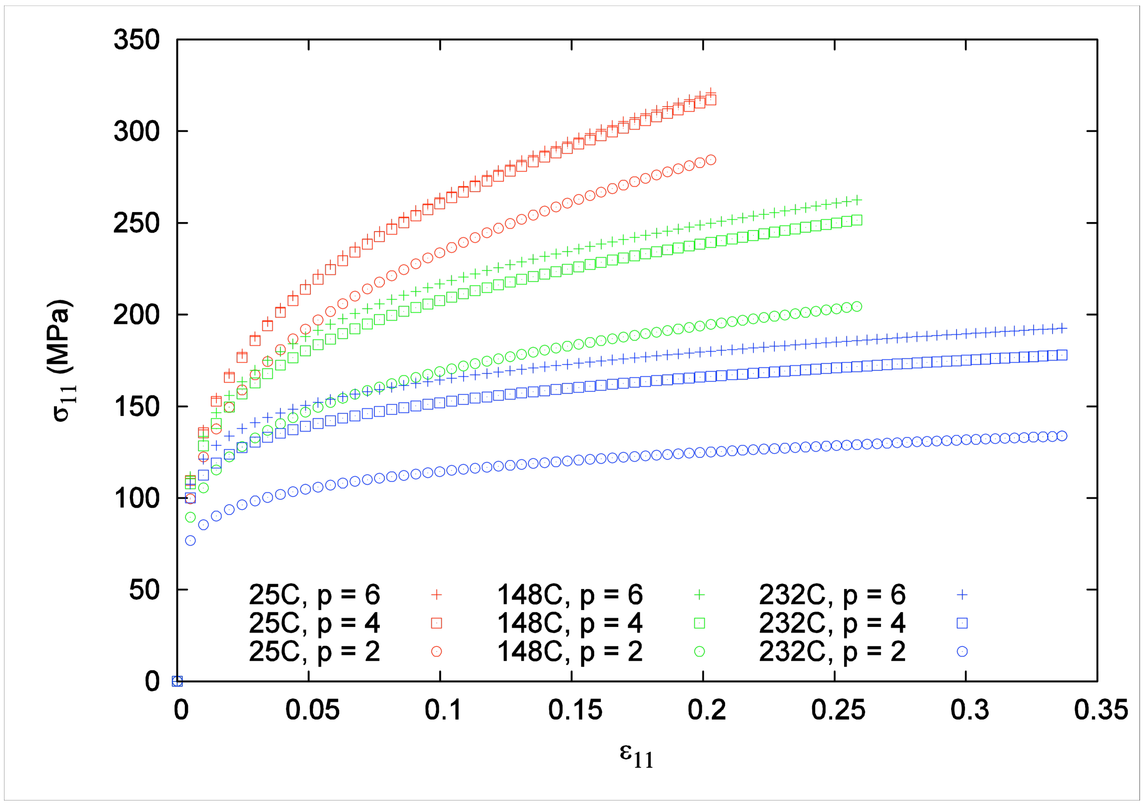

Figure 4-22 Uniaxial tension average macroscopic stress for varying thermal softening sensitivity.

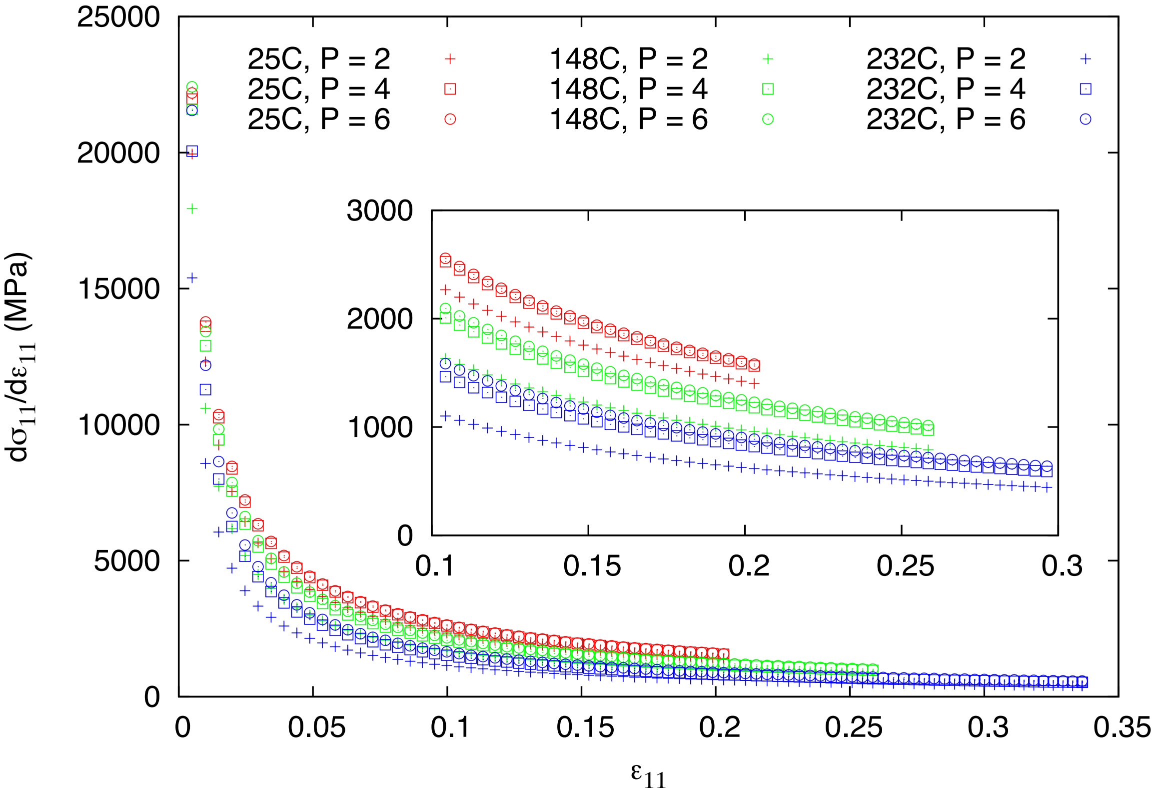

Figure 4-23 Uniaxial tension macroscopic hardening rates for varying thermal softening sensitivity.

Figure 4-23 presents hardening rates for the above softening sensitivity stress-strain plots. Here it is more obvious to see the translation of hardening rates between varying sensitivity indices. This is useful for modeling the slip governed hardening behaviour as it can be completely captured by the three hardening parameters (h_0, τ_0, n). The thermal softening sensitivity then softens all slip systems equally according to working temperature.

4.5.5 Elastic Stiffness Parameter Sensitivity

To show the significance of the variation of elastic constants and their effect on the total stress response, a sensitivity analysis is completed. It is not expected that the temperature dependence of the elastic stiffness significantly affects the results at plasticity dominated high strains. This is demonstrated in Figure 4-24, where the difference in stress responses between constant (evaluated at 25ºC) and temperature dependent C_{ij} simulations under uniaxial tension converges to zero after approximately 2% true strain. However, the simulation shows a noticeable difference between the stress responses during elastic loading and initial yielding. The thermally softened elastic stiffness results in a lower initial hardening and lower yielding than the constant elastic stiffness simulation.

Over the range of 25-232ºC, the elastic stiffness for FCC aluminum is not dramatically significant (see Figure 4-2), therefore another simulation is completed to see the effect of varying C_{ij} parameters to that of other FCC materials. Simulations are performed at three temperatures, 25ºC, 148ºC and 232ºC. To investigate the effect of the C_{ij} elastic coefficients on the stress response, two different FCC material's elastic properties are simulated and compared with that of aluminum. All other material parameters are left unchanged in these simulations. Single crystal elastic moduli for copper and lead were chosen. Copper exhibits approximately twice the C_{11} stiffness constant of aluminum and has similar temperature dependence. Lead has significantly lower stiffness constants than aluminum and much higher temperature dependence. This approach is taken rather than a simple scaling of elastic parameters to investigate the influence of physical values, since not only is the magnitude of the stiffness coefficients important, but also the relative magnitude between C_{11}, C_{12}, C_{44}. Elastic stiffness properties used for the sensitivity analysis are listed in table 4-5.

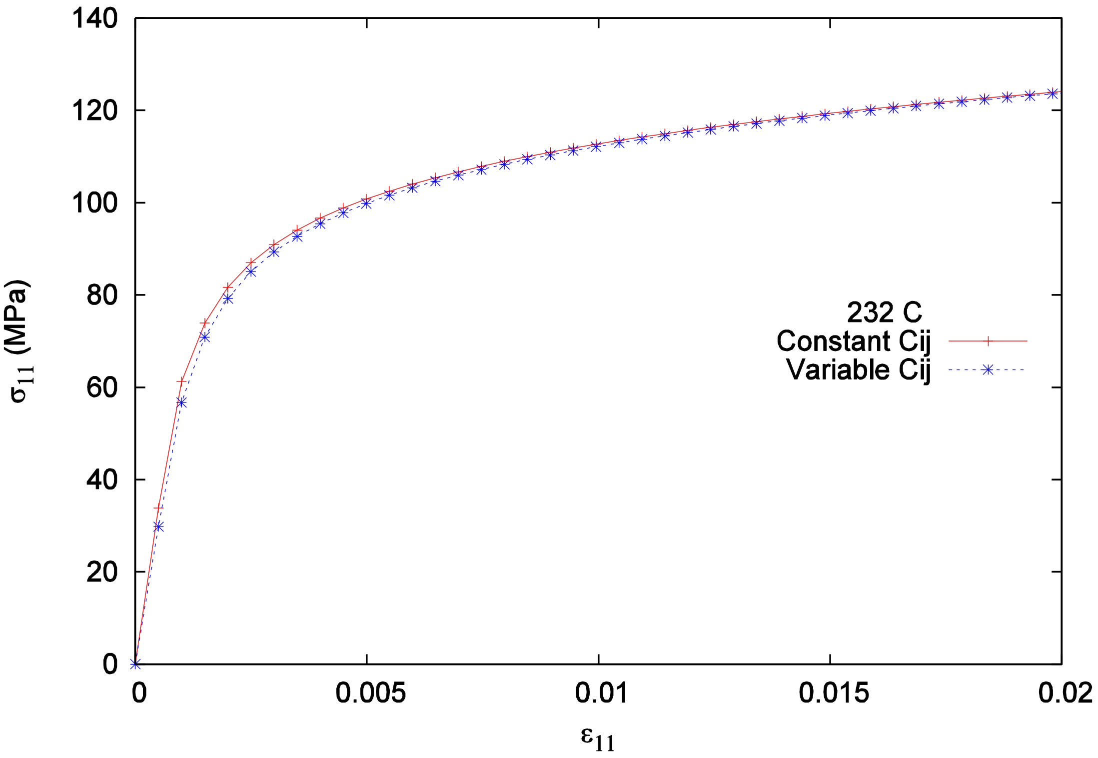

Figure 4-24 Constant C_{ij} vs. temperature variable C_{ij} under uniaxial tension at 232ºC.

Table 4-5 Elastic stiffness parameters for Al, Cu, and Pb (from Varshni, 1970).

Material		C_{ij}^0 *(10¹¹ dyn/cm²)*	s_{ij} *(10¹¹ dyn/cm²)*	t_{ij} *(°K)*
Aluminum	C_{11}	11.4	1.011	258.4
	C_{12}	6.19	0.205	293.6
	C_{44}	3.16	0.256	168.0
Copper	C_{11}	17.6	0.760	206.4
	C_{12}	12.5	0.238	158.4
	C_{44}	8.17	0.453	163.4
Lead	C_{11}	5.56	0.0949	43.5
	C_{12}	4.54	0.0774	66.2
	C_{44}	1.94	0.0389	24.6

Figures 4-25 to 4-27 present the results from the C_{ij} sensitivity analysis using the three material constants described previously up to 5% strain. The simulation results presented below show an average 50% difference in stress at initial yielding to 1% strain between aluminum and lead. At higher strains the difference remains high at approximately 10% between aluminum and lead at 5% strain at 25ºC, but is decreased at higher temperatures with only 3% difference at 232ºC at the same strain. In addition, copper exhibits the highest developed stress and the material with the lowest stiffness, lead, experiences the lowest stress. Hardening behaviour is similar for all temperatures; however, it is apparent that the stress-strain curves are converging with increasing plastic strain. The greatest variation occurs at very low strains, as expected from the previous results. It is also important to note that the high temperature dependence of lead is strongly represented by these results. The initial yielding in lead is drastically lower than copper and aluminum as the temperature is increased, which are relatively similar in regards to their elastic thermal sensitivity.

Previous work has taken little consideration into the effect of elastic stiffness parameters on material response; see e.g. Clayton, (2005) and Beyerlin et al. (2013). In some applications, such as bending, elastic stiffness is strongly involved in material response. Especially in the fabrication of components, elastic recovery in the form of springback after forming—most notably in bending—can severely affect the product performance. Springback introduces residual stresses to the material and is undesirable due to the negative effects on fatigue performance (Cleveland and Gosh, 2002). Burchitz (2005) studied springback and its predictability with regards to elastic modulus and found that a variation in elastic modulus, over yield strength and hardening rate, had the greatest effect on springback simulation results in sheet forming of a metal car roof. A similar study also found that a variable rather than constant elastic modulus better predicted springback experimental results (Kim et al., 2011). In their simulations it was shown that with a 10-20% decrease in elastic stiffness the shape of the final product changes considerably.

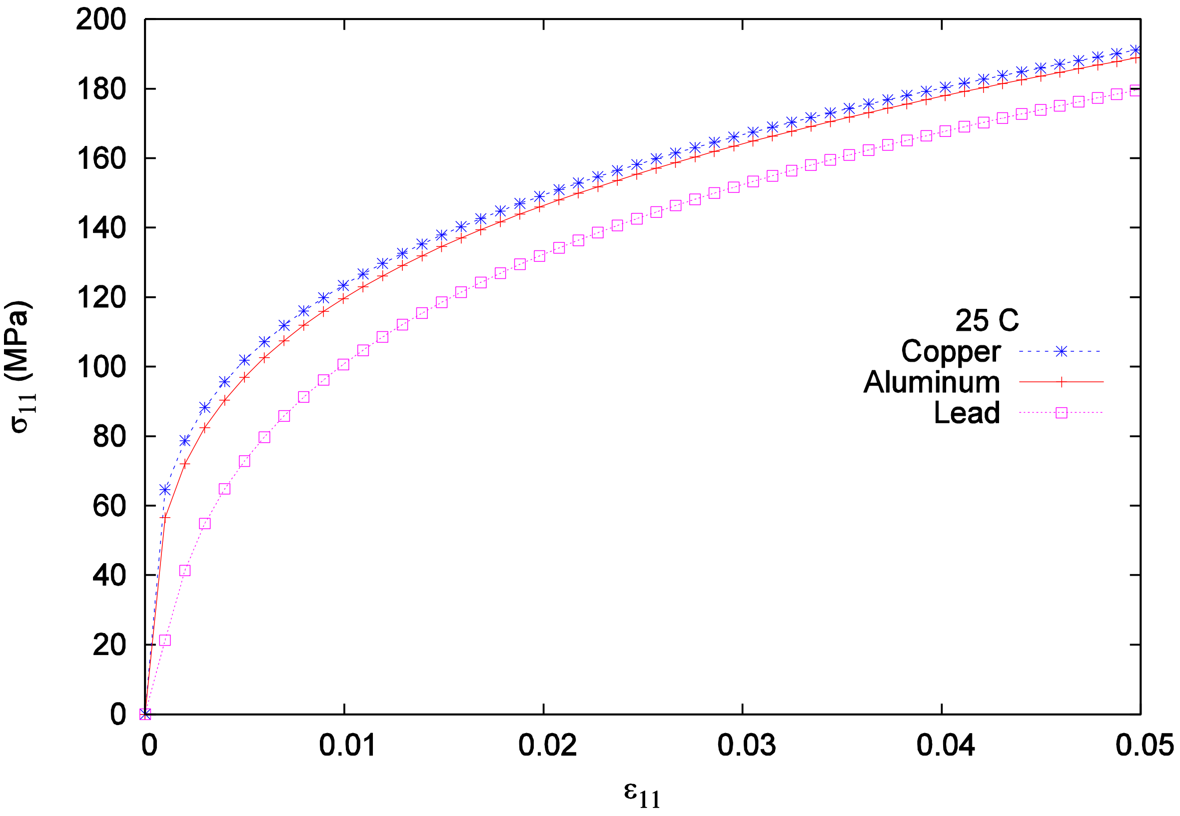

Figure 4-25 Uniaxial stress-strain response at 25ºC for elastic constants corresponding to Aluminum, Copper, and Lead.

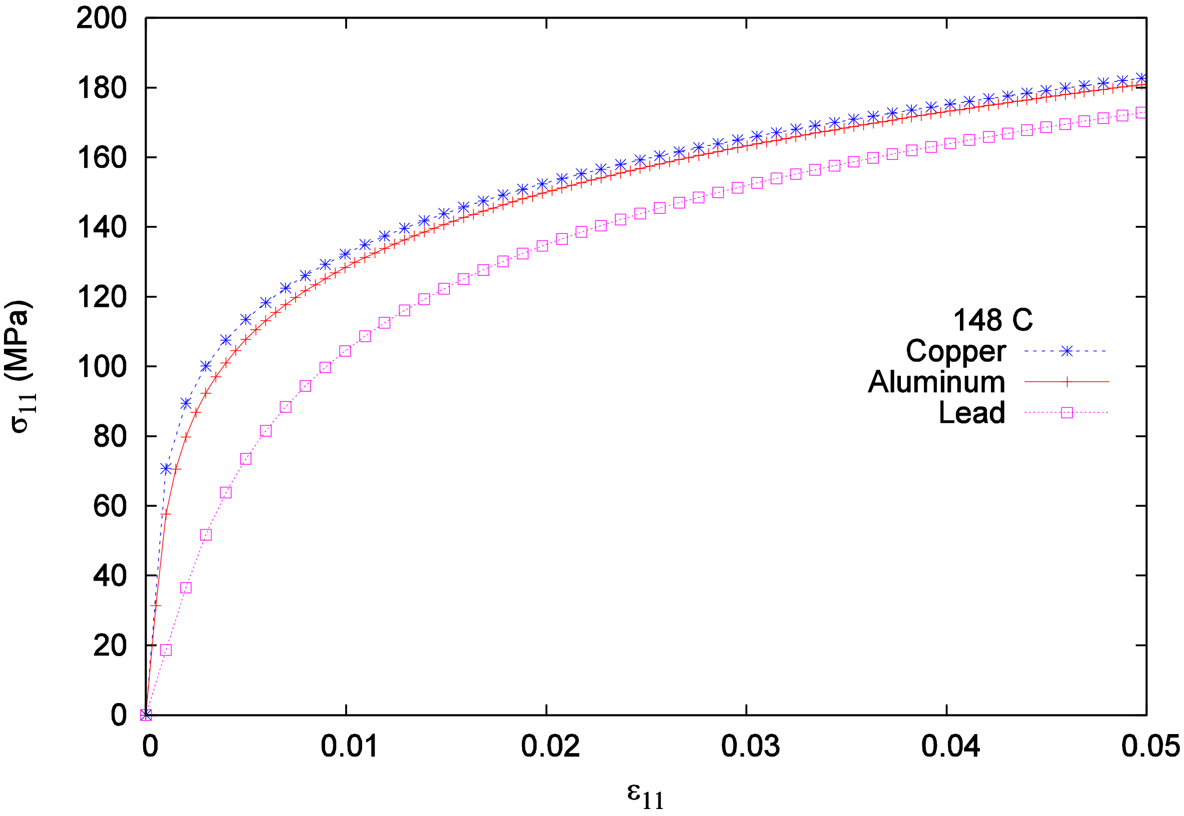

Figure 4-26 Uniaxial stress-strain response at 148ºC for elastic constants corresponding to Aluminum, Copper, and Lead.

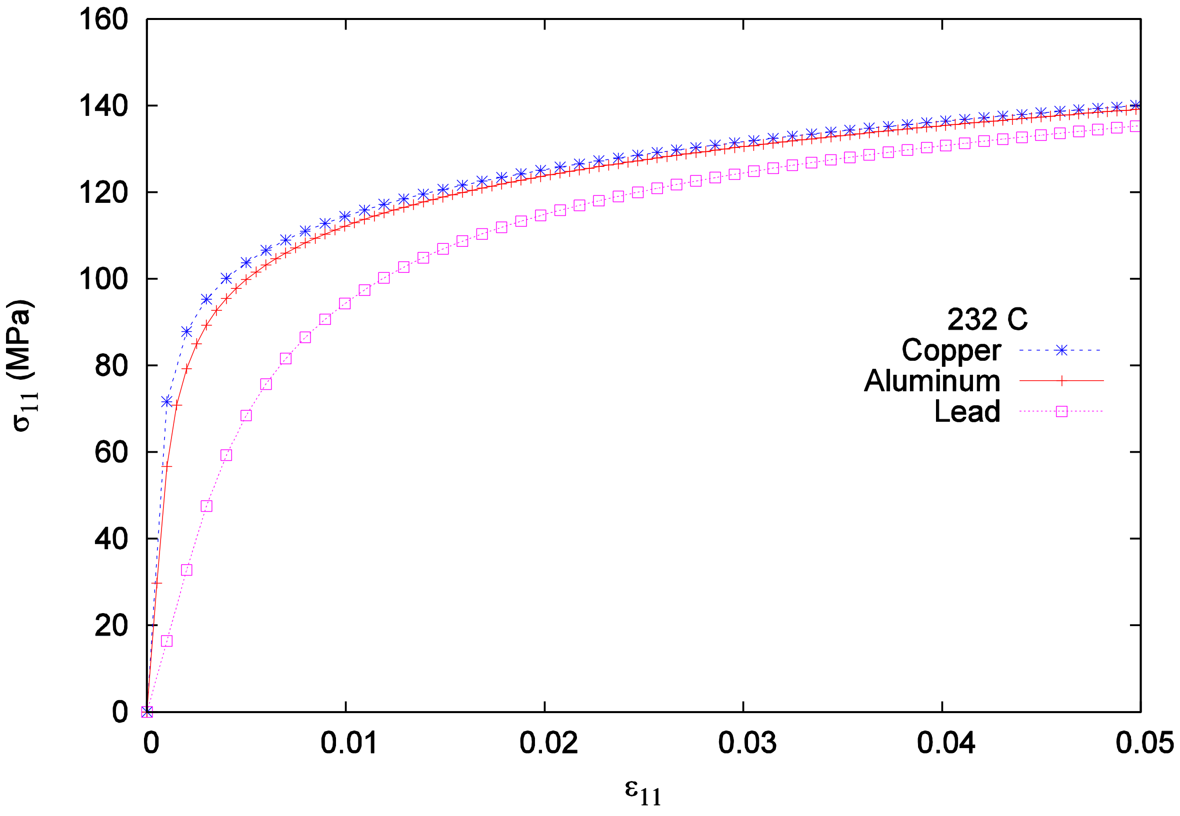

Figure 4-27 Uniaxial stress-strain response at 232ºC for elastic constants corresponding to Aluminum, Copper, and Lead.

4.6 Conclusions

In this chapter, a new three-dimensional thermo-elasto-viscoplastic (TEV) constitutive relation was developed to accurately model the behaviour of FCC polycrystals. The model employs the temperature dependence of the single crystal elastic coefficients, single slip hardening parameters, thermal slip-softening, rate sensitivity, and thermal deformation. The model was first calibrated using four uniaxial tension simulations and analytical equations were developed to represent the temperature dependence of single crystal hardening parameters for aluminum AA5754-O sheets. Validation simulations were then completed with simple shear tests. The following conclusions can be drawn from this study:

- Numerical equations developed to describe the temperature dependence of slip hardening parameters provided excellent hardening behaviour predictability between 25ºC and 232ºC in both uniaxial tension and simple shear. Initial hardening up to 20% strain is also well captured for uniaxial tension at 260ºC; however, high temperature deformation mechanisms, such as dynamic recrystallization and dynamic recovery, that may be present at this high energy state, were not captured by the new model.

- In agreement with findings in literature, the effect of temperature on texture evolution during uniaxial tension and simple shear simulations was insignificant. Texture evolution at room temperature was an accurate approximation for high temperature texture evolution below dynamic recrystallization and recovery temperatures.

- A new analytical thermal softening parameter was introduced to describe the slip softening behaviour as temperature increased. The relation was derived from experimental observation and well predicted the softening behaviour of FCC aluminum AA5754 at temperatures up to 232ºC when thermal sensitivity parameter was equal to four.

- Normalized simple shear simulations compared very well with experimental data at 25ºC, 148ºC and 232ºC, without any further adjustments. The model could therefore be calibrated by a single experiment of four tests and then employed in other deformation modes without the need for recalibration.

- Both in uniaxial tension and simple shear, the slip activity and strain localization increased with increasing temperature; however, this increase was extremely small, on the order of 1% variation between 25ºC and 232ºC.

- A comparison between elastic coefficients of different materials provided evidence that the material response depended on both the magnitude of the stiffness constants and the relative ratios between C_{11}, C_{12} and C_{44}.

Chapter 5

Part II: Modeling Formability of Aluminum Alloys at Elevated Temperatures Using a New Thermo-Elasto-Viscoplast Crystal Plasticity Framework

Edward Cyr[1], Mohsen Mohammadi[1,2], Raja K. Mishra[3], Kaan Inal[1]

[1] *Department of Mechanical and Mechatronics Engineering, University of Waterloo, Waterloo, Canada, N2L 3G1*

[2] *Department of Mechanical Engineering, University of New Brunswick, Fredericton, NB, Canada, E3B 5A3*

[3] *General Motors Research & Development Center, Warren, MI 48090, USA*

Abstract

Industrial processes often use high temperature forming of alloys such as aluminum that have unsatisfactory room temperature formability. Accurate forming models to integrate warm forming in production environment has been hampered by a lack of constitutive relations at elevated temperatures, forcing one to rely on experimental data for such integration. In this chapter, the new thermo elasto-viscoplastic (TEV) crystal plasticity constitutive framework developed by Cyr et al. (2015) is implemented in an Marciniak-Kuczynski (1967) analysis to predict the forming limit diagrams (FLDs) of the AA5754 and AA3003 aluminum alloys at elevated temperatures. The model takes into account the temperature dependence of the single crystal elastic coefficients, single slip hardening parameters, thermal softening, slip rate sensitivity, and the total deformation. Temperature dependent hardening parameters have been determined through curve fitting the simulated stress-strain response with experiments during uniaxial tension at room and elevated temperatures. The calibration of the TEV model for the single slip parameters in uniaxial tension is shown to provide accurate predictions of the experimental forming limit diagrams (FLDs) without the need for further curve fitting. The effects of elastic constants and thermal softening on FLD prediction are discussed, and equations are developed to predict the temperature dependence of single-slip hardening parameters and so-called initial imperfection parameter employed in the Marciniak-Kuczynski (M-K) analysis. The predictive capability of the new model is then demonstrated by FLD simulations for various elevated temperatures.

Keywords: *Crystal plasticity; forming limit diagram; temperature; M-K analysis; FCC; aluminum alloys.*

5.1 Introduction

Light-weight metals such as aluminum can be employed to replace low carbon steels; however, they are hindered by relatively poor formability at room temperature. In addition, new vehicle designs put higher demands on complex forming geometries and processes, further driving the need to improve the formability of aluminum alloys. Particular to automotive applications, sheet metal forming can be significantly improved by the process of warm forming (Li and Gosh 2003).

The concept of a forming limit diagram (FLD) as a measure of formability was first introduced by Keeler (1965) for the tension-tension domain and extended by Goodwin (1968) to the tension-compression domain. It has since been used as a standard tool to study the extent to which metal sheets can be deformed without localized necking or fracture. There has been extensive research on experimental FLD analysis since the 1960's (Hecker 1975, Ghosh and Hecker 1974) and more recently (Rees 1996, Kim et al. 2003, Banabic and Siegert 2004, Yoshida and Kuwabara 2007, Schwindt et al. 2015, Xu et al. 2015). Although the concept of experimental determination of FLD is simple, the implementation is difficult and very time consuming. In addition, there is a large scatter in experimental data resulting in not very accurate FLDs. To overcome this, much effort has been made to develop reliable simulation tools to numerically determine FLDs.

Early theoretical analysis of localized necking was based on Hill's criteria for rigid plastic solids (Hill 1952). This was not a realistic model for predicting necking in the biaxial strain regime. The first analytical approach to determining biaxial straining behaviour was by Marciniak and Kuczynski (1967) now known as the M-K approach. This method employed an artificial imperfection in an infinite sheet. Increasing load increases strain in the imperfection until the sheet fails, and predicts results for FLDs quite well (Marciniak and Kuczynski 1967, Wu et al. 1997). The M-K approach is now well established for sheet necking among scientists and engineers and is the method employed in this study.

The method was later improved in 80's and 90's to account for different aspects of forming processes on determining FLD (Marciniak et al. 1973, Hutchinson and coworkers 1978a,b,c). Phenomenological models to determine FLDs have been widely used and expanded to include many metal forming phenomena, such as material anisotropy, strain rate sensitivity, and microstructure (Barlat 1987, 1989). More recently, valuable contributions have been made to predict FLD curves with more accurate models (Ganser et al. 2000, Knockaert et al. 2002, Butuc et al. 2003, Stoughton and Zhu 2004, Eyckens et al. 2009, 2011, Wu et al. 2009, Allwood and Shoulder 2009, Zadpoor et al. 2009, Zhang et al. 2012, Franz et al. 2013, Chung et al. 2014a,b, Schindt et al. 2015). This has also been extended to include the effects of temperature on FLDs (Abedrabbo et al. 2006a,b, Khan and Baig 2007, Bagheriasl 2012, Li et al. 2013, Ghavam et al. 2014); however, these phenomenological models are very arduous to calibrate, requiring many experiments and are only valid for monotonic loading. For complex metal forming, this assumption of monotonic loading for predicting limit strains is not adequate. Physically based models, such as crystal plasticity, are generally more expensive to use. However, the parameters of the physics-based models are linked with microscopic deformation quantities and evolve with plastic deformation allowing for non-proportional loading analysis. With the advancement in computational power, these models are becoming more reasonable for numerical study (Inal, 2002).

Wu et al. (1997) introduced the first M-K and polycrystal model based on a Taylor type crystal plasticity formulation. Many recent studies have employed physics-based models for predicting FLDs. It has been well documented that phenomena such as initial imperfection, texture, hardening rate, and constitutive model affect prediction of FLDs (Wu et al. 1997, Inal et al. 2005, Wen et al. 2005, Neil and Agnew 2009, Signorelli et al. 2009, Yang et al. 2010, Serenelli et al. 2011, Chiba et al. 2013, Erinosho et al. 2013). However, none of these models address the effects of temperature and warm forming hardening behaviour on the FLD. The construction of these theoretical FLDs require an accurate constitutive model, such as the ones presented by Cyr et al. (2015) and Clayton (2005).

Warm forming allows for decreased flow stress and increased ductility in aluminum sheet alloys. This can yield a deeper draw and more stretching before failure without design modifications or material microstructure refinement. Experimental work conducted by Palumbo and Tricarico (2007) investigated optimizing the warm deep drawing process of circular AA5754 sheets. They demonstrated that uniform temperature increase during deformation improves formability. In addition, forming defects such as dynamic strain aging, the Portevin-Le Chatelier (PLC) effect and corresponding Luder’s bands resulting from interacting solutes and mobile dislocations can be avoided during deformation above a critical temperature (Abedrabbo et al. 2007). Van Den Boogaard et al. (2001) performed experimental work on the improved formability of AA5754 sheets during deep drawing where significant improvement in formability can be achieved by increasing the working temperature to 2500C. Van Den Boogard et al. (2006) later used a Bergstrom model to predict this behaviour but was unable to accurately predict the flow behaviour at high temperatures, i.e. above 2000C.

The strains developed in most forming processes, such as stamping, are far beyond strains recorded in uniaxial tension tests (Hosford and Caddell, 2011). Material deformation is uniform before necking and stress-strain data is recorded only up to the necking point. Post-necking is non-uniform and stress-strain data cannot be recorded by conventional uniaxial tension tests. Post-necking hardening behaviour has been studied by Mohammadi et al. (2014) for the purpose of determining a methodology to best predict limit strains for forming limit analysis using crystal plasticity. It was reported that, for the aluminum alloy considered in their work, the assumption of almost completely saturated stress behaviour for the post-necking regime produced forming limit curves that correlated the best with experimental results. At elevated temperatures, however, materials generally experience much larger deformation before strain localization than at room temperature.

There has been some recent work presented on the modeling of warm forming, using both dislocation based models and polycrystal plasticity based models. Kurukuri et al. (2009) applied the NES dislocation based model to improve on the work of Boogard et al. (2006). The work concluded that even with the correct description of a yield locus and the microstructure based work hardening model deep drawing simulations still differed from experimental results. Jain and Agnew (2007) described a temperature dependent material model developed for AZ31 magnesium alloy and later extended to predict forming limit curves over a temperature range of interest (Neil & Agnew, 2009). The model incorporates temperature dependent slip softening and hardening parameters, however the temperature dependences of the elastic coefficients and the initial imperfection are neglected. Furthermore, their work did not provide a method by which FLDs can be predicted without experimental data at the desired temperature.

A thermo-elasto-viscoplastic crystal plasticity formulation coupled with the well-known Taylor-type homogenization scheme is employed in this study to predict the limit strains of aluminum alloys AA5754 and AA3003 at various temperatures. The hardening model proposed by Asaro and co-workers (1985) is employed and calibrated using uniaxial tension experimental data for both materials at room temperature and at elevated temperatures. Forming limit diagrams are generated numerically and are compared with experimental data from Palumbo & Tricarico (2007) and Bagheriasl (2012). The effects of temperature on groove orientation and imperfection parameter are also studied. Finally, a parametric study of the effects of temperature dependent crystal elastic coefficients and thermal softening resistance index on the predicted FLDs for AA5754 at elevated temperatures is presented.

5.2 Thermo-Elasto-Viscoplastic (TEV) Crystal Plasticity Framework

The rate-dependent polycrystal plasticity framework developed by Asaro and Needleman (1985) and further by Inal et al. (2002) and Rossiter et al. (2010) is used as the basis of this analysis. The constitutive law is developed for a FCC single crystal and then is implemented in 3D finite element commercial software.

In order to completely capture the kinematics of deformation for a single crystal under both thermal and mechanical loads, the material and the total lattice deformation are decomposed into elastic and rigid body rotation, permanent plastic deformation, and thermal deformation. These deformations are shown in Figure 5-1.

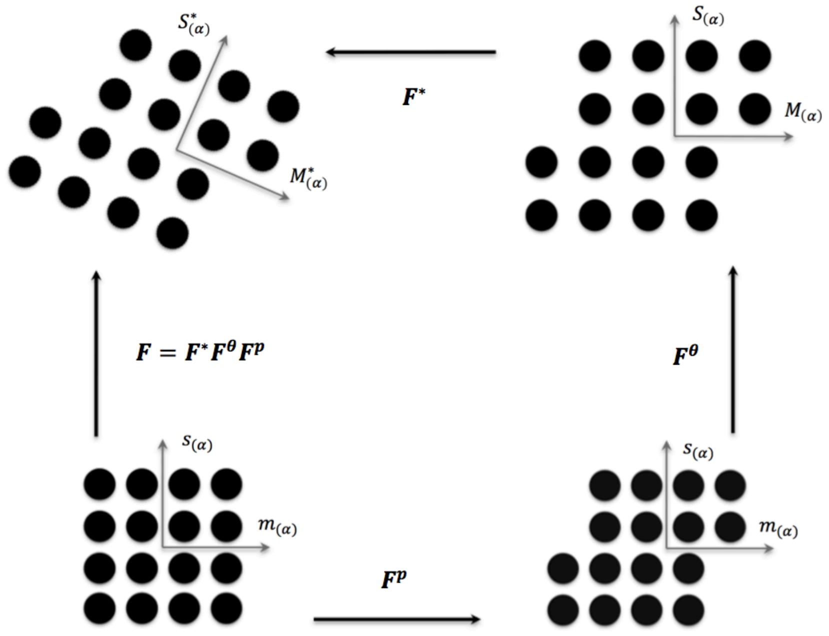

Figure 5-1 Decomposition of total deformation tensor to plastic, thermal expansion, and elastic - rigid body rotation components.

Thus, the total deformation gradient can then be written as

$$F = F^{*}F^{\theta}F^{P} \tag{5.1}$$

where, F^{P} considers only crystallographic slip and F^{*} embodies elastic deformation and rigid body rotation. Thermal deformation, F^{θ}, consists of the thermal expansion of the material and lattice during transient analysis. The spatial velocity gradient in the current configuration then becomes

$$L = \dot{F}^{*}F^{*-1} = L^{*} + L^{\theta} + L^{P} \tag{5.2}$$

where,

$$L^{*} = \dot{F}^{*}F^{*^{-1}} \tag{5.3}$$

$$L^{\theta} = \dot{F}^{*}\left(\dot{F}^{\theta}F^{\theta^{-1}}\right)F^{*^{-1}} \tag{5.4}$$

$$L^{P} = \dot{F}^{*}\dot{F}^{\theta}\left(\dot{F}^{P}F^{P^{-1}}\right)F^{\theta^{-1}}F^{*^{-1}} \tag{5.5}$$

The thermal deformation is assumed to be isotropic (Lee et al., 1997), i.e.

$$\dot{F}^{\theta}F^{\theta^{-1}} = \alpha_{T}\dot{\theta}\mathbf{I} \tag{5.6}$$

where θ is the temperature change measured from the reference state, α_{T} is the coefficient of thermal expansion representing change in length per unit current length per unit increment θ, and $\mathbf{I}$ is the unit identity tensor.

Introducing $\overset{\nabla}{\tau}$ as the Jaumann rate of the Kirchoff stress tensor τ, the elastic component of the single crystal constitutive law is written as,

$$\overset{\nabla}{\tau}{}^{*} = \dot{\tau} - W^{*}\tau + \tau W^{*} = \mathbf{L}D^{*} \tag{5.7}$$

where is the Jaumann rate of Kirchhoff stress tensor based on the lattice rotations, is the spin associated with rigid lattice rotation, is the fourth rank tensor of temperature dependent elastic moduli, and is the elastic strain rate. The Jaumann rate of Cauchy stress can be written in similar fashion as,

$$\overset{\nabla}{\sigma} = \mathbf{L}D - \dot{\sigma}^{0} - \sigma\, trD \tag{5.8}$$

where D is the total strain rate and $\dot{\sigma}^{0}$ is the slip-rate dependent viscoplastic-type stress rate.

The temperature dependence of elastic coefficients was studied by Varshni (1970). He proposed a physics-based model for FCC crystals, which is adopted in this study as follows,

$$C_{ij} = C_{ij}^{0} - \frac{s}{e^{t/T} - 1} \tag{5.9}$$

where C_{ij} and C_{ij}^{0} are elastic stiffness constants at temperature T and zero Kelvin respectively, t is related to Einstein characteristic temperature, and s is another known material constant greater than zero and related to zero-temperature harmonic elastic stiffness coefficient (Suzuki et al. 2011).

The rate-dependent equation for single-slip shear rates is governed by the power law expression defined as,

$$\dot{\gamma}_{\alpha} = \dot{\gamma}_{0} sgn \tau_{\alpha} \left| \frac{\tau_{\alpha}}{g_{\alpha}} \right|^{1/m} \tag{5.10}$$

where $\dot{\gamma}_{0}$ is the reference shear rate assumed constant for all slip systems, τ_{α} is the resolved shear stress on slip system α, exponent $1/m$ is the strain rate sensitivity index, and g_{α} is the temperature dependent hardness of the slip system. For the purposes of this study, the reference shearing rate is assumed to be $\dot{\gamma}_{0} = 0.001\ s^{-1}$ and the slip rate sensitivity is assumed to be $m = 0.02$. The presence of multi slip due to the resolved shear stress on each slip system as well as thermal softening is considered and the rate of strain hardening of the crystal is written as,

$$\dot{g}_{\alpha} = \sum_{\beta} h_{\alpha\beta} | \dot{\gamma}_{\alpha} | \left(1 - \left(\frac{T}{T_m} \right)^{\mathrm{p}} \right) \tag{5.11}$$

where $\dot{g}_{\alpha} = f(T, \gamma_a)$ is the single slip hardening rate and $g_{\alpha} |_{t=0}$ is assumed to be temperature dependent by $\tau_0(T)$. Current temperature T and melting temperature T_m are in Kelvin, exponent $\mathrm{p} = 4$ is used as the thermal softening intensity index, and γ_a is the total accumulated shear on all slip systems. The hardening moduli tensor $h_{\alpha\beta}$ is written as,

$$h_{\alpha\beta} = q_{\alpha\beta} h_{\beta}(T) \qquad \text{(no sum on } \beta) \tag{5.12}$$

Here, $q_{\alpha\beta}$ is the matrix describing latent hardening behaviour, and h_{β} is the temperature dependent single slip-hardening rate. This study will consider the latent hardening and self-hardening rates to be the same, such that $q = 1$. Asaro and Needleman (1985) considered the current hardness to evolve with total accumulated shear γ_a in the crystal such that,

$$\gamma_a = \int_0^t \sum_{\alpha} \left| \dot{\gamma}_{\alpha} \right| dt \tag{5.13}$$

The single crystal hardening law proposed by Chang and Asaro (1981) is employed in this study. It may also be assumed that hardening parameters are functions of temperature, as proposed by Cyr et al. (2015). The hardening law is written as,

$$h_\beta(T) = h_s(T) + \left[h_0(T) - h_s(T)\right] sech^2\left(\frac{h_0(T) - h_s(T)}{\tau_s(T) - \tau_0(T)} \cdot \gamma_a\right) \tag{5.14}$$

where $h_0(T)$ and $h_s(T)$ are temperature dependent reference and asymptotic hardening rates, respectively, and $\tau_s(T)$ is the temperature dependent shear stress saturation. To capture temperature the dependency hardening, parameters $h_0(T)$, $h_s(T)$, $\tau_0(T)$, and $\tau_s(T)$ are assumed functions of temperature such that,

$$h_0 = \bar{h}_0\left(1 - \left(\frac{T}{T_{h_0}}\right)^p\right)^q \tag{5.15}$$

$$h_s = \bar{h}_s\left(1 - \left(\frac{T}{T_{h_s}}\right)^p\right)^q \tag{5.16}$$

$$\tau_0 = \bar{\tau}_0\left(1 - \left(\frac{T}{T_{\tau_0}}\right)^p\right)^q \tag{5.17}$$

$$\tau_s = \bar{\tau}_s\left(1 - \left(\frac{T}{T_{\tau_s}}\right)^p\right)^q \tag{5.18}$$

where the barred parameters correspond to the zero temperature parameters, T is the working temperature and exponents p and q are fitting constants and are not necessarily the same for all hardening parameters. The terms T_i where $i = h_0, h_s, \tau_0, \tau_s$ are the critical temperatures corresponding to a point of sufficient thermal activation that slip can occur at zero stress. A benefit of this model is its ability to capture a range of hardening rates, including saturation, at high strains. Specific to this paper, the model is better able to predict the high strain and saturated hardening behaviour developed at warm forming temperatures than a simple power law model.

Classical Taylor assumptions, (Taylor, 1938), that the deformation of each grain is equivalent to the deformation of the polycrystal, are employed to obtain the macroscopic response of the polycrystal. Therefore, stress, stress rate, shear rate, and modulus values are a result of averaging over the total number of grains.

5.3 Marciniak and Kuczynski (M–K) Formulation

The Marciniak and Kuczynski (1967) approach is well known and details of the formulation in crystal plasticity framework can be found in literature; see e.g. (Wu et al., 1997). For completeness, a brief description is provided in this section. Figure 5-2 presents a schematic representation of the M-K model with axes orientations such that x_1 and x_2 are orthotropic directions in the plane of the sheet (rolling direction – RD, and transverse direction – TD, respectively) and x_3 is aligned with the sheet normal.

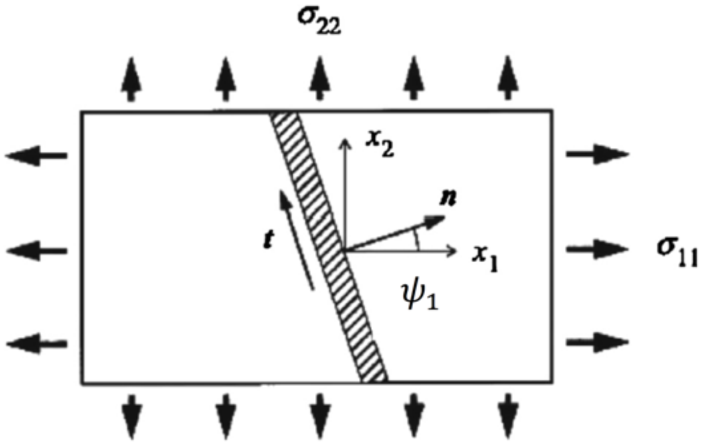

Figure 5-2 Schematic of the sheet metal, the groove, and geometric parameters used for the M-K FLD analysis.

An initial grove is present in the sheet with orientation angle equal to ψ_1 representing the angle between the groove perpendicular and the x_1 direction. The material properties inside the groove are denoted with $(\ )^b$ and thus the initial groove imperfection parameter f can be written as,

$$f = \frac{h^b(0)}{h(0)} \tag{5.19}$$

where $h^b(0)$ and $h(0)$ are the initial thicknesses inside and outside the band, respectively. It is noted that, the imperfection parameter represents groove thickness divided by sheet thickness, while the imperfection itself is one minus the imperfection parameter $(1-f)$. It is proposed that imperfection magnitude will also evolve with temperature similar to hardening parameters such that

$$log(1-f) = log(1-f_0)\left(1-\left(\frac{T}{T_f}\right)^p\right)^q \tag{5.20}$$

where f_0 corresponds to the band ratio at zero temperature, and T_f is the critical temperature where failure is no longer dependent on the imperfection.

The M–K formulation assumes a plane stress condition ($\sigma_{33} = 0$) so that,

$$\frac{D_{22}}{D_{11}} = \frac{\dot{\varepsilon}_{22}}{\dot{\varepsilon}_{11}} = \rho = const.; \quad D_{12} = 0; \quad W_{ij} = 0 \tag{5.21}$$

where $\dot{\varepsilon}_{11}$ and $\dot{\varepsilon}_{22}$ are the principal strain rates and D_{ij} and W_{ij} are two components of the strain rate and spin tensors respectively. Strain rate corresponding to D_{33} is calculated from the imposed plane stress conditions. Finally, the condition for the onset of necking is determined using $\dot{\varepsilon}^{b}_{33}/\dot{\varepsilon}_{33} \geq 10^5$. The full FLD can then be obtained by repeating this process for $-0.5 \leq \rho \leq 1.0$ with the corresponding ψ_1 that yields the lowest macroscopic strains at the onset of necking.

5.4 Material Properties

This section summarizes the properties of the materials used in this work as well as the calibrated hardening parameters for elevated temperatures. Elevated temperature deformation and formability of continuous cast aluminum AA5754 and aluminum AA3003 sheets are studied in this investigation.

5.4.1 AA5754

The aluminum-magnesium alloy AA5754 is commonly used in automotive applications and is strengthened through work hardening. Chemical composition of AA5754 is presented in Table 5-1.

Table 5-1 Chemical composition of AA5754 aluminum alloy.

Alloy	Mg	Mn	Cr	Fe	Si	Cu	Zn	Al
AA5754	3.1	0.25	<0.01	0.24	<0.10	0.02	-	Balance

Electron Back-Scatter Diffraction (EBSD) analysis is employed to obtain the initial textures. A statistically equivalent texture is generated from this data and the {111} stereographic pole figure of the initial texture is presented in Figure 5-3 for AA5754. The representative volume employed in this analysis consists of 541 grains for AA5754 representing a 1.1mm by 0.1mm scan area. The peak intensity is 3.64 times random.

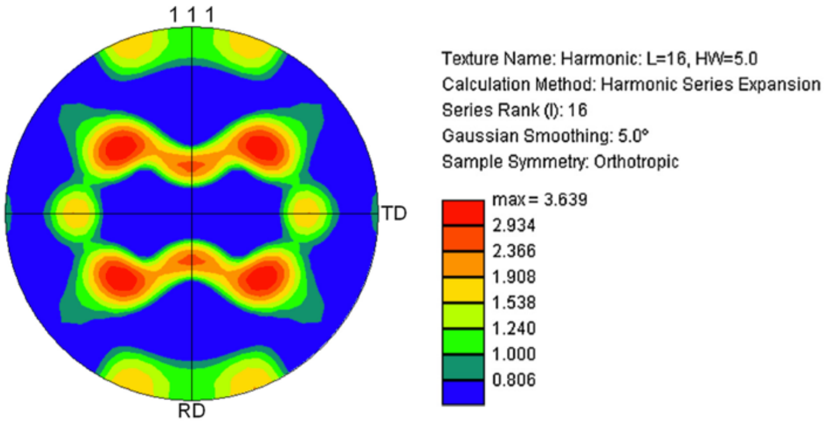

Figure 5-3 {111} stereographic pole figure calculated using Electron Backscatter Diffraction (EBSD) data taken from continuous cast AA5754. The peak intensity is 3.64 times random.

5.4.2 AA3003

The aluminum-manganese alloy AA3003 is a much softer material that undergoes significant work hardening. Chemical composition of AA3003 alloy is presented in Table 5-2.

Table 5-2 Chemical composition of AA3003 aluminum alloy.

Alloy	Mg	Mn	Cr	Fe	Si	Cu	Zn	Al
AA3003	-	1.0-1.5	-	<0.70	<0.60	0.05-0.20	<0.10	Balance

Data from EBSD analysis is used to obtain the initial texture. A statistically equivalent texture is generated from this data and the {111} stereographic pole figure of the initial texture is presented in Figure 5-4 for AA3003. The representative volume employed in this analysis consists of 1000 grains from a 5.3mm by 3.36mm scan area. The peak intensity is 3.16 times random.

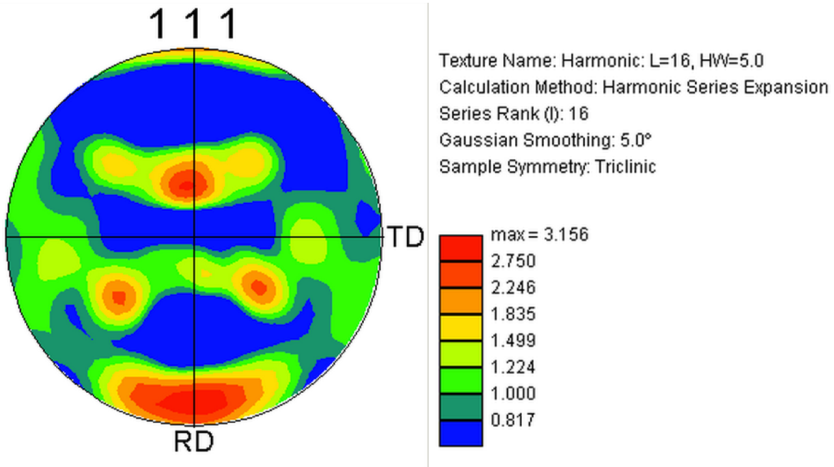

Figure 5-4 {111} stereographic pole figure of AA3003 sheet obtained from Electron Backscatter Diffraction (EBSD) data. The peak intensity is 3.16 times random.

5.5 Model Calibration

The crystal anisotropic elastic constants used for both AA5754 and AA3003 are determined from Varshni's equation (7). Values for C_{ij}^{0} are normalized to agree with the values employed in the FLD work by Mohammadi et al. (2014) at room temperature, considered as $C_{11} = 206\ GPa$, $C_{12} = 118\ GPa$ and $C_{44} = 54\ GPa$. In equation (5.10), reference plastic shearing rate $\dot{\gamma}_0 = 0.001\ s^{-1}$ and slip rate sensitivity parameter $m = 0.02$ are used for both alloys. It is also assumed that, the latent hardening and self-hardening rates are equal such that $q = 1$ in equation (5.12). Thermal softening resistance parameter in equation (5.11) is taken from Cyr et al. (2015) for aluminum materials.

5.5.1 AA5754

The material properties used to generate the simulated stress-strain curves are obtained by curve fitting uniaxial stress-strain simulations by crystal plasticity to experimental results (Rossiter et al. 2010) Three stress-strain curves at temperatures of 25ºC, 150ºC, and 200ºC for AA5754 are used to analyze the temperature dependence of the hardening parameters. Figure 5-5 shows the experimental stress-strain curves for AA5754 (Abedrabbo et al. 2007) and corresponding curves obtained from curve fitting using the crystal plasticity model. The material properties for AA5754 are listed in Table 5-3.

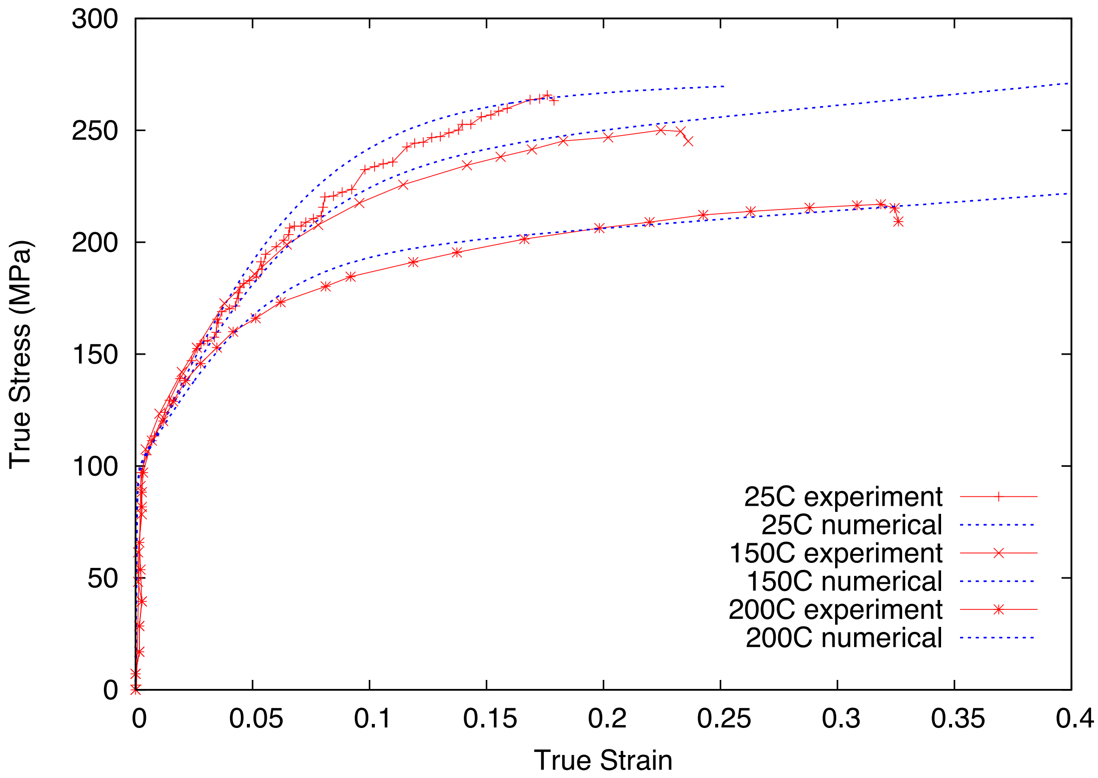

Figure 5-5 Uniaxial stress-strain curves for AA5754 and corresponding fitted curves generated with TEV crystal plasticity simulation at different temperatures.

Table 5-3 Material parameters for Asaro-Lowe hardening law (Harren et al. 1989) at three temperatures using AA5754 texture.

Temperature	$\tau_0\ (MPa)$	h_0/τ_0	τ_s/τ_0	h_s/τ_0
25^{0}C	33.0	7.5	2.75	0.01
150^{0}C	33.0	6.5	2.4	0.25
200^{0}C	33.0	6.0	2.0	0.2

5.5.2 AA3003

The same procedure explained in section 5.4.1.1 is repeated for AA3003 using three stress-strain curves (Bagheriasl, 2012) at temperatures 25ºC, 200ºC, and 250ºC. Figure 5-6 shows the experimental stress strain curve for AA3003 along with corresponding curves obtained from curve fitting with the crystal plasticity simulation using Asaro hardening with TEV crystal plasticity simulation. The material properties employed for AA3003 are listed in Table 5-4.

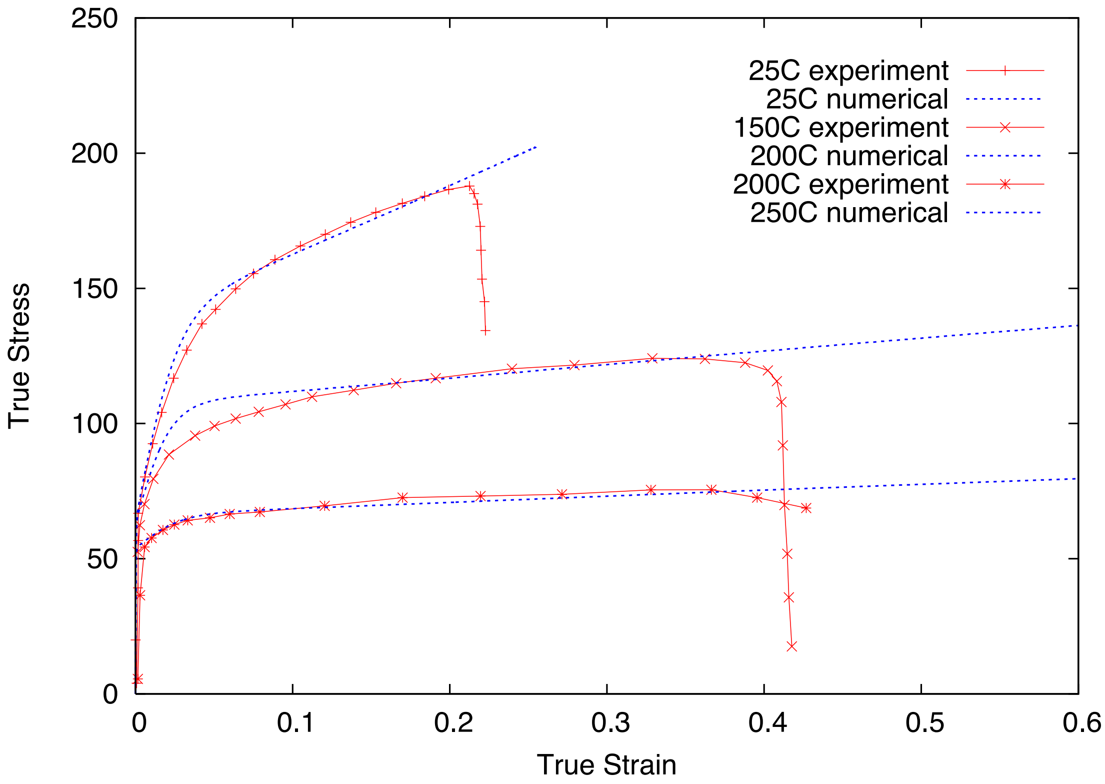

Figure 5-6 Uniaxial stress-strain curves for AA3003 at various temperatures and corresponding fitted curves generated with TEV crystal plasticity simulation at different temperatures.

Table 5-4 Material parameters for Asaro hardening law at three fitted simulation temperatures using AA3003 texture.

Temperature	$\tau_0\ (MPa)$	h_0/τ_0	τ_s/τ_0	h_s/τ_0
25⁰C	22.0	17.0	2.5	0.25
200⁰C	21.5	11.0	1.7	0.18
250⁰C	18.0	3.0	1.25	0.09

5.6 Results and discussion

The initial textures and stress-strain curves generated using the temperature dependent hardening parameters $\tau_0(T)$, $h_0(T)$, $\tau_s(T)$ and $h_s(T)$ determined for AA5754 and AA3003 in the previous section are employed in the M-K analysis to predict FLDs. The groove orientation ψ_1 is determined by changing the groove angle until the lowest forming strains are obtained. The lowest limit strains are used in the final FLD plots.

5.6.1 FLDs

It should be noted that the simulated imperfection parameter f associated with each temperature is different, and must be initially calibrated. This parameter is determined for each temperature by fitting the limit strain during in-plane plane strain (ε_{11}^0) to the corresponding experimental limit strain. Thus, the experimental limit strain for in-plane plane strain is as important as the experimental uniaxial stress-strain curve for the initial calibration of the M-K based FLD analysis. It is intuitive that a smaller imperfection yields larger critical strain at which sheet necking begins. The effect is greater for $\rho \geq 0.5$. The critical groove angle is determined by scanning increments of 5º on the range of ψ_1 to produce the minimum localization strain. Critical groove angle for in-plane plane strain ($\rho = 0$) is always assumed to be 0º.

5.6.1.1 AA5754

As mentioned above, the simulated limit strain for ε_{11}^0 is fit to the experimental data for each temperature by varying the initial imperfection. The imperfection parameters obtained for AA5754 are summarized in Table 5-5. Initial imperfection at room temperature was determined using the methodology of Wu et al. (1997) and Mohammadi et al. (2014) for AA5754, and agrees with the findings of approximately $f = 0.997$ at room temperature. The experimental FLD curves in different temperatures are taken from Naka et al. (2001) for 5xxx aluminum alloys. All experimental data correspond to low strain-rates.

Table 5-5 The imperfection parameter f associated with the simulated temperatures to generate FLDs for AA5754.

Temperature	25⁰C	150⁰C	200⁰C
Imperfection f	0.99698	0.99860	0.99995

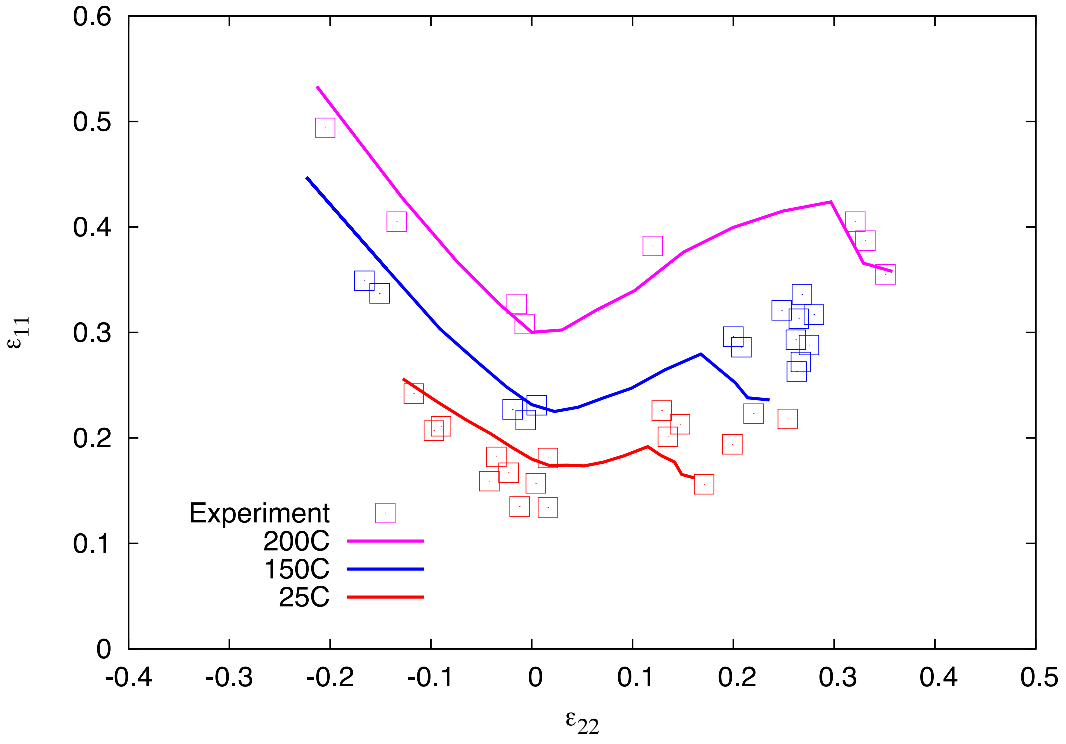

Figure 5-7 Predicted FLDs at 25ºC, 150ºC, and 200ºC along with the corresponding experimental FLD data (Naka et al. 2001) for AA5754. The groove orientation is allowed to change in order to record the minimum limit strains.

The predicted FLDs for the three simulated temperatures between 25ºC and 200ºC are presented in Figure 5-7 for AA5754. The simulations clearly show that the temperature has a significant effect on the formability of aluminum and the FLDs shift towards higher strains. Results agree reasonably well with the experimental FLD (Naka et al. 2001) for AA5xxx series aluminum alloys, however there are some differences. The simulated FLD curves over-predict the limit strains where the value of minor strain is negative, i.e. for left hand side and under-predicts limit strains in the biaxial region for the right hand side. The general behaviour of the FLDs are in very good agreement with the experimental FLDs. The negative minor strain region is almost linear, which is well captured in the simulated FLDs, as well the decrease in limit strain approaching the equi-biaxial region ($\rho > 0.6$) is predicted satisfactorily. Wu et al. (1997) reported similar trends for the formability of AA5754 at room temperature. It has been reported experimentally that in the biaxial regime, the orientation of initial failure in aluminum sheets is perpendicular to the major strain axis (Chien et al. 2004). However, numerical results predicted that the lowest limit strains approaching biaxial tension are produced when the initial groove orientation is not perpendicular to the major strain axis. The numerical results also under-predict the experimental FLD in the biaxial regime. Thus, a second FLD is simulated and presented in Figure 5-8 where the groove orientation is assumed to be fixed at zero degree to agree with the experimental observations. The results do increase the numerical FLD closer to the experimental curve in the biaxial region; however, the commonly observed drop in formability as $\rho > 0.6$ for 5xxx series aluminum is no longer predicted.

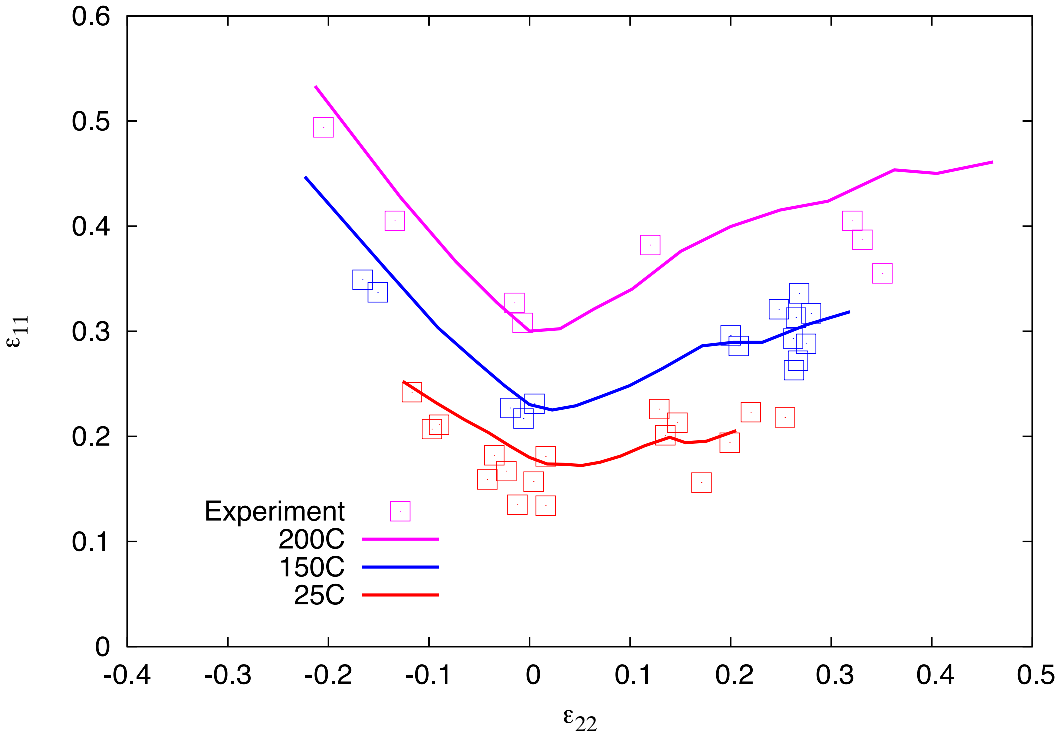

Figure 5-8 Predicted FLDs at 25ºC, 150ºC, and 200ºC along with the corresponding experimental FLD data for AA5754 texture when the groove orientation is fixed at 0º in the biaxial region to predict the limit strains.

Finally, to confirm the need for predicting high temperature hardening behaviour, another forming limit diagram is plotted comparing the forming limit curves of AA5754 at 200ºC with and without adjusting for temperature dependent hardening. If the forming limit curve can be scaled to fit experimental data simply by adjusting the imperfection factor *f*, then the forming limit curve at 200ºC should predict well the experimental data using hardening behaviour determined from the experimental data at 25ºC. As can be seen in Figure 5-9, this is not true, thus it is important for the FLD model to accurately capture the temperature dependent hardening behaviour to better predict the limit strains at elevated temperatures.

5.6.1.2 AA3003

The same procedure is used to calculate the FLDs for AA3003. The imperfection parameters employed for AA3003 at different temperatures are listed in Table 5-6. It is obvious that, temperature has significant effect on the initial imperfection, where the imperfection at 250ºC is in the order of 10^{-9} compared to 10^{-3} at room temperature. As with AA5754, the imperfection appears to exhibit a somewhat exponential dependence on temperature, which is discussed later.

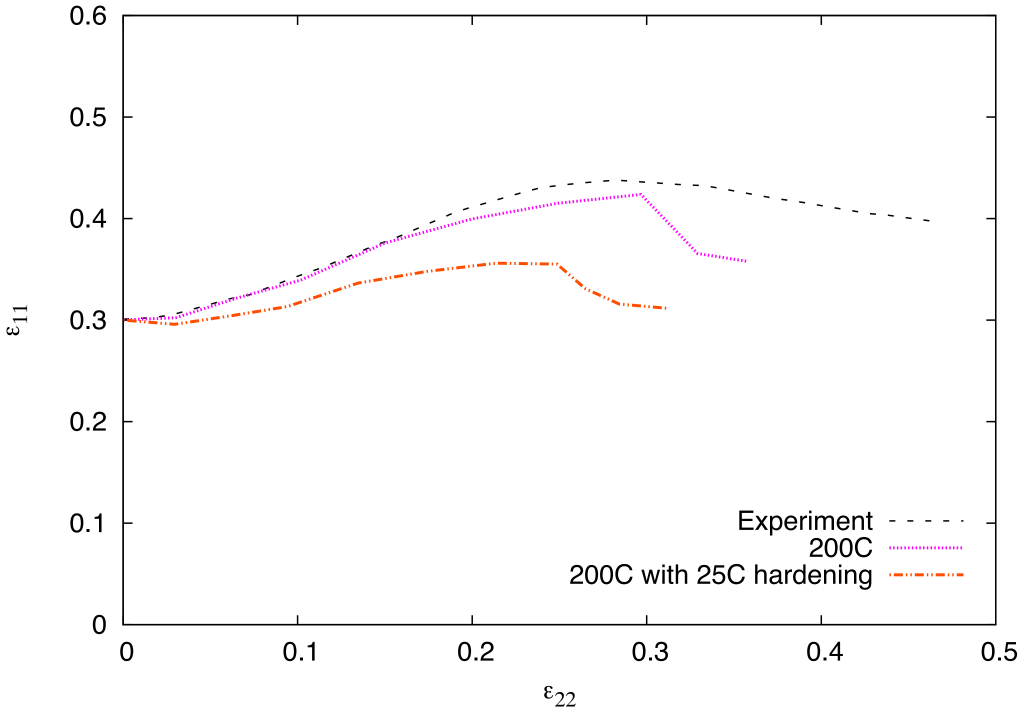

Figure 5-9 Comparison of FLDs with and without temperature dependent hardening at 200ºC along with the corresponding experimental FLD data for AA5754 texture. It is clear that correctly modeling hardening behaviour provides closer fit between simulation and experimental data.

Table 5-6 The imperfection parameter *f* associated with the simulated temperatures to generate FLDs for AA3003.

Temperature	25⁰C	150⁰C	250⁰C
Imperfection *f*	0.9975	0.999995	0.999999996

The predicted FLDs for AA3003 are shown in Figure 5-10 at 25ºC, 200ºC and 250ºC along with the experimental FLDs reported by Bagheriasl (2012). The predicted FLDs for AA3003 are generally in good agreement with the experimental ones.

Mohammadi et al. (2014) already demonstrated the effect of accurately capturing the post-necking hardening on FLD predictions. At high temperatures, the material can withstand almost twice the strain of that at room temperature before necking. Thus, measuring strain hardening behaviour from uniaxial tension tests at high temperatures will allow the predicted FLDs to better match the experimental FLDs at high temperatures.

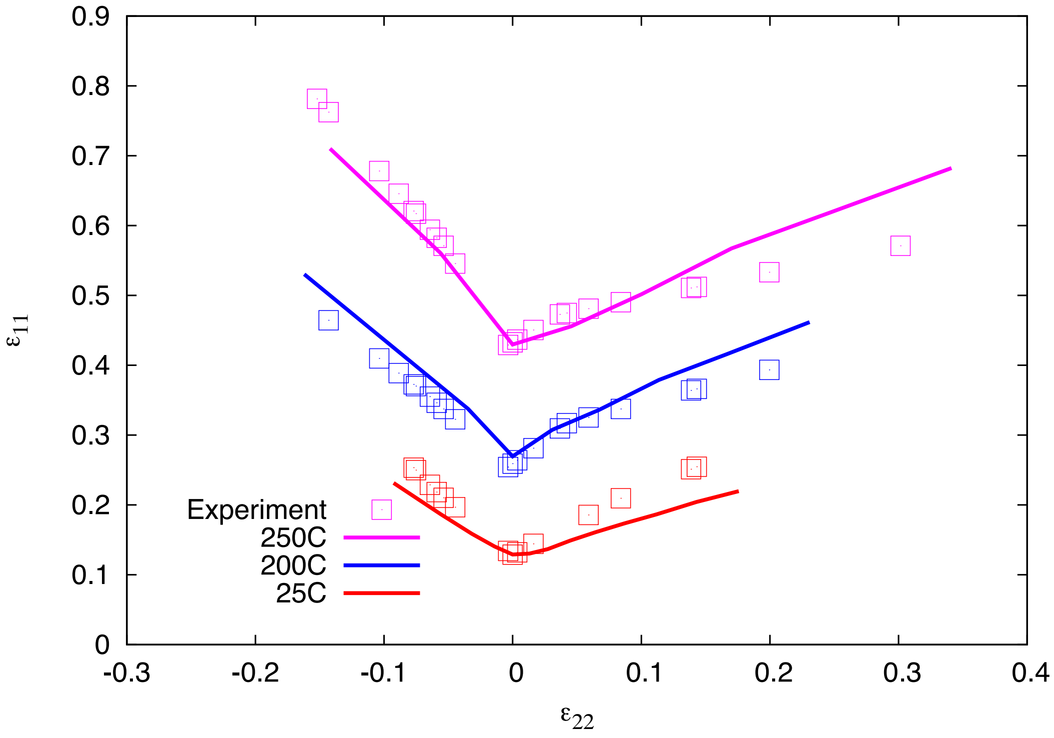

Figure 5-10 Predicted FLDs at 25ºC, 200ºC, and 250ºC along with the corresponding experimental FLD data for AA3003. The groove orientation is allowed to change in order of record the minimum limit strains.

5.6.2 Groove Orientations

Simulations have been conducted in 5° increments in the ψ_1 domain to determine the critical groove orientation that yields the minimum localization strains. The scanning range for $-0.5 < \rho \leq 0.0$ is from $0° \leq \psi_1 \leq 30°$, while for $0.0 < \rho \leq 1.0$ the scanning range is from $0° \leq \psi_1 \leq 60°$. This range is determined numerically by the highest groove orientation that leads to strain localization, i.e. values above these groove orientation angles do not result in necking. The critical groove orientations are not significantly affected by the initial imperfection f, however there is a significant effect from the hardening behaviour and texture. As determined by Mohammadi et al. (2014), high hardening behaviour, especially post-necking, yields unrealistic limit strains in the biaxial region and results in $\psi_1 = 0$ for all values of ρ. To account for this effect, stress-strain curves at room temperature were used for curve fitting such that post necking hardening is minimized.

5.6.2.1 AA5754

The predicted groove orientations that produce the limit strains are plotted versus ρ in Figure 5-11 for AA5754, indicating groove orientations are not significantly affected by temperature. Here, the critical groove angles decrease from $\psi_1 = 15°$, 20°, and 25° at $\rho = -0.5$ to $\psi_1 = 0°$ at $\rho = 0$ and increase again to $\psi_1 = 55°$ under equal biaxial tension. The high temperature 200ºC orientations are the most unstable from $0 < \rho < 0.8$ where the critical angle jumps from $\psi_1 = 0°$ at $\rho = 0.3$ and $\rho = 0.6$.

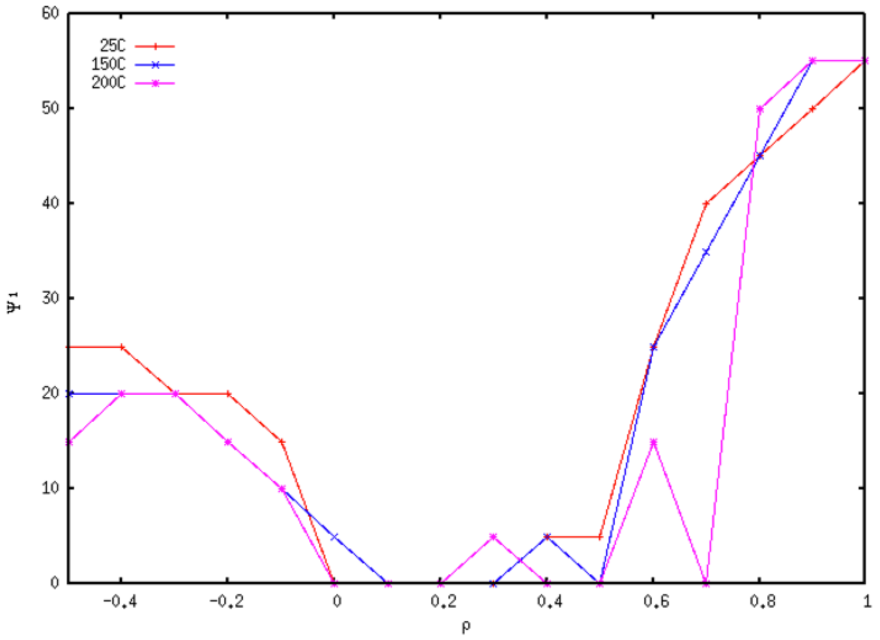

Figure 5-11 The critical groove orientation corresponding to lowest predicted limit strain versus loading path, ρ, for AA5754.

5.6.2.2 AA3003

AA3003 exhibits a much different response to temperature with respect to critical groove orientation. The initial yield stress and hardening of AA3003 greatly decreases with increasing temperature, compared to that of AA5754. Groove orientation behaviour at room temperature is similar for the two alloys. However, the critical orientations at high temperature for AA3003 is $\psi_1 = 0°$ for $\rho \geq 0$ at 200ºC and $\psi_1 = 0°$ for all values of ρ at 250ºC.

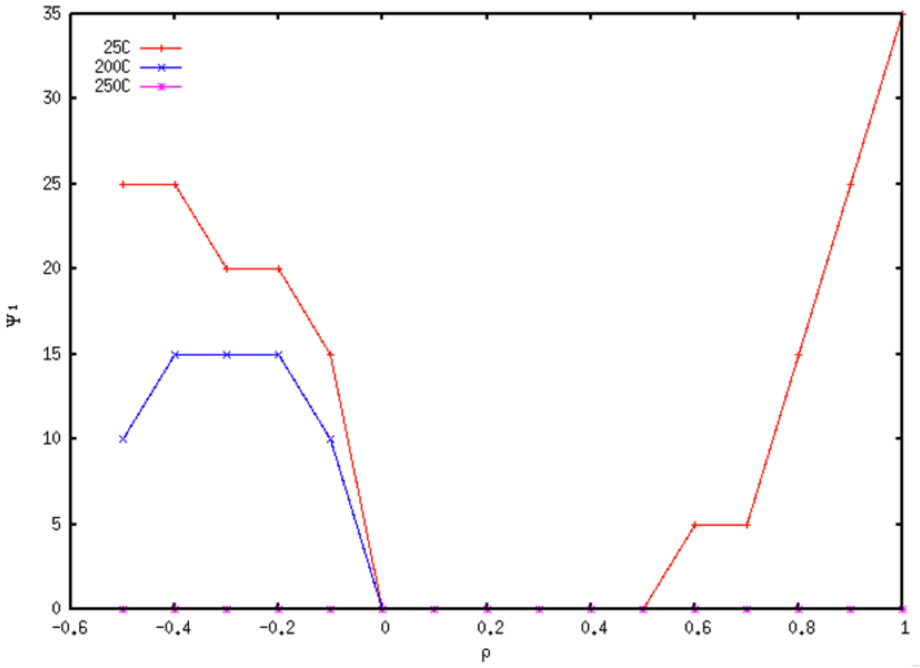

Figure 5-12 The critical groove orientation corresponding to lowest predicted limit strain versus loading path, ρ, for AA3003.

5.6.3 Effect of Thermal Softening

In this section, the effects of thermal softening resistance on the forming limit diagram and groove orientation are investigated. Previous studies have reported the effects of strain-rate sensitivity parameter, hardening parameters, and latent hardening on the numerical FLD for aluminum alloys (Wu et al. 1997); however, thermal softening has not previously been studied in a crystal plasticity FLD formulation. The thermal softening resistance parameter presented in equation (5.11) directly controls the hardening rate of each slip system. Due to the form of the hardening model, hardening is equal for all slip systems. The effect of softening resistance on the stress strain curve and hardening rates is described in detail in Cyr et al. 2015. For aluminum AA5754, a resistance value of p = 4 yields the best match to experimental uniaxial stress strain data.

In Figure 5-13, the numerical FLD is determined for three values of p = 2, 4, and 6 at 200ºC. Materials that show low thermal resistance are greatly affected by temperature increase well below melting temperature. For example, if thermal resistance is equal to two, the stress-strain curve is strongly affected by small temperature changes from room temperature. At the opposite end, if thermal resistance is equal to 6, the stress-strain curve remains relatively unchanged until temperature approaches melting point. The numerical stress-strain curve is exponentially dependent on the softening resistance parameter. The numerical FLD exhibits the same dependence, whereby the increase in limit strain is much less from p = 4 to 6 than from p = 2 to 4.

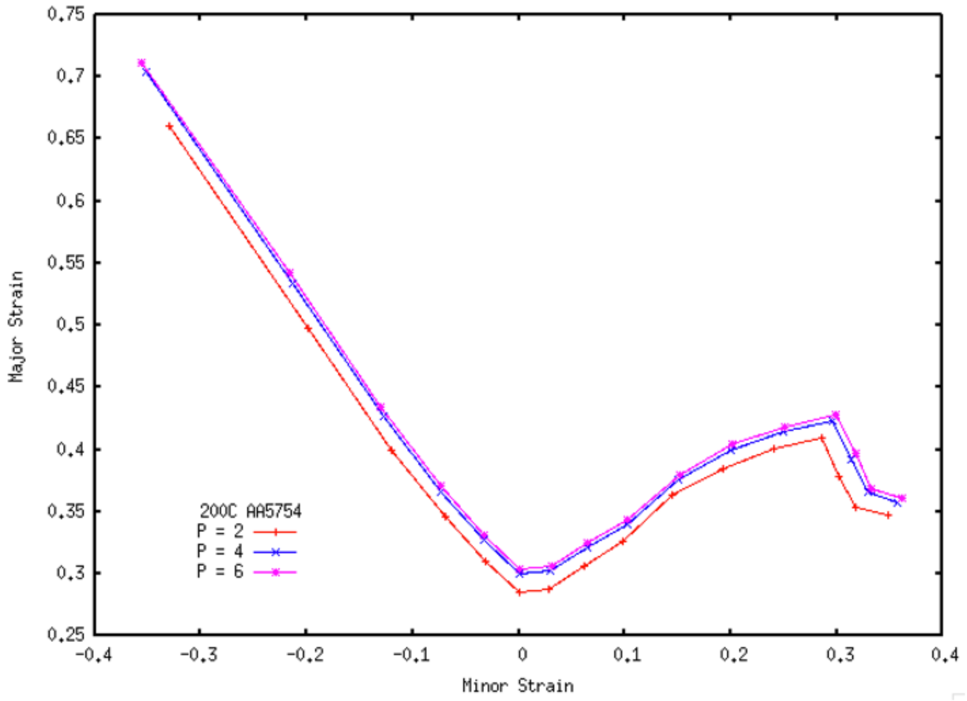

Figure 5-13 Effect of thermal softening resistance parameter “ p ” on forming limits for AA5754 at 200ºC.

Figure 5-14 presents the effect of thermal softening resistance on the limiting strain groove orientations. As with the limit strains, there is no major difference here. Orientations decrease from $\psi_1 = 20°$ to zero for $-0.5 \leq \rho \leq 0.0$ and increase again to $\psi_1 = 55°$ in equal biaxial tension. Mohammadi et al. (2014) reported that the groove orientations are significantly affected by the post-necking hardening behaviour. Thermal softening resistance does not significantly affect the post-necking behaviour of the stress-strain curve. Therefore, the groove orientation independence with respect to thermal softening is expected.

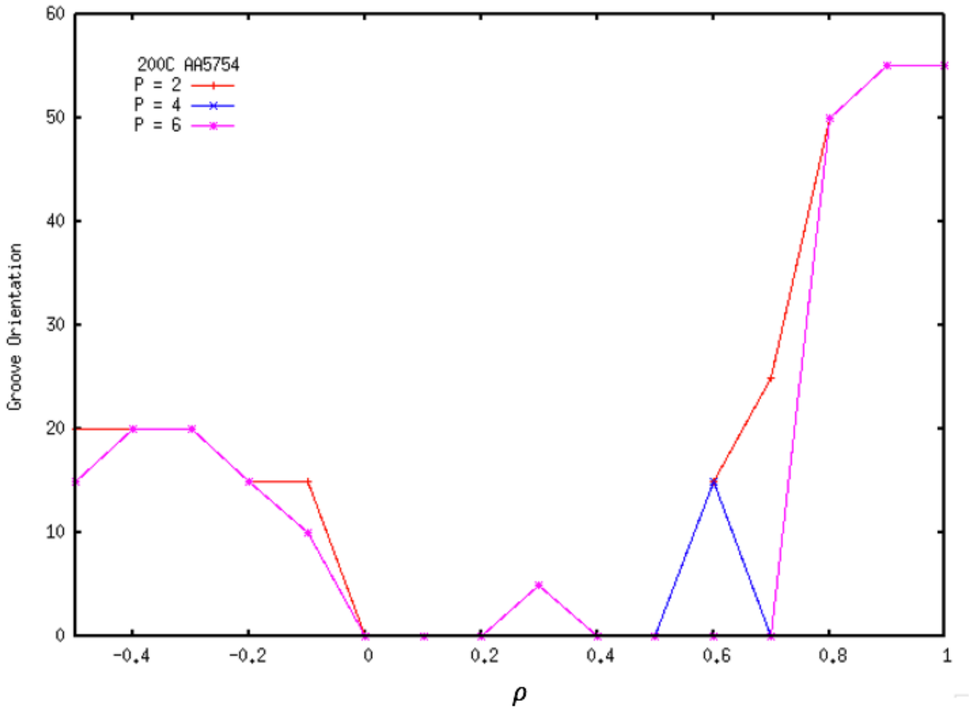

Figure 5-14 Effect of thermal softening resistance parameter " p " on groove orientations resulting in lowest limit strains for AA5754 at 200ºC.

5.7 Proposed Method for Predicting FLD up to Warm Forming Regime

In this section, a new method is proposed to predict the FLDs for AA3003 up to 300ºC, above which deformation mechanisms not considered in this study may be activated (cross-slip, dislocation climb and possibly recrystallization). Using the proposed equations proposed below to model the behaviour of hardening parameters and initial imperfection dimensions with respect to temperatures, FLDs are calculated at intervals of 25ºC from room temperature to 275ºC.

5.7.1 Effect of Temperature on Hardening Parameters

From the three simulated FLDs presented in the previous section for AA3003, hardening parameters and initial imperfection as a function of temperature are shown in Figures 5-15 and 5-16. To model this behaviour, equations (5.15)–(5.18) and (5.20), of similar form to Kocks et al. (1975) on the thermodynamics dependency of slip, is employed. This model also shares similarities to the form of the thermal softening relation presented by Cyr et al. (2015), where the parameters are exponentially dependent on the ratio of working temperature to some critical temperature. The Kocks equation describes glide resistance profiles for plastic slip and is written as

$$\Delta G = F_0 \left\{ 1 - \left(\frac{\sigma}{\hat{\tau}} \right)^p \right\}^q \tag{5.22}$$

where ΔG is the activation energy required to overcome obstacle strength $\hat{\tau}$ for an applied stress σ. Parameter F_0 is the activation energy required without the presence of an applied stress on the system. Thus, the activation energy ΔG decreases from F_0 to 0 as σ is raised from 0 to $\hat{\tau}$, provided both exponential material dependent parameters p and q are positive. The usefulness of this equation comes from the two adjustable parameters p and q. Essentially, p describes the shape of the "tail" (and describes the shape of the "top" ($\sigma \approx \hat{\tau}$).

The proposed equations (5.15)–(5.18) can be related to the Kocks-Mecking model of flow kinetics and the mechanical threshold model. The full derivation providing the link between phenomenological flow kinetics and crystal plasticity is presented in the Appendix section of this chapter. The below equation (5.23) assumes that temperature is related to activation energy, and the energy state at which zero applied stress is required corresponds to F_0. Furthermore, σ is analogous to the desired parameter and $\hat{\tau}$ represents the barred parameter value that the material would theoretically exhibit in the absence of thermal energy, i.e. zero Kelvin. If the equation is then rearranged into the form where temperature is the independent variable, it becomes

$$\sigma = \hat{\tau}\left\{1 - \left(\frac{\Delta G}{F_0}\right)^{1/q}\right\}^{1/p} \tag{5.23}$$

In this form, the similarity with the proposed equations is evident, where σ is the desired parameter as a function of a zero temperature parameter value $\hat{\tau}$, ΔG is the system free energy, which is linearly proportional to temperature, and F_0 is the activation energy for zero stress, or when the desired hardening parameter theoretically decays to zero. For the hardening parameters employed in this study, the critical temperature is not necessarily zero. It is noted that, the exponents p and q in equation (5.23) are not related to the thermal softening resistance or latent hardening, but rather they are fitting parameters used to model the behaviour of the crystal plasticity hardening parameters and initial imperfection factor.

The hardening parameters for the Asaro model employed in this study and their corresponding fit using equations (5.15)–(5.18) are shown in Figures 5-15 and 5-16. This equation is able to provide very good fits to the temperature dependence of material hardening parameters. Using these fits, equations (5.15)–(5.18) is also able to predict a temperature limit at which each parameter becomes zero. This predicted limit agrees with the upper limit of warm forming (300ºC) of AA3003, above which the material experiences almost no work hardening (McQueen, 2011).

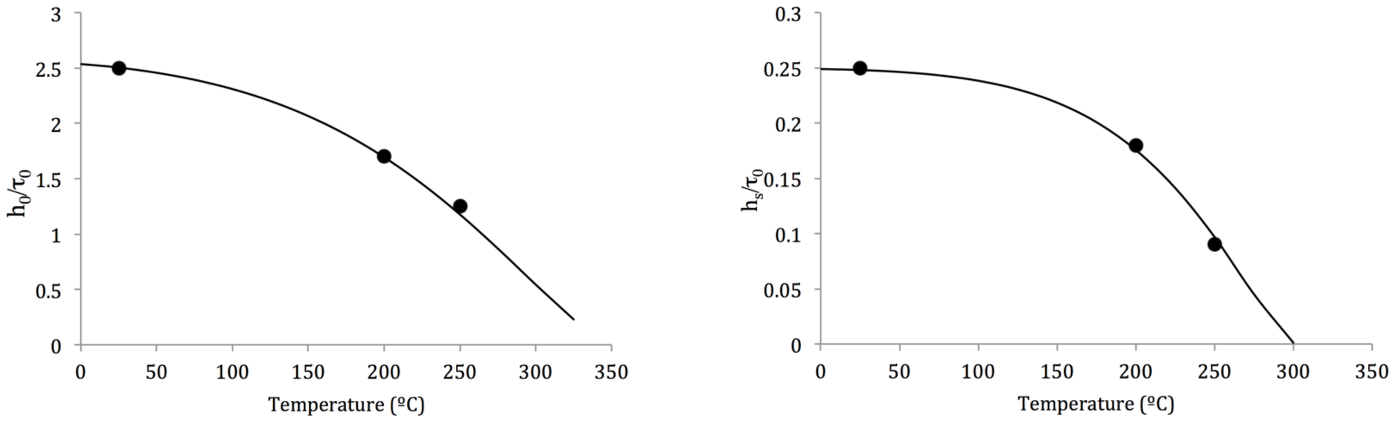

Figure 5-15 Initial hardening rates and saturated hardening rates for Asaro hardening law determined from AA3003 at 25ºC, 200ºC, and 250ºC, along with corresponding fits using equation (5.15) and (5.16).

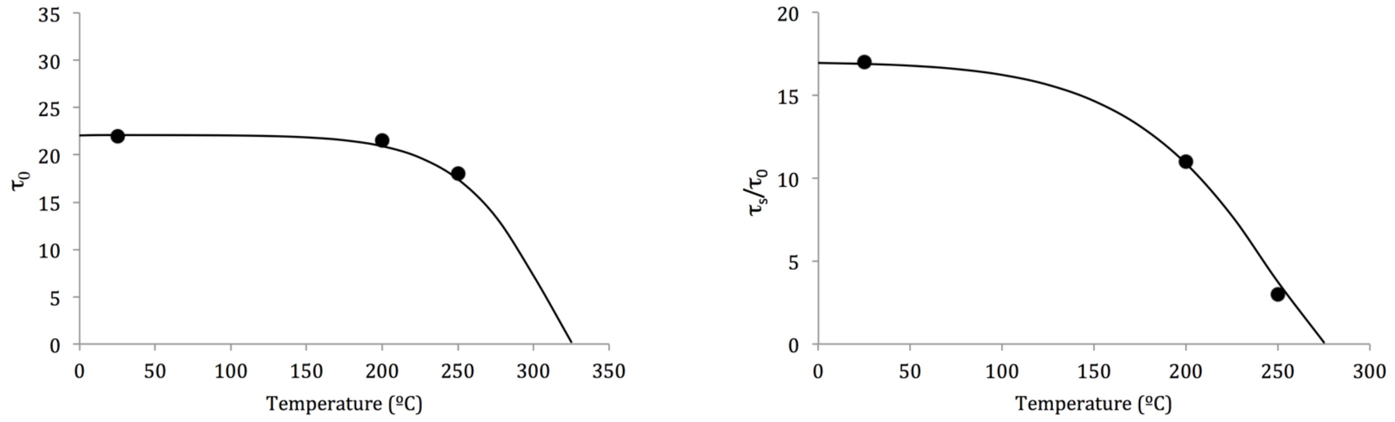

Figure 5-16 Initial slip strength and saturated slip strength from Asaro hardening law determined from AA3003 at 25ºC, 200ºC, and 250ºC, along with corresponding fits using equation (5.17) and (5.18).

The values of the model parameters are summarized in Table 5-7. The only parameter found to be constant for all fits is parameter. Parameters $\bar{h}_0$, $\bar{h}_s$, $\bar{\tau}_0$ and $\bar{\tau}_s$ are predictably close to the room temperature values, and p describes the concavity of the fit. The critical temperatures T_i, related to activation energy F_0, is the predicted energy condition at which the hardening parameter approaches zero. The value F_0 is an empirical coefficient representing the energy state where the material strength is lost; however, the model predicts the temperature corresponding to this vanishing stress energy is well below melting temperature. Other strengthening mechanisms must be present at greater temperatures/energies that this model does not account for. Therefore, above these temperatures, the Asaro hardening model as presented is no longer able to capture the physics of deformation due to new high temperature mechanisms, such as recovery.

Table 5-7 Fitting values using equation (5.15)–(5.18) for Asaro hardening parameters and AA3003 texture.

x	$\bar{x}$ (MPa)	T_i (K)	p	q
h_0	17.0	550	9	1.5
h_s	0.25	575	8	1.5
τ_0	22.1	600	14	1.5
τ_s	2.6	625	5	1.5

5.7.2 Effect of Temperature on Initial Imperfection

The last parameter required for a temperature dependent forming limit diagram is the initial imperfection parameter *f*. In this study, it is shown that increase in temperature significantly affects the imperfection parameter *f*. At 200ºC–250ºC the imperfection decreases to less than 10^{-5} whereas at room temperature it is recorded to be ~ 10^{-2}. This behaviour is predictable since materials that experience lower hardening rates initiate localized necking easier than materials with higher hardening rates.

The imperfection parameter represents the ratio of the groove thickness to the sheet thickness, whereas, the imperfection itself can be considered as the difference in thickness between the sheet and groove thickness divided by the sheet thickness, or $1 - f$. The temperature vs. $log(1 - f)$ relation is plotted in Figure 5-17. The behaviour of the imperfection shows a clear and predictable dependence on temperature. Equation (6.20) captures this behaviour with fitting parameters summarized in Table 5-8.

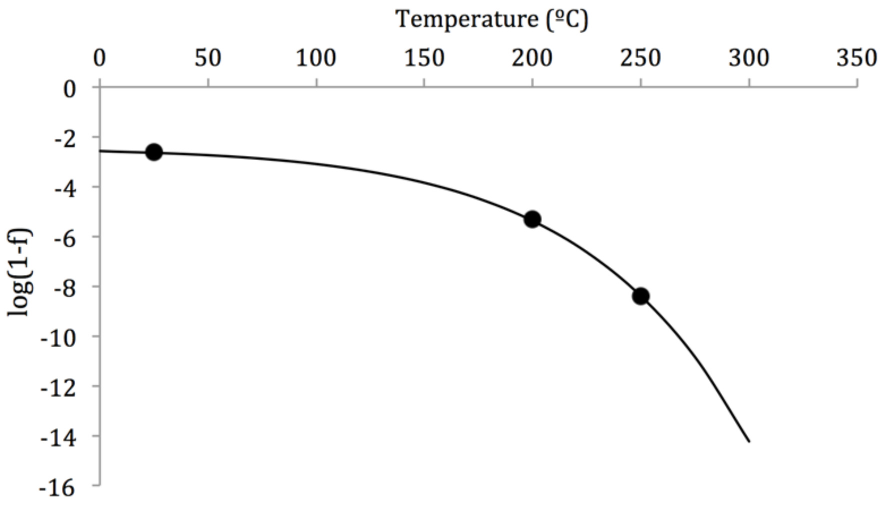

Figure 5-17 Initial imperfection for AA3003 (from section 6.5), curve fitted using equation (6.20).

Table 5-8 Fitting values using equation (6.20) for initial imperfection and AA3003 texture.

	$\log(1-f_0)$	T_f (K)	p	q
$\log(1-f)$	-2.5	0.127	6.2	1.5

The limitation to the imperfection parameter is not determined by decaying to zero, such as the hardening parameters, rather it is dependent on the numerical stability of the model. Simulations using the imperfection parameter and hardening parameters determined from equation (6.20) for 300ºC or above become numerically stable and never lead to localization in the groove. These simulations reach extremely high strains, which are never observed experimentally, and therefore 275ºC is highest temperature simulated.

5.7.3 FLD Predictions

Using these curves describing the temperature dependence of hardening parameters and initial imperfection, the forming limit diagrams can be predicted numerically for any forming temperature below 300ºC. Fig. 5-18 shows the FLD predicted at 100ºC using parameters predicted using equation (5.15)–(5.18) and (5.20) compared with experimental data. The plane strain yielding agrees very closely with the experimental data. The overall FLD prediction is quite satisfactory though the model slightly under predicts the experimental results away from the plane strain condition.

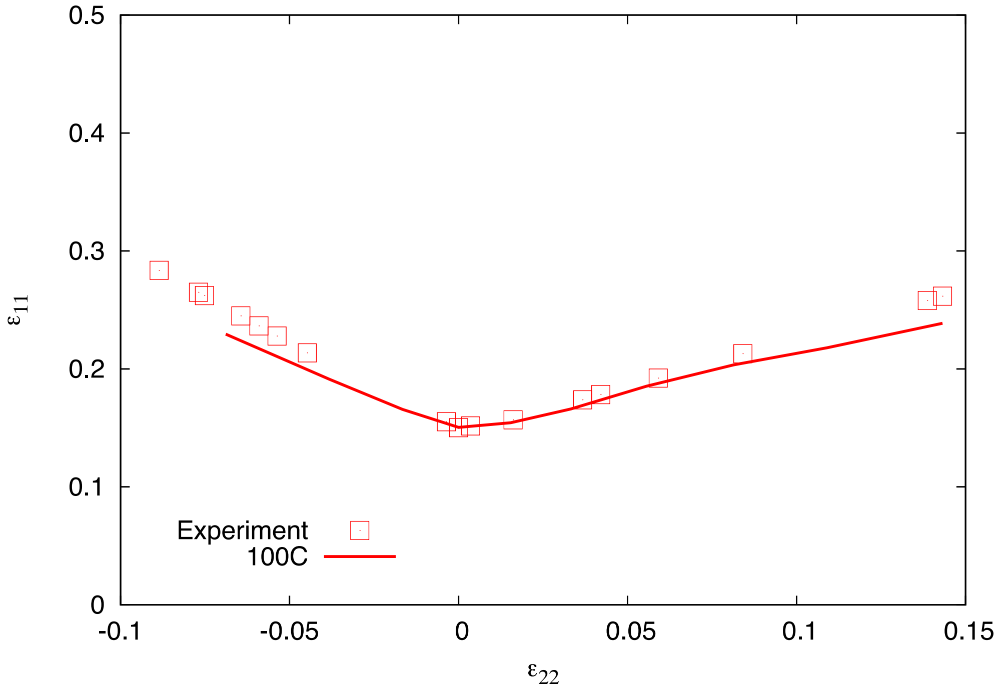

Figure 5-18 Simulated limit strains for AA3003 at 100ºC plotted with experimentally determined limit strains. Parameters for the simulation were determined using temperature dependency equations (5.15)–(5.18) and (5.20).

From equation (5.15)–(5.18) and (5.20), Figure 5-19 shows the predicted FLD for a range of temperatures between 25ºC and 275ºC for AA3003. The limit strains up to 275ºC compare well with available experimental data. Formability increases non-linearly above room temperature, and significant gains in formability are not apparent until above 100ºC. This also agrees with experimental findings (Bagheriasl, 2012). The simulations predict a decrease in formability at each temperature as the strain path approaches equal biaxial tension.

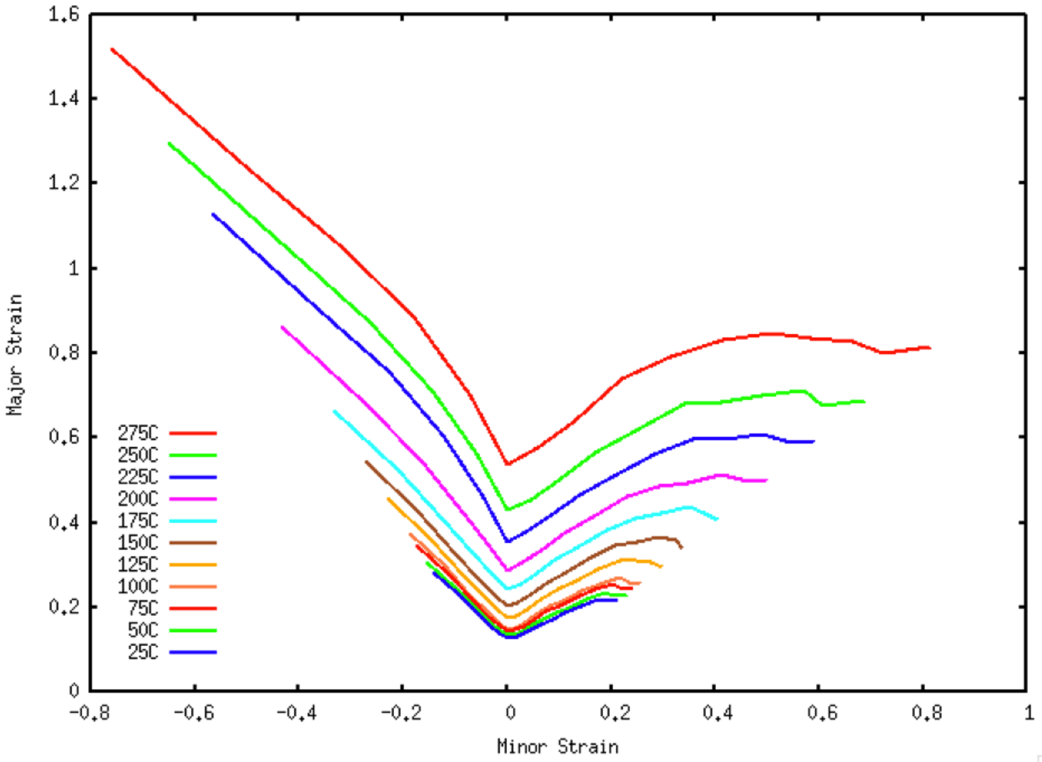

Figure 5-19 Simulated limit strains for AA3003 at warm forming temperatures. Hardening parameters and initial imperfection are determined using equations (5.15)–(5.18) and (5.20) and fitting parameters in Tables 5-7 and 5-8.

5.8 Summary and Conclusions

In this paper, a new numerical framework using a thermo elasto-viscoplastic (TEV) crystal plasticity formulation in the well-known M-K approach to calculate limit strains of aluminum alloys at elevated temperatures is presented. The model is calibrated to capture the formability of AA5754 and AA3003 aluminum alloys up to 300ºC. The model can take into account the temperature dependence of the single crystal elastic coefficients, single slip hardening parameters, thermal softening, slip rate sensitivity, and the total deformation. In addition, the new model is calibrated with experimental uniaxial tension curves. Temperature dependent hardening parameters are determined through curve fitting stress-strain data from uniaxial tension simulations at room temperature and elevated temperatures. Simulations show that the proposed model accurately predicts the forming limit diagrams (FLDs) at room temperature and elevated temperatures without the need for further curve fitting. It is found that the groove orientation yielding the lowest limiting strain in the biaxial regime reduced to $\psi_1 = 0^\circ$ when forming temperature is increased from room temperature to warm forming temperatures for both materials. Furthermore, simulations showed that increasing the thermal resistance increases the forming limit curve at a given temperature.

Finally, a new method for determining the temperature dependence of hardening parameters and the initial imperfection is presented. This formulation can be used to accurately predict forming limit curves at any temperature between room temperature and 300ºC without the need for any further calibration; including the imperfection parameter, *f*.

Chapter 6

Part III: Temperature-Dependent Plasticity: A New Constitutive Formulation for Polycrystalline Metals

Edward D. Cyr[1], Abhijit Brahme[1], Mohsen Mohammadi[2], Raj K. Mishra[3], Kaan Inal[1]

[1] *Department of Mechanical and Mechatronics Engineering, University of Waterloo, Waterloo ON, Canada, N2L 3G1*

[2] *Department of Mechanical Engineering, University of New Brunswick, Fredericton NB, Canada,*

[3] *General Motors Research & Development Center, Warren MI, 48090, USA*

Abstract

In an effort to improve metal formability and performance, high temperature forming has become a desired manufacturing process. Phenomenological plasticity models are widely used in this application, however lack any predictive capability concerning microstructure evolution during forming. Crystal plasticity models have been adopted in recent decades as an advantageous framework for modeling stress-strain response in a variety of loading conditions as well as the microstructural evolution, yet material hardening is formulated on a phenomenological basis. Many hardening models have been developed to understand and predict the deformation of metals at warm forming temperatures; however, few have fully integrated thermodynamic formulations and none are based on physical deformation mechanisms. Therefore, available crystal plasticity hardening models are unable to predict the high-strain behaviour of elevated temperature deformation.

In slip-dominated deformation, dislocation-dislocation interactions govern the strain-hardening behaviour, especially at elevated temperatures. Understanding the thermodynamics is the most important facet in predicting temperature dependent deformation. In this study, a new mechanistic constitutive theory for plasticity based on Taylor slip analysis and dynamic recovery is formulated from an energy balance between dislocation storage, dislocation accumulation, and dislocation recovery due to thermal activation with physically motivated hardening parameters that can be experimentally determined. The developed theory is used to simulate low-to-high temperature stress-strain behavior of pure aluminum. The temperature dependence of thermally activated mechanisms and their equivalent parameters are also presented and discussed. Finally, the model is validated with the accurate prediction of uniaxial stress-strain data at a new strain-rate and a sensitivity analysis of hardening parameters to the stress-strain response is presented and discussed.

Keywords: *Polycrystal hardening; dislocation; dynamic recovery; temperature; annihilation.*

6.1 Introduction

Hot deformation processing is a desirable method for shaping in industry due to the ability to refine microstructure, which significantly influences the mechanical response and can increase formability (Zhang et al., 2004; Li, et al., 2011). The understanding of high temperature deformation behaviour for hot working and the constitutive relations describing the material flow are two of the fundamental prerequisites for the implementation of forming technology in industry.

Dynamic softening mechanisms, such as dynamic recovery (DRV) often occur in aluminum alloys with high-stacking fault energies during deformation at elevated temperatures. Numerous reports on the high-temperature deformation behaviour and dynamic softening of aluminum alloys (and other FCC metals) have shown that the mechanisms contributing to softening and microstructure evolution during high-temperature deformation are highly sensitive to temperature and strain-rate (Clayton, 2005; Abedrabbro et al., 2007; Pandey et al., 2013; Ezatpour et al., 2014). Determination of the effects of temperature and strain rate on high-temperature deformation in metals has been a topic of discussion for decades (Argon, 1968; Kocks et al., 1975; Kocks, 1976, 2001; Anand, 1982; Mecking et al., 1986; Kocks & Mecking, 2003; Terentyev et al., 2015; Kooiman et al., 2015, 2016). Flow stress is the most basic measure for characterizing plastic deformation properties of metals and provides a means to determine the energy required to plastically deform a metal. The metal then dissipates this energy while undergoing plastic flow by the mechanisms of deformation, which can be evaluated with the aid of governing constitutive equations. The improvement of these constitutive models over recent decades have given rise to an incredible understanding of material behaviour on a fundamental level; however, in many cases at the expense of great complexity and subsequently increased difficulty in application.

Plasticity theories are widely used in research and industry covering a broad field of applications ranging from crash and extrusion simulations to modeling and optimization of material microstructures. However, classical phenomenological plasticity theories fail to predict the mechanical behaviour of micro-components and the corresponding material response. The methods of crystal plasticity have been successfully used in modeling non-homogeneous mechanical behaviour and has been applied extensively to study both heterogeneous plastic deformation and texture evolution (Roters et al. 2010). The material hardening, however, usually cannot be linked to any physical processes. These phenomenological models are adequate for the intended use of ambient temperature deformation, but are unable to predict material properties from experimental data or their temperature and strain dependence. It is essential for the investigation of complex deformation features during forming, such as temperature dependent and geometric softening, strain localization, and microstructure evolution, etc., that the material hardening models be derived from physical deformation mechanics.

In this chapters, a physical theory for temperature dependent strain hardening in FCC polycrystals is developed based on dislocation accumulation and recovery. The model is then fit with available pure aluminum uniaxial stress-strain data (Kocks, 1976) and temperature dependent hardening parameters are identified and investigated. The pre and post necking hardening behaviours are also analyzed. Finally, the resulting temperature dependencies and theory are used to predict the stress-strain curves at a new higher strain rate and a parameter sensitivity analysis is completed.

6.2 Background

Work hardening has always been a topic of great interest for scientists and engineers studying plastic deformation in metals. The work-hardening reflects the way in which arrays of stored dislocations, both geometrically-necessary and statistically-stored, impede the passage of moving dislocations. Individual dislocations act as point obstacles causing short-range interactions, and the collective array, a source of long-range internal stresses. Following the discovery of dislocations and dislocation theory, many concentrated efforts by the scientific community led to the description of the three stages of work hardening in single crystals: primary slip (stage I), multiple slip (stage II), and cross slip and recovery (stage III). The first stage is only observed in single crystals at low strain where hardening is governed by statistically-stored dislocations. Although flow stress theory and strain hardening is derived from single crystals, most metals strained in application are polycrystalline. By the addition of hardening particles or in polycrystals, the presence of these primary stages vanishes and the geometrically-necessary dislocations dominate. Therefore, the hardening of most polycrystalline metals is characterized by yielding, followed by a low-strain high-hardening stage II that transitions, often rapidly, into a lower hardening stage III. The theory on the initiation of stage III began with the work of Seeger and coworkers (Schoeck and Seeger, 1955; Seeger et al., 1959) which begins because cross-slip occurs upon sufficient local pile-up stresses. The model predicts an exponential variation of the onset of stage III with temperature, however, was met with controversy (Coulomb and Friedel, 1957). Much debate exists on the high-strain transition from a stage III to a stage IV hardening, where the stress-strain curve begins to plateau or become nearly linear, however this is typically not observed under uniaxial conditions due to localization.

Single crystal work hardening theories based simply on the concept of hardening stages have been employed in crystal plasticity framework and can successfully be tuned to match the polycrystal behavour; however, there still exists a significant gap in the connection between physical properties and mechanisms of deformation in explaining work hardening through the use of hardening laws. This is even more obvious at high temperatures, where conventional stage II to stage III transition broadens and the region of the stress-strain curve corresponding to each becomes unclear. In addition, the extremely low stage III hardening relative to the high stage II cannot be predicted with conventional crystal plasticity hardening models. Therefore, a hardening relationship based on the dislocations themselves, rather than the behaviour that manifests as multiple "stages" of hardening, must be developed in order to predict temperature dependent hardening.

The relationship between material strength and the square root of total dislocation density is well known as

$$\sigma = \sigma_0 + M\alpha\mu b\sqrt{\rho} \tag{6.1}$$

where M is the Taylor factor relating shear and normal stresses in polycrystals ($\sigma = M\tau$), α is a measure of the strengthening effect of dislocations, μ is the shear modulus and b is Burgers vector (Kuhlmann-Wilsdorf 1970). Initial material strength σ_0 is due greatly to alloying, precipitates, particles, grain size, and existing dislocations before any deformation has occurred. The significance of this equation is that all work hardening models from earlier theories attributing work hardening to dislocation pile-ups, tangles, jogs, and forest dislocations and newer statistical theories and models of decreasing mean free path all predict this proportionality of strength and the square root of dislocation density. This equation is also maintained by nearly all experimental results (Rodriguez 1996).

Taylor (1934) proposed that strength of a mobile dislocation could be predicted as the shear stress required to overcome a stable array of immobile (sessile) ±edge dislocations. The calculated stress was dependent on the inter-layer spacing of sessile dislocations. Since the plastic shear strain is related to the motion of dislocation, using Taylor's analysis of shear strain, the stress can be found to be proportional to the square root of the strain and exhibited the proportionality as follows

$$\frac{\tau}{\mu\sqrt{\gamma}} = \frac{\kappa\sqrt{b}}{\lambda} \tag{6.2}$$

where τ and γ are the shear stress and shear strain, respectively, μ is the shear modulus, b is Burgers vector, λ is the mean slip distance, and κ is a proportionality constant related to the sessile dislocation array. Taylor was able to estimate λ using calculated values of κ from modeled dislocation arrays and compared the magnitude with experimental observations (Taylor 1934). In addition, Taylor's model with parabolic stress-strain dependence predicts a constant λ .

More recent work (Saimoto & Van Houtte 2011) has provided evidence that the mean slip distance can be measured directly from the experimental stress-strain curve with a single variable ϕ using the following relation:

$$\lambda = \phi \frac{b}{2} \frac{\mu^2}{\tau} \frac{\partial \gamma}{\partial \tau_{|T,\dot{\gamma}}} \tag{6.3}$$

Here the hardening term $\partial\tau/\partial\gamma_{|T,\dot{\gamma}}$ is the slope of the shear stress-strain curve, however has previously been estimated as θ_{II} evaluated from a Stage II type hardening determination of [100] single crystals (Nabarro et al. 1964, Saimoto 2006). Consequently, the determination of mean slip distance can be a function of τ or γ. Based on this assumption, the calculation of λ to produce an incremental strain $\Delta\gamma$ is possible.

The Taylor model defines an increment in shear strain $\Delta\gamma$ to be equal to $N\tilde{A}b$, where N is the volume density of slip patches produced by a source of inter-obstacle spacing ℓ on slip patch area $\tilde{A}$, and b is the Burgers vector. An increase in dislocation length associated with the slipped area arises from the expanding perimeter of the propagating dislocation segment from the source. Dislocation length may also decrease due to annihilation interactions with other existing dislocation segments. The slipped area can be approximated as proportional to the square of the mean slip distance λ^2 assuming that λ is in the order of the average inter-obstacle spacing such that $\lambda \approx \ell$, which is true at low strains. By representing the increment in volume density of dislocations as $\Delta\rho/\lambda$, one can now describe the incremental change in statistical dislocation density per unit area, $\Delta\rho^{create}$, due to incremental shear strain as follows:

$$\Delta\rho^{create} = \frac{P}{A}\frac{\Delta\gamma}{\lambda b} \tag{6.4}$$

where $\frac{P}{A}$ is a unit-less parameter for the ratio of the expanding dislocation perimeter P divided by statistical annihilation factor A and is temperature dependent.

An estimation of P is possible through a quantitative analysis of the advance of a dislocation through a random array of obstacles (Friedel, 1964; Foreman and Makin, 1966, 1967; Kocks, 1967; Altintas, 1978). The analysis can be derived from the Altintas (1978) diagram of randomly dispersed point obstacles, shown in Figure 6-1. The algebraic relationships between the interobstacle spacing $\ell = \ell_s$, dislocation arc radius R, height of new sector h (assumed here that $h = \lambda$, mean slip distance), which are determined by the strength of obstacle parameter such that $\alpha \approx \cos\left(\frac{\psi}{2}\right)$. The initial length of the dislocation segment bound by obstacles A and C is equal to $2\ell_i = 2R\sin(\pi - \psi)$ and the final dislocation length $\ell_f = 2R(\pi - \psi)$. The ratio of the increase in dislocation length can therefore be calculated as $(\ell_f - \ell_i)/2\ell_i$. Given $\psi/2 = 65°$ corresponding to $\alpha = 0.4$, P for this analysis is approximately 0.2.

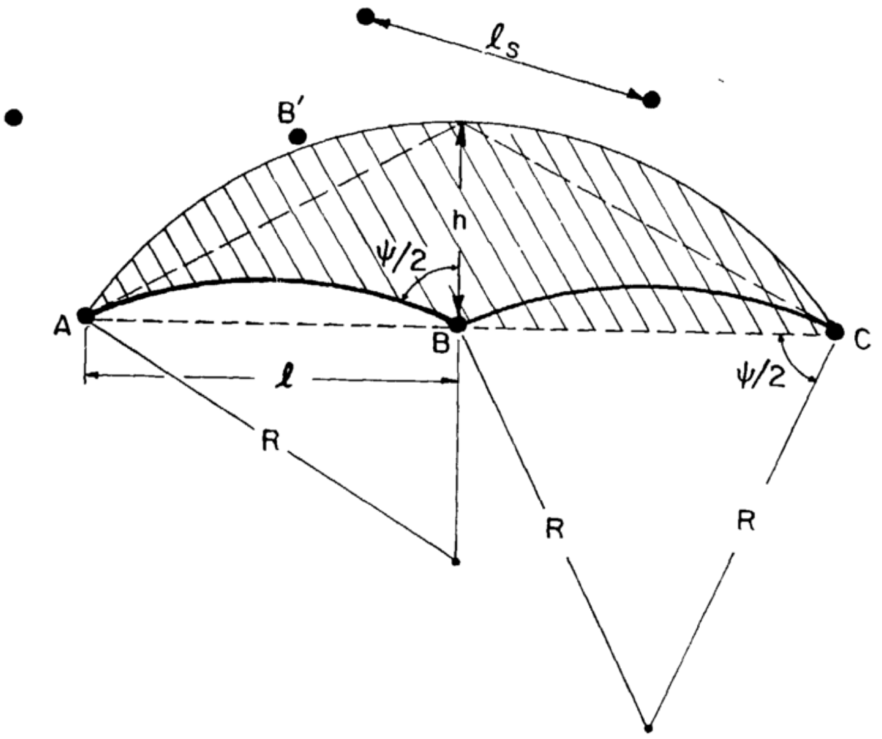

Figure 6-1 Geometry of randomly distributed obstacles. (Friedel, 1964).

If we take the well-known relationship in equation (6.1) between the strength of a polycrystal and the square root of the dislocation density, we can obtain

$$\frac{d\rho}{d\tau} = \frac{2\tau}{(\alpha\mu b)^2} \tag{6.5}$$

Therefore, for small increments in material strength and a given multiplicity of two, the required stored dislocation density must be equal to

$$\Delta\rho^{stored} = \frac{2(\tau\Delta\tau)}{(\alpha\mu b)^2} \tag{6.6}$$

Finally, we can equate the dislocation density stored due to increasing material strength and the dislocation content created necessary to accommodate an incremental shear strain in differential form,

$$\left|\frac{2(2\tau\partial\tau)}{(\alpha\mu b)^2}\right|^{stored} = \left|\frac{P}{A}\frac{\partial\gamma}{\lambda b}\right|^{created} \tag{6.7}$$

The above relationship represents the condition where dynamic recovery of dislocations due to thermodynamic recovery is not accounted for. The statistical annihilation of dislocation lines $\frac{1}{A}$ accounts for the statistical probability that two oppositely oriented mobile dislocations exist within a threshold proximity on a given slip plane and annihilate nearly instantaneously. This is experimentally very difficult to determine; however, statistical annihilation of new dislocations has been shown to be very important in order to predict the experimental stress-strain curve (Saimoto & Van Houtte, 2011).

6.3 Work Hardening Model

In all dislocation models, work hardening is a result of mobile dislocations that produce strain being pinned and therefore unable to exit through a surface, be absorbed by grain boundaries, or annihilating each other. Instead, some fraction of these mobile dislocations are stored in the crystals forming new obstacles to continued slip of other dislocations. As discussed previously, this is represented as the dislocation density created through shear straining, or $\Delta\rho^{created}$. If we now include the mechanisms facilitating recovery, the total change in dislocation density can be represented as follows

$$d\rho^{stored} = d\rho^{created} - d\rho^{recovered} \tag{6.8}$$

The first two terms have been described above, while the last term is the change in dislocation density due to recovery or rearrangement of previously stored dislocations. The recovery processes are still not well understood and various mechanisms have been proposed to describe them. The following proposed mechanism for recovery is rationalized from experimental observations in conjunction with accepted theories from dislocation mechanics.

A crystal with potential number of recovery sites in a differential area on a slip plane can be denoted as ρda where ρ is the stored dislocation density. If an average dislocation line length of ℓ_r is recovered or annihilated, the change in total dislocation line length $d\ell$ per volume V is written as

$$\frac{d\ell}{V} = \frac{\ell_r \rho da}{V} = d\rho^{recovered} \tag{6.9}$$

The importance of this relationship is the understanding that the probability of a dislocation being recovered is directly proportional to the probability that a moving dislocation discovers a recovery site, and therefore the dislocation density itself. This can now be linked to the shear increment by the following equation. Assuming a slip plane area da in a volume V shears a distance of one Burgers vector, the incremental shear can be represented as

$$d\gamma = \frac{bda}{V} \tag{6.10}$$

Combining the above two equations, the recovered dislocation density can now be written in terms of the shear increment as

$$d\rho^{recovered} = \frac{\ell_r}{b}\rho d\gamma = \Omega \rho d\gamma \tag{6.11}$$

where Ω is called the recovery factor which represents the average length of dislocation that is recovered normalized by the Burgers vector for a given shear increment. Finally, we combine this with equations (6.4), (6.6) and (6.8) to get the following:

$$\left|\frac{2(2\tau\partial\tau)}{(\alpha\mu b)^2}\right|^{stored} = \left|\frac{P}{A}\frac{\partial\gamma}{\lambda b}\right|^{created} - \left|\Omega\rho\partial\gamma\right|^{recovered} \tag{6.12}$$

By integration, one can write:

$$\left[\frac{2\tau^2}{(\alpha\mu b)^2}\right]_{\tau_1}^{\tau} = \left[\frac{P}{A}\frac{\gamma}{\lambda b} - \Omega\rho\gamma\right]_{\gamma_1}^{\gamma} \tag{6.13}$$

The difficulty now becomes the determination of dislocation density ρ. This is achieved implicitly by substitution of the Taylor expression from equation (6.1), which allows for a work hardening flow rule to be developed based on material parameters and internal state variables given by,

$$\tau = \alpha\mu b\sqrt{\frac{P}{A}\frac{\gamma}{\lambda b(2+\Omega\gamma)}} \tag{6.14}$$

To this point, the work hardening model assumes that the total dislocation density is approximately equal to the statistically stored dislocation density. This assumption is valid if the geometric slip distance λ_g is significantly larger than the slip distance for statistically stored dislocations λ_s. However, according to Ashby (1970), geometrically necessary dislocations begin to dominate if $\lambda_g < \lambda_s$ as measured from the length of the slip lines in work-hardened material. This becomes significant when (i) the recovery of statistically stored dislocations is great enough to increase λ_s approaching λ_g, and (ii) when microstructural effects at higher strains, such as the formation of dislocation cells, reduce λ_g. Using the Ashby approach, whereby it is assumed that the two dislocation densities can be added linearly in stress-strain space, their total contribution to the flow stress is given by the following equation:

$$\tau = \alpha\mu b\sqrt{\rho_s + \rho_g} \tag{6.15}$$

where

$$\rho_s = \frac{P}{A}\frac{\gamma}{\lambda b(2+\Omega\gamma)} \tag{6.16}$$

According to the definition proposed by Ashby (1970), geometric slip distance λ_g is characteristic of the microstructure as well as the type and distribution of hardening precipitates or particles in the material. In general, the density of geometrically necessary dislocations is related to the imposed shear strain and the slip distance λ_g through the relationship given as

$$\rho_g = \frac{\kappa}{b}\frac{\gamma}{\lambda_g} \tag{6.17}$$

where κ is a proportionality constant related to the microstructure geometry as well as the type and distribution of particles (Ashby, 1970).

Finally, the new flow rule follows from the substitution of equations (6.16) and (6.17) into (6.15):

$$\tau = \alpha\mu b\sqrt{\frac{\gamma}{\Lambda_s b(2+\Omega\gamma)} + \frac{\gamma}{\Lambda_g b}} \tag{6.18}$$

The capitalized Λ_s and Λ_g are material parameters related to the statistical and geometric slip distances such that $\frac{1}{\Lambda_s} = \frac{P}{A}\frac{1}{\lambda_s}$ and $\frac{1}{\Lambda_g} = \frac{\kappa}{\lambda_g}$.

It is noted that, work hardening does not explicitly account for time-rate dependence; however, this is considered in the determination of the recovery parameter discussed in the following section. The slip distance parameters will also have a rate dependence and a temperature dependence and is discussed in section 6.4.

6.3.1 Dynamic Recovery

It has been shown in many studies that FCC metals exhibit dynamic recovery – the dynamic annihilation of dislocations given sufficient dislocation density and thermal energy – at warm temperatures (Hirth & Lothe, 1967; Kocks, 1976; Gottstein, 2013). The mechanisms of dynamic recovery can be divided into (i) cross-slip and (ii) vacancy climb (Bergström & Hallen, 1982; Hallen, 1985). At low temperatures, well below ambient for aluminum, recovery is assumed to be assisted by the mechanism of cross-slip of screw dislocations. At ambient temperatures and above, the effects of cross-slip become nearly constant and can be considered athermal. However, vacancy climb dominates recovery at higher temperatures. A schematic of the effects of cross-slip and vacancy climb as mechanisms of recovery is presented in Figure 6-2.

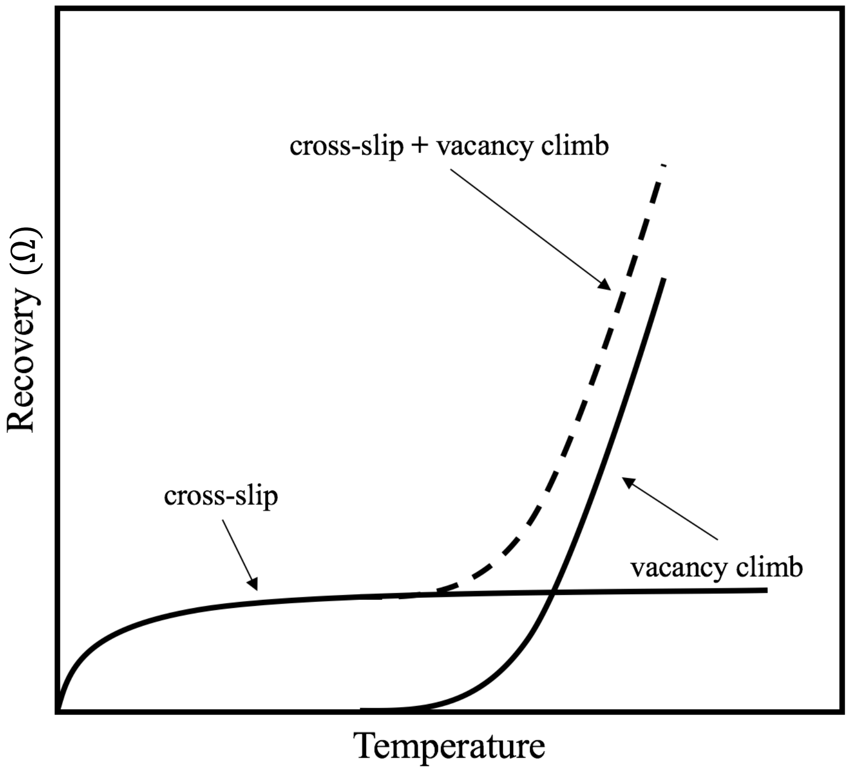

Figure 6-2 A schematic representation of recovery mechanisms in two components, at low temperatures recovery is assisted by cross-slip and at high temperatures recovery is dominated by vacancy climb.

Vacancy climb – or dislocation climb – may not significantly contribute to the deformation, but is an important mechanism in the recovery process (Kocks, 1976). Therefore, following Figure 6-2, it is reasonable to assume that dynamic recovery factor can be decomposed into two components as

$$\Omega = \Omega_0 + \Omega(\dot{\gamma}, T) \tag{6.17}$$

where Ω_0 is the athermal component and $\Omega(\dot{\gamma}, T)$ symbolizes a dynamic recovery factor dependent on strain rate $\dot{\gamma}$ and temperature T. In order to derive a theoretical expression for this dependence, a few assumptions must be made. Firstly, (i) the remobilization of sessile dislocations occurs primarily at dislocation cell walls where dislocation density is maximum. This is supported by high-powered electron microscopy studies (Bergrstöm, 1977; Gottstein, 2004; Mompiou et al., 2012). Following this, (ii) the remobilization mechanism is a result of vacancy climb of the sessile dislocations. This is favourable due to the supersaturation of vacancy sites quickly achieved during straining, and the exponential increase in vacancy mobility at elevated temperatures. (iii) During plastic deformation, these vacancies migrate to dislocation cell walls where they are absorbed, facilitating dislocation climb. Lastly, (iv) the diffusion of vacancies is governed by the Einstein relationship, such that:

$$\delta = \sqrt{2Dt} \tag{6.18}$$

where δ is the average distance moved by the vacancies during a time t, and D is the diffusion coefficient. By the assumption of vacancy supersaturation, the diffusion coefficient D can be defined by the Arrhenius relationship

$$D = D_0 \exp\left(-\frac{Q_m}{RT}\right) \tag{6.19}$$

where D_0 is a constant related to entropy of diffusion, Q_m is the energy of vacancy diffusion, R is the gas constant and T is absolute temperature.

Next we need a relationship for the number of vacancies that will reach the cell walls after some given time t, which will be denoted $\mathscr{N}$. This must be proportional to the density of vacancies n_0 and the average distance δ a vacancy has migrated after some time. Considering that a vacancy can approach the cell walls from either direction, the relationship can be written as

$$\mathscr{N} = 2n_0\delta = 2n_0\sqrt{2Dt} \tag{6.20}$$

According to the assumptions made previously, the remobilization of sessile dislocations in the cell walls is conducted via vacancy climb, therefore it is reasonable that recovery, or $\Omega(\dot{\gamma}, T)$, is proportional to the number of vacancies reaching the cell walls such that

$$\Omega(\dot{\gamma}, T) = \mathscr{K} n_0 \sqrt{2Dt} \tag{6.21}$$

with $\mathscr{K}$ representing a proportionality constant (including the factor of 2 from equation (6.20)).

Finally, we must determine an expression for the time dependence, t. If the average distance a vacancy travels in time t is given by equation (6.18), then an average time can be found for a dislocation to travel a distance δ. Therefore, we introduce the concept of average wait time, or the time between successive remobilizations of immobile dislocations. As recovery increases, it is expected that the mean wait time between these remobilizations will decrease. Letting $\bar{t}$ denote the average wait time, equation (6.21) can be rewritten as

$$\Omega(\dot{\gamma}, T) = \mathscr{K} n_0 \sqrt{2D\bar{t}} \tag{6.22}$$

Now let us assume, by differentiation of equation (6.11) with respect to time, that the rate of dislocation remobilization is

$$\frac{d\rho}{dt} = -\Omega\rho\dot{\gamma} \tag{6.23}$$

Assuming an initial dislocation content of the unstrained material as ρ_0, integration yields

$$\rho(t) = \rho_0\exp(-\Omega\dot{\gamma}t) \tag{6.24}$$

The average wait time of the immobile dislocations can now be determined by the following:

$$\bar{t} = \frac{\int_0^\infty t\rho(t)dt}{\int_0^\infty \rho(t)dt} = \frac{1}{\Omega\dot{\gamma}} \tag{6.25}$$

If we only consider thermal component of the total recovery, then $\bar{t}$ can be written as

$$\bar{t} = \frac{1}{\Omega(\dot{\gamma},T)\dot{\gamma}} \tag{6.26}$$

and can be inserted back into equation (6.22) yielding

$$\Omega(\dot{\gamma},T) = \mathscr{K}n_0\left(\frac{2D}{\Omega(\dot{\gamma},T)\dot{\gamma}}\right)^{1/2} \tag{6.27}$$

Lastly, solving for $\Omega(\dot{\gamma},T)$ and replacing D with its Arrhenius relationship gives

$$\begin{aligned}\Omega(\dot{\gamma},T) &= \left(\mathscr{K}n_0(2D_0)^{1/2}\right)^{2/3}\exp\left(-\frac{Q_m}{3RT}\right)\dot{\gamma}^{-1/3}\\ &= A_0\left(\frac{D_0}{\dot{\gamma}}\right)^{1/3}\exp\left(-\frac{Q_m}{3RT}\right)\end{aligned} \tag{6.28}$$

where A_0, which is proportional to $(\mathscr{K}n_0)^{2/3}$, is the only unknown parameter. The values of D_0, Q_m, and R are tabulated data, and temperature and strain rate are from experimental conditions.

6.3.2 Determination of hardening parameters

In the presented model, the material hardening depends on experimentally determined parameters relating to the evolving microstructure. Parameters λ_s, λ_g, $\frac{1}{\phi}$ and $\frac{P}{A}$ are initially assumed to behave independent of temperature and are calculated from room temperature experimental data. Recovery represented by Ω is determined according to the high-strain hardening behaviour at multiple temperatures to validate the temperature dependent equation (6.28). The procedure proposed to obtain these values is described in this section.

Firstly, stress-strain data is fit by a polynomial function (up to 5th or 6th order), and the value of σ_0 is first assumed as the zero-strain intercept of the polynomial function, as shown in Figure 6-3. From this, the flow shear stress $\tau = \dfrac{\sigma - \sigma_0}{M}$ versus the shear strain $\gamma = M\varepsilon$, where M is the Taylor factor such that $M = 3$ for this analysis, can be plotted.

The flow stress is related to the retained dislocation density ρ by the strength of obstacle parameter α, and therefore can be determined experimentally from the log(τ) vs. log(ρ) plot. However, the difficulty is measuring the retained dislocation density, whereby it is challenging to resolve dislocation density from other deformation debris (Saimoto, 2006). This leads to an under/over prediction of the dislocation content depending on the measuring method chosen (Schafler, 2005). However, an obstacle strength for aluminum of approximately 0.35-0.45 has been widely published (Hirth and Lothe, 1967; Saimoto, 2006; Park and Niewczas, 2008) and a value of 0.4 is assumed for this study.

For the determination of mean slip distance, it must first be assumed that under ideal conditions, during yielding the statistically-stored dislocation mean slip distance is equal to the interobstacle spacing, which is equal to the inverse root of retained dislocation density, i.e.

$$\lambda_s = \ell = \rho^{-1/2} \tag{6.29}$$

therefore, allowing the relation $\ell = \alpha\mu b/\tau$. From the experimental flow stress, the mean slip distance λ_s is then calculated by equation (6.3) and plotted. The slope of $d\tau/d\gamma$ is calculated as the instantaneous slope of the τ vs. γ polynomial. The value of $\dfrac{1}{\phi}$ is then optimized such that the curves of log(λ) and log(ℓ) plotted against log(τ) are equal for the lowest value of τ, as presented in Figure 6-3. For this analysis, the minimum value of λ_s is chosen as the characteristic mean slip distance. This has been hypothesized to correspond to the transitional point between stage II and stage III hardening (Saimoto and Van Houtte, 2011). The apparent transitional increase in mean slip distance is attributed to the formation of cellular structures and recovery mechanisms. In the cell interiors a lack of retained dislocation content increases the mean free path that dislocations can propagate before encountering an obstacle. However, the fact that activation work rather than a specific flow stress governs thermal activation allows this averaging procedure between cell walls and interiors, thus the mean slip distance can be approximated as a constant λ_{min}. This minimum slip distance is associated with the statistically-stored dislocations given that, at low strains, the relative slip distances are such that $\lambda_s \ll \lambda_g$.

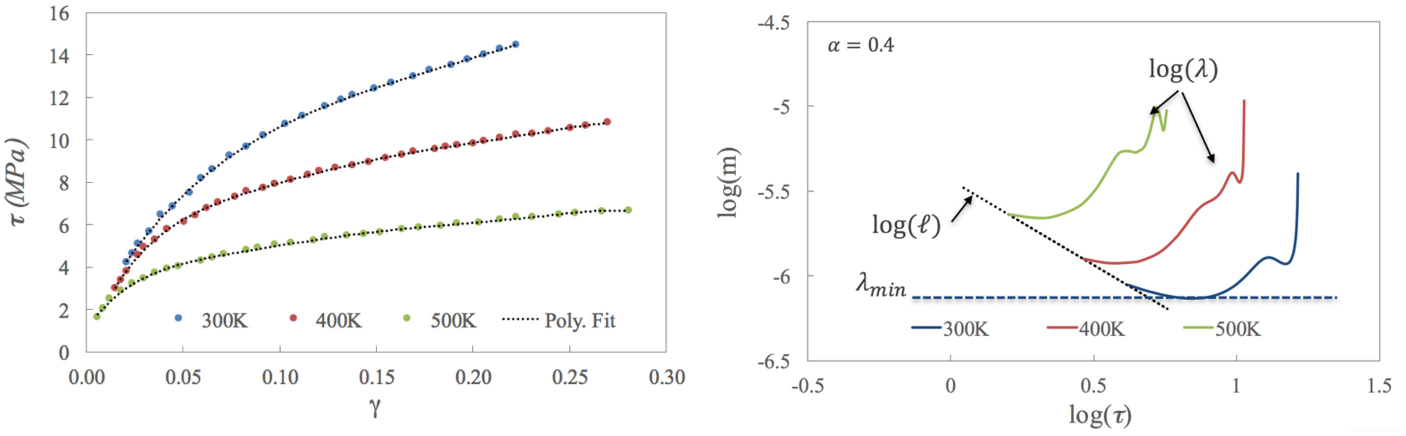

Figure 6-3 (left) polynomial fit to experimental stress-strain data of pure aluminum and (right) log(λ) and log(ℓ) jointly plotted vs. log(τ) with ϕ^{-1} adjusted to match log(λ) and log(ℓ) at low strains. The dotted tangent line depicts the minimum mean slip distance λ_{min}. The experimental stress-strain data is taken from Kocks (1976).

Finally, $\dfrac{P}{A}$ is determined by examination of the constitutive relations. Upon yielding, equation (6.3) can be integrated to the following form

$$\tau = \left(\frac{\phi}{\lambda_s} b\mu^2\gamma\right)^{1/2} \tag{6.30}$$

Equating this to the constitutive relation in equation (6.14) yields

$$\frac{\phi b\mu^2}{\lambda_s} = \frac{P}{A}\frac{(\alpha\mu b)^2}{\lambda_s b}\frac{1}{(2+\Omega\gamma)} \tag{6.31}$$

and the small strain assumption upon yielding allows $\Omega\gamma \ll 2$; therefore, the above relationship can be simplified to

$$\frac{P}{A} \approx \frac{2\phi}{\alpha^2} \tag{6.32}$$

Finally, the dynamic recovery Ω and mean slip distance parameter of geometrically-necessary dislocations Λ_g can be found by error minimization of the stress-strain plot. The recovery factor is first increased to match the curvature at the low-strain region of the curve. Subsequently, Λ_g is adjusted to match the high-strain stage III region of the stress-strain curve. Figure 6-4 demonstrates the effect of these parameters on the predicted shear stress-strain plot at room temperature. At $\Omega = 0$ the effects of recovery are removed and the curve over-predicts the strain hardening response upon sufficient dislocation accumulation at approximately 0.05 strain – a point related to the stage II-III transition. A recovery factor of $\Omega = 5.5$ provides the best fit to the experimental data at room temperature. Values of Λ_s and Λ_g are presented in Table 6-1.

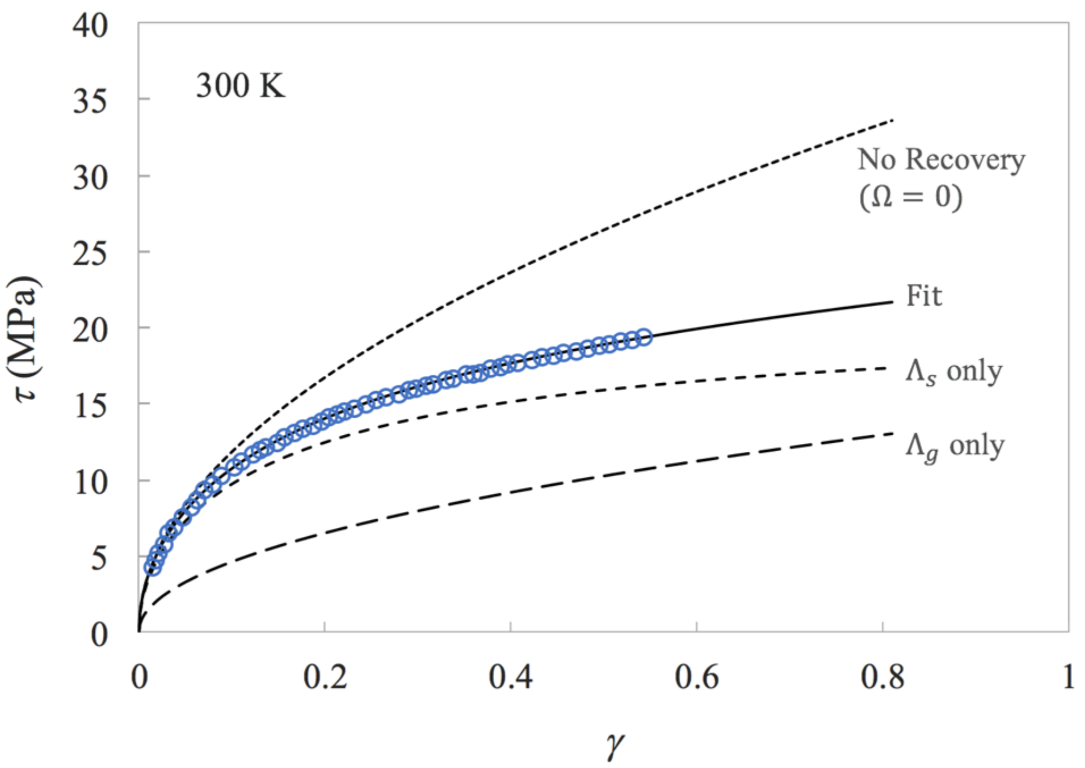

Figure 6-4 Fitted – curve (solid line) and its match with the experimental 99.99% pure aluminum data at 300K (Kocks 1976). The contribution of individual material hardening parameters and recovery is also presented as dashed lines. The geometric sum of the Λ_s and Λ_g curves produce the 'Fit' curve.

6.3.3 Elevated Temperature

Firstly, it must be considered that measured hardening parameters outlined in the previous section are temperature dependent. It has been shown experimentally that these material properties evolve with temperature, and strain (Niewczas et al., 2015). For obstacles of atomic dimensions, thermal activation of the dislocation is an important process. Foreman and Makin (1966, 1967) completed extensive research on dislocation movement through arrays of obstacles, including the effect of temperature. It was proposed that the stress required to propagate dislocations passed an obstacle decreased at an exponential rate with respect to temperature of the form

$$\left(\frac{\sigma}{\sigma_0}\right)^{\frac{2}{3}} = 1 - \left(\frac{T}{T_0}\right)^{\frac{p}{p+1}} \tag{6.33}$$

where σ_0 represents the strength at absolute zero and T_0 represents the temperature at which the stress to overcome an obstacle becomes vanishingly small, and p is a constant. This realization was attributed to the weakening line tension of dislocations; thus, the breaking angle to overcome the obstacle increases. It has also been proposed by Diak et al. (1998) that, particularly in aluminum, the dissolution of stacking fault tetrahedral at high temperatures – which act as strong obstacles – contributes to the above relationship. However, the consensus for aluminum has been that the obstacle strength parameter α undergoes negligible change with changing temperature, suggesting that the breaking angle to overcome obstacles is more or less constant (Diak et al. 1998; Saimoto 2006; Park and Niewczas 2008; Niewczas et al. 2015).

More difficult is statistical annihilation parameter and mean slip distance. It seems logical they would evolve with temperature and strain, as provided by equation (6.3); however, the interdependence of these parameters gives extreme difficulty in understanding the individual temperature and strain dependence. For instance, a variation in λ by fitting the geometric factor ϕ is balanced by $\frac{P}{A}$ from equation (6.32), and therefore the product of these terms is a constant. By analysis of equations (6.3) and (6.30)–(6.32), this product is directly proportional to $\tau\theta$ as:

$$\frac{P}{A}\frac{1}{\lambda} = \frac{4\tau\theta}{(\alpha\mu)^2 b} \tag{6.34}$$

where the minimum mean slip distance λ_{min} is synonymous with the maximum of the product of the flow stress and strain hardening rate $\tau\theta$.

Decades of research have been conducted on the understanding of the behaviour of dislocation propagation and mean slip distance (Taylor 1934; Cottrell and Stokes 1955; Basinski 1959; Foreman and Makin 1967; Louat 1978; Diak et al. 1998; Park and Niewczas 2008; Altintas 2011). What has been concluded is that, upon initial straining λ is nearly equal to the interobstacle spacing ℓ and increases during deformation to a length directly related to cell size. Many relations have been developed to represent this and the effects of temperature, with the most accepted presented in equation (6.3). The influence of temperature, however, is not well understood and thus far is inversely related to the flow stress and material hardening. It is expected that the product of $\frac{1}{A}$ and $\frac{1}{\lambda}$ decreases with increasing temperature. Saimoto (2006) showed that the increase in $\frac{1}{A}$ with debris formation following plastic strain is minimal, thus the strain dependence is ignored for this study. The mean slip distance λ is defined by its minimum (λ_{min}) and its strain dependence is implicitly strain dependent by the mechanism of recovery.

The overall effect of these parameters, following the assumptions and procedures outlined above, can be determined and each hardening parameter can be analyzed with respect to their individual temperature dependencies. The most pertinent is the correct determination of the three hardening parameters Λ_s, Λ_g and Ω ensuring an accurate depiction of temperature dependence. The method outlined in section 6.3.2 ensures that this is accomplished. Therefore, in the following section the model will be used to determine parameters Λ_s, Λ_g and Ω ranging from 200 to 600 Kelvin. Relationships between these parameters are discussed and presented graphically to present the temperature dependencies and the model's predictability.

6.4 Results

The analysis presented in this section is based on stress-strain data of 99.99% pure aluminum polycrystals by uniaxial tension deformation. The obtained experimental results are from the literature (Kocks 1976) for engineering stress and engineering strain in the normal direction and are digitized and converted to true stress and logarithmic strain. The data was then translated to reflect the averages of the shear flow stress τ and shear strain γ of all crystallites in a polycrystal through the Taylor factor. The calibration of simulation parameters, as described in section 6.3, is completed in this section for the pure aluminum at 100K temperature intervals from 200K to 600K. Pure aluminum was chosen due to the availability of data at multiple strain rates as well and the absence of alloying solutes and particles that contribute new hardening effects and can mask the true behaviour of the dislocation-dislocation interactions. In addition, the pure material is free of heat treatable particles, thus the observed thermal effects can be regarded as purely due to the behaviour of the dislocation obstacles and slip dominated deformation. It should also be noted that the grain boundaries will have an effect on the material strength; however, for this study the grain structure is of adequate size to ignore these effects.

6.4.1 Stress-Strain Calibration

By section 6.3, the hardening parameters are determined at 200K to 600K and presented in Table 6-1. The hardening parameters and their corresponding stress-strain curves are presented in Figure 6-5 along with the experimental data at a strain rate of $\dot{\varepsilon} = 1/min$. The obstacle strength parameter α is taken from literature data to be equal to 0.4 for all aluminum alloys at room temperature (Saimoto and Van Houtte, 2011) and its temperature dependence is assumed to be negligible in the chosen temperature range, as discussed by Kocks and Mecking (2003). This also corresponds to a constant approximation for $P = 0.2$ (see section 6.2). The experimental stress-strain data used for commercially pure (99.99%) aluminum is acquired from Kocks (1976).

The model captures the hardening behaviour very well, especially at high strain and high temperatures. At 200K, the experimental curve retains a very high hardening below shear strain $\gamma = 0.05$. This could indicate an exaggerated stage II-type hardening prolonged by lack of thermal motivation for stage III. Experimental stress-strain curves for low temperature aluminum presented by Jobba et al. (2015) also show a tendency towards a more linear hardening behaviour as the temperature is decreased below room temperature. This is motivated by two contributing factors: (i) low dislocation density and (ii) low thermal activation for vacancy climb. At sufficiently low temperatures and strain, the material recovery parameter becomes dependent on strain as well as temperature and strain-rate. Upon adequate dislocation accumulation, the dependency falls solely on temperature and strain rate. Near and above room temperature this is not observed, likely due to the added thermal energy facilitating the onset of dynamic recovery at very low strains.

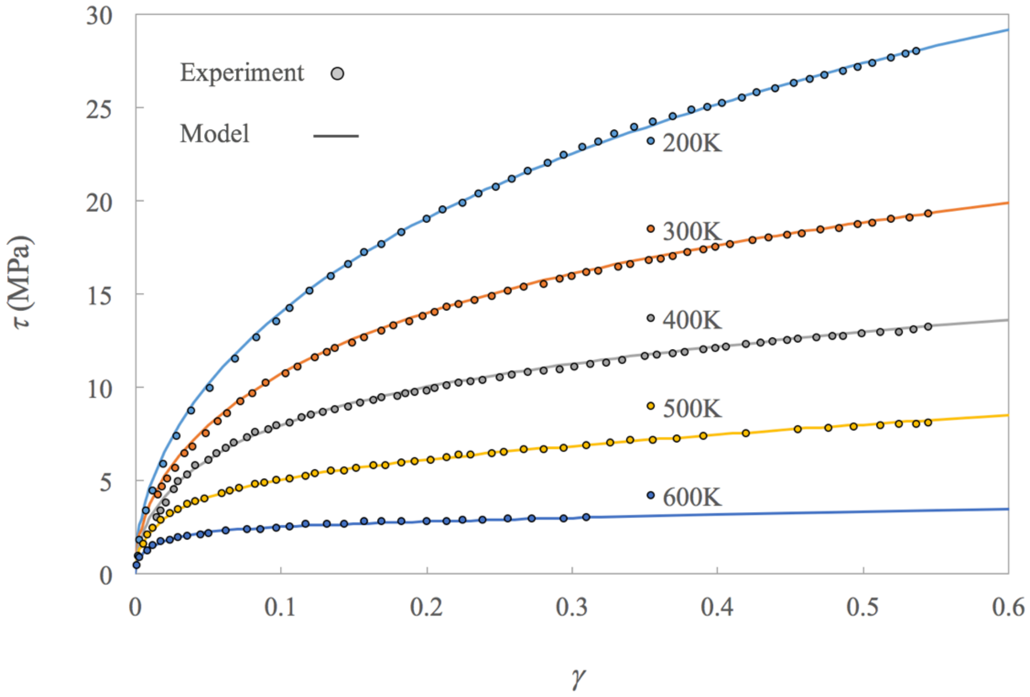

Figure 6-5 Experimental (points) and simulated (lines) $\tau - \gamma$ stress-strain curves at 200K to 600K for commercially pure aluminum ($\dot{\varepsilon} = 1/min$). Hardening parameters were determined by the method presented in section 6.3 and values presented in Table 6-1.

Table 6-1 Measured hardening parameters of 99.99% pure aluminum at 200K - 600K taken at strain rate of $\dot{\varepsilon} = 1/min$. The value for τ_0 was scaled with shear modulus $\mu(T)$ such that τ_0/μ is constant, as determined from Varshni (1970).

Alloy	***Temp.* (K)**	$\boldsymbol{\alpha}$	$\boldsymbol{\tau_0\ (MPa)}$	$\boldsymbol{\Lambda_s\ (\mu m)}$	$\boldsymbol{\Lambda_g (mm)}$	$\boldsymbol{\Omega}$
99.99% PURE ALUMINUM	200	0.4	0.1	14.8	0.450	2.5
	300	0.4	0.1	19.7	0.909	5.5
	400	0.4	0.096	28.3	1.330	11.5
	500	0.4	0.092	43.3	2.38	32.0
	600	0.4	0.087	75.6	15.4	75.0

6.4.2 Work Hardening

Essential features of the work hardening of polycrystals are: (i) a rapidly decreasing low-stress component affected strongly by initial microstructure, but upon some small amount of strain merges into (ii) a more linear decreasing section commonly known as stage III hardening followed by, permitting enough ductility, (iii) a saturated hardening level where a new stage IV is present. The concept of a stage IV was explained by Sevillano et al. (1980) as a constant hardening component of the stress-strain curve, but was later expanded to include further decrease in hardening by new hardening laws. Due to the low hardening levels of stage IV (typically $\theta < \tau$), it is troublesome to determine hardening mechanism that must compete with structural and geometrical instabilities. It has been proposed (Nabarro, 1989) that stage I defines a lower limit of strain hardening known as "easy glide" corresponding to a minimum dislocation storage due to the limited interaction of dislocations while only one slip system is active. In polycrystalline materials, this is overpowered by the high storage rate of multi-slip in stage II. It is supposedly observed in stage IV, however, that the minimum hardening corresponds to the level of stage I hardening, where the athermal storage of dislocations is effectively in balance with the dynamic recovery at the end of stage III.

The work hardening is determined by $d\tau/d\gamma$ of equation (6.15) given as,

$$\frac{d\tau}{d\gamma} = \alpha\mu b \frac{1}{2\sqrt{\rho_T}}\frac{d\rho_T}{d\gamma} \tag{6.35}$$

where $\rho_T = \rho_s + \rho_g$. In Figure 6-6, the normalized work hardening is plotted versus the shear stress for each generated stress-strain curve. For all temperatures above 200K, there appears to be an obvious transition in the hardening rate corresponding to a similar behaviour of stage II, III, and IV hardening. The transitional stresses exhibit an inverse relationship with temperature, which is driven by the rapidly decreasing work hardening at high temperatures. With the present model, it is difficult to determine a beginning of stage III hardening, so the representation of this zone drawn in Figure 6-6 by a dotted line is merely an estimate. However, the end of stage III is very pronounced at 300K and above by a sharp kink in the hardening curves. This can be attributed as a point of 'maximum recovery'. The warm temperatures between 300K and 500K appear to have similar saturated hardening that is very mildly dependent of temperature, but a significant decrease is observed at 600K. The hardening saturation largely depends on the microstructure evolution, which is captured by the model in Λ_g. A significant decrease in the stage IV hardening is suggested by the model that the microstructural properties that govern Λ_g (such as dislocation cells) begin to break down at this high temperature, allowing the geometric slip distance to grow such that the hardening behaviour in this regime becomes dominated by statistical storage and recovery. At the low temperature extreme, the opposite seems to be true. The effects of recovery are not well observed, however still present, and high hardening is due to the stable microstructural boundaries.

6.4.3 Dynamic Recovery

The expression dynamic recovery generally refers to a stage III process where there is a decrease in the hardening rate that is strongly dependent on temperature and strain rate. Presented in Figure 6-7 is the recovery factor Ω at the five fitted temperatures. To determine the value of material parameter A_0 from equation (6.28), these values are plotted vs. the exponential of the energy term, with $Q_m = 17{,}000\ cal \cdot mol^{-1}K^{-1}$ as provided by Hallén (1985) to provide a linear relationship with slope equal to $A_0\left(\frac{D_0}{\dot{\varepsilon}}\right)^{1/3}$ and intercept Ω_0. Here, the applied strain rate $\dot{\varepsilon}$ has been used for simplicity and it is assumed to be directly proportional to the shear strain rate by the Taylor factor.

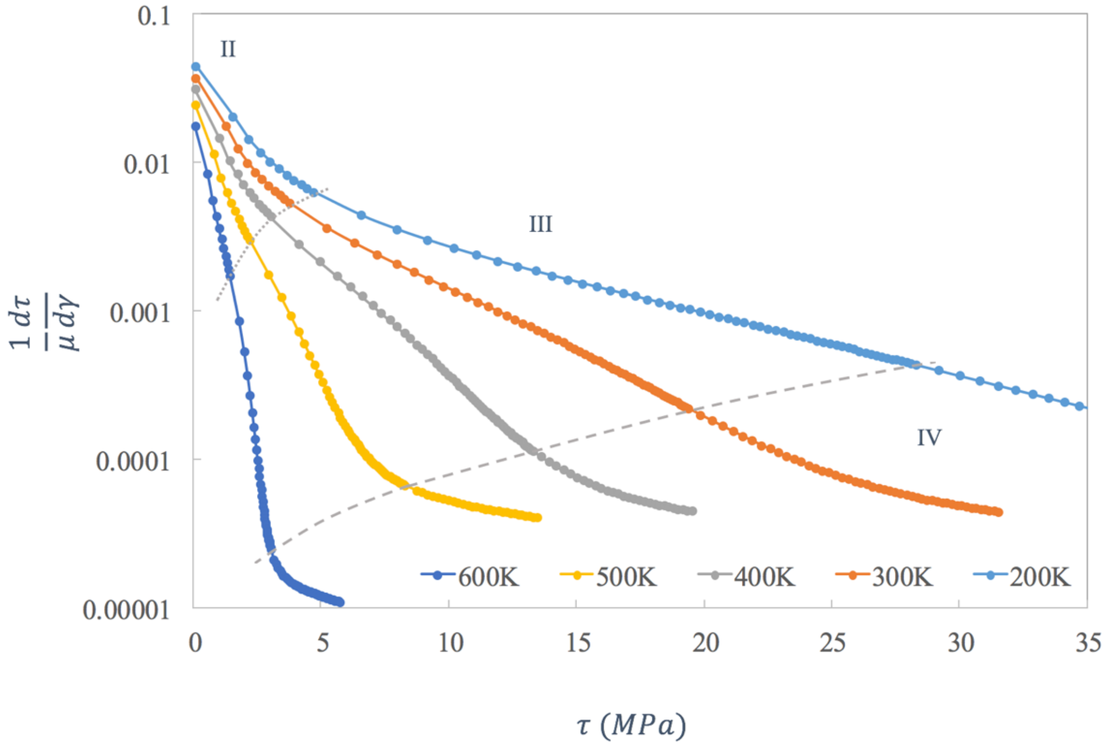

Figure 6-6 Work hardening versus flow stress of equation (6.35) at the five fitted temperatures. The work hardening is normalized by the temperature dependent shear modulus. The dotted line denotes an estimate of the τ_{III} transition from stage II to stage III. The dashed line represents the end of the experimental data with hardening extrapolated to show the model–predicted stage IV type hardening behaviour where the hardening plateaus.

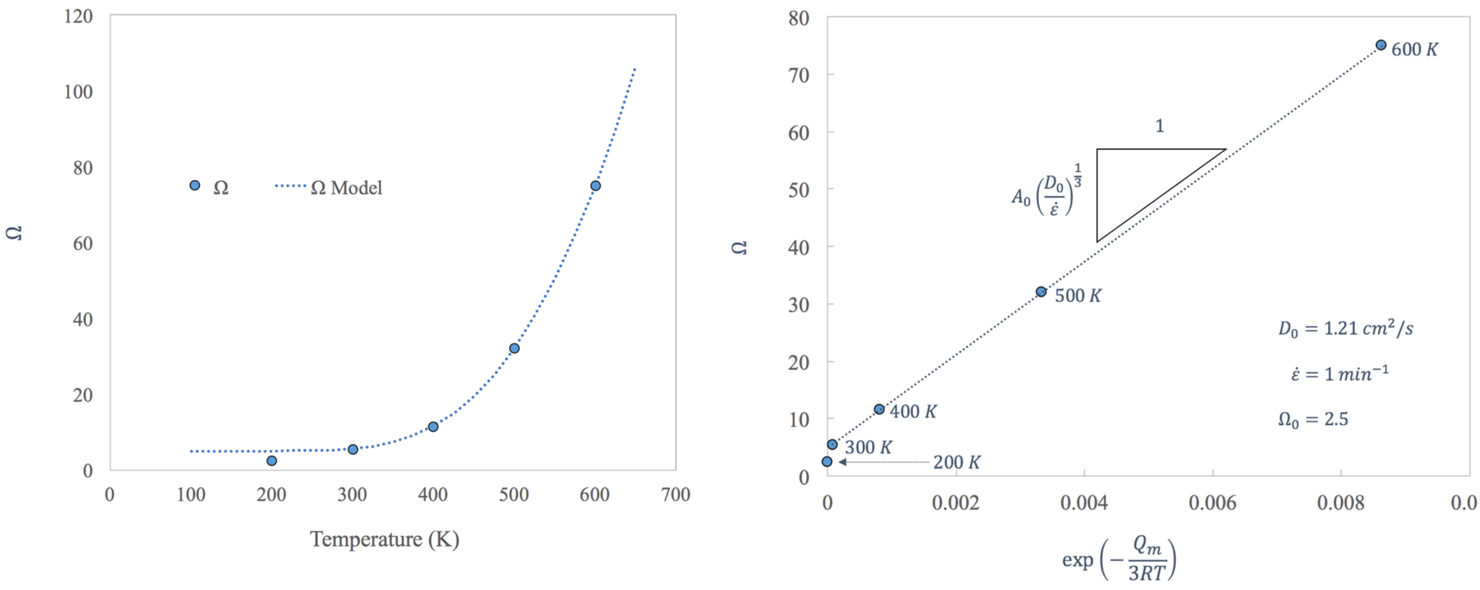

Figure 6-7 Presents (left) the dynamic recovery factor Ω vs. temperature for pure aluminum and equation (6.27) with parameters determined from fitting in (right), the dynamic recovery factor Ω plotted against $\exp\left(-\frac{Q_m}{3RT}\right)$ with, A_0 and Ω_0 determined from the linear fit.

The recovery parameters follow a very clear exponential relationship with material constants determined from a linear fit of Figure 6-7. The units for A_0 are determined from analysis of equation (6.28) and are related to the density of vacancies; thus, the recovery parameter Ω is a unit-less parameter. The value plotted for 200K is representative of the low temperature recovery mechanism of cross-slip as discussed in section 6.3.1. It is clear from the model that at this temperature, the thermal activation of the cross-slip mechanisms has a leading role in the recovery process, and recovery due to vacancy climb is nearly negligible. The dynamic recovery model presented does not consider the low temperature effect of cross-slip but assumes it to be a constant Ω_0. At extreme low temperatures the athermal Ω_0 becomes temperature dependent; however, Hallén (1985) showed experimentally that this effect is not observed in aluminum until below approximately 200K. Therefore, it is assumed that Ω_0 can be determined as the recovery factor measured at 200K.

Even if the model does not define the spatial distribution of dislocations, our physical picture that during straining dislocations are accumulated by storage processes in randomly distributed webs is very successful at predicting the data. The results presented are quite promising and show that a model for vacancy climb as the dominant mechanism for dynamic recovery is valid for a wide temperature range. This is important in predicting temperature dependent behaviour and ultimately warm forming behaviour where the material strength is significantly affected by material temperature and strain-rate.

6.4.4 Mean Slip Distance

For this study, the temperature dependence of the geometric-necessary and statistically-stored slip distance parameters Λ_g and Λ_s were investigated graphically. Systematically it was found that a linear relationship with temperature could be drawn with the inverse square-root of the slip distance parameter for statistically-stored dislocations, and simple the inverse of the slip distance parameter for the geometrically-necessary dislocation density. The difference in these dependencies is not known; however, it is suggested by the results that parameter Λ_s is related to the area swept by the statistically-stored dislocations. This would then allow the proposal that both types of dislocation slip distances, Λ_g and $\sqrt{\Lambda_s}$ hold the same inverse temperature dependencies. Figure 6-8 demonstrates this relationship, where the inverse of mean slip distance for both types decreases with increasing temperature. However, the value at 200K does not necessarily follow this pattern. This along with the presented findings for the dynamic recovery factor enhances the notion that different mechanisms inhibit the plastic flow below some low threshold temperature. Due to the relative magnitudes of the slip-distance parameters, the mean slip distance of geometric dislocations begins to dominate the behaviour at 200K, and this is shown as the rapid decrease in the geometric slip-distance parameter in Figure 6-8.

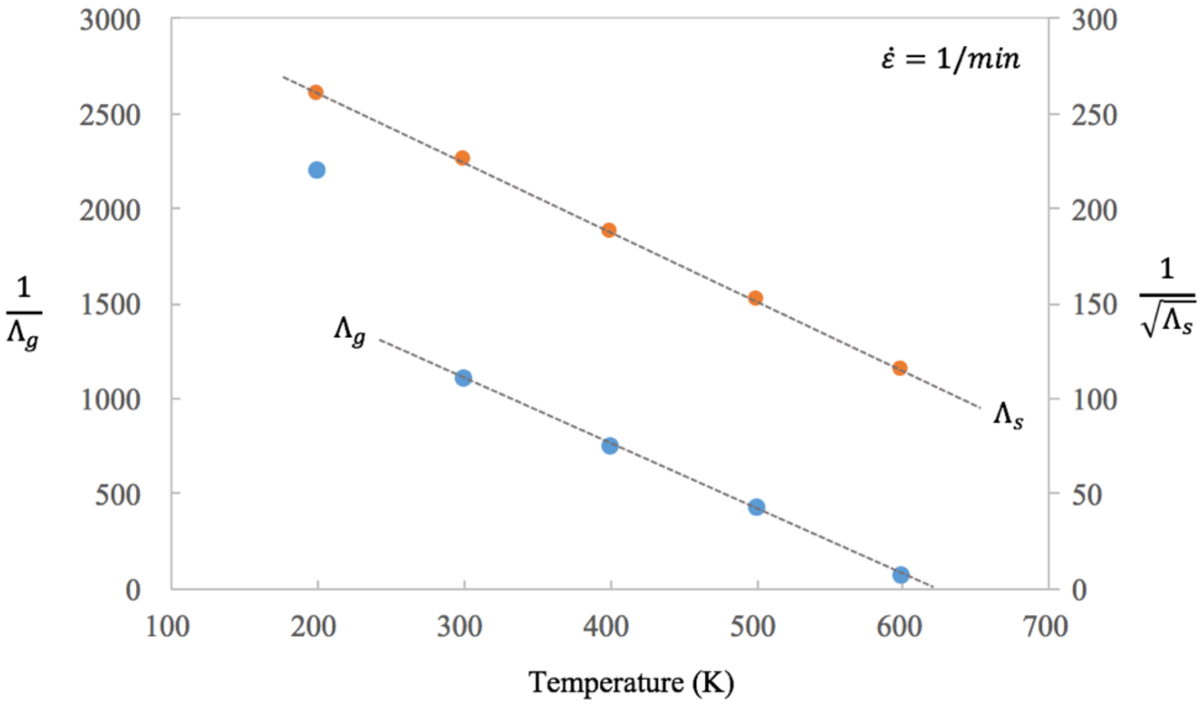

Figure 6-8 The linear dependencies of mean slip distance parameter and temperature at $\dot{\varepsilon} = 1/min$ are shown with blue (Λ_g) and orange (Λ_s) points representing the values determined from fitted data. The dotted lines highlight the linearity of the inverse square root of Λ_s and the inverse of Λ_g relationships with temperature. At 200K, the steep increase in $1/\Lambda_g$ alludes to a mechanism activation point, having significant effect on the geometric necessary dislocations.

It appears logical that a greater temperature dependency exists on the movement of statistically-stored dislocations. They are greatly affected by recovery, a thermodynamically motivated mechanism, and by dislocation theory are also dependent on the geometrically-necessary dislocation density (Ashby, 1970). However, the exact temperature dependence of mean free path of any type of dislocation is absent from the literature. There are many contributions to understanding and modeling dislocation mechanics with respect to microstructure and strain rate for a wide veriety of metals and alloys (Svendsen, 2002; Mianroodi et al., 2016; Terentyev et al., 2015), but the effect of temperature and thermal contributions directly affecting the movement, storage, and recovery in strain hardening has not been addressed. Even the descriptions of thermally activated glide of dislocations by Orowan (1940) and dislocation activation area by Kocks et al. (1975) along with the most widely accepted phenomenological description of thermally activated flow and strain hardening (Kocks and Mecking, 2003) do not present any findings or empirical theories on the activation of the slip distance with temperature. Therefore, only speculation on the mechanisms involved in these temperature dependencies can be made here.

6.4.5 Strain Rate Dependence

The explicit strain rate dependence is considered in the dynamic recovery formulation, as seen in equation (6.28). However, it must also be considered that, the mean slip distance parameters must also exude some rate dependence. The corollary between temperature and strain rate—whereby decreasing the deformation temperature will induce a similar behaviour as increasing the strain rate—also supports this. Since dislocation movement, recovery through vacancy climb, and annihilation are largely affected by thermodynamics, which is rate dependent itself due to diffusional processes, it is obvious that there must be rate dependence considered throughout. The uncertainty is predicting what the rate dependence should be for the mean slip distance parameters.

The simplest theory, is to assume a strain-rate dependence of the same distinction as with temperature. That is to assume that the inverse square-root of the statistically stored and inverse of geometric mean slip distance parameters behave in a linear fashion with strain-rate, as well as temperature. Due to diffusional considerations, it is also known that increasing strain-rate results in a decrease in mean slip distance of all dislocations. With this assumption, the results of increasing strain-rate should manifest as a linear translation of Figure 6-8 upward creating a second linear set of points parallel to the low strain-rate data.

As a final measure of the predictability of the recovery model, stress-strain responses for pure aluminum at $\dot{\varepsilon} = 100/min$ strain rate are simulated and compared with experimental data. Initially, a single temperature data set is required to fit the new strain rate and then all subsequent temperatures can be predicted by the model. This is completed in the following, with room temperature data as the calibrating set.

6.4.6 Model Validation

A validation of the model can be completed for a new data set at a new strain rate. For this study, the available data from the work of Kocks (1976) on work hardening of pure aluminum provides data for the currently calibrated $\dot{\varepsilon} = 1/min$ strain rate in uniaxial tension, and the higher strain rate $\dot{\varepsilon} = 100/min$ in uniaxial tension. Therefore, the data is consistent and it can be assumed that there are no effects of varying texture or microstructure between test samples.

For calibration of the model at a new strain rate, only one test needs to be completed to determine the mean slip distance parameters. The simplest test is at room temperature, or 300K. The hardening parameters are determined firstly at this temperature using the procedure outlined in the previous sections. In Figure 6-9 the calibrated $100/min$ slip distance parameters for Λ_s and Λ_g are shown as open points. The discussion in section 6.4.5 predicts that the corresponding points for elevated temperatures fall on the line parallel to the $1/min$ data and passing through this newly calibrated $100/min$ point. Two methods of verification can be employed: one where the elevated temperature parameters are measured and compared with expected results, the other is to predict these parameters from Figure 6-8 and compare the simulated and experimental stress-strain curves. The first method was chosen for convenience, and the results are presented for the mean slip distance parameters in Figure 6-9. The calibrated point at 300K is shown with a dotted line representing the expected values drawn parallel to the low strain-rate data. For both the geometrically-necessary and statistically-stored slip distance parameters, the results are a very good and match the prediction (dotted line) nearly exactly.

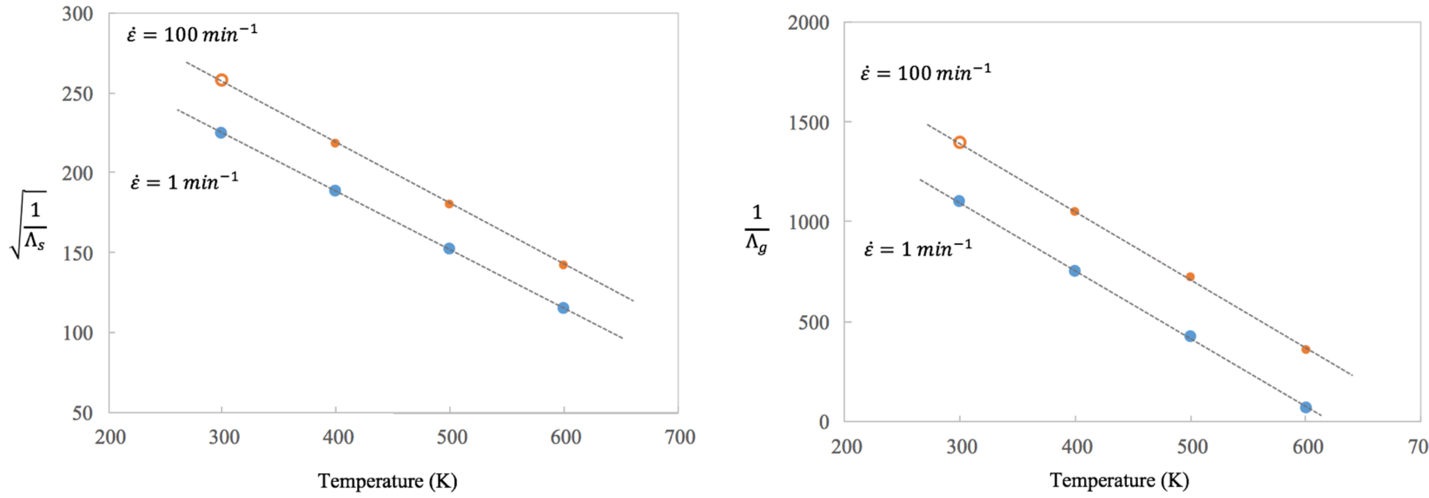

Figure 6-9 The vertical translation of slip distance parameters from $\dot{\varepsilon} = 1/min$ in blue (from Figure 6-8) to $\dot{\varepsilon} = 100/min$ in orange represents the strain-rate dependence of the mean slip distance parameters. In both cases, increasing the strain-rate results in an increase in the inverse slip distance—corresponding to a decrease in the mean slip distance of both statistically-stored and geometrically-necessary dislocation types.

The dynamic recovery factor, as with mean slip distance parameters, need only be calibrated one of two ways. The first through the theory outlined in section 6.3.1 and appropriately scaling previously measured low strain rate values to the higher strain rate. The second method requires two calibration points to determine the slope of the linear plot (Figure 6-10). The second method is simpler; however, it is ideal to have the ability to fit a new set of data with a single calibration. Given that the athermal recovery Ω_0 is constant with respect to temperature and strain rate, the recovery factor for other strain rates can be determined by solving equation (6.28) such that

$$\frac{\Omega(\dot{\gamma}_{100}, T) - \Omega_0}{\Omega(\dot{\gamma}_1, T) - \Omega_0} = \left(\frac{\dot{\gamma}_1}{\dot{\gamma}_{100}}\right)^{1/3} \tag{6.36}$$

For an increase in strain rate by 10^2, the approximate decrease in the thermal component of recovery factor due to vacancy climb $(\Omega - \Omega_0)$ is $10^{-2/3}$. The low temperature recovery mechanisms embodied in Ω_0 as cross-slip is assumed to be strain rate independent, especially in the temperature range studied. As shown in Figure 6-7, the recovery at 200K is assumed to be purely due to the low temperature cross-slip mechanism. Therefore, the measured value at 200K is taken to be $\Omega_0 = 2.5$. The one third exponent is derived from the determination of average time for a vacancy to remobilize an immobile dislocation, however, the data collected suggests a weaker strain rate dependence. An optimized fit reveals the rate sensitivity exponent to be equal to 1/5, which corresponds to the Nes and Marthinsen (2002) model for vacancy diffusion in courser grained pure FCC metals. Therefore, proper determination of the dynamic recovery factor can be given by

$$\Omega(\dot{\gamma}, T) = A_0 \left(\frac{D_0}{\dot{\gamma}}\right)^{1/5} \exp\left(-\frac{Q_m}{3RT}\right) \tag{6.37}$$

In Figure 10 the results for the measured (orange points) and expected decrease in recovery factor (dotted line) are presented. The relationship in equation (6.37) proves an accurate predictor of the recovery factor's rate sensitivity, as well as properly capturing the temperature dependence of moderate to high temperatures. It is interesting to note, possibly due to the low strength, that the increase in strain rate by a factor of 100 has nearly the same effect as decreasing the temperature by 100K. Similarly, the slip parameters Λ_s and Λ_g follow this trend. Physically, this suggests that the correspondence of temperature and strain rate are such that, for example, the deformation response is nearly identical between 400K at $\dot{\varepsilon} = 1/min$ and 500K at $\dot{\varepsilon} = 100/min$. This indeed does not consider the rate effects on fracture or damage and should not be mistaken as a suggestion that failure is also similar for these two conditions. This model is purely for deformation and does not consider any form of damage or other mechanisms leading to final failure or fracture.

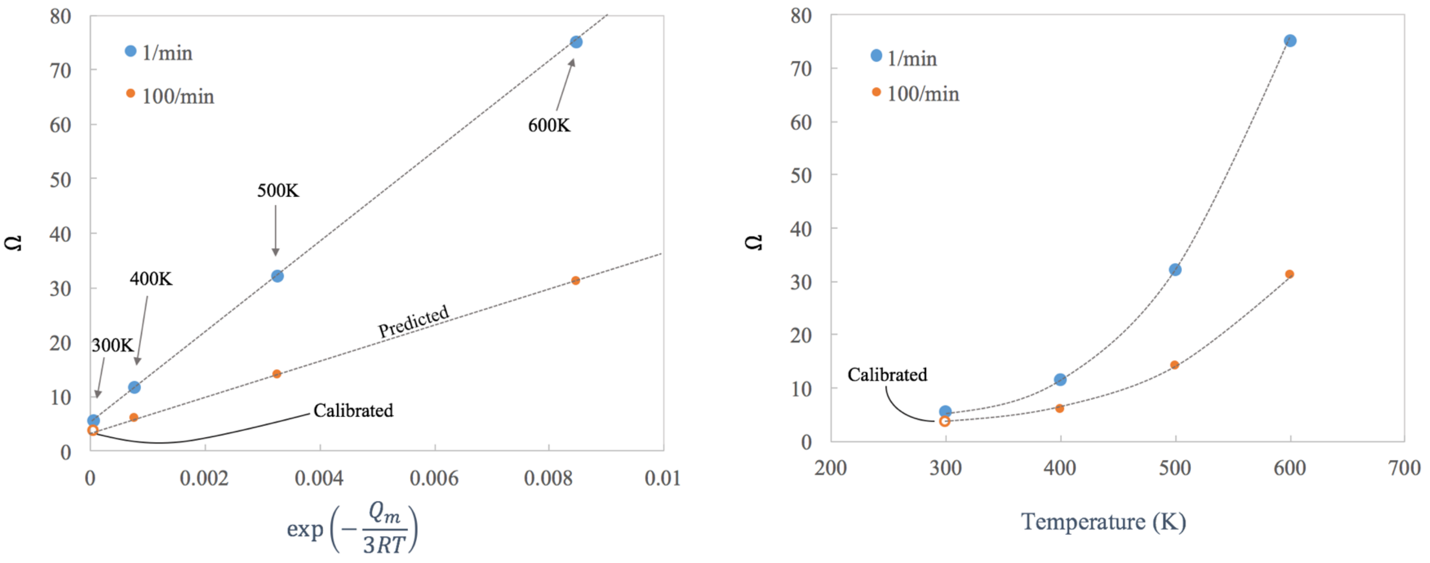

Figure 6-10 The measured low strain rate (blue) and predicted high strain rate (orange) dynamic recovery factors for pure aluminum between 300K and 600K. The open point represents the calibrated recovery factor used to determine the predicted values (dotted line) at higher temperatures. Although 200K is not shown, the recovery factor at both strain rates corresponds to the same $\Omega_0 = 2.5$.

Lastly, the predicted shear stress-strain curves for the three elevated temperatures and the calibrated room temperature are presented in Figure 6-11. The predictions are very good and reflect the capability of the given model. The basis of dislocation and recovery theories that are used to develop the model are fundamental to achieving this. The model also presents the significance of both dislocation types–statistical and geometric–on determining the stress-strain response. In Figure 6-11, the experimental data provided for 500K and 600K was only available to approximately 10% engineering strain, however, the simulation results nonetheless have been extrapolated beyond the experimental data to showcase the high strain hardening predictions.

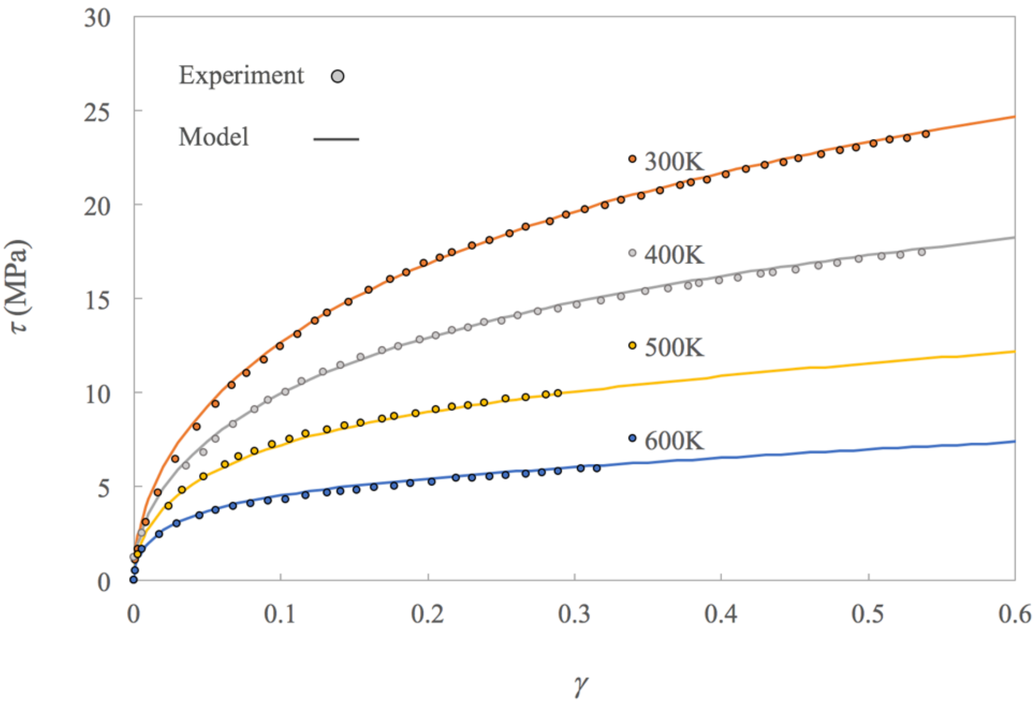

Figure 6-11 Predicted shear stress-strain curves for the four high strain rate ($\dot{\varepsilon} = 100/min$) and high temperature conditions corresponding to the material parameters shown in Figures 6-9 and 6-10. The 300K curve was calibrated to determine the high strain rate properties for the higher three temperatures. Experimental curves for 500K and 600K were only available to approximately 10% engineering strain.

6.5 Discussion

Another interesting outcome of this model, is the ability to study the interdependence of these internal variables. The most useful has been provided in Figure 6-11 as a plot between the inverse ratios of the mean slip distance parameters $1/\sqrt{\Lambda_s}$ and $1/\Lambda_g$. The plot shows that the slope relating these quantities remains a constant over the studied range of temperature *and* strain rate and manifests as a linear relationship. The data at 200K is not shown, however, as expected from Figure 6-8 the ratio does not hold for this low temperature. Again this provides further evidence that a thermally activated mechanism is likely made thermodynamically unavailable at this low temperature, and the mean slip distance corresponding to geometrical dislocations is dramatically decreased. The utility of Figure 6-12 is the predictive ability for determining one slip distance parameter, given its counterpart. The presented method can now provide a completely concrete method for determining hardening parameters, where the method to determine Λ_s is outlined in section 6.3 and Λ_g can be determined following Figure 6-12.

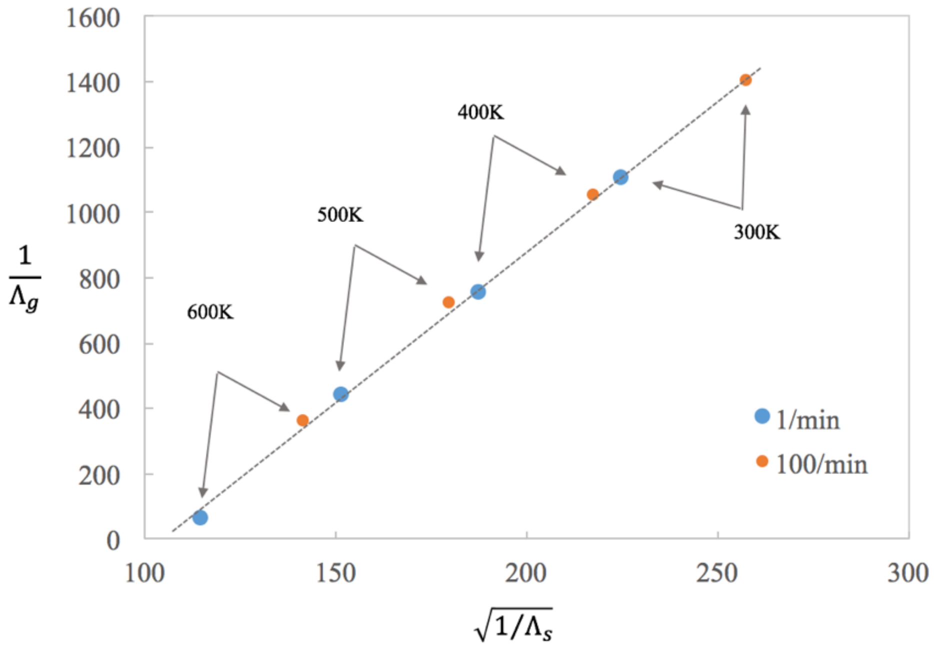

Figure 6-12 A plot of the inverse of geometric slip distance parameter versus the inverse root of statistical slip distance parameter. Both fitted ($\dot{\varepsilon} = 1/min$) and predicted $\dot{\varepsilon} = 100/min$ data points fall coincident with the dotted line, representing the constant ratio between these two parameters over the studied range of strain rates and temperatures. The utility of this diagram is the precise determination of the Λ_g parameter upon measuring Λ_s by the method outlined in section 6-3.

It has been accepted for decades that the statistically-stored dislocation content is dependent on geometrically-necessary dislocation accumulation as well as temperature and strain-rate (Ashby, 1970). Thusly, the relationship between the two slip distance parameters can be expected. In addition to this, the model also predicts the experimentally observed behaviour of the dislocation cellular structure with temperature and strain. This is an important mechanism that can influence a number of material properties from crack propagation to creep reduction. It is known that; (i) larger cells form at higher deformation temperatures and smaller cells at higher strains, (ii) the cell walls are comprised of dislocation tangles, where the dislocation density in the cell walls has been reported to be up to five times the average dislocation density, and (iii) cells formed at higher temperatures are more distinct—with thinner, well defined cell walls—than cells formed at lower temperatures (Staker and Holt, 1972; Thompson, 1977).

The model presented here is developed on the basis that the statistically stored-dislocations annihilate via dynamic recovery at the cell walls, and that the geometrically-necessary dislocations travel through the cell interior, accumulating at the cell walls, to accommodate shape change of the material. Therefore, the mean slip distance of the statistically-stored dislocations should be representative of an average dislocation density and always be less than the slip distance of geometrically-necessary dislocations, which is dependent on the cell size. During straining, simultaneous accumulation and recovery at the cell walls eventually reaches an equilibrium, whereby the cell walls remain at a relatively constant thickness. At low temperatures, this equilibrium may never be reached before failure, while at high temperatures this equilibrium state becomes evident.

Figure 6-13 represents this very well by plotting the stress from individual dislocation contributions. The form of the model affords the ability to distinguish the individual contributions of statistically-stored and geometrically-necessary dislocations, which—in nearly every modeling or experimental method—is either extremely arduous or impossible. This, however, is easily accomplished with the proposed model. At 300K, the stress due to statistically stored dislocations continuously increases, while at 500K a plateau is reached by $\gamma = 0.2$. The geometric component, at both temperatures, continues to grow indicating that the cell size of the substructure continues to increase with increasing strain. If the temperature increases further, Figure 6-12 predicts that the geometric slip-distance parameter will be infinitely large, which seems unrealistic unless this extreme growth in Λ_g represents a complete instability in the cellular substructure. In other terms, upon sufficient thermal energy, cell structures may no longer be stable and therefore no cellular substructure is developed to impede further propagation of moving dislocations. These predictions correspond with the so called "hot deformation" regime, where new mechanisms become prevalent, such as dynamic recrystallization.

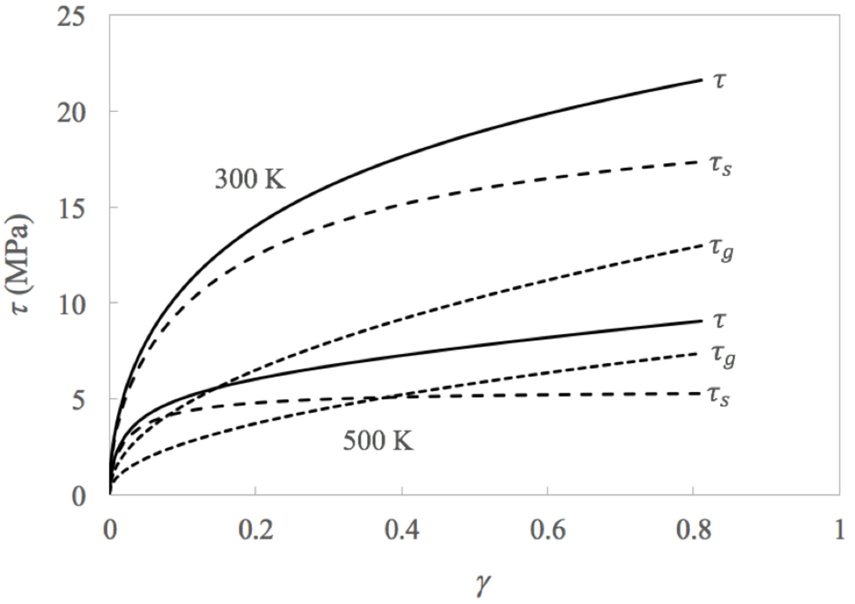

Figure 6-13 shows the individual contributions of the statistically-stored and geometrically-necessary dislocations according to the model. The plateau behaviour of the statistically-stored contribution represents an equilibrium between dislocation storage and recovery, and occurs at lower strains with increasing temperature. Solid black curves correspond to the fitted curves for 300K and 500K at $\dot{\varepsilon} = 1/min$ and hardening parameters shown in Figures 6-9 and 6-10.

For completeness, the sensitivity of each of the material slip distance parameters Λ_s and Λ_g and the dynamic recovery factor Ω is presented in the following. The plots in Figure 6-14 each show two solid curves representing the fitted data at 300K and 500K and strain rate $\dot{\varepsilon} = 1/min$. Each curve then has two dashed curves representing the marginal change in the parameter of interest. The degree in variation was arbitrarily determined to show similar variation at an arbitrary shear strain $\gamma = 0.8$. The slip distance parameter Λ_s has the greatest effect during the low strain region of the stress-strain curve, while the geometric slip distance parameter Λ_g gradually increases and is most noticeable at high strains. This further expresses the plateau effect of the statistically-stored dislocations, where the Λ_s has little effect on the material hardening at high strains. The Λ_g parameter, however, has a significant effect on hardening at high strains due to the strain dependence on the growth of dislocation cells.

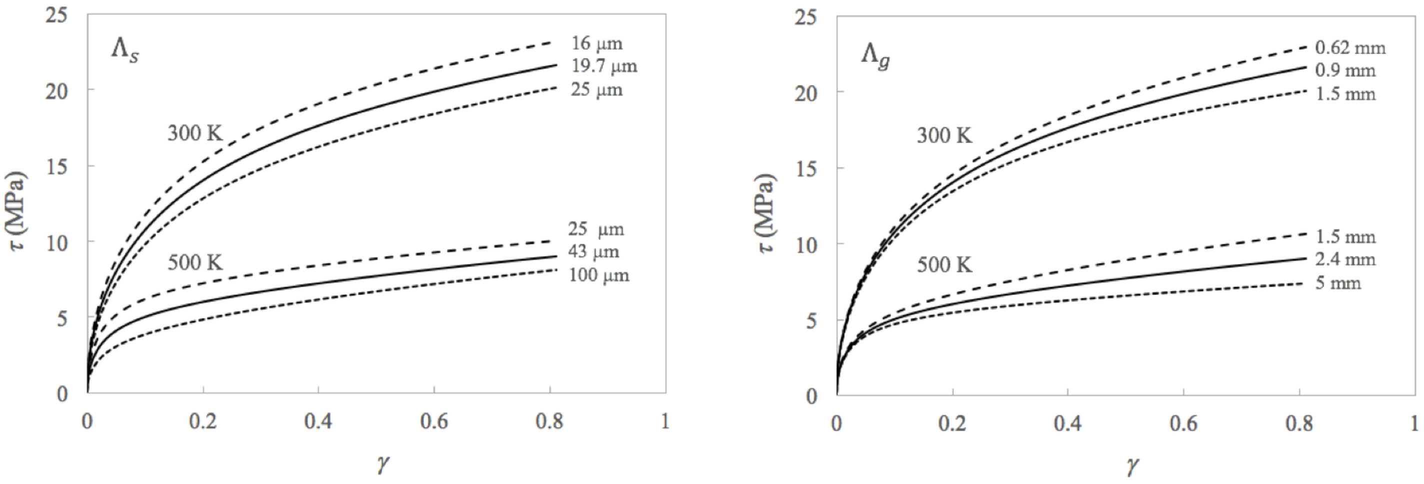

Figure 6-14 The plots show the sensitivity of the material hardening parameters Λ_s (left) and Λ_g (right) with values denoted at the end of each curve and all other parameters held constant. Solid black curves correspond to the fitted curves for 300K and 500K at $\dot{\varepsilon} = 1/min$ and hardening parameters shown in Figures 6-9 and 6-10.

Finally, Figure 6-15 shows the effect of the dynamic recovery factor Ω. At room temperature, the stress-strain response is highly sensitive due to the high rate of dislocation storage, while at the higher 500K simulation temperature the sensitive decreases dramatically due to the exponential behaviour with temperature. Since the recovery acts on the statistically-stored dislocations, the initial deviation reaches an apparent plateau and begins to approach parallel to the fitted curve. This is similar to the behaviour of the Λ_s parameter above, where dislocation accumulation and recovery reach an equilibrium and no longer contribute to the material strain hardening. This is most noticeable for the higher temperature simulation.

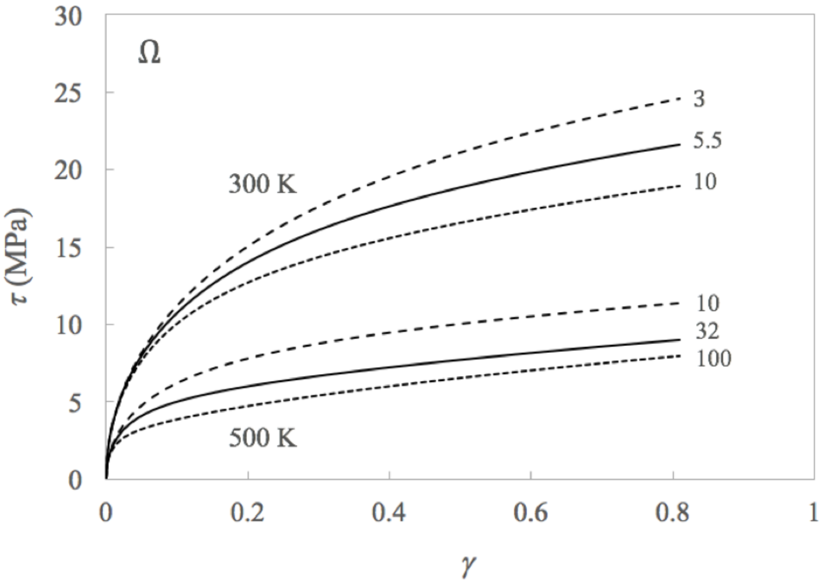

Figure 6-15 Relationship between flow stress and the recovery factor Ω sensitivity with values for recovery denoted at the end of each curve and all other parameters held constant. Solid black curves correspond to the fitted curves for 300K and 500K at $\dot{\varepsilon} = 1/min$ and hardening parameters shown in Figures 6-9 and 6-10.

6.6 Conclusions

In this study, a physical and mechanistic theory is derived based on the thermodynamic and mechanical balance between dislocation storage, accumulation, annihilation and recovery for a polycrystalline material. The theory is then developed into a new constitutive model and hardening law for simulating flow stress. The temperature and strain-rate dependence of hardening parameters embedded in the theory and have been calibrated and presented with experimental data. The temperature dependence of the hardening behaviour can be summarized by three important material parameters: mean slip distance of statistically-stored Λ_s, and geometrically-necessary Λ_g, dislocations and the dynamic recovery factor Ω. The following was concluded from the study:

- The material hardening parameters can be measured directly from the experimental stress-strain curves with the exception of the dynamic recovery factor which must be calibrated.
- The model can predict very well the stress-strain response of a large range of temperatures and at least of intermediate strain rates of $\dot{\varepsilon} = 1/min$ and $\dot{\varepsilon} = 100/min$.
- Dynamic recovery can be predicted from an Arrhenius-type relationship for the remobilization of immobile dislocation by vacancy climb and is temperature and strain-rate dependent.
- The contributions of the material hardening parameters as well as contributions of statistically stored and geometrically necessary dislocation densities can be extracted individually and easily using the model.
- Analysis of the temperature dependence of mean slip distance parameters show graphically an inverse square root proportionality of Λ_s and an inverse proportionality of Λ_g that is consistent at different intermediate strain rates. In addition, the proportionality of these two slip parameters is also constant for all studied warm temperatures and strain rates allowing for the prediction of one parameter given the other.

Chapter 7

Part IV: Temperature-Dependent Plasticity: A New Constitutive Formulation using Crystal Plasticity for 5xxx Series Al-Mg Aluminum Alloys

Edward D. Cyr[1], Abhijit Brahme[1], Raj K. Mishra[2], Kaan Inal[1]

[1] Department of Mechanical and Mechatronics Engineering, University of Waterloo, Waterloo ON, Canada, N2L 3G1

[2] General Motors Research & Development Center, Warren MI, 48090, USA

Abstract

Many models have been developed on the deformation phenomena of metals during high temperature forming, however none have fully integrated thermodynamic formulations based on deformation mechanisms, especially for crystal plasticity. This work presents a crystal plasticity based analysis with a Taylor polycrystal averaging scheme of warm forming employing a new microstructure and dislocation based strain hardening model (chapter 6) to simulate deformation behaviour or polycrystal Al-Mg aluminum alloys 5754 and 5182 at elevated temperatures. The hardening model is derived from and energy balance between dislocation storage, dislocation accumulation, and dislocation recovery due to thermal activation. Recovery is based on the mechanism of remobilization of immobile dislocations through vacancy climb. The constitutive formulation is also extended to include alloying effects due to solute strengthening of Mg. The material hardening properties of AA5754 sheet are characterized for a range of temperatures from 25ºC to 260ºC at constant strain rates using experimental data obtained from literature. A formulation for the kinematics of dynamic strain aging is presented and employed for room temperature simulations. The hardening characterization is then used to predict stress-strain behaviour of 5182 sheet over the same temperature range and strain rate. The model shows excellent predictability of experimental results. An analysis on the microstructural connection between temperature and stress-strain response is presented. The effects of temperature on model parameters is also discussed.

Keywords: *Crystal Plasticity, Dislocation, Recovery, Temperature, Dynamic Annihilation*

7.1 Introduction

For decades, mass reduction has been a priority in the automotive sector for improving fuel economy (Green & DiCicco, 2000). Many manufacturers have opted for substituting lightweighting aluminum alloys for typical steel applications. An application of particular interest in this study is the use of 5xxx series aluminum-magnesium sheet alloys in panel components. The difficulty with aluminum sheet, in the replacement of panel components, is the lower formability at room temperatures than in steels (Ayres & Wenner, 1979). In addition, surface quality of formed parts at room temperature is undesirable due to the Lüder's lines and serrated flow behaviour of Al-Mg sheet alloys (dynamic strain aging/PLC effect) (Robinson & Shaw, 1994). However, poor formability and surface finish can be greatly improved by warm forming (Li & Ghosh, 2003) without expensive production costs of refining microstructure to achieve the same outcome. The elevated temperature corresponds to a decreased flow stress and increased ductility of the sheet, which can allow deep drawing and stretch in panels competitive with steels without design modifications. The understanding of high temperature deformation behaviour for warm forming and the constitutive relations describing the material flow are two of the fundamental prerequisites for the implementation of forming technology in industry.

Available research for simulation of warm forming processes focuses only on the effect of elevated temperature on the evolution of the flow stress or hardening (Li & Gosh, 2003; Takata et al., 2000; Naka et al., 2001; Boogaard et al., 2001), rather than the the effect of elevated temperature on microstructural parameters that lead to this behaviour. Confidence in numerical analysis of plasticity of materials depends greatly on the accuracy of the constitutive model describing the behaviour of the material (Chung & Shah, 1992). This is of particular importance when the material exhibits anisotropy, such as rolled sheets. The importance of an appropriate material model for predicting even simple monotonic loading strain paths has been demonstrated (Brahme et al., 2011).

The flow stress is the most basic measure for characterizing plastic deformation properties of metals and provides a means to determine the energy required to plastically deform a material. The material then dissipates this energy while undergoing plastic flow by the mechanisms of deformation, which can be evaluated with the aid of governing constitutive equations. The improvement of these constitutive models over recent decades have given rise to an incredible understanding of material behaviour on a fundamental level; however, in many cases at the expense of great complexity and subsequently increased difficulty in application.

Crystal plasticity has been successfully used in modeling non-homogeneous mechanical behaviour and has been applied extensively to study both heterogeneous plastic deformation and texture evolution (Roters et al. 2010). The collectives of crystal plasticity with the finite element method (CPFEM) and Taylor polycrystal analysis have proven a very powerful tool for the investigation of such plastic phenomena as the Bauschinger effect (Kim et al., 2012), formability (Wu et al., 1997; Inal et al., 2005; Mohammadi et al., 2014), cyclic loading (Muhammad et al., 2015; Grilli et al., 2015), surface effects (Rossiter et al., 2013), texture evolution (Popova et al., 2015; Knezevic et al., 2013) and high rate deformation (Clayton, 2005), to list a few. However, little physical information is directly involved in the well-established crystal plasticity models as both the flow rule and hardening laws are phenomenological fits to the resolved strain rate by simple power law type expressions, or require complex calculations of strain gradients to predict dislocation contents (Gerken & Dawson, 2008; Elkhodary & Bakr, 2015). The material hardening, however, has not been linked to physical processes. Phenomenological models are satisfactory for the intended use of room temperature deformation, but are unable to predict material properties from experimental data or their temperature and strain dependence. It is essential for the investigation of complex deformation features during forming, such as temperature dependent and geometric softening, strain localization, and microstructure evolution, etc., that the material hardening models be derived from physical deformation mechanics.

Mechanisms, such as dynamic recovery (DRV) often occur in aluminum alloys with high-stacking fault energies during warm forming. Reports on the high-temperature deformation behaviour of aluminum alloys have shown that the mechanisms contributing to softening, recovery, and microstructure evolution are not well known and highly sensitive to temperature and strain-rate (Abedrabbro et al., 2007; Pandey et al., 2013; Ezatpour et al., 2014) and the determination of these effects has been a topic of discussion for decades (Argon, 1968; Kocks et al., 1975; Kocks, 1976, 2001; Kocks & Mecking, 1976, 2003).

In this work, a crystal plasticity based analysis with a Taylor polycrystal averaging scheme of warm forming employing a new microstructure and dislocation based strain hardening model (Cyr et al. 2016) to simulate deformation behaviour or polycrystal Al-Mg aluminum alloys 5754 and 5182 at elevated temperatures is presented. The material hardening properties of AA5754 sheet are characterized for a range of temperatures from 25ºC to 260ºC at constant strain rates using experimental data obtained from literature. The available experimental data was reported to be at constant low strain rate such that thermal straining effects can be neglected. A kinematic formulation to capture dynamic strain aging at room temperature is also implemented to accurately represent the temperature dependency of the material hardening. Finally, The hardening characterization is used to predict stress-strain behaviour of 5182 sheet over the same temperature range and strain rate.

7.2 Constitutive Relations

The well-known framework presented by Asaro and Needleman (1983) and reformulated by Cyr et al. (2015) to include thermal effects is employed in this research. The crystal plasticity framework can be condensed to a relationship used to update the shear rate on each slip system, denoted by $\dot{\gamma}_\alpha$, based on the currently resolved shear stress τ_α on the slip system α. Details of the single crystal constitutive model employed can be found in Inal et al. (2002) and Cyr et al. (2015). For completeness, a brief summary is presented in the following.

The total deformation is assumed to exist in three parts; (i) elastic part due to lattice distortion (including rigid rotation), (ii) thermal part due to expansion/contraction of the lattice, and (iii) plastic part as a result of dislocation motion and crystallographic slip. The numerical model incorporates 12 distinct slip systems for face-centered cubic (FCC) materials as principal deformation mechanisms. The elastic constitutive equation is written as:

$$\overset{\nabla}{\sigma}_{ij} = \mathbf{L}_{ijkl} D_{kl} - \dot{\sigma}^{0}_{ij} - \sigma_{ij} D_{kk} \tag{7.1}$$

where $\overset{\nabla}{\sigma}_{ij}$ is the Jaumann rate of Cauchy stress, $\mathbf{L}_{ijkl}$ is the elastic modulus tensor, D_{kl} is the strain rate tensor, and $\dot{\sigma}^{0}_{ij}$ is the viscoplastic-type stress rate, which depends on the slip rates.

7.2.1 Kinetics of Slip

The rate-dependent equation for single-slip shear rates is governed by the power law expression defined as,

$$\dot{\gamma}^{\alpha} = \dot{\gamma}_0 \mathrm{sgn}(\tau^{\alpha}) \left| \frac{\tau^{\alpha}}{\tau^{\alpha}_{y}} \right|^{\frac{1}{m}} \tag{7.2}$$

where $\dot{\gamma}_0$ is the reference shear rate assumed constant for all slip systems, τ_{α} is the resolved shear stress on slip system α, and τ^{α}_{y} is the temperature dependent slip system strength. The term $\mathbf{sgn}(\tau^{\alpha})$ denotes the sign of the resolved shear stress. Exponent $\frac{1}{m}$ is not to reflect physical behaviour of a rate sensitivity, but to conveniently ensure uniqueness of slip activity, which is spread over all available slip systems. The rate of strain hardening of the crystal evolves by,

$$\dot{\tau}^{\alpha}_{y} = \sum_{\beta} h_{\alpha\beta} \left| \dot{\gamma}^{\alpha} \right| \tag{7.3}$$

where $\dot{\tau}^{\alpha}_{y}$ is the single slip hardening rate. The hardening moduli tensor $h_{\alpha\beta}$ depends on deformation history and accumulated slip and is written as,

$$h_{\alpha\beta} = q_{\alpha\beta} h_{\beta} \qquad \text{(no sum on } \beta\text{)} \tag{7.4}$$

Here $h_{\beta} = h_{\beta}(T)$ is a temperature dependent single slip hardening rate, and $q_{\alpha\beta}$ is the matrix describing the latent hardening behaviour. Asaro and Needleman (1985) considered the current hardness to evolve with total accumulated shear γ_a in the crystal such that,

$$\gamma_a = \int_0^t \sum_{\alpha} \left| \dot{\gamma}^{\alpha} \right| dt \tag{7.5}$$

7.2.2 Material Hardening

The hardening rate is derived from the flow rule equations developed by Cyr et al. 2016 and modified to include strengthening effects from solute Mg written as,

$$\tau = \alpha \mu b \sqrt{\rho_s + \rho_g + \rho_{Mg}}. \tag{7.6}$$

The statistically-stored and geometrically-necessary dislocation densities ρ_s and ρ_g are determined from their respective slip distance parameters Λ_s and Λ_g such that,

$$\rho_s = \frac{\gamma_a}{\Lambda_s b(2 + \Omega\gamma_a)} \tag{7.7}$$

$$\rho_g = \frac{4\gamma_a}{\Lambda_g b}. \tag{7.8}$$

The term ρ_{Mg} denotes the increase in stored dislocation content and material strength due to the addition of magnesium solute atoms as obstacles. In a similar manner that ρ_s and ρ_g have been related to the associated slip distance of dislocations, it is assumed that ρ_{Mg} will also exude a proportionality with the slip distance of dislocations impeded by solute atoms. The assumption is also made that this new slip distance parameter Λ_{Mg}, which is proportional to ρ_{Mg}^{-1}, does not evolve with strain and is directly related to microstructure. Therefore, increasing the concentration of solute Mg in the material will decrease the slip parameter; however, thermo-mechanical processing that alters the dispersion of solute atoms will affect the effective slip-distance. Finally, equation (7.6) can be re-written in terms of mean slip parameters as

$$\tau = \alpha\mu b\sqrt{\frac{\gamma_a}{\Lambda_s b(2 + \Omega\gamma_a)} + \frac{4\gamma_a}{\Lambda_g b} + \frac{1}{\Lambda_{Mg} b}} \tag{7.9}$$

where $\rho_{Mg} = (\Lambda_{Mg} b)^{-1}$.

Dynamic recovery factor Ω, derived from the remobilization of sessile dislocations by vacancy climb, follows an Arrhenius-type temperature dependency as

$$\Omega = \Omega_0 + A_0\left(\frac{\dot{\varepsilon}}{D_0}\right)^{1/5} \exp\left(-\frac{Q_m}{3RT}\right) \tag{7.10}$$

Here, Ω_0 is assumed to be athermal for the studied temperature range and represents recovery due to the cross-slip mechanism. A_0 is a constant related to the density of vacancies, D_0 is the diffusion coefficient, Q_m is the activation energy of diffusion of vacancies, R is the gas constant and T is temperature.

Hardening can then be easily determined by the work hardening of the above flow rule as in

$$h_\beta = \frac{d\tau}{d\gamma_a} = \alpha\mu b\frac{1}{2\sqrt{\rho}}\frac{d\rho}{d\gamma_a} \tag{7.11}$$

where ρ is the total dislocation density ($\rho = \rho_s + \rho_g + \rho_{Mg}$). The new work hardening term $d\tau / d\gamma_a$ is dependent on experimentally determined parameters relating to the evolving microstructure and temperature (Cyr et al. 2016b) written as

$$\frac{d\rho}{d\gamma_a} = \frac{2}{\Lambda_s b(2 + \Omega\gamma_a)^2} + \frac{4}{\gamma_a b} \tag{7.12}$$

7.2.3 Critical Resolved Shear Stress (CRSS)

The crystal plasticity formulation requires an initial CRSS representing the undeformed yield strength of individual slip systems, denoted τ_{y0}. The developed model presented in this paper was used previously (Cyr et al., 2016c) to show that $\tau_{y0} \approx 0$ for pure aluminum. For aluminum alloys, the initial CRSS is highly influenced by the alloying content and grain structure. In the presented model the implied CRSS upon initial straining can be determined by evaluating the flow rule in equation (7.9) at zero accumulated strain such that,

$$\tau_{y0} = \alpha\mu\sqrt{\frac{b}{\Lambda_{Mg}}} \tag{7.13}$$

Following this, the term Λ_{Mg} can now be determined directly from the yield of the experimental stress strain curve.

7.3 Problem Formulation

A Taylor polycrystal averaging scheme is employed in a crystal plasticity framework (Cyr et al., 2015) to simulate uniaxial tension for aluminum sheets AA5754-O and AA5182-O. The reported chemical composition of these two simulated alloys is presented blow in Table 7-1. This crystal plasticity approach provides a fast method to account for grain interactions and morphologies providing more realistic predictions of strain partitioning due to the microstructure.

Table 7-1 Chemical composition of aluminum alloys (wt%).

	Al	Mg	Mn	Fe	Si	Cu	Ni	Ti	Zn
AA5182-O	Bal	4.3	0.34	0.21	0.03	<0.01	<0.01	<0.01	<0.01
AA5754-O	Bal	3.0	0.24	0.26	0.03	0.02	<0.01	<0.01	<0.01

7.3.1 Stress-Strain Curves and Initial Texture

The uniaxial tension stress–strain data used for the determination of the material parameters for the presented models is obtained from work published by Abedrabbo et al. (2007). They presented true stress–true strain data for AA5754-O and AA5182-O over a range from temperatures between 25ºC and 260ºC at constant strain rate $\dot{\epsilon} = 0.0083\ s^{-1}$ ($0.5/min$). This dataset was chosen since the material used for measurements is very similar to the material used to generate the simulated texture. The AA5754-O dataset is used to study temperature dependence of the model parameters, followed by testing the predictive capability of the new formulation on the AA5182-O data. The stress strain curves for AA5754-O are reproduced in Figure 7-1 where digitized experimental curves are presented as points and simulated curves are solid lines.

The initial texture used for simulation of both materials is shown in Figures 7-2 and 7-3 in the form of a {111} recalculated pole figure (PF) and orientation distribution function (ODF) respectively. The pole figure shows that the sheet has a reasonably weak texture with the peak intensity at approximately 1.8 times random. Both the pole figure and ODF show presence of mostly Cube with some Brass components. In the ODFs Cube intensity is the highest at 3.1 times random while intensity of Brass component is at 1.2 times random.

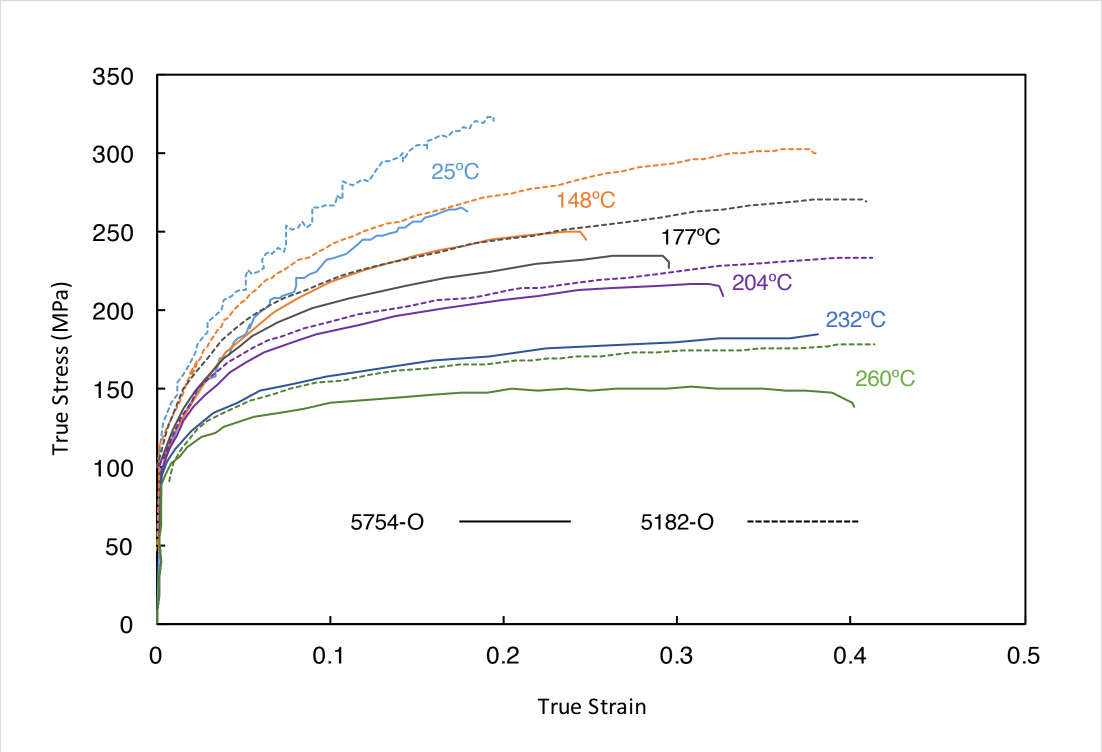

Figure 7-1 True stress-true strain curve reproduced from original data published in Abedrabbo et al. (2007), with solid lines used for AA5754 data, and dotted lines used for AA5182 data.

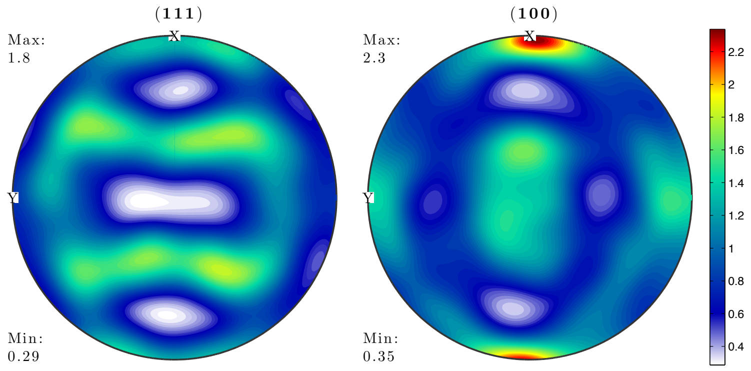

Figure 7-2 (111) and (100) recalculated pole figures of rolled sheet AA5754-O used as input. Axes directions X and Y correspond to RD and TD directions, respectively.

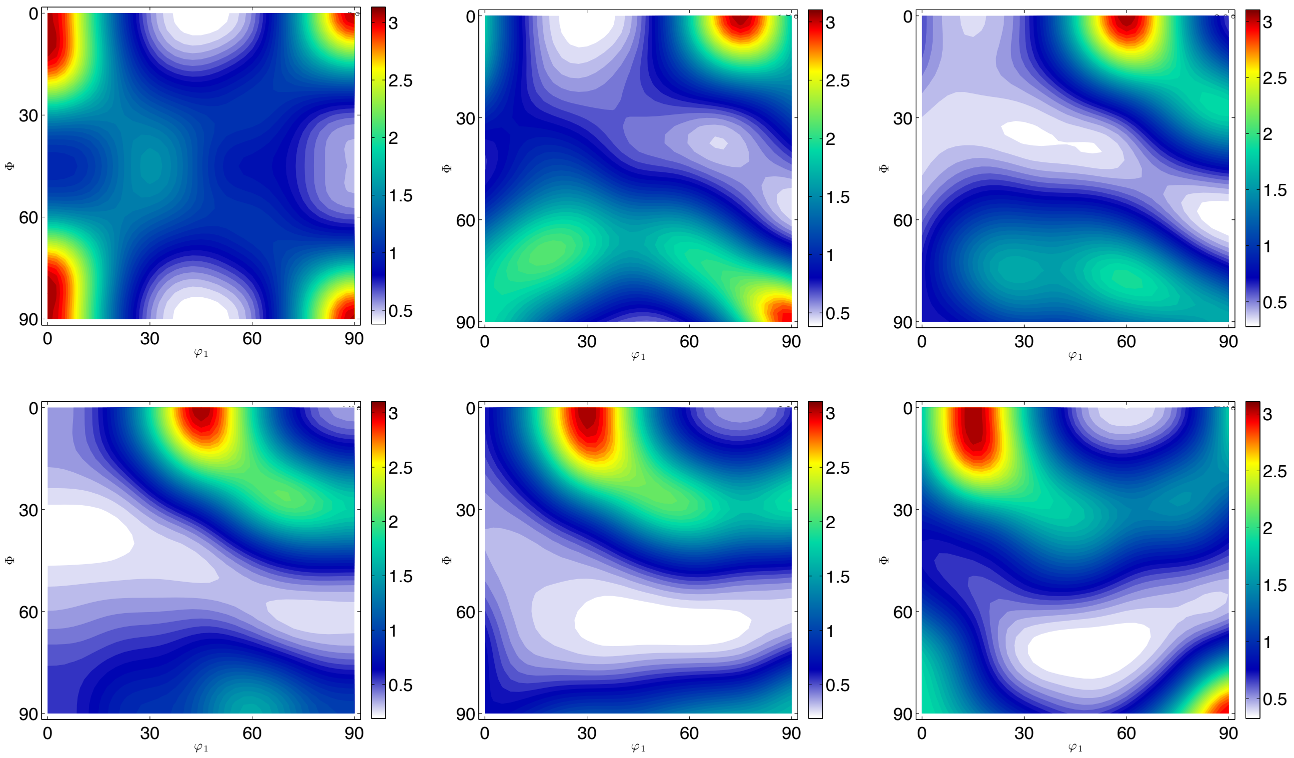

Figure 7-3 ODF sectioning with 15º sections of ϕ_2 from 0º to 75º of the input AA5754-O sheet texture. The ODF shows strong rotated cube and some copper and brass components, typical of rolled and annealed sheet.

7.4 Results

The simulated uniaxial tension curves at the six different temperatures with the experimental curves are presented in Figure 7-4. It is important that the model capture the hardening behaviour along the entire stress-strain curve to be able to correctly characterize the material parameters. The effective yield strength is a contribution of the initial texture, as well as the parameter Λ_{Mg}. The initial hardening is most strongly influenced by the mean-slip distance of statistically-stored dislocations, while the high-strain hardening is governed by geometrically-necessary slip and recovery of the statistically-stored dislocations. The material parameters used in these simulations are presented in Table 7-2. These parameters were obtained by the methods described in the previous section and in the previous chapter (Cyr et al., 2016).

Table 7-2 Hardening parameters from 5754-O simulated uniaxial tension tests. Slip distance parameters are in units of microns and were calculated from their inverse.

Temperature (ºC)	Λ_s (μm)	Λ_g (μm)	Λ_{Mg} (μm)	Ω
25	0.756	50.0	26.3	3.0
148	0.756	50.0	26.3	6.5
177	0.756	50.0	26.3	8.0
204	0.907	50.0	26.3	10
232	1.108	76.92	30.3	13
260	1.181	117.6	30.3	17

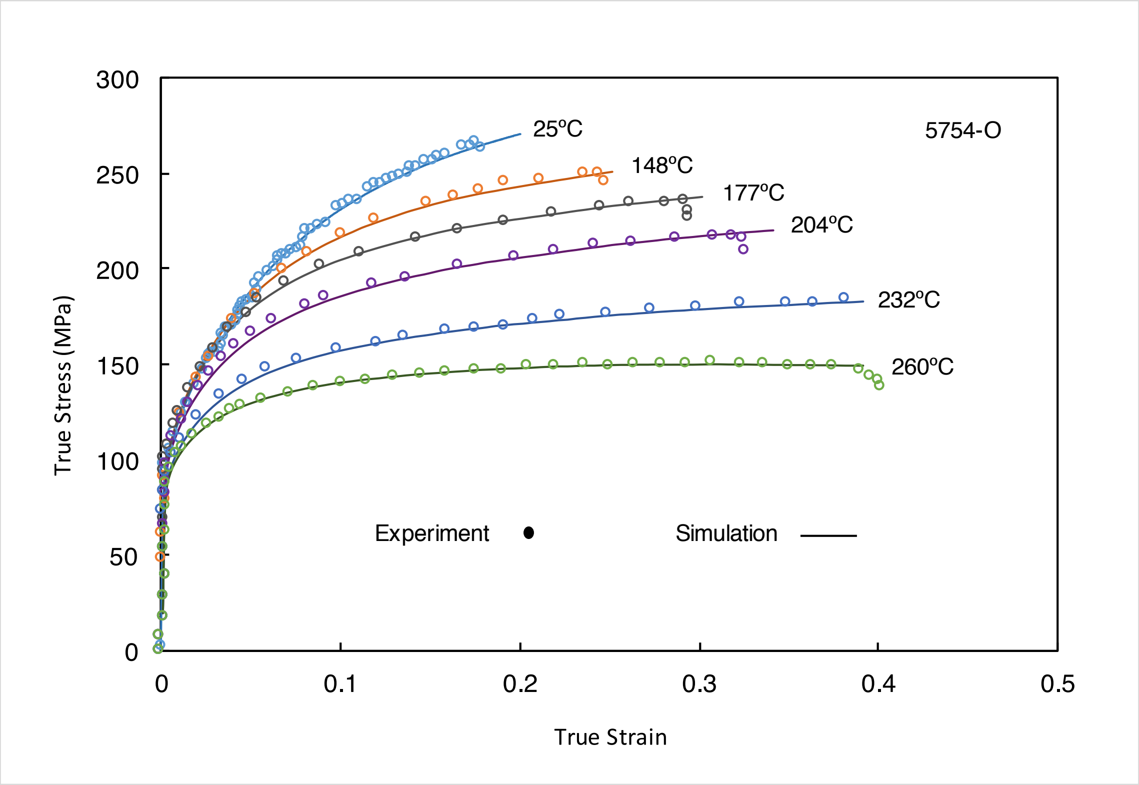

Figure 7-4 Simulated stress-strain curves at 25ºC, 148ºC, 177ºC, 204ºC, 232ºC, and 260ºC and experimental data plotted as points.

7.4.1 Dynamic Strain Aging

Aluminum alloys of the 5xxx (Al-Mg) series are considered non-heat-treatable alloys, and therefore great candidates for warm forming for structural components. Deformed Al-Mg alloys are characterized by relatively even distribution of dislocations due to an effect known as solute drag. This prevents re-arrangement of dislocations into lower energy structures and increases the work hardening rate. In fact, in Al-Mg systems, the solute drag effect is greater on work hardening than solution strengthening (Park & Niewczas, 2008). Lower temperature produces a similar effect, and it has been observed that this temperature effect is more sensitive in low solute alloys rather than highly alloyed systems. This reflects competing mechanisms of dynamic recovery and solute drag.

In essence, the solute drag effect is the disruption or impedance of dislocation motion due to solute Mg atoms. With sufficient energy and dislocation pile-up near solute particles, the dislocations suddenly pass the solute obstacle. The diffusion of Mg in the Al matrix facilitates this sudden passage of dislocations. Optimal conditions for solute drag to take effect are at sufficiently low temperatures while Mg still remains in solution and intermediate strain rates (on the order of 10^{-4} to 10^{-2} s^{-1}). At high strain rates, dislocation motion carries enough energy to sweep past the Mg obstacles, while at sufficiently low strain rates or high temperatures diffusion of Mg prevents drag. In this study, the experimental data falls inside this intermediate strain rate range, and the effect of the Mg solute drag can be observed as "jerky flow" at room temperature. Uniaxial tension data above this temperature (but below 148ºC) not shown in Figure 7-1 fall nearly coincident with the 25ºC curve up to 121ºC. Although the increasing recovery should be lowering the stress-strain curves, the competing solute drag works to stabilize the work hardening over a significant temperature range. Above this temperature (121ºC) at the given strain rate, the “jerky flow” behaviour ceases and the material flows uninhibited by Mg solute atoms.

7.4.1.1 Numerical Implementation

To capture the effects of solute drag in crystal plasticity, the kinetics of the slip formulation must be modified. Since this mechanism affects the actual motion of dislocations, and not necessarily the dislocation production or recovery, the solute drag effect is connected directly to the shear slip rate equation (7.2). In the current formulation, each slip system allows slip as determined by the ratio of the resolved shear stress to the slip system strength. From the discussion above, some amount of slip must be stopped until a threshold is reached. Over this threshold, slip is allowed to occur at an accelerated rate, resulting in a “jerky flow” behaviour. Thus equation (7.2) can be rewritten to show

$$\dot{\gamma}^{\alpha} = \dot{\gamma}_0; \qquad\qquad if \ \ \frac{\tau^{\alpha}}{\tau_y} < f_c \tag{7.14}$$

and

$$\dot{\gamma}^{\alpha} = \dot{\gamma}_1 \mathbf{sgn}(\tau^{\alpha}) \left| \frac{\tau^{\alpha}}{\tau_y^{\alpha}} \right|^{\frac{1}{m}}; \qquad if \ \ \frac{\tau^{\alpha}}{\tau_y} \geq f_c \tag{7.15}$$

where $f_c < 1$ is the critical ratio for slip on a given system α. For this work, it will be assumed that all slip systems accept the same critical parameter. The term $\dot{\gamma}_1$ represents the reference shear rate once slip has been allowed to occur. In order to lead to the “jerky flow” behaviour, this $\dot{\gamma}_1$ parameter must be sufficiently large, and decay to $\dot{\gamma}_0$ as temperature is increased. Similarly, f_c will decay to a value sufficiently small as temperature is increased such that drag is negligible.

In Figure 7-5, the effect of solute drag kinetics on the presented crystal plasticity simulation at room temperature is presented. For the entire polycrystal simulation, consisting of 1000 crystal orientations, the “jerky flow” behaviour can not be observed due to the Taylor averaging of individual crystal; however this effect can be seen when the number of crystals is reduced. The jerky flow curve was generated using a sample of 10 nearly cube orientations to demonstrate the individual crystal effect. The amplitude of the stress oscillations and the frequency are determined by the magnitude of $\dot{\gamma}_1$ and f_c, which are related experimental conditions of temperature and strain rate as well as the solute content. The correlation between these parameters and experimental conditions are beyond the scope of this work; however, the the best results were obtained in the range of $0.7 < f_c < 0.9$. The main focus of this study is using a fully consistent model to predict temperature dependency of microstructural parameters leading to material hardening. In addition, the solute drag effect is not apparent in warm forming conditions, so for this study is only considered in the room temperature simulations and equation (7.2) is employed for all elevated temperature simulations.

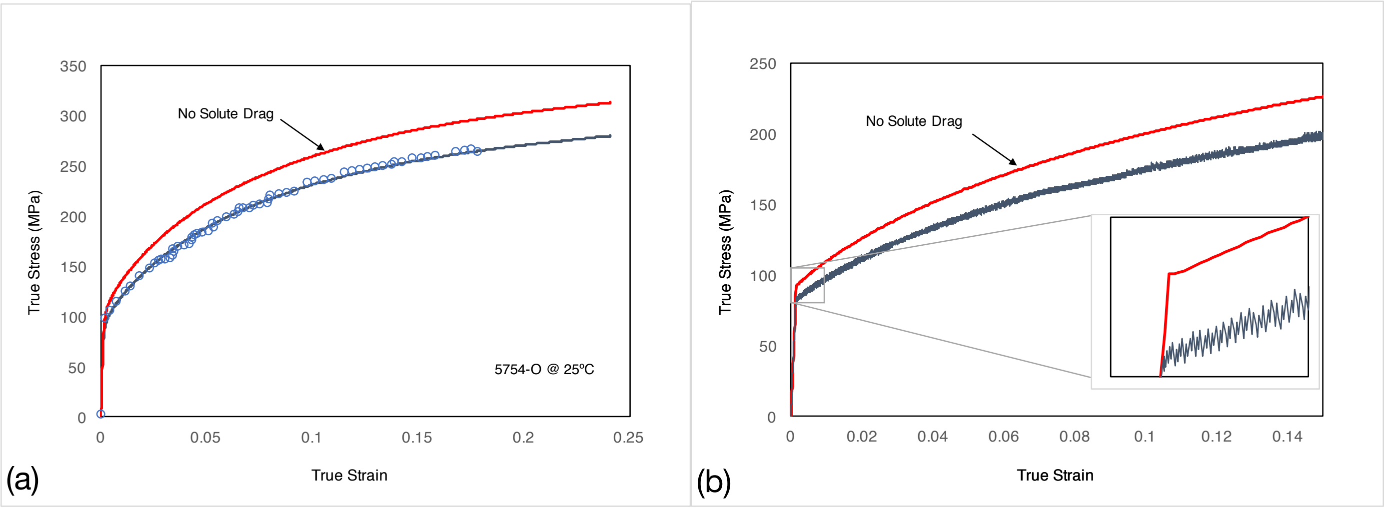

Figure 7-5 Stress-strain curves with and without the solute drag effect for (a) the simulated polycrystal and (b) cube orientation single crystal at room temperature. For simulating solute drag $f_c = 0.85$ and $\dot{\gamma}_1 / \dot{\gamma}_0 = 10^6$ provided the best results.

7.4.2 Temperature Dependency of Material Parameters

Figure 7-6 presents a graphical representation of the slip parameters presented in Table 7-1 for AA5754-O and their temperature evolution. The data shows that decreases in hardening at temperatures near room temperature are completely governed by recovery. This contradicts findings for pure aluminum in a previous study (Cyr et al., 2016) where slip-distance parameters show a temperature dependency in the entire temperature range studied. This suggests a strong influence of the material's alloying in the stabilization of microstructural parameters over low to intermediate temperatures. At sufficiently high temperatures; however, the slip-distance parameters begin to reclaim their temperature dependency. At the highest simulated temperatures, the parameter Λ_{Mg} also loses stability and begins to increase. It is believed that this is due to diffusion of Mg to high energy regions, such as grain boundaries, effectively reducing the strengthening due to dispersed Mg (Niewczas *et al*., 2015).

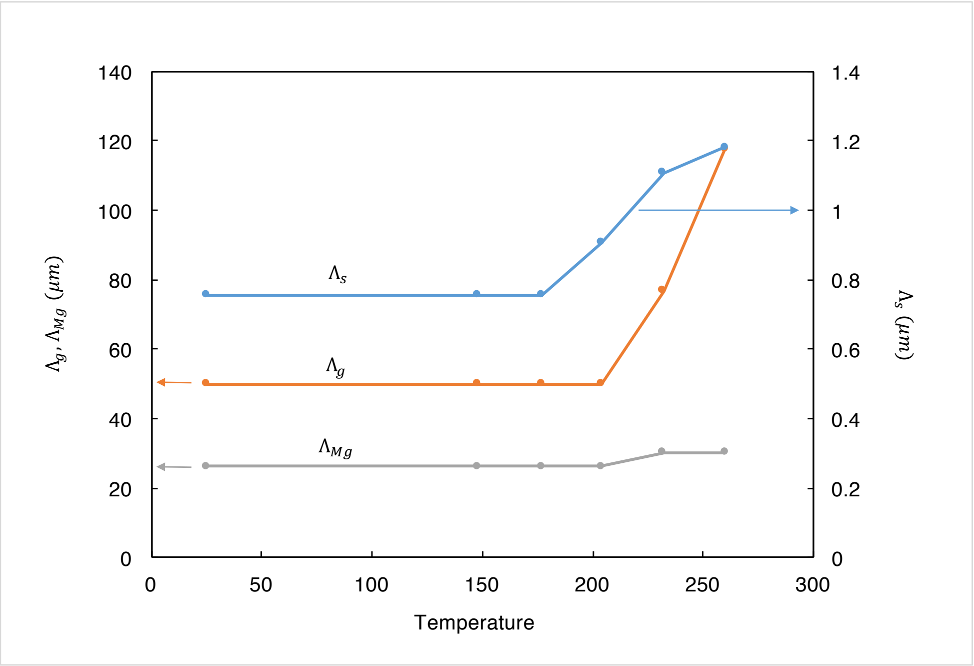

Figure 7-6 Temperature dependency of mean slip distance parameters for simulated AA5754-O.

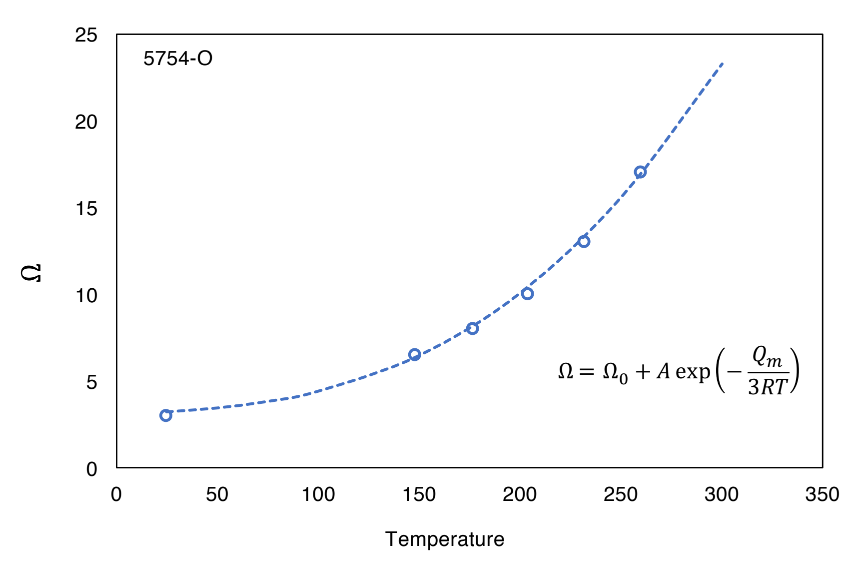

Figure 7-7 Temperature dependency of dynamic recovery factor for simulated AA5754-O with exponential according to equation (7.10). Fitting constants were determined to be $\Omega_0 = 3.0$ and $A = 2.9 \times 10^3$ and activation energy for diffusion Q_m taken from Cyr et al., (2016) for aluminum. R is the gas constant.

7.4.3 Mechanical Response of AA5182-O

Due to the similarities of the two materials, it is assumed that both will behave similarly in terms of their temperature dependencies. The 5182 alloy has increased yield strength due to higher alloying, which can be captured by the Λ_{Mg}. Alloy 5182 also experiences somewhat higher hardening than 5754 suggesting a minor difference in Λ_s and Λ_g between the two alloys. It is also assumed that the experimental preparation for both alloys was conducted in a similar fashion, such that their differences in texture and microstructure (grain size and shape, etc.) are negligible. Therefore, the same simulated texture, presented in Figures 7-2 and 7-3 will be used for 5182. Lastly, the recovery parameter should not significantly vary due to the composition similarities. However, the increase in Mg in 5182 may increase recovery by facilitating remobilization of immobile dislocations. Athermal recovery Ω_0 and the constant A_0 should therefore increase.

Presented in Figure 7-8 are the simulated stress-strain curves for 5182 as well as experimental points extracted from Abedrabbo et al. (2007). Material hardening constants were initially calibrated to the intermediate 148ºC data and 204ºC data. From this, and the predictions gathered from the 5754 simulations, the other hardening parameters were extrapolated. The simulated hardening parameters are presented in Table 7-3. The 5182 data-set did not have stress-strain data for 232ºC.

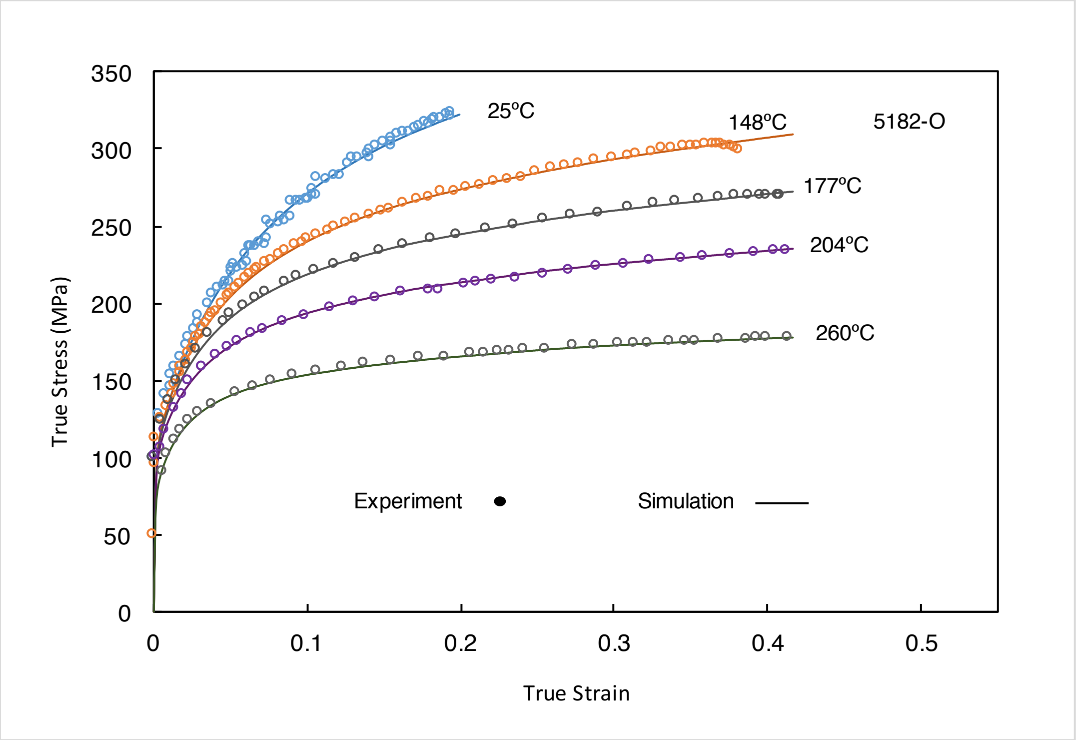

Figure 7-8 Simulated stress-strain curves at 25ºC, 148ºC, 177ºC, 204ºC, and 260ºC and experimental data plotted as points.

Table 7-3 Hardening parameters from 5182-O simulated uniaxial tension tests. Slip distance parameters are in units of microns and were calculated from their inverse.

Temperature (°C)	$\Lambda_s\ (\mu m)$	$\Lambda_g\ (\mu m)$	$\Lambda_{Mg}\ (\mu m)$	Ω
25	0.64	15	22	4.0
148	0.64	24	22	8.0
177	0.64	31	22	10.5
204	0.69	42	22	13.5
260	0.69	77	37	22

7.5 Discussion

It should be mentioned that all discussions presented below are based on the unique set of parameters obtained from the procedure explained previously and in Cyr et al. (2016). The analysis shows that the developed formulation is able to capture the entire stress-strain behaviour very well at all temperatures investigated. Here, the determined material parameters will be used to discuss the effects of magnesium additions and temperature on the two studies alloys.

7.5.1 Influence of Mg on Temperature Dependency

In Figure 7-9 the temperature dependency is plotted for the three slip-distance parameters for AA5182 with AA5754 for comparison. The behaviours of Λ_s and Λ_{Mg} show exact similarity to the results obtained for AA5754. The increased Mg content in AA5182 contributes to decreasing mean free path for all dislocations types and therefore strengthens the material. With the exception of Λ_g for AA5182, the mean slip distance is very stable over temperatures up to 200ºC, and all thermal softening is developed by dynamic recovery of dislocations. Above 200ºC, the model suggests that the microstructure begins to lose its order, allowing for greatly increased dislocation movement. The mean slip distance Λ_{Mg} shows that this is most likely due to Mg diffusion (Chen *et al*. 2016). While at low temperatures, the Mg can facilitate the subgrain structures, such as cellular formation and development of subgrain boundaries that effectively maintain the dependency of Λ_s and Λ_g on the distribution of Mg atoms, and less on temperature. At sufficiently high temperatures, where Mg can diffuse easily to, for example, grain boundaries, these stabilizing effects of Mg are lost and slip of geometrically-necessary and statistically-stored dislocations begin to grow rapidly as the subgrain structures are absolved. There is one parameter, however, that argues this idea. For the 4.3 wt% Mg AA5182, Λ_g is never stable and exudes a temperature dependency over the entire temperature range studied. As temperature decreases, Λ_g continues to decrease as well, contributing to increased work hardening of the 5182 alloy. This is the most significant difference between these two materials. It is known that higher Mg alloys will increase work hardening (Niewczas *et al*. 2015), however, this model predicts the underlying cause to be the increasing strengthening due to geometrically-necessary dislocations. In AA5182, the increased Mg content may diffuse to form less random distributions or clustering at lower temperatures weakening the subgrain structures and allowing Λ_g to grow more easily. It is likely this greatly increased work hardening from geometrically-necessary dislocations in AA5182 that give way to its high ductility at intermediate temperatures, compared to AA5754.

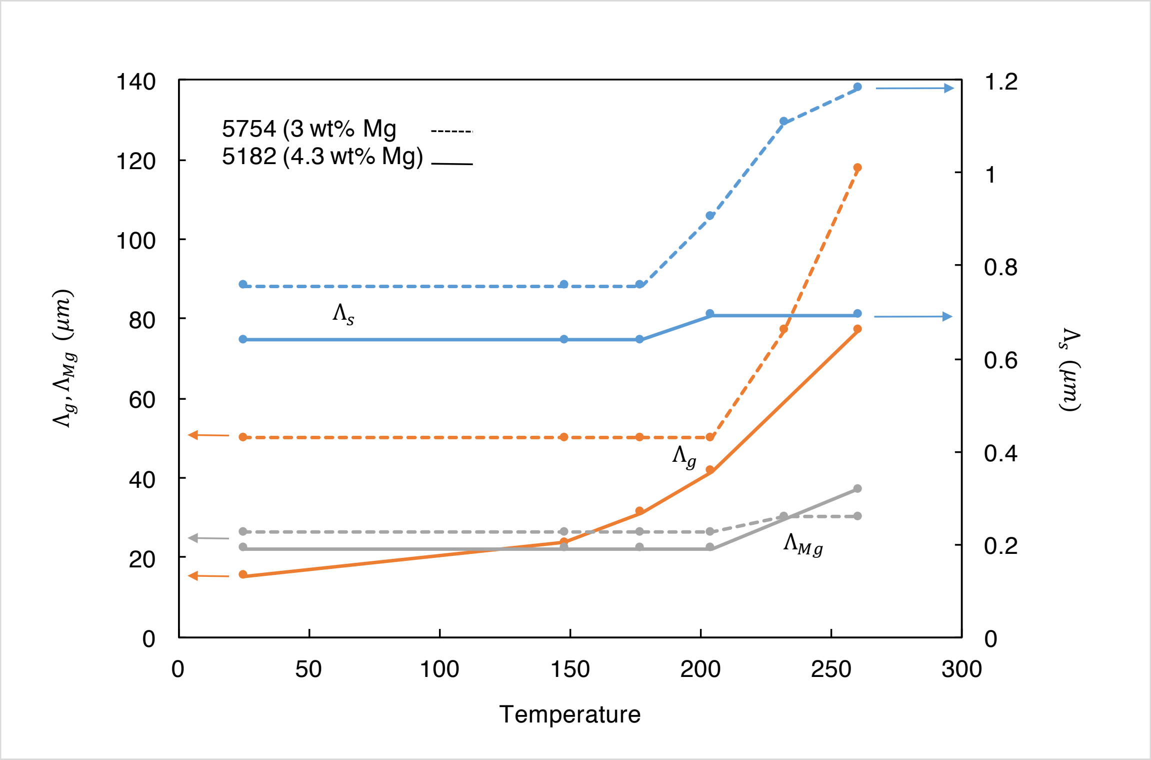

Figure 7-9 Temperature dependency of dynamic mean slip-distance parameters for simulated AA5182-O and AA5754-O for comparison.

Dynamic recovery presented in Figure 7-10 shows little variation between the two alloys. Increased Mg content increases the recovery for AA5182 over the entire temperature range as predicted in the previous section. Of the possibly explanations for this behaviour, the most likely is that Mg atoms contribute to the remobilization of immobile dislocations in a similar manner to vacancies. Elastic strains due to lattice mismatch near Mg solute may also attract vacancies, increasing the Mg diffusion. The effect of Mg, however, must be minimal due to the similarity of recovery factors between the studied alloys and pure aluminum (Cyr et al. 2016).

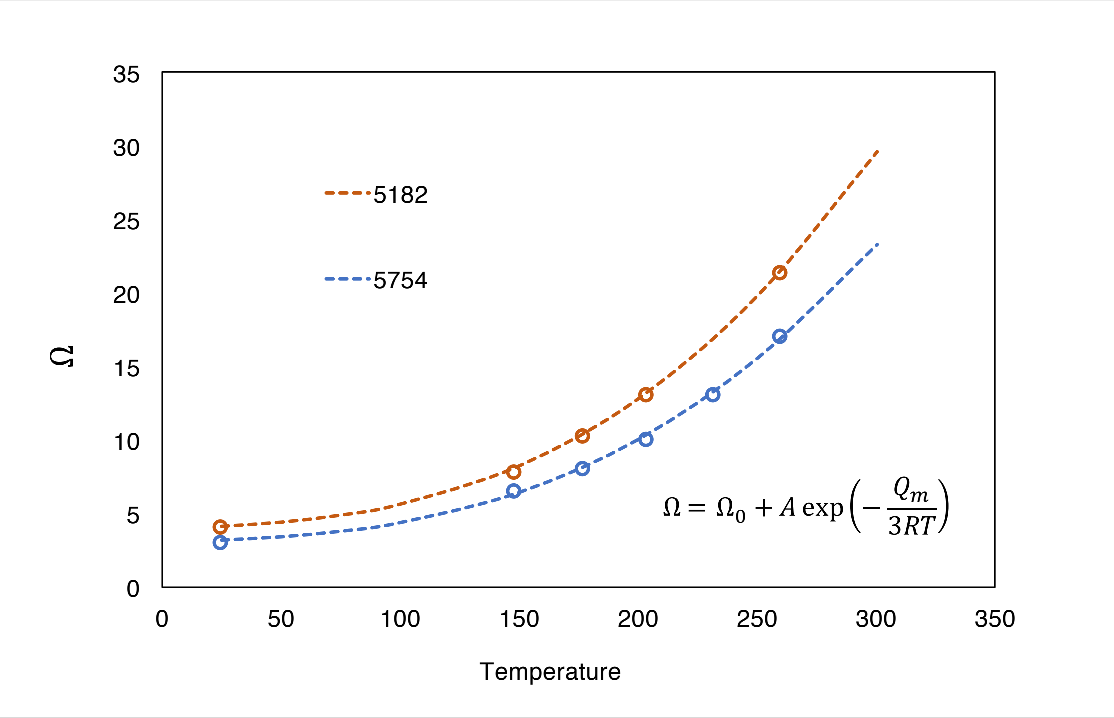

Figure 7-10 Temperature dependency of dynamic recovery factor for simulated AA5182-O and AA5754-O for comparison with equation (7.10). Fitting constants for AA5182 were determined to be $\Omega_0 = 3.5$ and $A = 3.9 \times 10^3$ and activation energy for diffusion Q_m taken from Cyr et al., (2016) for aluminum. R is the gas constant.

7.5.4 Strain Hardening

Finally, one can also study the effect of temperature on material behaviour by analyzing the material strain hardening. Presented in Figure 7-11 is the normalized strain hardening of the simulated AAA5182 $\tau - \gamma$ curves plotted against the normalized shear stress. The essential features of these hardening curves are the elastic regions of constant hardening, followed by rapidly decreasing low-stress regions, which are highly dependent on initial microstructure, followed by a linear decrease in hardening known as stage III type hardening. Finally the hardening begins to saturate with increasing strain and recovery until fracture. It has been proposed (Nabarro, 1989) that this region of fracture is related to the point at which the flow stress σ surpasses the material strain hardening.

In Figure 7-11, the most noticeable effect of temperature is a horizontal shift of the hardening curves toward the left side of the chart. Even with normalization of τ with the temperature dependent shear modulus μ, the curves migrate left from 148ºC to 260ºC. At 25ºC however, the hardening falls between the 204ºC and 260ºC curves due to the solute drag effect. From analysis of the slip-parameters and recovery, the 25ºC curve should be furthest to the right and experience the highest hardening, however the solute Mg suppresses this hardening behaviour at lower stresses. The hardening of 25ºC then crosses the lower temperature curves at sufficient stress and retains a higher work hardening than at elevated temperatures. This is less obvious from experimental data, but is very clearly represented in the model. The inset plot of the hardening curves in

Figure 7-11 highlights this point with an arrow marking the transition of the 25ºC curve across the intermediate temperature curves.

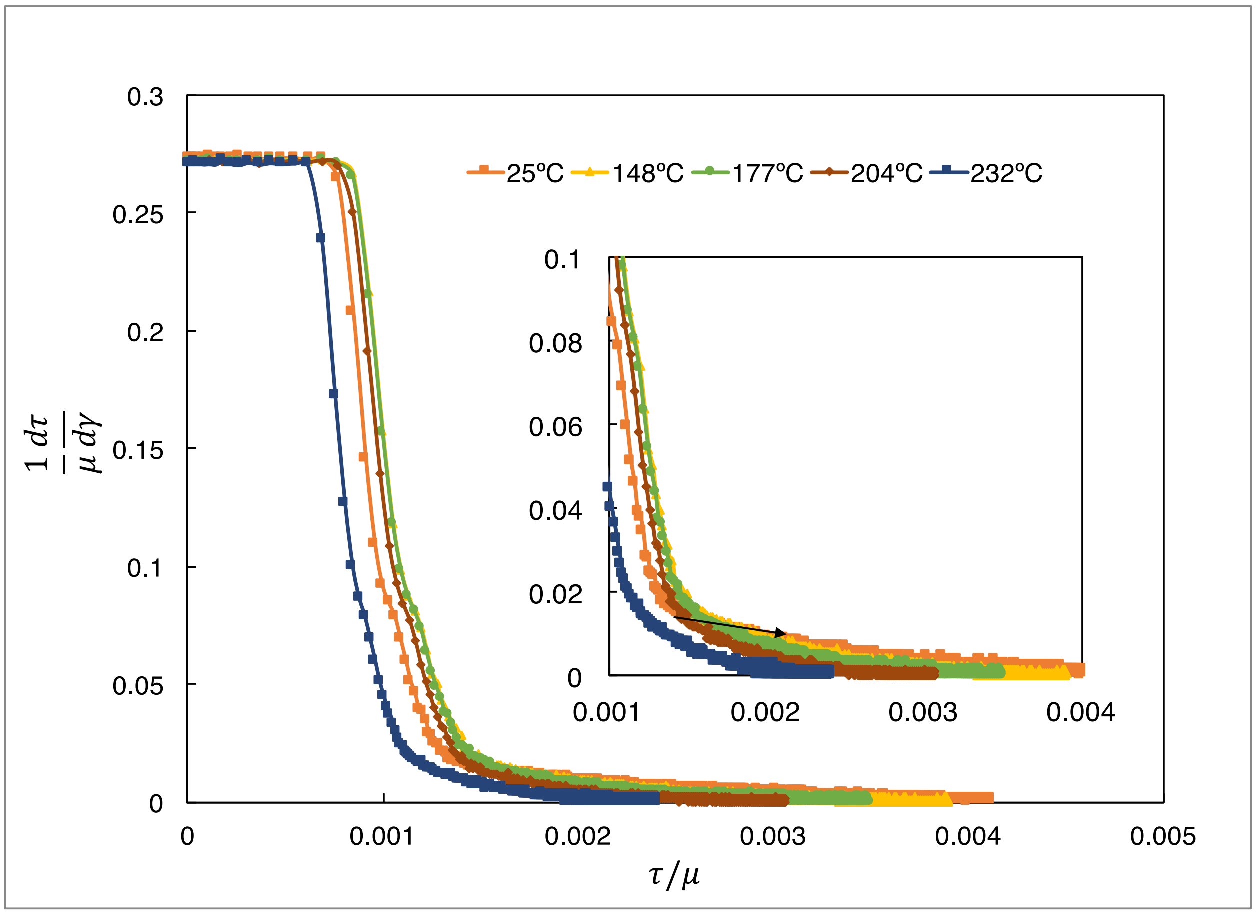

Figure 7-11 Normalized work hardening versus flow stress of simulated stress-strain curves for AA5182. The inset plot shows with an arrow the transition of the 25ºC hardening curve across the intermediate temperature curves due to the solute drag effect.

7.6 Conclusions

In this study, a physically based theory developed previously (Cyr et al., 2016) on the thermodynamic and mechanical balance between dislocation storage, accumulation, annihilation and recovery for a polycrystalline material is implemented into a temperature dependent crystal plasticity framework to study two Al-Mg alloys. The theory is modified to include solution strengthening effects due to Mg additions and written in a rate form hardening law for simulating flow stress. The temperature dependence of hardening parameters embedded in the theory have been calibrated and presented with experimental data of AA5754-O and AA5182-O from 25ºC up to 260ºC. The temperature dependence of the hardening behaviour can be summarized by four important material parameters: mean slip distance of statistically-stored Λ_s, geometrically-necessary Λ_g dislocations and the dynamic recovery factor Ω. The fourth is the newly introduced Λ_{Mg} parameter representing mean slip of dislocations impeded by solute Mg. The following was concluded from the study:

- There is a unique set of material hardening parameters that can be measured directly from the experimental stress-strain curves by the procedure outlined by Cyr et al. (2016) with the new parameter Λ_{Mg} determined from $\tau_{y0} = \alpha\mu\sqrt{b/\Lambda_{Mg}}$.

- The model is able to provide excellent fits to experimental data and good predictions of material hardening behaviour and temperature dependency.

- Dynamic recovery can be predicted from an Arrhenius-type relationship for the remobilization of immobile dislocation by vacancy climb with minimal calibration.

- The temperature dependency microstructural mechanisms governed by mean slip distance of dislocations is highly complex and difficult to determine a single temperature dependency in an alloyed polycrystalline system – unlike with pure aluminum (Cyr et al., 2016). However, it can be concluded that Mg additions are able to stabilize microstructure at intermediate temperatures (below 175ºC-200ºC) leaving dynamic recovery as the sole mechanisms driving temperature dependence of stress-strain response.

- Graphical analysis of the temperature dependence of mean slip distance parameters show that above approximately 175ºC to 200ºC there is a change in microstructure stability that allows for a sudden increase in dislocation mean free path for all types of dislocations. This is attributed to diffusion of solute Mg atoms facilitating the weakening of substructures, such as cell walls, and becoming significantly weaker obstacles themselves. The may also begin to diffuse to grain boundaries allowing for increased mean slip distance within grains.

- To capture the correct hardening response at room temperature, the effect of solute Mg on dynamic strain aging/solute drag must be accounted for. Without this effect, the model predicts an unrealistic decrease in hardening with decreasing temperature from 148ºC to 25ºC.

Chapter 8

Conclusions & Future Work

8.1 Elevated Temperature Behaviour

This thesis presents a focused study on the improvement of modeling temperature dependency and material deformation at elevated temperatures. Specifically, aluminum and its alloys are of key interest for warm forming processing, and a proper model for predicting elevated temperature behaviour is a requirement for computer-aided engineering. The difficulty of this problem is not taken lightly. The literature on this topic spans decades, and advancements in computer technology have afforded many recent advancements in modeling techniques. Crystal plasticity in particular has been widely received as a highly capably framework for studying the effects of microstructure on plastic deformation in metals, however most modeling attempts still rely on phenomenological single crystal hardening. This is not sufficient for predicting material behaviour, as it ignores thermo-mechanically influenced mechanisms that are the foundation of material hardening, such as dislocation mobility and dynamic recovery. In addition, alloying has a significant influence on these microstructural parameters.

8.2 Developed Model

The model motivation and development presented in this thesis begins with a complete temperature dependent crystal plasticity framework development. The model initially employs available phenomenological hardening laws and attempts to find some physically based temperature dependency of the hardening parameters to predicts stress-strain response in varying strain paths and forming limit strains. The models are satisfactory but are not excellent predictors of stress-strain response. The lack of a physical basis of the hardening models present further difficulty when attempting to predict high-strain behaviour in forming limit analysis. Following this work, a new constitutive formulation for hardening in polycrystalline metals is derived from a base of physical mechanisms contributing to hardening behaviour. The thermo-mechanical balance between dislocation accumulation and recovery forms the basis of the derivation. In pure metals, accumulation of two types of dislocations (statistically-stored and geometrically-necessary) are the driving forces for work hardening while dynamic recovery governs thermal softening. The model is used to characterize hardening behaviour of pure aluminum and is used to accurately predict temperature dependent behaviour at a new strain rate. Model also provides some direction towards explaining the temperature dependence of microstructural parameters representing the mean slip distance of dislocations, and their interdependence. Finally, the constitutive framework is introduced to the previously developed temperature dependent crystal plasticity framework to study Al-Mg automotive sheet alloys AA5754 and AA5182. The development of a rate form of the material hardening is modified to include solid solution strengthening due to Mg solute atoms. Kinetics of slip deformation to accommodate solute drag is also implemented for room temperature simulations. The model is used to characterize hardening behaviour of the AA5754 alloy and then used to predict AA5182 stress-strain response after initial calibration using to stress-strain curves. The work concludes the following:

- To properly predict the flow stress, a model based on physics and mechanisms of deformation must be employed to describe material hardening on a polycrystalline level.

- The developed temperature dependent crystal plasticity framework (TEV model) is able to capture well the texture and texture evolution. The model supports experimental evidence that texture evolution is not significantly affected by temperature.

- The hardening behaviour of polycrystalline aluminum can be characterized by a minimum of three parameters: (i) statistically-stored dislocations, (ii) geometrically-necessary dislocations (iii) and dynamic recovery. The presented model captures these quantities using the parameters of mean slip distance of dislocations Λ_s and Λ_g and dynamic recovery factor Ω.

- Strengthening due to alloying must be accounted for, caused by the interruption of dislocation movement due to solute atoms or particles. This is captured using a mean slip distance parameter Λ_{Mg} representing the impedance of dislocations due to solute Mg for Al-Mg alloys and does not evolve with strain.

- There is a unique set of these hardening parameters to describe each mechanical response condition, and they can be measured from a slip-distance analysis described in Chapter 6 and 7. In summary, Λ_s governs low-strain hardening rate, Λ_g affects hardening rate saturation, Λ_{Mg} is determined from yield, and recovery factor Ω affects the curvature of the stress-strain response.

- The model is able to capture stress-strain response of polycrystalline aluminum and the two studies 5754 and 5182 alloys with great precision.

8.3 Recommendations for Future Work

The work presented in this thesis provides an excellent tool for computer-aided engineering and material characterization. Unlike phenomenologically based material models, this could theoretically be used to understand material behaviour, rather than to simply fit data for modeling. Future use and development of this model should be considered for understanding and predicting behaviour of other alloys and metals where warm forming or high-temperature deformation is prescribed. The model can be modified to include effects for 6xxx series alloys of particular interest to high-temperature processing, such as extrusion and modeling heat affected zones of welded parts. The model could be used to account for the strain evolution, strengthening effects, and temperature dependency of secondary phases or precipitates in the material with the implementation of an appropriate Λ parameter. Precipitation would increase strength and hardening by working to decrease the mean free path of mobile dislocation. The model could also be extended to non-cubic crystalline materials, such as magnesium alloys, to study microstructural parameters leading to twinning and its temperature dependence.

Finally, this model would be an excellent tool for investigations in strain-rate dependency. Higher strain-rate processes are preferable due to increased through-put in manufacturing, therefore advanced models that can predict material response where temperature and strain-rate are important process parameters would be invaluable. This model provides the basis for a complete temperature and strain-rate dependent model, however significant experimental work would be needed to properly develop and model and characterize material parameters.

References

Abedrabbo, N., Pourboghrat, F., Carsley, J., 2006. Forming of aluminum alloys at elevated temperatures – Part 1: Material characterization, International Journal of Plasticity, 22, 314-341.Alterthum, H., 1922. Zur Theorie Der Rekristallisation. Z. Metallkd. 14, 417–424.

Abedrabbo, N., Pourboghrat, F., Carsley, J., 2007. Forming of AA5182–O and AA5754–O at elevated temperatures using coupled thermo-mechanical finite elements models, International Journal of Plasticity, 23, 841-875.

Acharya, A., Beaudoin, A.J., 2000. Grain-size effect in viscoplastic polycrystals at moderate strains, Journal of the Mechanics and Physics of Solids, 48, 2213–30.

Agarwal, S., Briant, C.L., Krajewski, P.E., Bower, A.F., Taleff, E.M., 2007. Experimental validation of two-dimensional finite element method for simulating constitutive response of polycrystals during high temperature plastic deformation, Journal of Materials Engineering and Performance, 16, 170–8.

Alers, G.A., Waldorf, D.L., 1961. Variation of the elastic moduli at the superconducting transition, Physics Review Letters, 6, 677–679.

Allwood, J.M., Shoulder, D.R. 2009 Generalised forming limit diagrams showing increased forming limits with non-planar stress states, International Journal of Plasticity 25, 1207–1230.

Altintas, S., 1978. Plastic deformation of crystals: Analytical and computer simulation studies of dislocation glide [Ph. D. Thesis].

Altintas, S., 2011. Plastic deformation of crystals: analytical and computer simulation studies of dislocation glide. Lawrence Berkeley National Laboratory.

Amirkhizi, A.V., Nemat-Nasser, S., 2007. A framework for numerical integration of crystal elasto-plastic constitutive equations compatible with explicit finite element codes, International Journal of Plasticity, 23, 1918–37.

Amodeo, R. J., Ghoniem, N. M., 1990. Dislocation dynamics. I. A proposed methodology for deformation micromechanics. The American Physical Society, 41, 6958 – 6967.

Anand, L., 1982. Constitutive equations for the rate-dependent deformation of metals at elevated temperatures. Journal of engineering materials and technology, 104(1), pp.12-17.

Anand, L., 2004. Single-crystal elasto-viscoplasticity: application to texture evolution in polycrystalline metals at large strains, Computer Methods in Applied Mechanics and Engineering, 193, 5359–83.

Anderson, M.P., Srolovitz, D.J., Grest, G.S., Sahni, P.S., 1984a. Computer simulation of grain growth—I. Kinetics, Acta Metallurgica, 32 (5), 783–791.

Argon, A.S., 1968. Dislocation dynamics. Materials Science and Engineering, 3(1), pp.24-32.

Arsenlis, A., Parks, D.M., 1999. Crystallographic aspects of geometricallynecessary and statistically-stored dislocation density, Acta Materialia, 47(5), 1597–611.

Arsenlis, A., Parks, D.M., 2002. Modeling the evolution of crystallographic dislocation density in crystal plasticity, Journal of the Mechanics and Physics of Solids, 50(9), 1979–2009.

Arsenlis, A., Parks, D.M., Becker, R., Bulatov, V.V., 2004. On the evolution of crystallographic dislocation density in non-homogeneously deforming crystals, Journal of the Mechanics and Physics of Solids, 52(6), 1213–46.

Arsenlis, A., Tang, M., 2003. Simulations on the growth of dislocation density during Stage 0 deformation in BCC metals, Modelling and Simulation in Materials Science and Engineering, 11, 251–64.

Asaro, R.J., 1983. Crystal Plasticity, ASME. Journal of Applied Mechanics, 50(4b), 921–934.

Asaro, R.J., Needleman, A., 1985. Texture development and strain hardening in rate dependent polycrystals, Acta Metallurgica, 33, 923–53.

Asaro, R.J., Rice, J.R., 1977. Strain localization in ductile single crystals. Journal of the Mechanics and Physics of Solids, 25, 309–38.

Ashby, M.F., 1970. The deformation of plastically non-homogeneous materials, Philosophical Magazine, 21, 399–424.

Avrami, M., 1939. Kinetics of phase change I, general theory. J. Chem. Phys. 7 (12), 1103–1112.

Avrami, M., 1940. Kinetics of phase change II, Transformation time relations for random distribution of nuclei. J. Chem. Phys. 8, 212–224

Ayres, R.A. and Wenner, M.L., 1979. Strain and strain-rate hardening effects in punch stretching of 5182-0 aluminum at elevated temperatures. Metallurgical Transactions A, 10(1), pp.41-46.

Bachu, V., Kalidindi, S.R., 1998. On the accuracy of the predictions of texture evolution by the finite element technique for fcc polycrystals, Materials Science and Engineering A, 257, 108–17.

Bagheriasl, R., 2012. Formability of Aluminum Alloy Sheet at Elevated Temperature, University of Waterloo, PhD Thesis.

Balasubramanian, S., Anand, L., 2002. Plasticity of initially textured hexagonal polycrystals at high homologous temperatures: application to titanium, Acta Materialia, 50, 133–48.

Banovic, S. W., Iadicola, M. A., Foecke, T. 2008 Textural development of AA 5754 sheet deformed under in-plane biaxial tension, Metallurgical and Materials Transactions A 39, 2246–2258.

Barbe, F., Decker, L., Jeulin, D., Cailletaud, G., 2001. Intergranular and intragranular behavior of polycrystalline aggregates. Part 1: F.E. model., International Journal of Plasticity,17, 513–36.

Barlat, F., 1987. Crystallographic texture, anisotropic yield surfaces and forming limits of sheet metals, Materials Science and Engineering, 91, 55–72.

Barton, N.R., Knap, J., Arsenlis, A., Becker, R., Hornung, R.D., Jefferson, D.R., 2001. Embedded polycrystal plasticity and adaptive sampling, International Journal of Plasticity, 24, 242–66.

Basinski, Z.S., 1959. Thermally activated glide in face-centred cubic metals and its application to the theory of strain hardening. Philosophical Magazine, 4(40), pp.393-432.

Bassani, J.L., Wu, T.Y., 1991. Latent hardening in single crystals II: analytical characterization and predictions, Proceedings of the Royal Society of London A, 435, 21–41.

Bate, P., 1999. Modelling deformation microstructure with the crystal plasticity finite-element method, Philosophical Transactions of the Royal Society of London A, 357, 1589–601.

Bate, P.S., An, Y.G., 2004. Plastic anisotropy in AA5005 Al–1Mg: predictions using crystal plasticity finite element analysis, Scripta Materialia, 51, 973–7.

Bate, P.S., Hutchinson, W.B., 2005. Grain boundary area and deformation, Scripta Materialia, 52, 199–203.

Beaudoin, A.J., Dawson, P.R., Mathur, K.K., Kocks, U.F., Korzekwa, D.A., 1994. Application of polycrystal plasticity to sheet forming, Computer Methods in Applied Mechanics and Engineering, 117, 49–70.

Beaudoin, A.J., Dawson, P.R., Mathur, K.K., Kocks, U.F., 1995. A hybrid finite element formulation for polycrystal plasticity with consideration of macrostructural and microstructural linking, International Journal of Plasticity, 11, 501–21.

Beaudoin, A.J., Mathur, K.K., Dawson, P.R., Johnson, G.C., 1993. Three-dimensional deformation process simulation with explicit use of polycrystal plasticity models, International Journal of Plasticity, 9,833–60.

Beaudoin, A.J., Mecking, H., Kocks, U.F., 1996. Development of localized orientation gradients in fcc polycrystals, Philosophical Magazine A, 73, 1503–17.

Beck, P., Hu, H., 1966. ASM Seminar on Recrystallization. Grain Growth and Texture, Met. Park, Ohio, USA.

Becker, R., 1991. Analysis of texture evolution in channel die compression—I. Effects of grain interaction, Acta Metallurgica et Materialia, 39, 1211–30.

Becker, R., 1998. Effects of strain localization on surface roughening during sheet forming, Acta Materialia, 46, 1385–401.

Becker, R., Butler, J.F., Hu, H., Lalli, L.A., 1991. Analysis of an aluminum single crystal with unstable initial orientation (001) in channel die compression, Metallurgical Transactions A, 22, 45–58.

Becker, R., Panchanadeeswaran, S., 1995. Effects of grain interactions on deformation and local texture in polycrystals, Acta Materialia, 43, 2701–19.

Bergström, Y. and Hallén, H., 1982. An improved dislocation model for the stress-strain behaviour of polycrystalline α-Fe. Materials Science and Engineering, 55(1), pp.49-61.

Bergström, Y, 1977. Metallers Plastiska Deformation, Royal Institute of Technology, Stockholm.

Bertram, A., Böhlke, T., Kraska, M., 1997. Numerical simulation of deformation induced anisotropy of polycrystals, Computational Materials Science, 9, 158–67.

Bhatia, M.L., Cahn, R.W., 1978. Proc. R. Soc. London, Ser. A 302, 341.

Bhattacharyya, A., El-Danaf, E., Kalidindi, S.R., Doherty, R.D., 2001. Evolution of grain-scale microstructure during large strain simple compression of polycrystalline aluminum with quasi-columnar grains: OIM measurements and numerical simulations, International Journal of Plasticity, 17, 861–83.

Bieler, T.R., Eisenlohr, P., Roters, F., Kumar, D., Mason, D.E., Crimp, M.A., et al., 2009. The role of heterogeneous deformation on damage nucleation at grain boundaries in single phase metals, International Journal of Plasticity, 25, 1655–83.

Bishop, J.F.W., Hill, R., 1951b. A theoretical derivation of the plastic properties of a polycrystalline face centered metal, Philosophical Magazine, 42, 1298–307.

Bishop, J.F.W., Hill. R., 1951a. A theory of the plastic distortion of a polycrystalline aggregate under combined stresses, Philosophical Magazine, 42, 414–27.

Bishop, J.F.W., Hill. R., 1951a. A theory of the plastic distortion of a polycrystalline aggregate under combined stresses, Philosophical Magazine, 42, 414–27.

Bitzek, E., Derlet, PM., Anderson, PM., Van Swygenhoven H., 2008. The stress–strain response of nanocrystalline metals: a statistical analysis of atomistic simulations, Acta Materialia, 56, 846–4857.

Borg, U., Niordson, C.F., Kysar, J.W., 2008. Size effects on void growth in single crystals with distributed voids, International Journal of Plasticity, 24, 688–701.

Bornand, M., Huang, K., 1954. Dynamical Theory of Crystal Lattices, Oxford University Press, Oxford.

Bower, A.F., Wininger, E., 2004. A two-dimensional finite element method for simulating the constitutive response and microstructure of polycrystals during high temperature plastic deformation, Journal of the Mechanics and Physics of Solids, 52, 1289–317.

Brahme, A.P., 2005. Modelling Mocrostructure Evolution During Recrstallization, Thesis.

Brahme, A., Alvi, M.H., Saylor, D., Fridy, J., Rollett, A.D., 2006. 3D reconstruction of microstructure in a commercial purity aluminum, Scripta Materialia, 55, 75–80.

Brahme, A.P., Inal, K., Mishra, R.K., Saimoto, S., 2011. A new strain hardening model for rate-dependent crystal plasticity, 50, 2898–2908.

Brahme, A., Staraselski, Y., Mishra, R.K., Inal, K., 2012. A new model to predict grain nucleation during dynamic recrystallization, In: The 9th International Conference on Magnesium Alloys and their Applications (Mg 2012).

Bridgman, P. W. 1952 "Studies in Large Plastic Flow and Fracture", McGraw Hill, New York.

Bronkhorst, C.A., Kalidindi, S.R., Anand, L., 1992. Polycrystalline plasticity and the evolution of crystallographic texture in FCC metals, Philosophical Transactions of the Royal Society of London A, 341(1662), 443–77.

Brown, S.B., Kim, K.H., Anand, L., 1989. An internal variable constitutive model for hot working of metals, International Journal of Plasticity, 5, 95–130.

Bruzzi, M.S., McHugh, P.E., O’Rourke, F., Linder, T., 2001. Micromechanical modelling of the static and cyclic loading of an Al 2124-SiC MMC, International Journal of Plasticity, 17, 565–99.

Burgers, W.G., 1941. Rekristallisation, verformter Zustand und Erholung. Akademischer Verlagsgesellschaft, Leipzig.

Burgers, W.G., Louwerse, P.C., 1931. Über den Zusammenhang zwischen Deformationsvorgang und Rekristallisationstextur bei Aluminium. Z Phys. 67, 605–678.

Burke, J.E., Turnbull, D., 1952. Recrystallization and grain growth. Prog. Met. Phys. 3, 220–292. (London: Pergamon Press).

Butuc, M.C., Gracio, J.J., Barata da Rocha, A 2003 A theoretical study on forming limit diagrams prediction, Journal of Materials Processing Technology 142, 714–724.

Cahn, R.W., 1950. A new theory of recrystallization nuclei, Proceedings of the Physical Society - Section A, 63 (4), 323.

Cahn, I.R.W., 1966. In: Margohn, H. (Ed.), In Recovery, Recrystallization and Grain Growth. ASM, Metals Park, OH, pp. 99.

Cahn, R.W. (Ed.), 1965. Physical Metallurgy. North-Holland Publishing Co., Amsterdam. Also 2nd, 3rd, and 4th editions.

Carpenter, H.C.H., Elam, C.F., 1920. Crystal growth and recrystallization in metals, J. Inst. Met. 24, 83–131.

Chang, Y.W., Asaro, R.J., 1981. An experimental study of shear localization in aluminum-copper single crystals, 29, 241–257.

Chen, R., Xu, Q., Guo, H., Xia, Z., Wu, Q. and Liu, B., 2016. Modeling the precipitation kinetics and tensile properties in Al-7Si-Mg cast aluminum alloys. Materials Science and Engineering: A.

Chen, Y.P., Lee, W.B., To, S., 2007. Influence of initial texture on formability of aluminum sheet metal by crystal plasticity FE simulation, Journal of Materials Processing Technology, 192–193, 397–403.

Cheong, K-S., Busso, E.P., 2004. Discrete dislocation density modelling of single phase FCC polycrystal aggregates, Acta Materialia, 52, 665–5675.

Cheong, K-S., Smillie, M.J., Knowles, D.M., 2007. Predicting fatigue crack initiation through image-based micromechanical modeling, Acta Materialia, 55, 1757–68.

Chiba, R., Takeuchi, H., Kuroda, M., Hakoyama, T., Kuwabara, T. 2013 Theoretical and experimental study of the forming-limit strain of half-hard AA1100 aluminum alloy sheet, Computational Materials Science 77, 61–71.

Chien, W. Y., Pan, J., Tang, S. C. 2004 A combined necking and shear localization analysis for aluminum sheets under biaxial stretching conditions, International Journal of Plasticity 20, 1953–1981.

Choi, S.H., 2003. Simulation of stored energy and orientation gradients in cold-rolled interstitial free steels. Acta Materialia, 51, 1775–88.

Chung, K., Kim, H., Lee, C. 2014 Forming limit criterion for ductile anisotropic sheets as a material property and its deformation path insensitivity. Part I: Deformation path insensitive formula based on theoretical models. International Journal of Plasticity 58, 3–34.

Chung, K., Kim, H., Lee, C. 2014 Forming limit criterion for ductile anisotropic sheets as a material property and its deformation path insensitivity, Part II: Boundary value problems. International Journal of Plasticity 58, 35–65.

Clareborough, L.M., Haregraves, M.E., West, G.W., 1955. The release of energy during annealing of deformed metals. In: Proceedings of the Royal Society, A, vol. 232.

Clarke, A.P., Humphreys, F.J., Bate, P.S., 2003. Lattice rotations at large second-phase particles in polycrystalline aluminum, Materials Science Forum, 426, 399–404.

Clayton, J.D., 2005. Dynamic plasticity and fracture in high density polycrystals: Consitutive modeling and numerical simulations, Journal of Mechanics and Physics of Solids, 53, 261-301.

Coppieters, S., Cooreman, S., Sol, H., Van Houtte, P., Debruynea, D. 2011 Identification of the post-necking hardening behaviour of sheet metal by comparison by comparison of the internal and external work in the necking zone, Journal of Materials Processing Technology 211, 545–552.

Cottrell, A.H. and Stokes, R.J., 1955, December. Effects of temperature on the plastic properties of aluminium crystals. In Proceedings of the Royal Society of London A: Mathematical, Physical and Engineering Sciences (Vol. 233, No. 1192, pp. 17-34). The Royal Society.

Coulomb, P. and Friedel, J., 1957. Dislocations and Mechanical Properties of Crystals. New York.

Counts, W.A., Braginsky, W.A., Battaile, C.C., Holm, E.A., 2008. Predicting the Hall–Petch effect in fcc metals using non-local crystal plasticity, International Journal of Plasticity, 24, 1243–63.

Curtin, W.A., Miller, R.E., 2003. Atomistic/continuum coupling in computational materials science, Modelling and Simulation in Materials Science and Engineering, 11, R33–68.

Curtin, W.A., Miller, R.E., 2003. Atomistic/continuum coupling in computational materials science, Modelling and Simulation in Materials Science and Engineering, 11, R33–68.

Cyr, E., Mohammadi, M., Inal, K., Misra, R.K., 2015. A three dimensional (3D) thermo-elasto-viscoplastic constitutive model for FCC polycrystals, International Journal of Plasticity, 70, 166–190.

Czochralski, J., 1927. Geschichtlicher Beitrag zur Frage der Rekristallisation. Z. Metallkd. 19, 316–320.

daFonseca, J.Q., Oliver, E.C., Bate, P.S., Withers, P.J., 2006. Evolution of intergranular stresses during in situ straining of IF steel with different grain sizes, Materials Science and Engineering A, 437, 26–32.

Dawson, P.R., 1984. A model for the hot or warm forming of metals with special use of deformation mechanism maps. International Journal of Mechanical Sciences, 26, 227-244.

Deka, D., Joseph, D.S., Ghosh, S., Mills, M.J., 2006. Crystal plasticity modeling of deformation and creep in polycrystalline Ti-6242, Metallurgical and Materials Transactions A, 37, 1371–88.

Delannay, L., Beringhier, M., Chastel, Y., Loge, R.E., 2005. Simulation of cupdrawing based on crystal plasticity applied to reduced grain samplings, Materials Science Forum, 495–497, 1639–44.

Delannay, L., Jacques, P.J., Kalidindi, S.R., 2006. Finite element modeling of crystal plasticity with grains shaped as truncated octahedrons, International Journal of Plasticity, 22, 1879–98.

Delannay, L., Kalidindi, S.R., Van Houtte, P., 2002. Quantitative prediction of textures in aluminium cold rolled to moderate strains, Materials Science and Engineering A, 336, 233–44.

Delannay, L., Melchior, M.A., Signorelli, J.W., Remacle, J.F., Kuwabara, T., 2009. Influence of grain shape on the planar anisotropy of rolled steel sheets—evaluation of three models, Computational Materials Science, 45, 739–43.

Diak, B.J., Upadhyaya, K.R. and Saimoto, S., 1998. Characterization of thermodynamic response by materials testing. Progress in materials science, 43(4), pp.223-363.

Diard, O., Leclercq, S., Rousselier, G., Cailletaud, G., 2005. Evaluation of finite element based analysis of 3D multicrystalline aggregates plasticity: application to crystal plasticity model identification and the study of stress and strain fields near grain boundaries, International Journal of Plasticity, 21, 691–722.

Dick, T., Cailletaud, G., 2006. Fretting modelling with a crystal plasticity model of Ti6Al4V, Computational Materials Science, 38, 113–25.

Ding, R., Guo, Z.X., 2001. Coupled quantitative simulation of microstructural evolution and plastic flow during dynamic recrystallization, Acta Materialia, 49 (16), 3163–3175.

Doherty, R.D., 2005. Primary recrystallization. In: Cahn, R.W., et al. (Eds.), Encyclopedia of Materials: Science and Technology. Elsevier, pp. 7847–7850.

Doherty, R.D., Cahn, R.W., 1972. Nucleation of new grains in recrystallization of cold worked metals. J. Less Common Met. 28 (2), 279–296.

Doherty, R.D., Hughs, D.A., Humphreys, F.J., Jonas, J.J., Juul Jensen, D., Kassner, M.E., King, W.E., McNelley, T.R., McQueen, H.J., Rollet, A.D., 1997. Current issues in recrystallization: a review. Mater. Sci. Eng., A 238, 219–274.

Dunne, F.P.E., Walker, A., Rugg, D., 2007. A systematic study of hcp crystal orientation and morphology effects in polycrystal deformation and fatigue, Proceedings of the Royal Society of London A, 463, 1467–89.

Einstein, A., 1907. Die Plancksche Theorie der Strahlung und die Theorie der spezifischen Wärme, Annalen Physik, 22, 180–190.

Elkhodary, K.I. and Bakr, M.A., 2015. Single crystal plasticity with bend–twist modes. Journal of the Mechanics and Physics of Solids, 79, pp.44-66.

Engler, O., 1997. Influence of particle stimulated nucleation on the recrystallization textures in cold deformed Al-alloys Part II – Modeling of recrystallization textures. Scr. Mater. 37, 1675–1683.

Engler, O., Vatne, H.E., Nes, E., 1996. The roles of oriented nucleation and oriented growth on recrystallization textures in commercial purity aluminium. Mater. Sci. Eng., A 205, 187–198.

Erieau, P., Rey, C., 2004. Modeling of deformation and rotation bands and of deformation induced grain boundaries in IF steel aggregate during large plane strain compression, International Journal of Plasticity, 20, 1763–88.

Erinosho, T.O., Cocks, A.C.F., Dunne, F.P.E. 2013 Texture, hardening and non-proportionality of strain in BCC polycrystal deformation, International Journal of Plasticity 50, 170–192.

Evers, L.P., Brekelmans, W.A.M., Geers, M.G.D., 2004a. Scale dependent crystal plasticity framework with dislocation density and grain boundary effects, International Journal of Solids and Structures, 41(10), 5209–30.

Evers, L.P., Brekelmans, W.A.M., Geers, M.G.D., 2004b. Non-local crystal plasticity model with intrinsic SSD and GND effects, Journal of the Mechanics and Physics of Solids, 52(10), 2379–401.

Evers, L.P., Parks, D.M., Brekelmans, W.A.M., Geers, M.G.D., 2002. Crystal plasticity model with enhanced hardening by geometrically necessary dislocation accumulation, Journal of the Mechanics and Physics of Solids, 50(11), 2403–24.

Ewing, J.A., Rosenhain, W., 1899. The crystalline structure of metals. Proc. R. Soc. 65, 85–90.

Ewing, J.A., Rosenhain, W., 1900a. The crystalline structure of metals. Philos. Trans. R. Soc., A 195, 353–372.

Ewing, J.A., Rosenhain, W., 1900b. The crystalline structure of metals. Philos. Trans. R. Soc., A 195, 279–301.

Eyckens, P., Van Bael, A., Van Houtte, P. 2009 Marciniak-Kuczynski type modeling of the effect of through-thickness shear on the forming limits of sheet metal, International Journal of Plasticity 25, 2249–2268.

Eyckens, P., Van Bael, A., Van Houtte, P. 2011 An extended Marciniak-Kuczynski model for anisotropic sheet subjected to monotonic strain paths with through-thickness shear. International Journal of Plasticity 27, 1577–1597.

Ezatpour, H.R., Sabzevar, M.H., Sajjadi, S.A. and Huang, Y., 2014. Investigation of work softening mechanisms and texture in a hot deformed 6061 aluminum alloy at high temperature. Materials Science and Engineering: A, 606, pp.240-247.

Faghihi, D., Voyiadjis, G.Z., Park, T., 2013. Coupled thermomechanical modeling of small volume FCC metals. Journal of Engineering Materials and Technology, 135, 021003-1-021003-17.

Faivre, P., Doherty, R.D., 1979. Nucleation of recrystallization in compressed aluminium – studies by electron microscopy and Kikuchi diffraction. J. Mater. Sci. 14 (4), 897–919.

Follansbee, P.S., Kocks, U.F., 1988. A constitutive description of the deformation of copper based on the use of the mechanical threshold stress as an internal state variable, Acta Metallurgica, 36, 82–93.

Foreman, A.J.E. and Makin, M.J., 1966. Dislocation movement through random arrays of obstacles. Philosophical magazine, 14(131), pp.911-924.

Foreman, A.J.E. and Makin, M.J., 1967. Dislocation movement through random arrays of obstacles. Canadian Journal of Physics, 45(2), pp.511-517.

Forest, S., 1998. Modeling slip, kink and shear banding in classical and generalized single crystal plasticity, Acta Materialia, 46, 3265–81.

Franz, G., Abed-Meraim, F., Berveiller, M. 2013 Strain localization analysis for single crystals and polycrystals: Towards microstructure-ductility linkage. International Journal of Plasticity 48, 1–33.

Friedel, J., Dislocations, 1964. Oxford, 70, pp.15-24.

Fu, H-H., Benson, D.J., Meyers, M.A., 2004. Computational description of nanocrystalline deformation based on crystal plasticity, Acta Materialia, 52, 4413–25.

Ganapathysubramanian, S., Zabaras, N., 2002. A continuum sensitivity method for finite thermo-inelastic deformations with applications to the design of hot forming processes. International Journal for Numerical Methods in Engineering, 55, 1391-1437.

Ganser, H. -P., Werner, E. A., Fisher, F. D. 2000 Forming limit diagrams: a micromechanical approach, International Journal of Mechanical Sciences 42, 2041–2054.

Gerard, C., Cailletaud, G., Bacroix, B., 2013. Modeling of latent hardening produced by complex loading paths in FCC alloys, 42, 194-212.

Gerken, J.M., Dawson, P.R., 2008a. A crystal plasticity model that incorporates stresses and strains due to slip gradients, Journal of the Mechanics and Physics of Solids, 56, 1651–72.

Gerken, J.M., Dawson, P.R., 2008b. A finite element formulation to solve a non-local constitutive model with stresses and strains due to slip gradients, Computer Methods in Applied Mechanics and Engineering, 197, 1343–61.

Ghavam, K., Bagheriasl, R., Worswick, M. 2014 Analysis of non-isothermal deep drawing of aluminum alloy sheet with induced anisotropy and rate sensitivity at elevated temperatures, Journal of Manufacturing Science and Engineering 136, 011006-1–011006-16

Ghosh, A. K., Hecker, S. S. 1974 Stretching limits in sheet metals: In-plane vs. out-of-plane deformation, Metallurgical Transactions B 5, 2161–2164.

Girifalco, L.A., 2000. Statistical Mechanics of Solids, Oxford University Press, New York, NY, United States of America.

Goetz, R.L., Seetharaman, V., 1998. Modeling dynamic recrystallization using cellular automata, Scripta Materialia, 38 (3), 405–413.

Goh, C-H., Neu, R.W., McDowell, D.L., 2003. Crystallographic plasticity in fretting of Ti–6AL–4V, International Journal of Plasticity, 19, 1627–50.

Goodwin, G. M. 1968 Application of strain analysis to sheet metal problems in press shop, Sheet Metal Industries 60, 767–774.

Gottstein, G. ed., 2004. Integral materials modelling. Institute of Physics Publishing.

Gottstein, G., 2013. Physical foundations of materials science. Springer Science & Business Media.

Gottstein, G., Shvindlerman, L.S., 1999. Grain Boundary Migration in Metals: Thermodynamics, Kinetics, Applications, vol. 9, CRC Press.

Graf A., Hosford W. 1994 Influence of strain path changes on forming limit diagrams of A1 6111 T4, International Journal of Mechanical Sciences 36, 897–910.

Greene, D.L. and DeCicco, J., 2000. Engineering-Economic Analyses of Automotive fuel Economy Potential in the United States 1. Annual Review of Energy and the Environment, 25(1), pp.477-535.

Grilli, N., Janssens, K.G. and Van Swygenhoven, H., 2015. Crystal plasticity finite element modelling of low cycle fatigue in fcc metals. Journal of the Mechanics and Physics of Solids, 84, pp.424-435.

Groh, S., Marin, E.B., Horstemeyer, M.F., Zbib, H.M., 2009. Multiscale modeling of the plasticity in an aluminum single crystal, International Journal of Plasticity, 25, 1456-1473.

Gronostajski, J. Z., Zimniak, Z. 1992 Theoretical simulation of sheet behaviour in forming processes, Journal of Materials Processing Technology 31, 57–63.

Gurtin, M.E., Anand, L., Lele, S.P., 2007. Gradient single-crystal plasticity with free energy dependent on dislocation densities, Journal of the Mechanics and Physics of Solids, 55, 1853–78.

Haessner, F., (Ed.), 1978. Recrystallization. Dr. Riederer Verlag, Stuttgart.

Hall, E.O., 1951. The deformation and ageing of mild steel. III: discussion of results, Proceedings of the Physical Society B, 64, 747.

Hallberg, H., Wallin, M., Ristinmaa, M., 2010. Simulation of discontinuous dynamic recrystallization in pure cu using a probabilistic cellular automaton, Computational Materials Science, 49 (1), 25–34.

Hallén, H., 1985. A theory of dynamic recovery in FCC metals. Materials Science and Engineering, 72(2), pp.119-123.

Han, T-S., Dawson, P.R., 2007. A two-scale deformation model for polycrystalline solids using a strongly-coupled finite element methodology, Computer Methods in Applied Mechanics and Engineering, 196, 2029–43.

Hansen, B.L., Beyerlein, I.J., Bronkhorst, C.A., Cerreta, E.K., Dennis-Koller, D., 2013. A dislocation-based multi-rate single crystal plasticity model, International Journal of Plasticity, 44, 129-146.

Harewood, F.J., McHugh, P.E., 2006. Investigation of finite element mesh independence in rate dependent materials. Computational Materials Science, 37, 442–53.

Harewood, F.J., McHugh, P.E., 2007. Comparison of the implicit and explicit finite element methods using crystal plasticity, Computational Materials Science, 39, 481–94.

Harren, S., Lowe, T., Asaro, R. J., Needleman, A. 1989 Analysis of Large Strain Shear in Rate-Dependent Cubic Polycrystals: Correlation Micro- and Macromechanics, Philisophical Transactions of the Royal Society of London. Series A 328, 443–500.

Hartig, C., Mecking, H., 2005. Finite element modelling of two phase FeCu polycrystals, Computational Materials Science, 32, 370–7.

Hasija, V., Ghosh, S., Mills, M.J., Joseph, D.S., 2003. Deformation and creep modeling in polycrystalline Ti–6Al alloys, Acta Materialia, 51, 4533–49.

Hecker, S. S. 1975 Formability of aluminum alloy sheets, Journal of Engineering Materials Technology 97, 66–73.

Hesselbarth, H.W., Göbel, I.R., 1991. Simulation of recrystallization by cellular automata. Acta Metallurgica et Materialia, 39 (9), 2135–2143.

Hidnert, P. and Krider, H.S., 1952. Thermal expansion of aluminum and some aluminum alloys. Journal of Research of the National Bureau of Standards, 48(3), pp.209-220.

Hill, R. 1952 On discontinuous plastic states, with special reference to localized necking in thin sheets, Journal of the Mechanics and Physics of Solids 1, 19–30.

Himmel, L. (Ed.), 1962. Recovery and Recrystallization of Metals. AIME. Published by Interscience Publishers (1963).

Hirth, J.P., Lothe, J., 1982. Theory of Dislocations 2nd Ed., John Wiley & Sons.

Hosford, W. F., Caddell, R. M. "Metal Forming: Mechanics and Metallurgy", Cambridge University Press, New York, 2011.

Hu, X.H., Jain, M., Wu, P.D., Wilkinson, D.S., Mishra, R.K., 2010, A macro-micro multi-level modeling scheme to study the effect of particle distribution on wrap-bendability of AA5754 sheet alloys. Journal of Materials Processing Technology, 210, 1232-1242.

Hull, D., Bacon, D.J., 2001. Introduction to Dislocations 4th Ed., Butterworth-Heinemann, Great Britain.

Humphreys, F.J., 1992a. Modeling mechanisms and microstructures of recrystallization. Mater. Sci. Technol. 8, 135–143.

Humphreys, F.J., 1997. A unified theory of recovery, recrystallization and grain growth, based on the stability and growth of cellular microstructures-i the basic model. Acta Mater. 45, 4231–4240.

Humphreys, F.J., Ferry, M., 1997. Applications of electron backscattered diffraction to studies of annealing of deformed metals. Mater. Sci. Technol. 13 (1), 85–90.

Humphreys, F.J., Hatherly, M., 1995. Recrystallization and Related Annealing Phenomena, vol. 8. Pergamon Press, Oxford, 235.

Humphreys, F.J., Hatherly, M., 2004. Recrystallization and Related Annealing Phenomena. Elsevier.

Hutchinson, J. W., Neale, K. W., Needleman, A. 1978(a) Sheet Necking I: validity of plane stress assumptions of the long-wavelength approximation, in: Koistinen K. P., Wang N. -M. (Eds.), Mechanics of Sheet Metal Forming, Plenum, New York, pp. 111–126.

Hutchinson, J. W., Neale, K. W. 1978(b) Sheet Necking II: time independent behaviour, in: Koistinen K. P., Wang N. -M. (Eds.), Mechanics of Sheet Metal Forming, Plenum, New York, pp. 127–153.

Hutchinson, J. W., Neale, K. W. 1978(c) Sheet Necking III: strain-rate effects, in: Koistinen K. P., Wang N. -M. (Eds.), Mechanics of Sheet Metal Forming, Plenum, New York, pp. 269–285.

Iadicola, M. A., Foecke, T., Banovic, S. W. 2008 Experimental observations of evolving yield loci in biaxially strained AA5754-O, International Journal of Plasticity 24, 2084–2101.

Inal, K., 2002. Numerical simulation of sheet metal forming processes and localized deformation phenomena for fcc polycrystals. National Library of Canada, University of Sherbrooke, PhD Thesis.

Inal, K., Simha, H.M., Mishra, R.K., 2008. Numerical modeling of second-phase particle effects on localized deformation, Journal of Engineering Materials Technology, 130, 021003.

Inal, K., Wu, P.D., Neale, K.W., 2002. Finite element analysis of localization in FCC polycrystalline sheets under plane stress tension, International Journal of Solids and Structures, 39, 3469–3486.

Jain, A., Agnew, S.R., 2007. Modeling the temperature dependent effect of twinning on the behavior of magnesium alloy AZ31B sheet, Materials Science and Engineering A, 462, 29–36.

Jobba, M., Mishra, R.K. and Niewczas, M., 2015. Flow stress and work-hardening behaviour of Al–Mg binary alloys. International Journal of Plasticity, 65, pp.43-60.

Johnson, W.A., Mehl, R.F., 1939. Reaction kinetics in the process of nucleation and growth. Trans. Metall. Soc. AIME 135, 416–458.

Kabirian, F., Khan. A.S., Pandey, A., 2013, Negative to positive strain rate sensitivity in 5XXX series aluminum alloys: Experiment and constitutive modeling, International Journal of Plasticity, 2013, In Press.

Kalidindi, S.R., 1998. Incorporation of deformation twinning in crystal plasticity models, Joural of the Mechanics and Physics of Solids, 46, 267–90.

Kalidindi, S.R., Bronkhorst, C.A., Anand, L., 1992. Crystallographic texture evolution in bulk deformation processing of fcc metals, Journal of the Mechanics and Physics of Solids, 40, 537–69.

Kalidindi, S.R., Schoenfeld, S.E., 2000. On the prediction of yield surfaces by the crystal plasticity models for fcc polycrystals, Materials Science and Engineering A, 293, 20–129.

Kalidindi, SR., 2001. Modeling anisotropic strain hardening and deformation textures in low stacking fault energy fcc metals, International Journal of Plasticity, 17, 837–60.

Kalisher, S., 1881. Über den Einfluss der Wärme auf die Molekularstruktur des Zinks. Ber. Dtsch. Chem. Ges. XIV, 2727–2753.

Kang, J., Wilkinson, D.S., Jain, M., Embury, A.J., Beaudoin, A.J., Kim, S., Mishra, R., Sachdev, A.K., 2006. On the sequence of inhomogeneous deformation processes occurring during tensile deformation of strip cast AA5754, Acta Materialia, 54, 209–218.

Keeler, S. P. 1965 Determination of forming limits in automotive stampings, Sheet Metal Industries 42, 683–691.

Keh, A.S., Weissman, S., 1963. In: Thomas, G., Washburn, J. (Eds.), Deformation Structure in Body-centered Cubic Metals. Electron Microscopy and Strength of Crystals. Interscience, New York, pp. 231–300.

Khan, A.S., Baig, M., 2011, Anisotropic responses, constitutive modeling and the effects of strain-rate and temperature on the formability of aluminum alloy, International Journal of Plasticity, 27, 522-538.

Khan, A. S., Huang, S. “Continuum Theory of Plasticity”, John Wiley and Sons, Inc., New York, NY, 1995.

Kim, H-K., Oh, S-I., 2003. Finite element analysis of grain-by-grain deformation by crystal plasticity with couple stress, International Journal of Plasticity, 19, 1245–70.

Kim, J.H., Kim, D., Barlat, F. and Lee, M.G., 2012. Crystal plasticity approach for predicting the Bauschinger effect in dual-phase steels. Materials Science and Engineering: A, 539, pp.259-270.

Kim, J.H., Kim, D., Lee, Y.-S., Lee, M.-G., Chung, K., Kim, H.-Y., Wagoner, R.H., 2013, A temperature-dependent elasto-plastic constitutive model for magnesium alloy AZ31 sheets, International Journal of Plasticity, 50, 66-93.

Kim, K-H., Kim, H-K., Oh, S-I., 2006. Deformation behavior of pure aluminum specimen composed of a few grains during simple compression, Journal of Materials Processing Technololgy, 171, 205–13.

Klopp, R.W., Clifton, R.J., Shwaki, T.G., 1985. Pressure-shear impact and the dynamic viscoplastic response of metals, Mechanics of Materials, 4, 375-385.

Knezevic, M., Beyerlein, I.J., Brown, D.W., Sisneros, T.A. and Tomé, C.N., 2013. A polycrystal plasticity model for predicting mechanical response and texture evolution during strain-path changes: application to beryllium. International Journal of Plasticity, 49, pp.185-198.

Knockaert, R., Chastel, Y., Massoni, E. 2002 Forming limits prediction using rate-independent polycrystalline plasticity, International Journal of Plasticity 18, 231–247.

Kocks, U.F., 1967. Statistical treatment of penetrable obstacles. Canadian Journal of Physics, 45(2), pp.737-755.

Kocks, U.F., 1976. Laws for work-hardening and low-temperature creep, Journal of Engineering Materials and Technology, 76-85.

Kocks, U.F., 2001. Realistic constitutive relations for metal plasticity. Materials Science and Engineering: A, 317(1), pp.181-187.

Kocks, U.F., Argon, A.S., Ashby, M.F., 1975. Thermodynamics and Kinetics of Slip. In: Chalmers, B., Christian, J.W. and Massalski, T.B., Eds., Progress in Materials Science, Pergamon Press, Oxford.

Kocks, U.F. and Mecking, H., 2003. Physics and phenomenology of strain hardening: the FCC case. Progress in materials science, 48(3), pp.171-273.

Kocks, U.F., Tome, C.N., Wenk, H.R., Mecking, H., 2001. Texture and Anisotropy, Cambridge University Press, Cambridge.

Kok, S., Beaudoin, A.J., Tortorelli, D.A., 2002. A polycrystal plasticity model based on the mechanical threshold, International Journal of Plasticity 18, 715-741.

Kolmogorov, A.N., 1937. Statistical theory of crystallization of metals. Izv. Akad. Nauk SSSR, Met. 1, 355–359.

Kooiman, M., Hütter, M. and Geers, M.G.D., 2015. Microscopically derived free energy of dislocations. Journal of the Mechanics and Physics of Solids, 78, pp.186-209.

Kooiman, M., Hütter, M. and Geers, M.G.D., 2016. Free energy of dislocations in a multi-slip geometry. Journal of the Mechanics and Physics of Solids, 88, pp.267-273.

Kröner, E., 1961. On the plastic deformation of polycrystals, Acta Metallurgica, 9, 155–61.

Kröner, E., 1961. On the plastic deformation of polycrystals, Acta Metallurgica, 9, 155–61.

Kuchnicki, S.N., Cuitiño, A.M., Radovitzky, R.A., 2006. Efficient and robust constitutive integrators for single-crystal plasticity modeling, International Journal of Plasticity, 22, 1988–2011.

Kuhlmann-Wilsdorf, D., 1970. A critical test on theories of work-hardening for the case of drawn iron wire. Metallurgical Transactions, 1(11), pp.3173-3179.

Kumar, D., Bieler, T.R., Eisenlohr, P., Mason, D.E., Crimp, M.A., Roters, F., et al., 2008. On predicting nucleation of microcracks due to slip-twin interactions at grain boundaries in duplex c-TiAl, Journal of Engineering Materials Technology, 130, 021012-1–021012-12.

Kuroda, M., Tvergaard, V. 2000 Effect of strain path change on limits of ductility of anisotropic metal sheets, International Journal of Mechanical Sciences 42, 867–887.

Kuroda, M., Tvergaard, V., 2004, Shear band development in anisotropic bent specimens, European Journal of Mechanics: A, 23, 811-821.

Kuroda, M., Tvergaard, V., 2007, Effects of texture on shear band formation in plane strain tension/compression and bending, International Journal of Plasticity 23, 244-272.

Kuroda, M., Tvergaard, V., 2008. On the formulations of higher-order strain gradient crystal plasticity models, Journal of the Mechanics and Physics of Solids, 56, 1591–608.

Kurukuri, S., Van Den Boogaard, A.H., Miroux, A., Holmedal, B., 2009. Warm forming simulation of Al-Mg sheet, Journal of Materials Processing Technology, 209, 5636-5645.

Kysar, J.W., Gan, Y.X., Mendez-Arzuza, G., 2005. Cylindrical void in a rigidideally plastic single crystal. Part I: anisotropic slip line theory solution for face-centered cubic crystals, International Journal of Plasticity, 21, 1481–520.

Lee, B.-J., Vecchio, K.S., Ahzi, S., Schoenfeld, S., 1997, Modeling the mechanical behaviour of Tantalum, Metallurgical and Materials Transactions A, 28A, 113-122.

Lee, M.G., Wang, J., Anderson, P.M., 2007. Texture evolution maps for upset deformation of body-centered cubic metals, Materials Science and Engineering A, 463, 263–70.

Leibfried, G., Ludwig, W., 1961. Theory of anharmonic effects in crystals, Solid State Physics, 12, 275–444.

Li, D., Ghosh, A., 2003. Tensile deformation behavior of aluminum alloys at warm forming temperatures. Materials Science and Engineering A. 352, 279-286.

Li, D., Ghosh, A., 2004. Biaxial warm forming behaviour of aluminum sheet alloys. Journal of Materials Processing Technology, 145, 281-293.

Li, H., Choo, H., Liaw, P., 2007. The effect of temperature on strain rate sensitivity in nanocrystalline Ni-Fe alloy, Journal of Applied Physics, 101, 063536.

Li, H., Wu, C., Yang, H., 2013. Crystal plasticity modeling of the dynamic recrystallization of two-phase titanium alloys during isothermal processing, International Journal of Plasticity, 51, 271–291.

Li, H.J., Jiang, Z., Han, J.T., Wei, D.B., Pi, H.C., Tieu, A.K., 2008. Crystal plasticity finite element modeling of necking of pure aluminium during uniaxial tensile deformation, Steel Research International, 2, 655–62.

Li, H.W., Yang, H., Sun, Z.C., 2008. A robust integration algorithm for implementing rate dependent crystal plasticity into explicit finite element method, International Journal of Plasticity, 24, 267–88.

Li, H.Z., Wang, H.J., Liang, X.P., Liu, H.T., Liu, Y. and Zhang, X.M., 2011. Hot deformation and processing map of 2519A aluminum alloy. Materials Science and Engineering: A, 528(3), pp.1548-1552.

Li, J., Carsley, J., Stoughton, T., Hector Jr., L., Hu, S. 2013 Forming limit analysis for two-stage forming of 5182-O aluminum sheet with intermediate annealing. International Journal of Plasticity 45 21–43.

Li, L., Anderson, P.M., Lee, M-G., Bitzek, E., Derlet, P., Van Swygenhoven H., 2009. The stress–strain response of nanocrystalline metals: a quantized crystal plasticity approach, Acta Materialia, 57, 812–22.

Li, S., Donohue, B.R., Kalidindi, S.R., 2008. A crystal plasticity finite element analysis of cross-grain deformation heterogeneity in equal channel angular extrusion and its implications for texture evolution, Materials Science and Engineering A, 480, 17–23.

Li, S., Kalidindi, S.R., Beyerlein, I.J., 2005. A crystal plasticity finite element analysis of texture evolution in equal channel angular extrusion, Materials Science and Engineering A, 410–411, 207–12.

Li, S.Y., Van Houtte, P., Kalidindi, S.R., 2004. A quantitative evaluation of the deformation texture predictions for aluminium alloys from crystal plasticity finite element method, Modelling and Simulation in Materials Science and Engineering, 12, 845–70.

Liu, W.H., Zhang, X.M., Tang, J.G., Du, Y., 2007. Simulation of void growth and coalescence behavior with 3D crystal plasticity theory, Computational Materials Science, 40, 130–9.

Liu, G., Scudino, S., Li, R., Kühn, U., Sun, J., Eckert, J., 2011. Coupling effect of primary voids and secondary voids on the ductile fracture of heat-treatable aluminum alloys, Mechanics of Materials, 43, 556–566.

Loge, R., Bernacki, M., Resk, H., Delannay, L., Digonnet, H., Chastel, Y., et al., 2008. Linking plastic deformation to recrystallization in metals using digital microstructures, Philosophical Magazine, 88(30), 3691–712.

Louat, N., 1978. On the thermal activation of dislocation motion through random point obstacles. Acta Metallurgica, 26(10), pp. 1597-1604.

Ma, A., Roters, F., 2004. A constitutive model for fcc single crystals based on dislocation densities and its application to uniaxial compression of aluminium single crystals, Acta Materialia, 52(12), 3603–12.

Ma, A., Roters, F., Raabe, D., 2006a. A dislocation density based constitutive model for crystal plasticity FEM including geometrically necessary dislocations, Acta Materialia, 54, 2169–79.

Ma, A., Roters, F., Raabe, D., 2006b. On the consideration of interactions between dislocations and grain boundaries in crystal plasticity finite element modeling—theory, experiments, and simulations, Acta Materialia, 54, 2181–94.

Mahabunphachai, S., Koc, M., 2010. Investigations on forming of aluminum 5052 and 6061 sheet alloys at warm temperatures, Materials & Design, 31, 2422-2434.

Marketz, W.T., Fischer, F.D., Clemens. H., 2003. Deformation mechanisms in TiAl intermetallics—experiments and modeling, International Journal of Plasticity, 19, 281–321.

Marketz, W.T., Fischer, F.D., Kauffmann, F., Dehm, G., Bidlingmaier, T., Wanner, A., et al., 2002. On the role of twinning during room temperature deformation of TiAl based alloys, Materials Science and Engineering A, 329– 331, 177–83.

Marciniak, Z., Kuczynski, K., 1967. Limit strains in the processes of stretch-forming sheet metal, International Journal of Mechanical Sciences, 9, 609–620.

Marciniak, Z., Kuczynski, K., Pokora, T. 1973 Influence of the plastic properties of a material on the forming limit diagram for sheet metal in tension, International Journal of Mechanical Sciences 15, 789–800.

Mayama, T., Sasaki, K., Kuroda, M., 2008. Quantitative evaluations for strain amplitude dependent organization of dislocation structures due to cyclic plasticity in austenitic stainless steel 316L, Acta Materialia, 56, 2735–43.

Mayeur, J.R., McDowell, D.L., Neu, R.W., 2008. Crystal plasticity simulations of fretting of Ti–6Al–4V in partial slip regime considering effects of texture, Computational Materials Science, 41, 356–65.

McDowell, D.L., 2008. Viscoplasticity of heterogeneous metallic materials, Materials Science and Engineering R, 62, 67–123.

McGarry, J.P., O'Donnell, B.P., McHugh, P.E., McGarry, J.G., 2004. Analysis of the mechanical performance of a cardiovascular stent design based on micromechanical modeling, Computational Materials Science, 31, 421–38.

McHugh, P.E., Mohrmann, R., 1997. Modelling of creep in a Ni base superalloy using a single crystal plasticity model, Computational Materials Science, 9, 134–40.

McQueen, H.J., Spigarelli, S., Kassner, M.E., Evangelista, E., 2011. Hot Deformation and Processing of Aluminum Alloys, CRC Press.

Mecking, H., Nicklas, B., Zarubova, N. and Kocks, U.F., 1986. A "universal" temperature scale for plastic flow. Acta Metallurgica, 34(3), pp.527-535.

Meissonnier, F.T., Busso, E.P., O'Dowd, N.P., 2001. Finite element implementation of a generalised non-local rate-dependent crystallographic formulation for finite strains, Computational Materials Science, 17, 601–40.

Melchior, M.A., Delannay, L., 2006. A texture discretization technique adapted to polycrystalline aggregates with non-uniform grain size, Computational Materials Science, 37, 557–64.

Merklein, M., Lechler, J., Geigner, M. 2006 Characterization of the flow properties of the quenchable ultra-high strength steel 22MnB5, in: Annals of the CIRP 1, 229–232.

Mianroodi, J.R., Hunter, A., Beyerlein, I.J. and Svendsen, B., 2016. Theoretical and computational comparison of models for dislocation dissociation and stacking fault/core formation in fcc crystals. Journal of the Mechanics and Physics of Solids.

Miehe, C., 1996. Exponential map algorithm for stress updates in anisotropic multiplicative elastoplasticity for single crystals, International Journal for Numerical Methods in Engineering, 39, 3367–90.

Miehe, C., Schröder, J., Schotte, J., 1999. Computational homogenization analysis in finite plasticity simulation of texture development in polycrystalline materials, Computer Methods in Applied Mechanics and Engineering, 171, 387–418.

Mika, D.P., Dawson, P.R., 1998. Effects of grain interaction on deformation in polycrystals, Materials Science and Engineering A, 257, 62–76.

Mika, D.P., Dawson, P.R., 1999. Polycrystal plasticity modeling of intracrystalline boundary textures, Acta Materialia, 47, 1355–69.

Miller, M.P., Turner, T.J., 2001. A methodology for measuring and modeling crystallographic texture gradients in processed alloys, International Journal of Plasticity, 17, 783–805.

Mohammadi, M., Brahme, A.P., Mishra, R.K., Inal, K., 2014. Effects of post-necking hardening behaviour and equivalent stress-strain curves on the accuracy of M-K based forming limit diagrams, Computational Materials Science, 85, 316–323.

Mompiou, F., Caillard, D., Legros, M. and Mughrabi, H., 2012. In situ TEM observations of reverse dislocation motion upon unloading in tensile-deformed UFG aluminium. Acta Materialia, 60(8), pp.3402-3414.

Murphy, BP., Cuddy, H., Harewood, F.J., Connolley, T., McHugh, P.E., 2006. The influence of grain size on the ductility of micro-scale stainless steel stent struts, Journal of Materials Science Materials in Medicine, 17, 1–6.

Musienko, A., Tatschl, A., Schmidegg, K., Kolednik, O., Pippan, R., Cailletaud, G., 2007. Three-dimensional finite element simulation of a polycrystalline copper specimen, Acta Materialia, 55, 4121–36.

Nabarro, F.R.N., 1989. Work hardening and dynamical recovery of FCC metals in multiple glide. Acta metallurgica, 37(6), pp. 1521-1546.

Naka, T., Torikai, G., Hino, R., Yoshida, F., 2001 The effects of temperature and forming speed on the forming limit diagram for type 5083 aluminum-magnesium alloy sheet, Journal of Materials Processing Technology 113, 648–653.

Nakamachi, E., Tam, N.N., Morimoto, H., 2007. Multi-scale finite element analyses of sheet metals by using SEM-EBSD measured crystallographic RVE models, International Journal of Plasticity, 23, 450–89.

Nakamachi, E., Xie, C.L., Harimoto, M., 2001. Drawability assessment of BCC steel sheet by using elastic/crystalline viscoplastic finite element analyses, International Journal of Mechanical Sciences, 43, 631–52.

NAO Sciences. Effectiveness and impact of corporate average fuel economy (CAFÉ) standards. Washington, DC: National Academies Press; 2002.

Neale, K.W., 1993. Use of crystal plasticity in metal forming simulations, 1993, International Journal of Mechanical Sciences, 1993, 35, 1053–63.

Neil, C.J., Agnew, S. R. 2009 Crystal plasticity-based forming limit prediction for non-cubic metals: application to Mg alloy AZ31B, International Journal of Plasticity 25, 379–398.

Nes, E. and Marthinsen, K., 2002. Modeling the evolution in microstructure and properties during plastic deformation of fcc-metals and alloys–an approach towards a unified model. Materials Science and Engineering: A, 322(1), pp.176-193.

Niewczas, M., Jobba, M. and Mishra, R.K., 2015. Thermally activated flow of dislocations in Al–Mg binary alloys. Acta Materialia, 83, pp.372-382.

Nye, J.F., 1953. Some geometrical relations in dislocated crystals, Acta Metallurgica, 1, 53–62.

Ocenasek, J., Rodriguez Ripoll, M., Weygand, S.M., Riedel, H., 2007. Multigrain finite element model for studying the wire drawing process, Computational Materials Science, 39, 23–8.

Okumura, D., Higashi, Y., Sumida, K., Ohno, N., 2007. A homogenization theory of strain gradient single crystal plasticity and its finite element discretization, International Journal of Plasticity, 23, 1148–66.

Orowan, E., 1934. Zur Kristallplastizität: iii. Über den Mechanismus des Gleitvorganges. Z. Phys. 89, 634–659.

Orowan, E., 1940. Problems of plastic gliding. Proceedings of the Physical Society, 52(1), p.8.Park, D.Y. and Niewczas, M., 2008. Plastic deformation of Al and AA5754 between 4.2 K and 295K. Materials Science and Engineering: A, 491(1), pp.88-102.

Palumbo, G., Tricarico, L., 2007. Numerical and experimental investigations on the Warm Deep Drawing process of circular aluminum alloy specimens. Journal of Materials Processing Technology, 184, 115-123.

Pandey, A., Khan, A.S., Kim, E., Choi, S., Gnaupel-Herold, T., 2013. Experimental and numerical investigation of yield surface, texture, and deformation mechanisms in AA5754 over low to high temperatures and strain rates, International Journal of Plasticity, 41, 165–188.

Park, D., Niewczas, M., 2008. Plastic deformation of Al and AA5754 between 4.2 K and 295 K, Materials Science and Engineering, 491, 88-102.

Park, S.J., Han, H.N., Oh, K.H., Raabe, D., Kim, J.K., 2002. Finite element simulation of grain interaction and orientation fragmentation during plastic deformation of BCC metals, Materials Science Forum, 408- 4, 371–6.

Patil, S.D., Narasimhan, R., Biswas, P., Mishra, R.K., 2008. Crack tip fields in a single edge notched aluminum single crystal specimen. Journal or Engineering Materials Technology, 130, 021013.

Petch, N.J., 1953. The cleavage strength of polycrystals, Journal of the Iron and Steel Institute, 25.

Peirce, D., Asaro, R.J., Needleman, A., 1982. An analysis of nonuniform and localized deformation in ductile single crystals, Acta Metallurgica, 30, 1087–119.

Peirce, D., Asaro, R.J., Needleman, A., 1983. Material rate dependence and localized deformation in crystalline solids, Acta Metallurgica, 31, 1951–76.

Perzyna, P., 1988. Temperature and rate dependent theory of plasticity of crystalline solids, Revue de Physique Appliquee, No 4, 445-459.

Polanyi, M., 1934. Über eine Art Gitterstörung die einen Kristall plastich machen könnte. Z. Phys. 89, 660–664.

Pond, R.C., Casey, S.M., 1992. Topological theory of line-defects on crystal surfaces, and their interactions with bulk and interfacial defects. In: Equilibrium

Prasad, Y.V.R.K., Sasidhara, S., 1997. Hot working guide: a compendium of processing maps, American Society of Metals International. Structure and Properties of Surfaces and Interfaces. Springer, pp. 139–174.

Popova, E., Staraselski, Y., Brahme, A., Mishra, R.K., Inal, K., 2015. Coupled crystal plasticity – Probabilistic cellular automata approach to model dynamic recrystallization in magnesium alloys, International Journal of Plasticity, 66, 85–102.

Potirniche, G.P., Hearndon, J.L., Horstemeyer, M.F., Ling, X.W., 2006. Lattice orientation effects on void growth and coalescence in fcc single crystals, International Journal of Plasticity, 22, 921–42.

Raabe, D., 1999. Introduction of a scalable three-dimensional cellular automaton with a probabilistic switching rule for the discrete mesoscale simulation of recrystallization phenomena, Philosophical Magazine A, 79 (10), 2339–2358.

Raabe, D., 2000. Yield surface simulation for partially recrystallized aluminum polycrystals on the basis of spatially discrete data, Computational Materials Science, 19, 13–26.

Raabe, D., 2002. Cellular automata in materials science with particular reference to recrystallization simulation, Annual Review of Materials Research, 32, 53–76.

Raabe, D., 2007. Recrystallization models for the prediction of crystallographic textures with respect to process simulation, Journal of Strain Analysis for Engineering Design, 42, 253–68.

Raabe, D., 2014. In – Physical Metallurgy 5th Ed., Recovery and Recrystallization: Phenomena, Physics, Models, Simulation, Elselvier B.V., 2291–2396.

Raabe, D., Becker, R., 2000. Coupling of a crystal plasticity finite element model with a probabilistic cellular automaton for simulating primary static recrystallization in aluminum, Modelling and Simulation in Materials Science and Engineering, 8, 445–62.

Raabe, D., Klose, P., Engl, B., Imlau, K-P., Friedel, F., Roters, F., 2002. Concepts for integrating plastic anisotropy into metal forming simulations, Advanced Engineering Materials, 4, 169–80.

Raabe, D., Roters, F., 2004. Using texture components in crystal plasticity finite element simulations, International Journal of Plasticity, 20, 339–61.

Raabe, D., Sachtleber, M., Weiland, H., Scheele, G., Zhao, Z., 2003. Grain-scale micromechanics of polycrystal surfaces during plastic straining, Acta Materialia, 51, 1539–60.

Raabe, D., Sachtleber, M., Zhao, Z., Roters, F., Zaefferer, S., 2001. Micromechanical and macromechanical effects in grain scale polycrystal plasticity experimentation and simulation, Acta Materialia, 49(17), 3433–41.

Raabe, D., Wang, Y., Roters, F., 2005. Crystal plasticity simulation study on the influence of texture on earing in steel, Computational Materials Science, 34, 221–34.

Raabe, D., Zhao, Z., Mao, W., 2002. On the dependence of in-grain subdivision and deformation texture of aluminum on grain interaction, Acta Materialia, 50, 4379–94.

Raabe, D., Zhao, Z., Park, S-J., Roters, F., 2002. Theory of orientation gradients in plastically strained crystals, Acta Materialia, 50, 421–40.

Raabe, D., Zhao, Z., Roters, F., 2004. Study on the orientational stability of cube-oriented FCC crystals under plane strain by use of a texture component crystal plasticity finite element method, Scripta Materialia, 50, 1085–90.

Radhakrishnan, B., Sarma, G.B., 2008. Coupled simulations of texture evolution during deformation and recrystallization of fcc and bcc metals, Materials Science and Engineering A, 494 (1), 73–79.

Radhakrishnan, B., Sarma, G.B., Zacharia, T., 1998. Modeling the kinetics and microstructural evolution during static recrystallization Monte Carlo simulation of recrystallization, Acta Materialia, 46 (12), 4415–4433.

Radhakrishnan, B., Sarma, G., Weiland, H., Baggethun, P., 2002. Simulations of deformation and recrystallization of single crystals of aluminum containing hard particles, Modelling and Simulation in Materials Science and Engineering, 8, 737–50.

Ravichandran, N., Prasad, Y .V .R.K., 1991. Dynamic recrystallization during hot deformation of aluminum: a study using processing maps. Metallurgical Transactions A, 22, 2339-2348.

Rezaee-Bazzaz, A., Noori, H., Mahmudi, R. 2011 Calculation of forming limit diagrams using Hill's 1993 yield criterion, International Journal of Mechanical Sciences 53, 262–270.

Rice, J.R., 1971. Inelastic constitutive relations for solids: an internal variable theory and its application to metal plasticity, Journal of the Mechanics and Physics of Solids, 19, 433–55.

Ritz, H., Dawson, P.R., 2009. Sensitivity to grain discretization of the simulated crystal stress distributions in FCC polycrystals, Modelling and Simulation in Materials Science and Engineering, 17.

Roberts, W., Ahlblom, B., 1978. A nucleation criterion for dynamic recrystallization during hot working, Acta Metallurgica, 26 (5), 801–813.

Robinson, J.M. and Shaw, M.P., 1994. Microstructural and mechanical influences on dynamic strain aging phenomena. International Materials Reviews, 39(3), pp.113-122.

Rollett, A.D., Raabe, D., 2001. A hybrid model for mesoscopic simulation of recrystallization, Computational Materials Science, 21 (1), 69–78.

Rosenhain, W., 1914. An Introduction to Physical Metallurgy. Constable, London.

Rossi, M., Chiappini, G., Sasso, M. 2010 Characterization of aluminum alloys using 3D full field measurement, in: Proceedings of the SEM Annual Conference, Indianapolis, Indiana, USA.

Rossiter, J., Brahme, A., Simha, H., Inal, K., Mishra, R., 2010. A new Crystal Plasticity Scheme for Explicit Time Integration Codes to Simulate Deformation in 3D Microstructures: Effects of Strain Path, Strain Rate and Thermal Softening on Localized Deformation in the Aluminum Alloy 5754 During Simple Shear, International Journal of Plasticity, 26(12), 1702-1725.

Rossiter, J., Brahme, A., Inal, K., Mishra, R., 2013. Numerical Analysis of Surface Roughness during Bending of FCC Single Crystals and Polycrystals. International Journal of Plasticity, 46, 82-93.

Roters, F., Eisenlohr, P., Hantcherli, L., Tjahjanto, D.D., Bieler, T.R., Raabe, D., 2010. Overview of constitutive laws, kinematics, homogenization and multiscale methods in crystal plasticity finite-element modeling: Theory, experiments, applications. Acta Mater. 58, 1152–1211.

Roters, F., Jeon-Haurand, H.S., Raabe, D., 2005. A texture evolution study using the texture component crystal plasticity FEM, Materials Science Forum, 495–497, 937–44.

Roters, F., Wang, Y., Kuo, J-C., Raabe, D., 2004. Comparison of single crystal simple shear deformation experiments with crystal plasticity finite element simulations, Advanced Engineering Materials, 6(8), 653–6.

Sachs, G., 1928. Zur Ableitung einer Fliessbedingung, Z VDI, 72, 734–6.

Sachs, G., 1928. Zur Ableitung einer Fliessbedingung, Z VDI, 72, 734–6.

Sachtleber, M., Zhao, Z., Raabe, D., 2002. Experimental investigation of plastic grain interaction, Materials Sciemce and Engineering A, 336(1-2), 81–7.

Saimoto, S., 2006. Dynamic dislocation–defect analysis. Philosophical Magazine, 86(27), pp.4213-4233.

Saimoto, S., Van Houtte, P., 2009. Recovery studies of cold rolled aluminum sheet using X-ray line broadening and activations volume determinations, Acta Materialia, 57, 4822–4834.

Saimoto, S., Van Houtte, P., 2011. Constitutive relation based on Taylor slip analysis to replicate work-hardening evolution, Acta Materialia, 59, 602–612.

Salem, A.A., Kalidindi, S.R., Semiatin, S.L., 2005. Strain hardening due to deformation twinning in a-titanium: constitutive relations and crystal-plasticity modeling, Acta Materialia, 53, 3495–502.

Sarma, G.B., Dawson, P.R., 1996a. Effects of interactions among crystals on the inhomogeneous deformations of polycrystals, Acta Materialia, 44, 1937–53.

Sarma, G.B., Dawson, P.R., 1996b. Texture predictions using a polycrystal plasticity model incorporating neighbor interactions, International Journal of Plasticity, 12(8), 1023–54.

Sarma, G.B., Radhakrishnan, B., 2004. Modeling microstructural effects on the evolution of cube texture during hot deformation of aluminum, Materials Science and Engineering A, 385, 91–104.

Sarma, G.B., Radhakrishnan, B., Zacharia, T., 1998. Finite element simulations of cold deformation at the mesoscale, Computational Materials Science, 12, 105–23.

Schafler, E., Simon, K., Bernstorff, S., Hanák, P., Tichy, G., Ungár, T. and Zehetbauer, M.J., 2005. A second-order phase-transformation of the dislocation structure during plastic deformation determined by in situ synchrotron X-ray diffraction. Acta materialia, 53(2), pp. 315-322.

Schoeck, G. and Seeger, A., 1955. Report on the Conference of Defects in Crystalline Solids, Bristol, 1954. London: The Physical Society.

Schwindt, C., Schlosser, F., Bertinetti, M.A., Stout, M., Signorelli, J.W. 2015 Experimental and Visco-Plastic Self-Consistent evaluations of forming limit diagrams for anisotropic sheet metals: An efficient and robust implementation of the M-K model. International Journal of Plasticity, 73, 62–99.

Sebald, R., Gottstein, G., 2002. Modeling of recrystallization textures: interaction of nucleation and growth. Acta. Mater. 50, 1587–1598.

Seeger, A., Berner, R., Wolf, H., 1959. Z. Physic, 155, pp.247

Semiatin, S.L., Weaver, D.S., Goetz, R.L., Thomas, J.P., Turner, T.J., 2007. Deformation and recrystallization during thermomechanical processing of a nickel-base superalloy ingot material, Materials Science Forum, 550, 129–40.

Serenelli, M.J., Bertinetti, M.A., Signorelli J.W. 2011 Study of limit strains for FCC and BCC sheet metal using polycrystal plasticity, International Journal of Solids and Structures 48, 1109–1119.

Sevillano, J.G., Van Houtte, P. and Aernoudt, E., 1980. Large strain work hardening and textures. Progress in Materials Science, 25(2-4), pp.69-134.

Signorelli, J.W., Bertinetti, M.A., Turner, P.A. 2009 Predictions of forming limit diagrams using a rate-dependent polycrystal self-consistent plasticity model, International Journal of Plasticity 25, 1–25

Sinha, S., Ghosh, S., 2006. Modeling cyclic ratcheting based fatigue life of HSLA steels using crystal plasticity FEM simulations and experiments, International Journal of Fatigue, 28, 1690–704.

Siska, F., Forest, S., Gumbsch, P., 2007. Simulations of stress strain heterogeneities in copper thin films: texture and substrate effects, Computational Materials Science, 39, 137–41.

Slagle, O.D., McKinstry, H.A., 1967. Temperature dependence of the elastic constants of the alkali halides. I. NaCl, KCl, and KBr, Journal of Applied Physics, 38, 437–446.

Smith, C.S., 1948. Grains, phases and interfaces, an interpretation of microstructure. Trans. Metall. Soc. AIME 175, 15.

Sorby, H.C., 1886. The application of very high powers to the study of the microscopical structure of steel. J. Iron Steel Inst. 30 (1), 140–145.

Sorby, H.C., 1887. On the microscopical structure of iron and steel. J. Iron Steel Inst. 31 (1), 255–288.

Srikanth, A., Zabaras, N., 1999. A computational model for the finite element analysis of thermoplasticity coupled with ductile damage at finite strains. International Journal for Numerical Methods in Engineering, 45, 1569-1605.

Srolovitz, D.J., Grest, G.S., Anderson, M.P., 1986. Computer simulation of recrystallization–I. Homogeneous nucleation and growth. Acta. Metall. 34, 1833–1845.

Staker, M.R. and Holt, D.L., 1972. The dislocation cell size and dislocation density in copper deformed at temperatures between 25 and 700 C. Acta Metallurgica, 20(4), pp.569-579.

Staroselsky, A., Anand, L., 1998. Inelastic deformation of polycrystalline face centered cubic materials by slip and twinning, Journal of the Mechanics and Physics of Solids, 46, 671–96.

Staroselskya, A., Anand, L., 2003. A constitutive model for hcp materials deforming by slip and twinning: application to magnesium alloy AZ31B, International Journal of Plasticity, 19, 1843–64.

Stead, J.E., 1898. The crystalline structure of iron and steel. J. Iron Steel Inst. 53 (1), 145–205.

Stoughton, T. B. 2000 A general forming limit criterion for sheet metal forming, International Journal of Mechanical Sciences 42, 1–27.

Stoughton, T. B., Zhu, X. 2004 Review of theoretical models of the strain-based FLD and their relevance to the stress-based FLD, International Journal of Plasticity 20, 1463–1486.

Suzuki, Y. Fanelli, V.R., Betts, J.B., Freibert, F.J., Meilke, C.H., Mitchell, J.N., Ramos, M., Saleh, T.A., Migliori, A., 2011. Temperature dependence of elastic moduli of polycrystalline beta plutonium, Physical Review B, 84, 064105-1 – 064105-11.

Svendsen, B., 2002. Continuum thermodynamic models for crystal plasticity including the effects of geometrically-necessary dislocations. Journal of the Mechanics and Physics of Solids, 50(6), pp.1297-1329.

Swan, P.R., 1963. In: Thomas, G., Washburn, J. (Eds.), Dislocations Arrangements in Face Centered Cubic Metals. Electron Microscopy and Strength of Crystals. Interscience, New York, pp. 131–181.

Takaki, T., Tomita, Y., 2010. Static recrystallization simulations starting from predicted deformation microstructure by coupling multi-phase-field method and finite element method based on crystal plasticity, International Journal of Mechanical Sciences, 52 (2), 320–328.

Takaki, T., Yamanaka, Y., Higa, Y., Tomita, Y., 2007. Phase-field model during static recrystallization based on crystal-plasticity theory, Journal of Computer-Aided Materials Design, 14, 75–84.

Takaki, T., Hisakuni, Y., Hirouchi, T., Yamanaka, A., Tomita, Y., 2009. Multi-phase-field simulations for dynamic recrystallization, Computational Materials Science, 45 (4), 881–888.

Takata, K., Ohwue, T., Saga, M. and Kikuchi, M., 2000. Formability of Al-Mg alloy at warm temperature. In Materials science forum (Vol. 331, pp. 631-636). Trans Tech Publications.

Tang, J.G., Zhang, X.M., Chen, Z.Y., Deng, Y.L., 2006. Simulation of rolling deformation texture of fcc metals with crystal plasticity finite element model, Materials Science and Technology, 22, 1171–6.

Taylor, G.I., 1934. The mechanism of plastic deformation of crystals. Part I-Theoretical. Proc. R. Soc. London 145 (A), 312–387.

Taylor, G.I., 1938. Plastic strain in metals. Journal of the Institute of Metals, 62, 307–24.

Terentyev, D., Xiao, X., Dubinko, A., Bakaeva, A. and Duan, H., 2015. Dislocation-mediated strain hardening in tungsten: Thermo-mechanical plasticity theory and experimental validation. Journal of the Mechanics and Physics of Solids, 85, pp.1-15.

Thomason, P. F. 1990 Ductile Fracture of Metals, Pergamon Press. Pgs. 188-207, Great Britain.

Thompson, A.W., 1977. Substructure strengthening mechanisms. Metallurgical Transactions A, 8(6), pp.833-842.

Tikhovskiy, I., Raabe, D., Roters, F., 2006. Simulation of the deformation texture of a 17 stainless steel using the texture component crystal plasticity FE method considering texture gradients, Scripta Materialia, 54, 1537–42.

Tikhovskiy, I., Raabe, D., Roters, F., 2007. Simulation of earing during deep drawing of an Al-3 (AA 5754) using a texture component crystal plasticity FEM, Journal of Materials Processing Technology, 183, 169–75.

Tjahjanto, D.D., Roters, F., Eisenlohr, P., 2007. Iso-work-rate weighted-Taylor homogenization scheme for multiphase steels assisted by transformation-induced plasticity effect, Steel Research International, 78, 777–83.

Toros, S., Ozturk, F., 2010. Modeling uniaxial, temperature and strain rate dependent behavior of Al–Mg alloys, Computational Materials Science, 49, 333-339.

Toros, S., Ozturk, F., Kacar, I., 2008, Review of warm forming of aluminum-magnesium alloys. Journal of Materials Processing Technology, 207, 1-12.

Tugcu, P., Neale, K.W., Wu, P.D., Inal, K., 2004. Crystal plasticity simulation of the hydrostatic bulge test, Textures and Microstructures, 20, 1603–53.

Turkmen, H.S., Dawson, P.R., Miller, M.P., 2002. The evolution of crystalline stresses of a polycrystalline metal during cyclic loading, International Journal of Plasticity, 18, 941–69.

Turkmen, H.S., Loge, R.E., Dawson, P.R., Miller, M.P., 2003. On the mechanical behavior of AA 7075-t6 during cyclic loading, International Journal of Fatigue, 25, 267–81.

Van den Boogaard, A.H., Bolt, P.J. and Werkhoven, R.J., 2001. Aluminum sheet forming at elevated temperatures. Simulation of Materials Processing: Theory, Method and Applications, pp.819-824.

Van Den Boogaard, A.H., Huetink, J., 2006. Simulation of aluminum sheet forming at elevated temperatures. Computer Methods in Applied Mechanics and Engineering, 195, 6691-6709.

Van Den Boogaard, A.H., Werkhoven, R.J., Bolt, P.J., 2001. Modeling of Al–Mg sheet forming at elevated temperatures. International Journal of Forming Processes, 4, 361-375.

Van Houtte, P., Delannay, L., Kalidindi, SR., 2002. Comparison of two-grain interaction models for polycrystal plasticity and deformation texture prediction, International Journal of Plasticity, 18, 359–77.

Van Houtte, P., Kanjarla, A.K., Van Bael, A., Seefeldt, M., Delannay, L., 2006. Multiscale modelling of the plastic anisotropy and deformation texture of polycrystalline materials, European Journal of Mechanics—Solids, 25, 634–48.

Van Houtte, P., Van Bael, A., Seefeldt, M., Delannay, L., 2005. The application of multiscale modelling for the prediction of plastic anisotropy and deformation textures, Materials Science Forum, 495–497, 31–41.

Varshni, Y. P., 1970. Temperature dependence of the elastic constants, Physical Review B, 2, 3952-3958.

Velmanirajan, K., Anuradha, K., Syed Abu Thaheer, A., Narayanasamy, R., Madhavan, R., Satyam Suwas, 2014. Experimental investigation of forming limit, void coalescence and crystallographic textures of aluminum alloy 8011 sheet annealed at various temperatures, Archives of Civil and Mechanical Engineering, 14, 398–416.

Venkataramani, G., Kirane, K., Ghosh, S., 2008. Microstructural parameters affecting creep induced load shedding in Ti-6242 by a size dependent crystal plasticity FE model, International Journal of Plasticity, 24, 428–54.

Venkatramani, G., Ghosh, S., Mills, M., 2007. A size-dependent crystal plasticity finite-element model for creep and load shedding in polycrystalline titanium alloys, Acta Materialia, 55, 971–3986.

Vitek, V., Mrovec, M., Bassani, J.L., 2004. Influence of non-glide stresses on plastic flow: from atomistic to continuum modeling, Materials Science and Engineering A, 365, 31–7.

Vogler, T.J., Clayton, J.D., 2008. Heterogeneous deformation and spall of an extruded tungsten alloy: plate impact experiments and crystal plasticity modeling, Journal of the Mechanics and Physics of Solids, 56, 297–335.

Wagoner, R.H., Nakamachi, E., Germain, Y., 1988. Analysis of sheet forming operations using the finite element method, In: Proceedings of IDDRG working groups, Toronto, p. 1.

Watchman Jr., J.B., Tefft, W.E., Lam Jr., D.G., Apstein, C.S., 1961. Exponential temperature dependence of Young's modulus for several oxides, Physics Review, 122, 1754–1759.

Watanabe, I., Terada, K., deSouza, E.A., Peric, D., 2008. Characterization of macroscopic tensile strength of polycrystalline metals with two-scale finite element analysis, Journal of the Mechanics and Physics of Solids, 56, 1105–25.

Wei, Y.J., Anand, L., 2004. Grain-boundary sliding and separation in polycrystalline metals: application to nanocrystalline fcc metals, Journal of the Mechanics and Physics of Solids, 52, 2587–616.

Wei, Y.J., Su, C., Anand, L., 2006. A computational study on the mechanical behavior of nanocrystalline fcc metals, Acta Materialia, 54, 3177–90.

Wen, X.Y., Zhai, T., Xiao, C.H., Ningileri, S., Li, Z., Lee, W.B., Das, S. 2005 A dislocation-model of forming limit diagrams of FCC metal sheet with combination of cube and copper orientations, Materials Science and Engineering A 402, 149–157.

Wever, F., 1924. Über die Walzstruktur kubisch kristallisierender Metalle. Z. Phys. 28, 69–90.

Wu, H. -C. "Continuum Mechanics and Plasticity", Chapman and Hall/CRC Press, United States of America, 2004.

Wu, P.D., Embury, J.D., Lloyd, D.J., Huang, Y., Neale, K.W. 2009 Effects of superimposed hydrostatic pressure on sheet metal formability, International Journal of Plasticity 25, 1711–1725.

Wu, P. D., Graf, A., MacEwan, S. R., Lloyd, D. J., Jain, M., Neale, K. W. 2005 On forming limit stress diagram analysis, International Journal of Solids and Structures 42, 2225–2241.

Wu, P.D., Neale, K.W., Van der Giessen, E., 1997. On crystal plasticity FLD analysis, Proceedings of the Royal Society A, 453, 1831–1848.

Wu, P.D., Neale, K.W., Van Der Giessen, E., Jain, M., Makinde, A., MacEwan, S.R., 1998. Crystal plasticity forming limit diagram analysis of rolled aluminum sheet, Metallurgical and Materials Transactions A, 29, 527–535.

Xie, C.L., Nakamachi, E., 2002. Investigations of the formability of BCC steel sheets by using crystalline plasticity finite element analysis, Materials and Design, 23, 59–68.

Xu, B., Yonezu, A., Yue, Z., Chen, X., 2009. Indentation creep surface morphology of nickel-based single crystal superalloys, Computational Materials Science, 46, 275–85.

Xu, Z.T., Peng, L.F., Fu, M.W., Lai, X.M. 2015 Size effect affected formability of sheet metals in micro/meso scale plastic deformation: Experiment and modeling. International Journal of Plasticity 68, 34–54.

Yang, M., Dong, X., Zhou, R., Cao, J. 2010 Crystal plasticity-based forming limit prediction for FCC materials under non-proportional strain-path, Materials Science and Engineering A 527, 6607–6613.

Yoon, J.W., Barlat, F., Gracio, J.J., Rauch, E., 2005. Anisotropic strain hardening behavior in simple shear for cube textured aluminum alloy sheets, International Journal of Plasticity, 12, 2426–2447.

Yoshida, K., Kuwabara, T. 2007 Effect of strain hardening behaviour on forming limit stresses of steel tube subjected to non-proportional loading paths, International Journal of Plasticity 23, 1260–1284.

You, X., Connolley, T., McHugh, P.E., Cuddy, H., Motz, C., 2006. A combined experimental and computational study of deformation in grains of biomedical grade 316LVM stainless steel, Acta Materialia, 54, 4825–40.

Yu, J., Maniatty, A.M., Knorr, D.B., 1997. Model for predicting thermal stresses in thin polycrystalline films, Journal of the Mechanics and Physics of Solids, 45, 511-534.

Yue, Z.F., 2005. Surface roughness evolution under constant amplitude fatigue loading using crystal plasticity, Engineering Fracture Mechanics, 72, 749–57.

Zadpoor, A.A., Sinke, J., Benedictus, R., 2009 Formability prediction of high strength aluminum sheets, International Journal of Plasticity 25, 2269–2297.

Zaefferer, S., Kuo, J-C., Zhao, Z., Winning, M., Raabe, D., 2003. On the influence of the grain boundary misorientation on the plastic deformation of aluminum bicrystals, Acta Materialia, 51(16), 4719–35.

Zambaldi, C., Roters, F., Raabe, D., Glatzel, U., 2007. Modeling and experiments on the indentation deformation and recrystallization of a single-crystal nickel-base superalloy, Materials Science Engineering A, 454– 455, 433–40.

Zamiri, A., Bieler, T.R., Pourboghrat, F., 2009. Anisotropic crystal plasticity finite element modeling of the effect of crystal orientation and solder joint geometry on deformation after temperature change, Journal of Electronic Materials, 38, 231–40.

Zhang, H., Lin, G.Y., Peng, D.S., Yang, L.B. and Lin, Q.Q., 2004. Dynamic and static softening behaviors of aluminum alloys during multistage hot deformation. Journal of materials processing technology, 148(2), pp.245-249.

Zhang, F., Bower, A.F., Mishra, R.K., Boyle, K.P., 2009. Numerical simulations of necking during tensile deformation of aluminum single crystals, International Journal of Plasticity, 25, 49–69.

Zhang, L., Wang, J. 2012 Modelling the localized necking in anisotropic sheet metals. International Journal of Plasticity 39, 103–118.

Zhang, M., Zhang, J., McDowell, D.L., 2007. Microstructure-based crystal plasticity modeling of cyclic deformation of Ti–6Al–4V, International Journal of Plasticity, 23, 1328–48.

Zhang, Z. L., Hauge, M., Ødegård, J., Thaulow, C. 1999 Determining material true stress-strain curve from tensile specimens with rectangular cross sections, International Journal Solids and Structures 36, 3497–3516.

Zhao, Z., Kuchnicki, S., Radovitzky, R., Cuitiño, A., 2007. Influence of ingrain mesh resolution on the prediction of deformation textures in fcc polycrystals by crystal plasticity FEM, Acta Materialia, 55, 2361–73.

Zhao, Z., Mao, W., Roters, F., Raabe, D., 2001. Introduction of a texture component crystal plasticity finite element method for anisotropy simulations, Advanced Engineering Materials, 3, 984–90.

Zhao, Z., Mao, W., Roters, F., Raabe, D., 2004. A texture optimization study for minimum earing in aluminum by use of a texture component crystal plasticity finite element method, Acta Materialia, 52, 1003–12.

Zhao, Z., Radovitzky, R., Cuitiño, A., 2004. A study of surface roughening in fcc metals using direct numerical simulation, Acta Materialia, 52(20), 5791–804.

Zhao, Z., Ramesh, M., Raabe, D., Cuitiño, A., Radovitzky, R., 2008. Investigation of three-dimensional aspects of grain-scale plastic surface deformation of an aluminum oligocrystal, International Journal of Plasticity, 24, 2278–97.

Zhuang, W.M., Wang, S.W., Cao, J., Lin, L.G., Hart, C., 2008. Hydroforming of micro tubes: crystal plasticity finite element modeling, Steel Research International, 1, 293–300 .

Zienkiewicz, O.C., Taylor, R.L., 2005. The finite element method for solid and structural mechanics, 6th ed. Butterworth-Heinemann.

Appendix

Kinetics of Plastic Flow

The crystal plasticity description of plastic flow on slip system α is governed by the equation

$$\dot{\gamma}^{\alpha}(T) = \dot{\gamma}_0 \left(\frac{\tau^{\alpha}}{g^{\alpha}(T)} \right)^{1/m} \tag{A.1}$$

where the numerator τ^{α} is the resolved stress on slip system α and denominator $g^{\alpha}(T)$ is the current strength of the slip system. The exponent $1/m$ is the rate sensitivity parameter equal to 0.02 for this study. $\dot{\gamma}_0$ is the reference slip rate equal to 0.001 s^{-1} .

Since the rate dependence of plastic flow is governed by the above equation, it is convenient to find a description of the hardening $g^{\alpha}(T)$ as a function of temperature only. In order to obtain this description, the assumption must be made that the strain rate effects can be sufficiently captured by the strain rate sensitivity parameter m and the temperature dependence of the strain hardening is taken as some reference strain-rate. It is also noted that this model is for low-strain rate deformation, and simulations are carried out at a constant strain rate $\dot{\varepsilon} \approx 10^{-3} s^{-1}$.

The mechanical threshold stress model (Follansbee and Kocks, 1988, Kocks and Mecking, 2003) presents a good phenomenological description of the temperature dependence of the data collected with convincing physical basis. The well-known relation between activation energy and temperature/strain rate is given by

$$\frac{\Delta G}{\mu b^3} = \left(\frac{kT}{\mu b^3} \right) ln \left(\frac{\dot{\varepsilon}_0}{\dot{\varepsilon}} \right) \tag{A.2}$$

where μ is the shear modulus, b is the Burger's vector, T is temperature, k is the Boltzmann constant, $\dot{\varepsilon}$ is the applied strain rate, and $\dot{\varepsilon}_0$ is the reference strain rate equal to 10^7 s^{-1} (Kocks and Mecking, 2003). In Kocks' description, a relationship exists through a scaling stress that brings the stress-strain curves of various temperatures to unison. This dependence was found systematically and the following relationship was concluded.

$$\Delta G = F_0 \left\{ 1 - \left(\frac{\sigma}{\sigma_0} \right)^{p} \right\}^{q} \tag{A.3}$$

The parameter definitions are described in section 5.6.1 with $\sigma_0 = \hat{\tau}$. Rearrangement of equation (A.3) yields

$$\sigma = \sigma_0 \left\{ 1 - \left(\frac{\Delta G}{F_0} \right)^{1/q} \right\}^{1/p} \tag{A.4}$$

where arbitrary constants p and q can be substituted as $1/q$ and $1/p$. Substituting the temperature and strain rate dependence of ΔG leaves

$$\sigma = \sigma_0 \left\{ 1 - \left(\frac{kT}{F_0} ln \left(\frac{\dot{\varepsilon}_0}{\dot{\varepsilon}} \right) \right)^{p} \right\}^{q} \tag{A.5}$$

where where is the total activation energy of the system at zero stress. Therefore, at sufficient temperature and low strain-rate approaching F_0, the flow becomes thermodynamically driven and does not require increasing stress. In this paper, recalling that the model is employed with constant and low applied strain-rates, the term $ln(\dot{\varepsilon}_0/\dot{\varepsilon})$ is modeled as a constant. Therefore, at constant strain rates, the Kocks-Mecking model is very similar to the model presented in equation (5.15)–(5.18). It is shown here again in its general form:

$$x = \bar{x} \left\{ 1 - \left(\frac{T}{T_x} \right)^{p} \right\}^{q} \tag{A.6}$$

where x and $\bar{x}$ denote the hardening parameters $(h_0, h_s, \tau_0, \tau_s)$. Each hardening parameter has a physically motivated relation to deformation phenomena, is can be assumed that each parameter may behave according to the proposed temperature dependence model, yielding equation (A.6).